Observations of tropical cirrus by elastic backscatter lidars and the development of a cloud and aerosol retrieval algorithm for Raman lidars

Tyler J. Thorsen

A dissertation
submitted in partial fulfillment of the
requirements for the degree of

Doctor of Philosophy

University of Washington

2014

Reading Committee:

Qiang Fu, Chair

Thomas P. Ackerman

Roger T. Marchand

Program Authorized to Offer Degree:
Atmospheric Sciences

University of Washington

Abstract

Observations of tropical cirrus by elastic backscatter lidars and the development of a cloud and aerosol retrieval algorithm for Raman lidars

Tyler J. Thorsen

Chair of the Supervisory Committee:
Professor Qiang Fu
Department of Atmospheric Sciences

Tropical cirrus cloud properties from elastic backscatter lidars— namely the Atmospheric Radiation Measurement (ARM) program's ground-based micropulse lidars (MPL) and the spaceborne Cloud-Aerosol Lidar Infrared Pathfinder Satellite Observations (CALIPSO) lidar— are examined. The MPL detects significantly less cirrus clouds relative to CALIPSO, particularly during the daytime. However, the MPL samples enough cirrus at night to provide similar statistics of macrophysical and optical properties as CALIPSO. Both sets of lidar observations are supplemented with cloud radar observations to calculate radiative heating rate profiles from a ground-based and spaceborne perspective. The inferred radiative effect of clouds is much smaller when using the ground-based data, mostly due to the lack of cirrus detected by the MPL. The relatively new and more advance ARM Raman lidar (RL) is shown to be more sensitive to cirrus than the ARM MPL and detects a similar amount of cirrus as CALIPSO. Daytime measurements using the RL elastic channel are relatively unaffected by the solar background and are therefore suited for checking the observed diurnal cycles from the MPL and CALIPSO. Comparisons with RL observations show that the geometrical thickness of cirrus from the MPL and CALIPSO datasets are biased thin during the daytime due to increased noise.

Various upgrades since its conception have made the ARM RL a viable tool for cloud studies as demonstrated by this thesis. Since the ARM RL was not originally designed for cloud observations, the current automated processing algorithms do not identify all clouds nor attempt to retrieve cloud extinction profiles. Therefore an improved Feature detection and EXtinction retrieval (FEX) algorithm is developed. The approach of FEX is to use multiple quantities to identify features (clouds and aerosols) using range-dependent context-sensitive detection thresholds. The use of multiple quantities provides complementary depictions of cloud and aerosol locations. The extinction profiles are directly retrieved using the Raman method, which are supplemented by other retrieval methods developed for elastic backscatter lidars. A classification of feature type is made guided by the atmosphere's thermodynamic state and the feature's scattering properties. The contribution of multiple scattering, which is significant for hydrometeors, is explicitly considered for each of the ARM RL channels. The FEX framework is also suitable for other advance lidars, i.e. high spectral resolution lidars (HSRL). The continuously operated, automated ARM RLs paired with FEX provide an enormous wealth of water vapor, temperature, aerosol and cloud data unmatched by other remote sensing systems.

TABLE OF CONTENTS

Page

List of Figures iii

List of Tables xiv

Chapter 1: Introduction 1

Chapter 2: Comparison of the CALIPSO satellite and ground-based observations of cirrus clouds at the ARM TWP sites 5

2.1 Introduction 5

2.2 Datasets 6

2.3 Comparison Methodology 9

2.4 Sampling Issues 11

2.5 Comparisons of CALIPSO and Ground-based Lidar Cloud Observations 16

2.6 Summary 47

Appendix 50

2.A Merging CALIPSO's Multi-resolution Layers 50

2.B TTL Cloud Diurnal Biases 53

Chapter 3: Cloud effects on radiative heating rate profiles over Darwin using ARM and A-train radar/lidar observations 57

3.1 Introduction 57

3.2 Data and Methodology 59

3.3 Comparison of ARM and A-train Cloud and Radiative Heating Profiles 65

3.4 Attribution of Cloud Radiative Forcing Differences 72

3.5 Summary 80

Appendix 82

3.A Retrieved Ice Cloud Properties 82

3.B Impact of MPL Attenuation and Sensitivity on Cloud Fraction 87

Chapter 4: Macrophysical properties of tropical cirrus clouds from the CALIPSO satellite and from ground-based micropulse and Raman lidars 91
4.1 Introduction 91
4.2 Datasets 93
4.3 Comparison Method 96
4.4 Results 98
4.5 Summary 116

Chapter 5: Automated retrieval of cloud and aerosol properties from the ARM Raman lidar, part 1: feature detection 118
5.1 Introduction 118
5.2 The ARM Raman lidar 119
5.3 Feature detection algorithm 120
5.4 Feature discrimination 141
5.5 Performance assessments 145
5.6 Summary 152
Appendix 153
5.A Depolarization calibration 153

Chapter 6: Automated retrieval of cloud and aerosol properties from the ARM Raman lidar, part 2: extinction 155
6.1 Introduction 155
6.2 The ARM Raman lidar 156
6.3 Inversion of the elastic and Raman lidar equations 157
6.4 Retrieval algorithm 160
6.5 Results 181
6.6 Summary 193

Chapter 7: Conclusion 194
7.1 Summary 194
7.2 Future directions 197

Bibliography 205

LIST OF FIGURES

Figure Number Page

2.1 Map of the three ARM TWP sites: Darwin, Manus and Nauru (left to right, red dots), a subset of CALIPSO ground tracks (blue lines) and the 1.25° × 5° latitude-by-longitude box from which CALIPSO observations are taken from (heavy black line). 8

2.2 Monthly distribution of profiles available at each ARM TWP site for CALIPSO (black line) and ground-based (red line) observations relative to the total number of profiles (dashed line) and the total number of cloudy profiles (solid line). The distribution of profiles in the unrestricted datasets are given in the top panel. The distribution of profiles in the ice and TTL restricted datasets are given in the middle and bottom panel, respectively. Percentages in each month are calculated relative to the total number of observations in the entire sampling period. 12

2.3 Percentage of profiles which are attenuated during each month relative to the total number of cloudy profiles for that month for CALIPSO (black) and ground-based (red) observations. Solid lines show the percent attenuated for the full set of observations. Nighttime only observations are given as dashed lines and daytime only as dotted lines. 13

2.4 Nighttime transparent cloud fraction profiles (panel a and c). CALIPSO cloud fraction (5 km resolution) is given as a solid line for Manus (black), Nauru (blue) and Darwin (red) while the ground-based cloud fraction is given as dashed lines. The shaded regions represent the 95% confidence interval due to CALIPSO's sampling uncertainty. Cloud fraction is shown for (a) the native (1 and 5 minutes averaged) ground-based observation and (c) the cloud fraction derived using the ground-based "pixel" method described in the text. The difference (ground-based minus CALIPSO) in cloud fraction at each altitude bin is shown for (b) the native ground-based observations and (d) the ground-based "pixel" observations. Regions of statistically significantly differences are indicated by a thick line. 23

2.5 PDFs of (a) ice and (b) TTL cloud top heights (top row) and cloud base heights (bottom row) from CALIPSO (black line) and ground-based (red line) datasets. The shaded region represents the 95% confidence interval due to CALIPSO's sampling uncertainty. The three ARM sites are shown (left to right): Manus, Nauru and Darwin. 28

2.6 PDFs of (a) ice and (b) TTL cloud geometrical thickness from CALIPSO (black line) and ground-based (red line) datasets. The shaded region represents the 95% confidence interval due to CALIPSO's sampling uncertainty. The three ARM sites are shown (left to right): Manus, Nauru and Darwin. 29

2.7 Frequency of the number of ice cloud layers per profile from CALIPSO and ground-based datasets for the three ARM TWP sites. The bounds on CALIPSO's 95% confidence interval are given as red lines. 31

2.8 PDFs of (a) ice and (b) TTL cloud optical depths from CALIPSO L2 v3.01 cloud product (black line) and the CALIPSO optical depth retrieval of Yang et al. (2010) (blue line). The shaded region on each CALIPSO retrieval represents the 95% confidence interval due to the sampling uncertainty. Ground-based optical depths are shown for the lidar ratio fixed at 25 sr (red line) and the variable lidar ratio retrieval (green line). The three ARM TWP sites are shown (left to right): Manus, Nauru and Darwin. The top row of plots shows the optical depths from $0.01 \leq \tau < 0.2$ and the bottom row shows $0.2 \leq \tau \leq 3$. The upper-right corner of each plot gives the percent of observations which fall within the plotted optical depth range. The mean optical depth within each range is denoted with an "x" along the x-axis. 35

2.9 PDFs of ice cloud top heights (top row) and cloud base heights (bottom row) from CALIPSO (black line) and ground-based (red line) datasets during the (a) nighttime and (b) daytime. The shaded region represents the 95% confidence interval due to CALIPSO's sampling uncertainty. The three ARM sites are shown (left to right): Manus, Nauru and Darwin. 39

2.10 PDFs of ice cloud geometrical thickness from CALIPSO (black line) and ground-based (red line) datasets during the (a) nighttime and (b) daytime. The shaded region represents the 95% confidence interval due to CALIPSO's sampling uncertainty. The three ARM sites are shown (left to right): Manus, Nauru and Darwin. 40

2.11 Frequency of the number of ice cloud layers per profile during the (a) nighttime and (b) daytime from CALIPSO and ground-based datasets for the three ARM TWP sites. The bounds on CALIPSO's 95% confidence interval are given as red lines. The number of layers in the ground-based data is derived using the MPL "pixel" method, which is described in the text. 41

2.12 PDFs of ice cloud optical depths from CALIPSO L2 v3.01 cloud product (black line) and the CALIPSO optical depth retrieval of Yang et al. (2010) (blue line) during the (a) nighttime and (b) daytime. The shaded region on each CALIPSO retrieval represents the 95% confidence interval due to the sampling uncertainty. Ground-based optical depths are shown for the lidar ratio fixed at 25 sr (red line) and the variable lidar ratio retrieval (green line). The three ARM TWP sites are shown (left to right): Manus, Nauru and Darwin. The top row of plots shows the optical depths from $0.01 \leq \tau < 0.2$ and the bottom row shows $0.2 \leq \tau \leq 3$. The upper-right corner of each plot gives the percent of observations which fall within the plotted optical depth range. The mean optical depth within each range is denoted with an "x" along the x-axis. 42

2.13 PDFs of the highest cloud top heights (top row) and lowest cloud base heights (bottom row) from CALIPSO (black line) and ground-based (red line) ice cloud datasets. The dashed line gives the ground-based ice cloud PDF for the datasets which has been averaged to an equivalent spatial resolution of 5 km. The shaded region represents the 95% confidence interval due to CALIPSO's sampling uncertainty. The three ARM sites are shown (left to right): Manus, Nauru and Darwin. 44

2.14 PDFs of ice cloud column optical depths from (a) CALIPSO L2 v3.01 cloud product (black line) and (b) the CALIPSO optical depth retrieval of Yang et al. (2010) (black line). The shaded region represents the 95% confidence interval due to CALIPSO's sampling uncertainty. Ground-based ice cloud column optical depths are shown for the lidar ratio fixed at 25 sr (red line) and the variable lidar ratio retrieval (green line). The dashed lines give the ground-based column optical depths for datasets which have been averaged to an equivalent spatial resolution of 5 km. The three ARM TWP sites are shown (left to right): Manus, Nauru and Darwin. The top row of plots shows the optical depths from $0.01 \leq \tau < 0.2$ and the bottom row shows $0.2 \leq \tau \leq 3$. 46

2.15 A fictitious schematic of CALIPSO's multi-resolution cloud layer detection. Colors represent cloud layers found at 5 km (red), 20 km (green) and 80 km (blue) of horizontal averaging. Hashing indicates a cloud layer being identified at multiple horizontal resolutions. White represents regions of clear air. 51

2.16 Frequency of the number of ice cloud layers per profile from the CALIPSO 5 km cloud product for the three ARM TWP sites. Overlapping and adjacent layers are not merged together. 52

2.17 PDFs of TTL cloud top heights (top row) and cloud base heights (bottom row) from CALIPSO (black line) and ground-based (red line) datasets during the (a) nighttime and (b) daytime. The shaded region represents the 95% confidence interval due to CALIPSO's sampling uncertainty. The three ARM sites are shown (left to right): Manus, Nauru and Darwin. 54

2.18 PDFs of TTL cloud geometrical thickness from CALIPSO (black line) and ground-based (red line) datasets during the (a) nighttime and (b) daytime. The shaded region represents the 95% confidence interval due to CALIPSO's sampling uncertainty. The three ARM sites are shown (left to right): Manus, Nauru and Darwin. 55

2.19 PDFs of TTL cloud optical depths from CALIPSO L2 v3.01 cloud product (black line) and the CALIPSO optical depth retrieval of Yang et al. (2010) (blue line) during the (a) nighttime and (b) daytime. The shaded region on each CALIPSO retrieval represents the 95% confidence interval due to the sampling uncertainty. Ground-based optical depths are shown for the lidar ratio fixed at 25 sr (red line) and the variable lidar ratio retrieval (green line). The three ARM TWP sites are shown (left to right): Manus, Nauru and Darwin. The top row of plots shows the optical depths from $0.01 \leq \tau < 0.2$ and the bottom row shows $0.2 \leq \tau \leq 3$. The upper-right corner of each plot gives the percent of observations which fall within the plotted optical depth range. The mean optical depth within each range is denoted with an "x" along the x-axis. 56

3.1 CloudSat and CALIPSO cloud mask from the DARDAR-MASK product on 25 December 2010. The legend gives the terminology used in this study when delineating clouds by lidar/radar instrument(s). 66

3.2 Vertical profiles of the mean ARM (black line) and A-train (red line) (a) net, (b) shortwave, and (c) longwave clear-sky heating rate. 67

3.3 Vertical profiles of the mean ARM (black) and A-train (red) (a) net, (b) shortwave, and (c) longwave cloud radiative forcing calculated using clouds detected by radar (dashed line) and clouds detected by the combination of radar and lidar (solid line). 68

3.4 Vertical cloud fraction profiles of (a) combined radar and lidar observations (solid line) and (b) radar (dashed line) and lidar (dotted line) observations for the ARM (black) and A-train (red) datasets. 69

3.5 Height dependant probability density functions (HPDFs) of cloud visible extinction (colors) derived from (a) ARM and (b) A-train observations. Also given are the mean in-cloud profiles of cloud visible extinction derived from ARM (brown line) and A-train (red line) observations. For HPDFs, altitude is divided into 1 km bins and extinction into 50 logarithmically-space bins from 10^{-4} to 10^{3} km^{-1}. 71

3.6 MPL (black line) and CALIPSO (red line) horizontal sampling imposed by the amount of averaging of the lidar signal. 73

3.7 Vertical profiles of the mean (a) net, (b) shortwave, and (c) longwave cloud radiative forcing. Shown is the ARM (purple line) and A-train (orange line) observations which are forced to have the same mean combined radar and lidar cloud fraction profiles. The shading indicates the maximum and minimum cloud forcing from all iterations. The mean cloud radiative forcing profiles derived from the unmodified ARM (black line) and A-train (red line) observations are also given. 76
3.8 Vertical cloud fraction profiles of (a) clouds detected by radar only, (b) clouds detected by lidar only and (c) cloud detected by both radar and lidar. Shown is the ARM (purple line) and A-train (orange line) observations which are forced to have the same mean combined radar and lidar cloud fraction profiles. The shading indicates the maximum and minimum cloud fraction from all iterations. The cloud fraction profiles derived from the unmodified ARM (black line) and A-train (red line) observations are also given. 77
3.9 Vertical profiles of the mean (a) net, (b) shortwave, and (c) longwave cloud radiative forcing. Shown is the ARM (purple line) and A-train (orange line) observations which are forced to have the same mean radar only/lidar only/ both radar and lidar cloud fraction profiles. The shading indicates the maximum and minimum cloud forcing from all iterations. The mean cloud radiative forcing profiles derived from the unmodified ARM (black line) and A-train (red line) observations are also given. 79
3.10 Height dependant probability density functions (HPDFs) of ice cloud visible extinction (colors) derived from ARM (left column: a,c,e) and A-train (right column: b,d,f) observations. Also given are the mean in-cloud profiles of ice cloud visible extinction derived from ARM (brown line) and A-train (red line) observations. The HPDFs and mean profiles are shown separately for the cloud layers detected by radar (top row: a,b), lidar (middle row: c,d) and both radar and lidar (bottom row: e,f). For HPDFs, altitude is divided into 1 km bins and extinction into 50 logarithmically-space bins from 10^{-4} to 10^{3} km^{-1}. 84
3.11 Same as Figure 3.10, but for ice water content in 50 logarithmically-space bins from 10^{-5} to 10^{1} $g\ m^{-3}$. 85
3.12 Same as Figure 3.10, but for ice particle effective radius in 2.5 μm bins. 86

3.13 Vertical profiles of the difference in daytime (left column: a,c) and nighttime (right column: b,d) cloud fraction between the unmodified A-train observations and the A-train observations where the mean combined radar and lidar cloud fraction profiles has been forced to match (see text). Differences (top row: a,b) are taken for three categories of ARM profiles: clear-sky (teal line), profiles with clouds transparent to the MPL (red line) and profiles with clouds which completely attenuate the MPL (blue line). The total difference (black line) is also given. The differences in these three categories are also shown as a percentage of the total cloud fraction difference (bottom row: c,d). The shading indicates the maximum and minimum differences from all iterations. 90

4.1 Median signal-to-noise ratio (SNR) in the clear-sky portion of profiles transparent to the lidar derived from the CALIPSO observations during the MPL sampling period (black), CALIPSO observations from the RL sampling period (blue), MPL observations (green) and RL observations (red). Profiles are shown separately for daytime (a) and nighttime (b). SNR profiles depicted as solid lines are calculated using the signals averaged to their respective amount of horizontal and vertical averaging used for deriving the cloud masks. Profiles depicted as dashed lines are calculated using approximately the same horizontal and vertical averaging for all three lidars. RL and MPL observations are collocated in time (± 4 hours) to CALIPSO overpasses. 102

4.2 Transparent cirrus cloud fraction profiles for MPL (green), RL (red) and CALIPSO (black) observations from June 2006 through August 2011 (a-c) and December 2010 through December 2012 (d-f). Profiles are shown separately for observations from all times (a/d), only daytime (b/e) and only nighttime (c/f). MPL and RL observations collocated in time (± 4 hours) to CALIPSO overpasses are depicted as solid lines. The shading on each line represents the 95% confidence interval due to statistical uncertainty. Dashed lines denote MPL and RL profiles derived using all available data. 106

4.3 The difference between the day and night mean transparent cirrus cloud fraction profiles for MPL (green), RL (red) and CALIPSO (black) observations from June 2006 through August 2011 (a) and December 2010 through December 2012 (b). MPL and RL observations collocated in time (± 4 hours) to CALIPSO overpasses are depicted as solid lines. The shading on each line represents the 95% confidence interval due to statistical uncertainty. Dashed lines denote MPL and RL profiles derived using all available data. 107

4.4 Total ice cloud fraction profiles for RL (red) and CALIPSO (black) observations from December 2010 through December 2012. Profiles are shown separately for observations from all times (a), only daytime (b) and only nighttime (c). RL observations collocated in time (± 4 hours) to CALIPSO overpasses are depicted as solid lines. The shading on each line represents the 95% confidence interval due to statistical uncertainty. Dashed lines denote RL profiles derived using all available data. 108

4.5 Probability density functions (PDFs) of cirrus cloud layer geometrical thickness in profiles transparent to the lidar for MPL (green), RL (red) and CALIPSO (black) observations from June 2006 through August 2011 (a-c) and December 2010 through December 2012 (d-f). Profiles are shown separately for observations from all times (a/d), only daytime (b/e) and only nighttime (c/f). MPL and RL observations collocated in time (± 4 hours) to CALIPSO overpasses are depicted as solid lines. The shading on each line represents the 95% confidence interval due to statistical uncertainty. Dashed lines denote MPL and RL profiles derived using all available data. Bin size for the PDFs is 0.5 km. 114

4.6 Hourly median cloud thickness anomaly relative to the median nighttime thickness for MPL (green 'x'), RL (red dot) and CALIPSO (black circle) observations. CALIPSO observations are shown for the June 2006 through August 2011 (black 'x' inside circle) and December 2010 through December 2012 (black dot inside circle) sampling periods. CALIPSO (black plus inside circle) and MPL (green cross) data from June 2006 through August 2011 forced to match RL's monthly sampling is also shown. Times when the RL sample size is poor are connected using a dotted line. Sunrise occurs at approximately 6 and sunset at 18. 115

5.1 Schematic comparing the expected molecular signal (left) to the signal measured by the lidar (right). 121

5.2 (a) Scattering ratio derived using the elastic and nitrogen channels, (b) scattering ratio derived using the low elastic and nitrogen channels, (c) scattering ratio derived using only the elastic channel, and (d) depolarization ratio after the final iteration of FEX for December 24, 2010 at Darwin. 126

5.3 Flow diagram for feature detection in the FEX algorithm. 129

5.4 The initial threshold (dashed blue) and final threshold (solid blue) for the profile at 19:58:00 UTC in Fig. 5.2 for the (a) scattering ratio derived using only the elastic channel and (b) depolarization ratio. For the scattering ratio derived using only the elastic channel, the initial profile (gray line) and final profile (black line) is given. Features identified in these ratios on the initial and final iteration are noted by the color in the bars on the right hand side of each panel—features which have been determined to be false detections are denoted by yellow and true feature denoted by blue. For reference, the expected clear-sky ratio is given as a dashed red line. 138

5.5 Feature mask on the final iteration of FEX for the ratios given in Fig. 5.2. Each color represents a different combination of the four ratios— scattering ratio derived using the elastic and nitrogen channels (EN), scattering ratio derived using the low elastic and nitrogen channels (ENL), scattering ratio derived using only the elastic channel (E), and depolarization ratio (D)— which detected the feature. Panel (a) shows the feature mask before any attempt was made to remove false detections. Panel (b) gives the final mask, which has had false detections removed. 139

5.6 (a) Scattering ratio derived using the elastic and nitrogen channels, (b) scattering ratio derived using the low elastic and nitrogen channels, (c) scattering ratio derived using only the elastic channel, and (d) depolarization ratio after the final iteration of FEX for May 10, 2013 at Darwin. (e) Feature mask where each color represents a different combination of the four ratios which detected the feature: scattering ratio derived using the elastic and nitrogen channels (EN), scattering ratio derived using the low elastic and nitrogen channels (ENL), scattering ratio derived using only the elastic channel (E), and depolarization ratio (D). 140

5.7 The (a) daytime and (b) nighttime cloud occurrence profiles for cloud detected by any ratio (gray), the scattering ratio derived using the low elastic and nitrogen channels (red), the scattering ratio derived using the elastic and nitrogen channels (green), the scattering ratio derived using only the elastic channel (blue), and the depolarization ratio (brown) at Darwin from December 2010 through December 2013. 141

5.8 The median threshold profiles (red) for points where the laser beam has not been completely attenuated and the median ratio value (blue) for points where that ratio detected a feature. Separate panels are shown for each ratio— (a,b) the scattering ratio derived using the low elastic and nitrogen channels, (c,d) the scattering ratio derived using the elastic and nitrogen channels, (e,f) the scattering ratio derived using only the elastic channel, and (g,h) depolarization ratio — and for (top row: a,c,e,g) daytime and (bottom row: b,d,f,h) nighttime profiles. The shaded region on both the threshold and ratio profiles encompasses the 5th to 95th percentiles from their respective distributions. 144

5.9 The cloud occurrence profile from the ARM DEP product (red) and from the new FEX algorithm (blue) described in this work at Darwin from December 2010 through December 2013. 146

5.10 The cloud occurrence profile from the MPL cloud mask (Wang and Sassen, 2001) (green) and RL-FEX cloud mask (blue) from December 2010 through August 2011 for (a) all pixels and (b) only pixels where both the MPL and RL SNR is greater than 3 in profiles where no rain was detected. 147

5.11 The cloud occurrence in transparent profiles from the RL at 2 min and 30 m of averaging (blue) and from the CALIPSO VFM product (red). The profile from the RL data averaged to 9 min and 30 m, which is approximately equivalent to CALIPSO's averaging below 8.2 km, is given in brown. The profile from the RL data averaged to 15 min and 60 m, which is approximately equivalent to CALIPSO's averaging above 8.2 km, is given in gray. Profiles are shown separately for the (a) daytime and (b) nighttime observations. This comparison includes CALIPSO profiles that fall within 200 km of the Darwin site from December 2010 through December 2013. The RL data are limited to times within ±2 hours of CALIPSO overpasses. 150

5.12 FEX feature mask for May 10, 2013 at Darwin when 9 min and 30 m of averaging is performed. Each color represents a different combination of the four ratios which detected the feature: scattering ratio derived using the elastic and nitrogen channels (EN), scattering ratio derived using the low elastic and nitrogen channels (ENL), scattering ratio derived using only the elastic channel (E), and depolarization ratio (D). 151

6.1 Flow diagram for the extinction retrieval in the FEX algorithm. Blue and red boxes denote the retrievals of particulate backscatter coefficient and lidar ratio, respectively. The best-estimate calculations occur in boxes with yellow backgrounds. Both the lidar ratio and particulate backscatter coefficient are retrieved at the laser wavelength $\lambda_0 = 355$ nm. The second subscripts given indicate the channels used to derive each quantity with E denoting the elastic channel, N denoting the nitrogen channel, EN denoting that both the elastic and nitrogen channels are used, and BE denoting a best-estimate derived from the combination of several quantities. 162

6.2 Feature classification thresholds using depolarization (δ) and particulate backscatter ($\beta_{p,BE}$) for (a) separating clouds and aerosol for bins without rain (see section 6.4.1) and (b) determining the cloud phase in the mixed phase temperature regime, i.e. a wet-bulb temperature (T_w) less than 0°C and a temperature (T) greater than −40°C. In panel (b), the horizontally oriented ice (HOI) thresholds are identified by a white dashed line and are only applied when the lidar ratio ($S'_{p,EN}$) is less than 12 sr. 168

6.3 Theoretical lidar ratio at 355 nm as a function of median volume radius (solid lines) for gamma droplet size distributions with $\mu = 0.5$ (gray), $\mu = 2$ (blue), $\mu = 10$ (pink), $\mu = 20$ (orange). Also shown is the median liquid cloud (red) and rain (purple) lidar ratios directly retrieved by FEX (Table 6.2). Values from the TWP and SGP RL are given as dashed and dotted lines, respectively. The lidar ratio threshold used by FEX to identify rain and horizontally oriented ice (HOI) is depicted as a dashed black line. 169

6.4 Distributions of depolarization (δ) and best-estimate particulate backscatter ($\beta_{p,BE}$) of pixels identified as clouds from August 2008 through July 2013 at the SGP site. The thresholds used to separate liquid from ice clouds (Fig. 6.2) are given as a black line with the upper left region for ice and the lower right region for liquid. 170

6.5 Feature classification for August 10, 2009 at the SGP site. Shown is the inputs used by the classification scheme: (a) depolarization ratio (δ), (b) particulate backscatter ($\beta_{p,BE}$) and (c) lidar ratio ($S^{'}_{p,EN}$). The resulting classification is given in panel (d) with pixels classified as either liquid cloud (red), rain (purple), ice (black), horizontally oriented ice (HOI; brown) or aerosol (gray). The 0°C contour of wet bulb temperature (T_w; blue line) and -40°C contour of temperature (T, green line) are also shown in panel (d). 171

6.6 The probability density functions (PDFs) of directly retrieved lidar ratios by FEX from August 2008 through July 2013 at the SGP site (dashed lines) and December 2010 through May 2014 at the TWP site (solid lines). Separate PDFs are given for each feature type: (a) aerosol, (b) rain, (c) liquid cloud, (d) ice cloud, and (e) horizontally oriented ice (HOI). A bin size of 1 sr is used in all panels. The PDF of HOI for TWP is not shown due its small sample size. . . . 178

6.7 FEX's retrievals on December 25, 2012 at the Darwin TWP site. (a) The scattering ratio derived using only the elastic channel, (b) the classification of features as either liquid cloud (red), rain (purple), ice (black), horizontally oriented ice (HOI; brown) or aerosol (gray), (c) the lidar ratio derived using the Raman method applied to the high channel signals, (d) the lidar ratio derived using the Raman method applied to the low channel signals, (e) the best-estimate lidar ratio, and (f) flag indicating the type of retrievals used in the best-estimate lidar ratio. Shades of red/blue in panel (f) denote the level of smoothing (Table 6.1) used for the Raman method for the high/low channel signals. Other colors in panel (f) denote those pixels where the lidar is determined by: interpolation (purple), transmission-loss method (green), profile-averaged (brown), object-averaged (pink), daily-averaged (orange), and climatological values (black). 179

6.8 The vertical occurrence of feature types at the (a) TWP site and (b) SGP site. The feature types given are liquid cloud (red), rain (purple), ice (black), horizontally oriented ice (HOI; brown) or aerosol (gray). The ice occurrence profile includes both random oriented ice (ROI) and HOI. The aerosol occurrence profiles has been scaled by a factor of 0.25. 182

6.9 The frequency of values used in the particulate backscatter best-estimate at the TWP site with values obtained from: the scattering ratio derived using both the low elastic and nitrogen channels (red), the scattering ratio derived using both the high elastic and nitrogen channels (blue), and the Fernald solution to the elastic lidar equation (black). Frequency is normalized by the number of bins at each altitude with a feature either (a,d) aerosol, (b,e) liquid cloud or (c,f) ice cloud. Frequency profiles are shown separately for (a,b,c) daytime and (d,e,f) nighttime profiles. 186

6.10 The frequency of values used in the lidar ratio best-estimate at the TWP site with values obtained from: the Raman method using the low channel signals (blue), the Raman method using the high channel signals (red), interpolation (purple), the transmission-loss method (green), profile-averages (brown), object-averaged (pink), daily-averages (orange), and climatological values (black). Frequency is normalized by the number of bins at each altitude with a feature either (a,d) aerosol, (b,e) liquid cloud or (c,f) ice cloud. Frequency profiles are shown separately for (a,b,c) daytime and (d,e,f) nighttime profiles. 187

6.11 The frequency of smoothing levels (Table 6.1) used in the lidar ratio derived from the Raman method using the high channel signals at the TWP site. Increasingly darker shades of red represent larger amounts of smoothing. Frequency is normalized by the number of bins at each altitude with a feature either (a) aerosol, (b) liquid cloud or (c) ice cloud. 188

6.12 Box plot of the relative error in the particulate extinction retrievals by neglecting multiple scattering at the TWP (left) and SGP (right) site. The colored boxes give the interquartile ranges with the thick black line denoting the median. The whiskers give the 5th and 95th percentiles. The error in HOI for TWP is not shown due its small sample size. 190

6.13 Comparison of aerosol optical depth derived from RL-FEX and a collocated sun photometer at the (a,b) TWP and (c,d) SGP site. Panels (a,c) are for the subset of profiles where the directly-retrieved extinction coefficients are available for all aerosol bins above 1.5 km and (b,d) for all profiles regardless of the type of retrieval used. The one-to-one line is shown in red. Summary statistics are given in the lower right of each panel: the sample size (N), the slope of the linear regression line, the correlation coefficient (r), the root-mean-squared error (RMS, relative to the mean RL optical depth), the bias error (mean difference relative to the mean RL optical depth). 192

LIST OF TABLES

Table Number Page

2.1 Cloud fraction 16

2.2 Cloud fraction, nighttime observations only. 17

2.3 Cloud fraction, daytime observations only. 17

2.4 Mean [km] and pseudo-standard deviation (parentheses, km) of ice cloud tops, bases and geometrical thickness. The 95% confidence interval for CALIPSO' sampling uncertainty is given in brackets. 25

2.5 Same as Table 2.4, but for TTL clouds. 26

4.1 Ratio of the median daytime background RMS noise to that at night for profiles transparent to the lidar. 100

4.2 Median cirrus cloud layer geometrical thicknesses (km) in transparent profiles. Bold values indicate that the difference between day and night is statistically significant. 110

4.3 CALIPSO cirrus cloud layer median geometrical thicknesses (km) derived from the L2 CPro product in transparent profiles. Layer thickness is also derived after applying two different extinction (α) thresholds to the data. Bold values indicate that the difference between day and night is statistically significant. . . 112

5.1 Specifications of the ARM RL transmitter and receiver channels used for feature detection in this study. 120

5.2 Hierarchy of calibration types and altitude regions used by FEX. Calibrations constants are taken as the median over all samples and interpolated constants are obtained using a cubic spline interpolant. The 2–9 km and 5–9 km altitude regions are not used for deriving $C^L_{\lambda_0}$ and C^L_{E,N_2}, respectively. Also given is the multiplicative factor use to modify the probability P used by the spatial filter to reduce false detections. 131

5.3 The calibration type used in each profile (percent). The relative uncertainties (in percents) are given in parentheses for the per-tweak and per-profile calibration constants. The standard deviation is determined in each per-tweak or per-profile region and the relative uncertainties are added in quadrature to obtain the uncertainties given in this table. The frequency of default calibrations includes the use of either per-day or historical calibrations. 132

5.4 Comparison between RL-FEX and MPL cloud detection (which uses the algorithm of Wang and Sassen (2001)) at Darwin from December 2010 through August 2011. Only the subset of pixels where both the RL and MPL SNR is greater than 3 are compared. Percentages are given relative to the detection of RL-FEX. 148
5.5 Same as Table 5.3, but for the depolarization misalignment angle. 154

6.1 Window sizes used for the 2-dimension Gaussian filter (see section 6.4.2.2) for the various smoothing levels. Window sizes are given as the number of height bins followed by the number of time bins. There is no smoothing in level 1. . . . 174
6.2 Median and standard deviation of the directly-retrieved lidar ratios for each feature type from December 2010 through May 2014 at the TWP site and from August 2008 through July 2013 at the SGP site. 176
6.3 Particle radii used in the multiple scattering model. Standard deviations are given in parentheses. For aerosols the bracketed values give the minimum and maximum sizes in the aerosol categories from Omar et al. (2005). 183

ACKNOWLEDGMENTS

I'd like first to thank my advisor, Qiang Fu, for his guidance and infectious optimism and excitement. The work in this thesis would not be possible without the expertise of my coauthors: Jennifer Comstock, Rob Newsom, Dave Turner, Mark Vaughan, and Dave Winker. My thesis committee consisting of Tom Ackerman, Roger Marchand and Rob Wood all provided valuable feedback throughout various stages of this work. I'd also like to thank Eugene Clothiaux whose exceptional teaching and mentoring abilities got me started in this field as an undergraduate. Although they were a deterrent to getting work done, I'd also like to thank the friends I've made during my time in Seattle. Finally, a special thank you to Amanda: a special lady that I hang out with sometimes.

DEDICATION

to all the trees that gave their lives to print this document

Chapter 1

INTRODUCTION

Remotely determining the vertical and temporal structures of clouds and aerosols is essential for understanding atmospheric processes and the climate system as a whole. Various remote sensors are used to characterize the atmosphere, but only active instruments, such as radars and lidars, can provide unambiguous vertical profiles of cloud and aerosol properties. While millimeter-wavelength radars (e.g. Clothiaux et al., 2000; Hogan and Illingworth, 2000; Stephens et al., 2002) are quite sensitive to clouds, lidars are needed to detect the smallest of particles and optically thin targets. Furthermore only lidars can provide vertical profiles of aerosol properties. Lidars also have the capability to provide unparalleled range-resolved observations of cloud and aerosol extinction— an essential prerequisite for inferring atmospheric radiative heating profiles. In tandem with cloud radars, lidars are needed to fully resolve radiative heating rate profiles (Feldman et al., 2008; Yang et al., 2010; Thorsen et al., 2013a) and top-of-the-atmosphere fluxes (Haladay and Stephens, 2009; Borg et al., 2011; Sun et al., 2011). A particular focus of this thesis is on lidar observations of cirrus clouds which are optically thin, but widespread and therefore important regulators of the global radiation balance (Liou, 1986; Fu et al., 2000, 2002).

In the tropical atmosphere cirrus clouds are especially prevalent (e.g., Winker and Trepte, 1998; Wang et al., 1998; Fu et al., 2007; Dessler and Yang, 2003; Massie et al., 2010) making them a crucial component of the tropical energy budget. In terms of quantity, unequaled observations of tropical cirrus can be had from the Cloud-Aerosol Lidar Infrared Pathfinder Satellite Observations (CALIPSO) lidar (Winker et al., 2009, 2010) and the Department of Energy Atmospheric Radiation Measurement (ARM Ackerman and Stokes, 2003) program's Tropical Western Pacific (TWP) sites: Manus, Nauru and Darwin. The TWP sites each have operated a micropulse lidar (MPL; Campbell et al., 2002) near-continuously for multiple years providing a dataset of cirrus with a large temporal coverage. As a compliment to the TWP times series CALIPSO, in its sun-synchronous orbit, provides near-global observations of cirrus clouds but only observes a single point twice during the day (around 1:30 and 13:30 local time). The complimentary temporal and spatial coverages along with the prevalence of the CALIPSO and TWP datasets is the motivation for the comparison of the two in Chapter 2. In Chapter 2 a thorough comparison of CALIPSO and MPL cirrus cloud fraction, optical depth, geometrical thickness and cloud top and base height is performed at the three ARM TWP sites. Special attention is given to the subset of cirrus that occur in the tropical tropopause layer.

In Chapter 3 the lidar datasets used in Chapter 2 are supplemented by collocated cloud radar observations to investigate the accuracy of tropical radiative heating rate profiles from the current suite of spaceborne and ground-based instruments. An accurate knowledge of radiative heating is essential for understanding tropical circulations. For example, the vertical distribution of radiative heating in the tropical tropopause layer (e.g., Yang et al., 2010; Lin et al., 2013) places constraints on various atmospheric processes (Hartmann et al., 2001; Gettelman et al., 2004; Corti et al., 2005; Fu et al., 2007). In the tropics, assessing the full profile of radiative heating over large-scales is important as it approximately balances latent heating (Stephens, 2005) and exerts control over general circulation patterns (Slingo and Slingo, 1988, 1991; Raymond, 2000). Radiative heating also aids in the development and maintenance of clouds (e.g., Lilly, 1988; Ackerman et al., 1988; Hall and Vonder Haar, 1999; Dinh et al., 2010). Profiles of radiative heating are typically not observed directly, but rather are calculated using a radiative transfer model. This requires specification of the atmospheric state including profiles of cloud properties. More accurate cloud vertical extent and properties are achieved by combining the ARM MPL observations with ARM millimeter cloud radar (MMCR; Clothiaux et al., 2000) observations. Analogous to the ARM MMCR is the CloudSat cloud radar orbiting in formation with the CALIPSO satellite as part of the A-train satellite constellation (Stephens et al., 2002). Previous studies documenting radiative heating in the tropics using either ARM or A-train observations have used cloud inputs from radar only (Fueglistaler and Fu, 2006; Mather et al., 2007; McFarlane et al., 2007; Mather and McFarlane, 2009; L'Ecuyer et al., 2008) or have merged separate radar and lidar cloud properties retrievals (L'Ecuyer et al., 2008; Haladay and Stephens, 2009; Kato et al., 2010; Yang et al., 2010). In Chapter 3 ARM and A-train cloud radiative effects are compared over the ARM Darwin site using more accurate combined radar/lidar retrievals for ice clouds.

In December 2010, the ARM program began operating a Raman lidar (RL; Goldsmith et al., 1998) at the Darwin TWP site and the latter portion of this thesis shifts towards focusing on this more advance lidar. Chapter 4 gives the results of a exploration of its capabilities motivated by the results in Chapter 2 and 3. These two chapters show that the frequency of occurrence of cirrus clouds in the MPL observations are significantly less than CALIPSO making inferring tropical radiative heating rates using the MPL+MMCR combination much less accurate than the A-train. Since the ARM RL transmits a more powerful laser beam and has a larger telescope than the MPL one of the goals in Chapter 4 is to quantify the presumed improved sensitivity of the ARM RL and compare it to CALIPSO. Furthermore, Chapter 2 documents diurnal cycles in tropical cirrus that occur in both MPL and CALIPSO observations— during the daytime, cirrus clouds occur less frequently and are geometrically thinner. While it is possible that the observed diurnal cycles could indicate real geophysical phenomena, they could also be due to increased noise during the daytime associated with the solar background. Both the MPL and CALIPSO lasers operate at 532 nm, which is in a region of maximum solar energy. Therefore daytime MPL and CALIPSO observations must contend with a large amount of additional noise during the daytime which may cause biases. Unlike the MPL and CALIPSO, the RL elastic channel operates at a wavelength of 355 nm where the sun emits less energy. The impact of daytime noise is explicitly quantified for each lidar in Chapter 4 and the RL observations are used to determine the effects of daytime noise on both MPL and CALIPSO observations of cirrus clouds.

The results in Chapter 4 show that the ARM RL is capable of providing more accurate cirrus macrophysical properties than either CALIPSO or the MPL. In addition to better macrophysical properties, a Raman lidar can intrinsically separate signals from molecules and particulates (unlike elastic backscatter lidars, e.g. the MPL and CALIPSO) allowing for directly retrieved particulate (cloud and aerosol) backscatter and extinction coefficients (Ansmann et al., 1990). However, the ARM Raman lidar was originally conceived as a means for high-quality observations of water vapor and aerosols only and, since the RL was designed to be a continuously operated instrument, automated algorithms were designed to process the data (Turner et al., 2002). While cloud observations were originally considered of secondary importance for this system, Chapter 4 demonstrates that the ARM RL is viable tool for cloud observations. However, the identification of clouds is treated in a simple manner in current ARM RL data products and many clouds, especially cirrus, are not identified (in Chapter 4, a cirrus mask was created from the smoothed depolarization ratio). Furthermore, no attempt is made to retrieve cloud extinction in the current generation of ARM RL data products. Therefore the main goal of Chapters 5 and 6 is to develop a new automated algorithm for Feature detection and EXtinction retrieval (FEX) in order to fully realize the potential of the ARM RL. The FEX algorithm objectively identifies features (i.e. clouds and aerosols) and retrieves their extinction and backscatter profiles over the full extent of the troposphere. Extinction is retrieved by FEX directly using the Raman method in addition to other methods developed for elastic backscatter lidars to obtain the best possible extinction estimate for all detected features. In support of an accurate extinction retrieval, a classification of feature type is made and multiple scattering effects are explicitly considered. The feature detection and extinction methodologies are presented in Chapters 5 and 6, respective, accompanied by validation of the retrieval performance using multiple years of data from the TWP RL and the RL at ARM Southern Great Plains (SGP) site.

The material in Chapters 2–4 has previously been published (Thorsen et al., 2011, 2013a,b) and Chapters 5 and 6 are, as of writing this thesis, currently under review for publication (Thorsen et al., 2014; Thorsen and Fu, 2014). Therefore each chapter reads mostly independently of one another although each chapter's introduction and summary sections has been rewritten to be brief and avoid any egregious repetition. Chapter 7 presents conclusions from this thesis including a summary of all chapters and a discussion of possible future directions.

Chapter 2

COMPARISON OF THE CALIPSO SATELLITE AND GROUND-BASED OBSERVATIONS OF CIRRUS CLOUDS AT THE ARM TWP SITES

The contents of this chapter are reproduced from: Thorsen, T. J., Q. Fu, and J. Comstock, 2011, J. Geophys. Res., 116 (D21), D21 203, doi: 10.1029/2011JD015970. The Introduction and Summary sections have been revised from their original form and minor modifications have been made throughout the text.

2.1 Introduction

In the tropical atmosphere cirrus clouds are especially prevalent (e.g., Winker and Trepte, 1998; Wang et al., 1998; Fu et al., 2007; Dessler and Yang, 2003; Massie et al., 2010) making them a crucial component of the tropical energy budget. In this region a large quantity of observations are available from two different sets of lidar observations: (1) the CALIOP instrument on board the CALIPSO satellite (Winker et al., 2010) and (2) MPLs at the three ARM TWP sites: Manus, Nauru and Darwin (Ackerman and Stokes, 2003). The ground-based observations provide continuous measurements while CALIPSO, in its sun-synchronous orbit, observes a point only twice during the day (around 1:30 and 13:30 local time). CALIPSO is capable of near-global observations of cirrus clouds whereas the ARM TWP observations provide a point measurement at three sites. While the presence of optically thick low clouds can obscure overlying cirrus clouds from the view of the ground-based lidar, the CALIPSO satellite, with its space-borne viewpoint, virtually eliminates the possibility that the lidar will become fully attenuated before observing a potential cirrus cloud layer. The ARM TWP sites have been collecting MPL observations starting in early 1999 for Manus and Nauru and 2002 at Darwin. CALIPSO was launched in June 2006 into an orbit which passes the same track about every 16 days.

The intent of this chapter is to compare cirrus clouds from these two sets of lidar observations and examine and understand any discrepancies between them. Dupont et al. (2010) performed a similar comparison among CALIPSO observations and four different ground-based lidars located in the midlatitudes. In this study we examine tropical cirrus clouds which play an important role in determining the energy budget in the TTL. A thorough analysis and understanding of the limitations in observing tropical cirrus is needed before an accurate estimation of the radiative energy budget can be made. In addition, the complimentary strengths of each instrument—the temporal coverage of the MPL and the spatial coverage of CALIPSO—could prove useful for the further study of cirrus clouds. Before this is done these datasets need to be evaluated against each other.

We focus on comparing statistics of macrophysical and optical properties of cirrus clouds in the vicinity of the three TWP sites. Statistics for the subset of cirrus clouds which reside in the TTL are also examined. Section 2.2 describes both the CALIPSO and ARM TWP lidar datasets used in this study. The methods used to compare the two sets of observations are given in section 2.3 and data sampling issues are discussed in section 2.4. The resulting comparisons of macrophysical and optical properties as well as potential sources of biases are given in section 2.5. Summary and conclusions are given in section 2.6.

2.2 Datasets

2.2.1 CALIPSO

The CALIPSO satellite was launched in April 2006 into a sun-synchronous orbit as part of the A-Train satellite constellation (Winker et al., 2010). The main instrument on board CALIPSO is CALIOP, a 2-wavelength (532 nm and 1064 nm) polarization sensitive lidar which is capable of detecting clouds with an optical depth of 0.01 or less (with sufficient averaging) and optical depths as large as 5. In this study, we use the CALIPSO L2 v3.01 5 km cloud layer product. The vertical resolution of the CALIPSO data is 30 m from the surface to 8.2 km and 60 m from 8.2 to 20.2 km. Cloud layers are identified by examining the enhancement of the return signal relative to the molecular background using a threshold algorithm (Winker et al., 2009). The cloud product also reports an opacity flag which determines the point at which the lidar beam has become completely attenuated and no lower return signal (possibly from the surface or a cloud/aerosol layer below) can be identified. Extinction retrievals of cloud and aerosol layers are described in Young and Vaughan (2009). Further details of the extinction retrieval used in the CALIPSO cloud product are discussed during comparisons of optical depth statistics (section 2.5.4).

The CALIPSO cloud product reports quality flags to indicate the confidence in both the layer classification and extinction retrieval. In this study we do not consider layers with cloud-aerosol discrimination (CAD) scores (Liu et al., 2010b) greater than 100, which represent highly uncertain cloud features. The extinction QC flag is used to remove layers with the possibility for large errors (i.e. any of bits 4-9 being set in the extinction QC flag).

The CALIPSO L2 v3.01 data products were released in May 2010 and includes several improvements over the previous version of data products, v2.01. Updates relevant to this study include the removal of a software bug which caused a significant overestimate of low cloud fraction (Vaughan et al., 2010). Also updated is the algorithm used to discriminate between cloud and aerosol (Liu et al., 2010b) and improved daytime calibration (Powell et al., 2010) which results in more accurate estimates of layer properties.

Cloud and aerosol layers are identified in CALIPSO backscatter using a algorithm called the selective iterative boundary locator (SIBYL; Vaughan et al., 2009) which detects layers using multiple horizontal resolutions. Multiple passes are made through the data and the amount of horizontal averaging increases with each pass. After cloud layers are identified at a particular horizontal resolution they are removed before moving on to further averaging. In the 5 km L2 v3.01 cloud product three horizontal averages are considered: 5, 20 and 80 km. In this study we consider CALIPSO cloud properties retrieved at all three horizontal averages. All cloud layers, regardless of the amount of averaging performed, are interpolated to a 5 km grid. This multiscale averaging approach can lead to a single cloud layer being reported as multiple layers which overlap in the vertical. In order to properly compare CALIPSO cloud properties to the ground-based dataset (which does not use a multiscale averaging algorithm) overlapping layers are merged together. Further details on the merging of CALIPSO's multi-resolution layers are given in Appendix A.

Observations from the CALIPSO L2 v3.01 1 km cloud product are also considered in this study. In this data product all data is averaged to 1 km, multiple horizontal resolutions are not used. Cloud optical depths are not retrieved in the 1 km cloud product.

2.2.2 ARM TWP

The ARM TWP sites consist of three facilities at Manus, Nauru and Darwin the locations of which are shown in Figure 2.1. Cloud boundaries are determined using the threshold algorithm of Wang and Sassen (2001) and extinction is calculated following Comstock and Sassen (2001). Details of the ground-based extinction retrievals used in this study are discussed when comparing optical depth statistics (section 2.5.4).

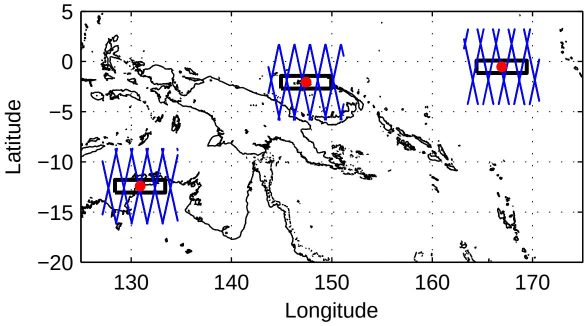

Figure 2.1: Map of the three ARM TWP sites: Darwin, Manus and Nauru (left to right, red dots), a subset of CALIPSO ground tracks (blue lines) and the 1.25° × 5° latitude-by-longitude box from which CALIPSO observations are taken from (heavy black line).

The MPL operates at a wavelength of 532 nm with a vertical resolution of 30 m. Profiles are averaged from their 30-second native temporal resolution to 1 minute during the night and 5 minutes during the day in order to obtain a signal-to-noise ratio (SNR) sufficient for an accurate extinction and cloud boundary retrieval. Since profiles undergo a larger amount of averaging during the day we are left with a disproportionate amount of night profiles in our set of observations. Therefore, cloud properties retrieved during the daytime are scaled by a factor of five when we consider the dataset as a whole.

Attenuation of the MPL signal is identified following the procedure of Lo et al. (2006). A profile of the molecular backscatter coefficients at 532 nm are calculated using pressure and temperature observations from collocated radiosonde profiles. Several checks are then implemented to determine signal attenuation. First, the backscatter signal throughout the cloud layer must be greater than the minimum of positive backscatter in the whole profile. Second, the decrease in measured backscatter above the cloud must be proportional to the decrease in the molecular backscatter to within 4%. If at least 4 points (120 m) above the cloud layer conform to this requirement then it is assumed that the MPL signal was not attenuated by the cloud layer. The performance of this method was validated using an alternative method with radar (MMCR) observations at the Darwin site. Attenuation was determined by comparing the MPL cloud top height to the radar cloud top height (Clothiaux et al., 2000). If the MPL cloud top height is lower than the radar cloud top height by more than 1 km than the MPL signal is assumed to be attenuated. Attenuation determined in this manner at Darwin agreed with the method used in this study 78% of the time.

Cloud optical depths from the ground-based observations are subjected to thresholds to remove uncertain retrievals. Visual inspection of the retrieved cloud boundaries reveal that the MPL is capable of retrieving clouds with $\tau \sim 3$ and clouds as thin as $\tau \sim 5\text{x}10^{-3}$. Clouds with optical depths outside this range are considered uncertain and are removed. Imposing this restriction removes less than 2% of all clouds at any of the three TWP sites.

2.3 Comparison Methodology

We consider 31 months, June 2006–December 2008, of CALIPSO L2 5 km v3.01 and ground-based observations from the ARM TWP sites: Manus, Nauru and Darwin. For CALIPSO data we define a region around each ARM site to compile statistics from— a 1.25° × 5° latitude-by-longitude box centered on each site (Figure 2.1). Larger spatial domains and different areas were also considered. We found that the spatial domain chosen strikes a balance between an area large enough to collect an adequate number of observations and small enough to be representative of the ground-based site.

Comparisons made between the two sets of lidar observations are done so using two types of datasets: restricted and unrestricted. From a ground-based perspective clouds at higher altitudes are frequently masked by the presence of low water clouds which fully attenuate the lidar signal. While from a space-borne perspective low clouds which attenuate the lidar signal have no effect on the ability to observe high clouds. However including such cases would introduce a high-cloud bias into the CALIPSO statistics relative to the ground-based observations; i.e., the same profile viewed from a ground-based perspective would not observe high clouds. In the restricted datasets we only include profiles fully transparent to the lidar signal in order to have a fair comparison.

Both instruments have ranges of optical depths for which cloud boundary and extinction retrievals are considered reliable. The MPL can accurately detect clouds with optical depth from approximately 5x10^{-3} to 3 and CALIOP from 0.01 to 5 (Winker et al., 2009). Therefore, in the restricted datasets, only clouds whose optical depth fall with the common sensitivity of both instruments are considered— $0.01 \leq \tau \leq 3$.

The unrestricted datasets use all lidar profiles available in each dataset, only profiles where data quality is questionable are excluded.

This study centers on the statistical comparisons of ice and TTL cloud properties. Clouds are defined by the altitude of their cloud base. Both the CALIPSO and ground-based datasets derive cloud altitudes relative to mean sea level. A cloud with a base greater than 7 km is considered as an ice cloud. Radiosonde observations at the three TWP sites show that an altitude of 7 km corresponds to a mean temperature of $-11.2\ ^{\circ}C$ during the sampling period. The subset of ice clouds which reside in the TTL are defined as clouds with bases greater than 14 km. The mean temperature at 14 km is $-65.7\ ^{\circ}C$. The standard deviation of the radiosonde temperatures at these two altitudes are less than $2.5\ ^{\circ}C$. Variations in the mean temperature at both 7 km and 14 km among the three TWP sites are less than $0.5\ ^{\circ}C$.

Adopting a simple definition of ice clouds based on the altitude of the cloud base could be problematic. Studies have shown that supercooled and mixed-phase clouds can occur above 7 km in the tropics (e.g. Zhang et al., 2010). However these clouds are typically optically thick and therefore would not be included in our restricted datasets. We confirmed this assumption by using the phase information provided in the CALIPSO L2 cloud retrieval. Less then 1.5% of CALIPSO cloud observations in the restricted ice cloud datasets contain water according to the CALIPSO L2 cloud product's assessment of cloud phase.

While we apply the more general classification of ice clouds to our datasets it is assumed that the majority of these ice clouds are cirrus clouds. Other types of ice clouds, such as those associated with altostratus, nimbostratus, or cumulonimbus, are assumed to be excluded from our datasets by the requirement that the optical depth be less than 3. Therefore it is reasonable to assume that nearly all clouds classified as ice clouds in this study are cirrus clouds. The CALIPSO L2 cloud product provides an assessment of cloud type based on the cloud top altitude, phase, opacity and cloud fraction. According to this classification 100% of clouds in our restricted ice cloud datasets are cirrus clouds.

2.4 Sampling Issues

2.4.1 Availability of Data

Cloud property statistics are taken from observations over an extended period of time. Differences in sampling during this time period can cause observations to favor the cloud characteristics of a particular season. The MPLs at all three TWP sites suffer from occasional data quality issues during our analysis period. Those times are identified and removed. Our analysis period (June 2006–December 2008) does not evenly sample all months; therefore, both the ground-based and CALIPSO observations are more representative of cloud properties from June through December.

Figure 2.2 shows the sampling per month of all the ground-based and CALIPSO lidar profiles in the unrestricted datasets (top row of panels, labeled "All"). The sampling is given as a percentage of the total number of observations for each dataset, that is Figure 2.2 gives the fraction of the total number of available profiles which fall within a given month. The top row of panels in Figure 2.2 shows this fraction relative to the total number of profiles in the unrestricted datasets (dashed line) and relative to the total number of cloudy profiles in the unrestricted datasets (solid line). Both the distribution of all and cloudy profiles agree best at Nauru with an average difference of 1.7%, followed by Manus (2.5%) and Darwin (5%). No ground-based data is available at Darwin for March or April due to poor data quality during both 2007 and 2008. In addition the sample size at Darwin is poor during the months of February and May.

In Figure 2.2 the panels labeled "Ice" and "TTL" show the distribution of cloudy profiles in the restricted datasets which contain ice and TTL clouds, respectively. Sampling differences are similar to those in the unrestricted datasets. Again Nauru exhibits the best agreement with an average difference of 1.9%, followed by Manus (3.4%) and Darwin (6.9%). Overall these results suggest that the error introduced into cloud property comparisons due to the difference in seasonal sampling could be significant at Darwin and is minimal at both Nauru and Manus.

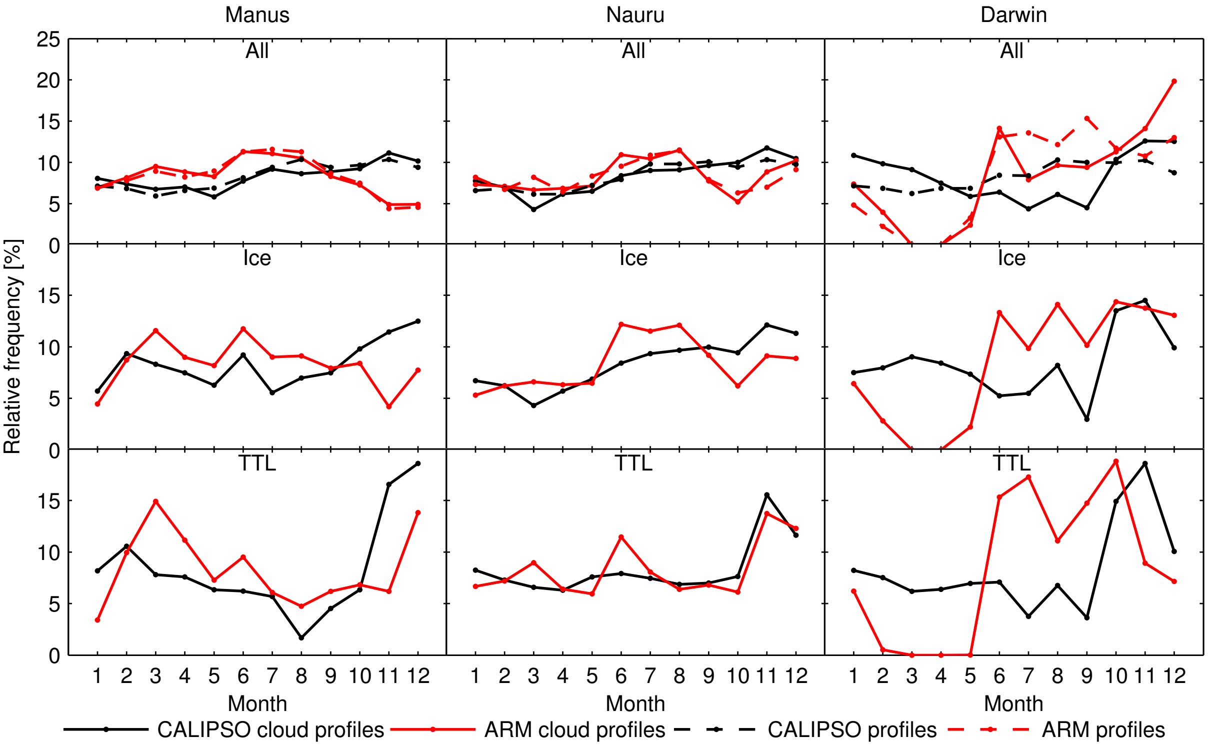

Figure 2.2: Monthly distribution of profiles available at each ARM TWP site for CALIPSO (black line) and ground-based (red line) observations relative to the total number of profiles (dashed line) and the total number of cloudy profiles (solid line). The distribution of profiles in the unrestricted datasets are given in the top panel. The distribution of profiles in the ice and TTL restricted datasets are given in the middle and bottom panel, respectively. Percentages in each month are calculated relative to the total number of observations in the entire sampling period.

2.4.2 Attenuated Profiles

A particular focus in this study is comparisons made using only transparent profiles, i.e. the restricted datasets. Therefore the amount of profiles which are attenuated plays a critical role in determining the overall sampling. Figure 2.3 shows the percentage of profiles which are attenuated for each month relative to the total number of cloudy profiles. CALIPSO observations are shown in black and ground-based in red. The ground-based observations contain a larger percentage of attenuated profiles (solid red line) relative to CALIPSO (solid black line) over nearly all months and locations. Also shown is the percent of attenuated profiles separated into day (dotted lines) and night (dashed lines) observations. Comparisons of the daytime observations show that the ground-based MPL frequently has difficulty penetrating through the entire atmosphere. Approximately 70% of daytime cloud profiles in the ground-based observations are attenuated. During the night, ground-based and CALIPSO observations show similar fractions of attenuated profiles. The difference between the fraction of attenuated profiles during the daytime and nighttime from CALIPSO is much less than that observed in the ground-based profiles. The impact of the diurnal bias in the ground-based observations is discussed further in section 2.5.5.

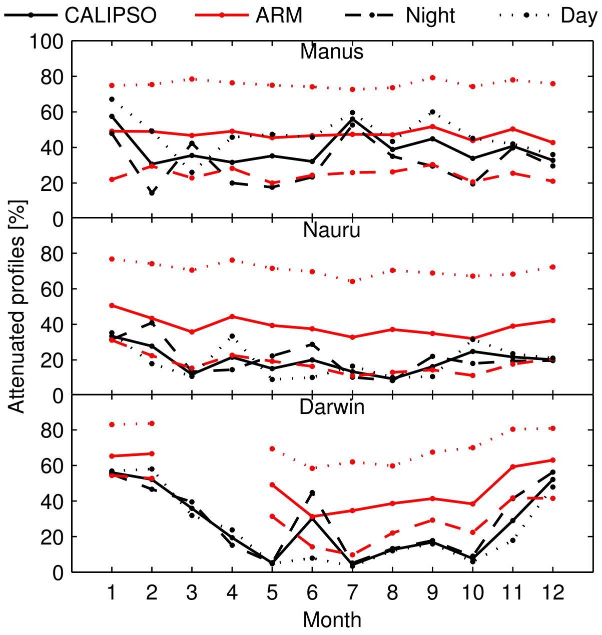

Figure 2.3: Percentage of profiles which are attenuated during each month relative to the total number of cloudy profiles for that month for CALIPSO (black) and ground-based (red) observations. Solid lines show the percent attenuated for the full set of observations. Nighttime only observations are given as dashed lines and daytime only as dotted lines.

2.4.3 MPL Data Quality at Darwin

During much of our sampling period the MPL performance at Darwin is sub-optimal. After an upgrade to a polarized version of the MPL at Darwin in August 2006 the output power dropped 40% by December 2006. In May 2007 the MPL at Darwin was replaced to resolve an unrelated issue which restored the output power to normal levels. But the previous decline in output power continued unabated until November 2008 when the installation of a new pump diode restored the output power to normal levels. The reduction in power over a large portion of our observing period reduced the sensitivity significantly. While we still present comparisons at Darwin for completeness, the results at Manus and Nauru are more useful for quantifying differences in cloud properties between CALIPSO and the MPL.

Data quality issues at Darwin preclude ground-based observations during March and April from our analysis. In addition, sample size is greatly reduced during the months of February and May due to data quality. It follows that these underrepresented months could cause larger discrepancies at Darwin and perhaps overwhelm the MPL's poor output power effect. To test this we assessed the impact of the missing data by removing the same period from the CALIPSO data and by examining monthly statistics (not shown). Doing so showed that the Darwin MPL still showed indications of poorer performance than either the Manus and Nauru MPLs. Therefore we can conclude that underrepresented months in the Darwin dataset are not responsible for the MPL's poor performance during our sampling period.

2.4.4 Sampling Uncertainty of CALIPSO Observations

In this study we focus on statistical comparisons between two sets of observations, which requires that we assess the statistical significance of any differences found. Ground-based cloud profiles are retrieved from MPL data every 1 minute (night) or 5 minutes (day) continuously, barring any instrument issues. This creates a large sample size which minimizes the sampling uncertainty in statistics derived from ground-based profiles. CALIPSO observations occurring inside the sampling area (the $1.25° \times 5°$ latitude-by-longitude box centered on each ARM site) provide far fewer observations relative to the ground-based data. In addition to a smaller sample size, CALIPSO profiles along a single transect in the sampling area are strongly correlated with each other. This further reduces an already small sample size into an even smaller number of independent samples since only observations in different overpasses are completely independent of each other. Therefore CALIPSO observations do not comply with the independent sampling assumption and standard statistical tests (e.g. the t-test) cannot be used to determine statistical significance. Note that adjacent ground-based profiles also are strongly correlated with each other, reducing the number of independent samples. However, the continuous ground-based observations create such a large sample size it can be assumed that the ground-based sampling uncertainty is insignificant.

The bootstrap technique (Efron, 1982) can be used to estimate sampling uncertainty when the independent sampling assumption is not valid. In this method the original data is treated as the parent population. A large number of resamplings are performed using the original data which generates multiple artificial (bootstrap) samples. Each bootstrap sample is constructed to be the same size as the original data. The resampling is performed with replacement so, in general, bootstrap samples contain repeated values of the original dataset and entirely exclude others. The statistic of interest is then calculated for each of the large number of bootstrap samples. The distribution of this statistic calculated from the bootstrap samples can then be used to construct a confidence interval.

For variables such as cloud fields there is considerable autocorrelation which would be destroyed by the bootstrap resampling process. To preserve the correlation inherent to cloud fields the sampling uncertainty of CALIPSO is estimated using the moving-block bootstrap method (Wilks, 1997). This extension of the bootstrap technique resamples sets of consecutive data (blocks) instead of single points.

Sampling uncertainty is derived for probability density functions (PDFs), means of cloud top height, base height, geometrical thickness, optical depth and the number of cloud layers per profile. An entire CALIPSO profile is considered as a single sample and a block is a consecutive number of profiles along a given transect. Blocks of profiles are resampled many times and the PDF or mean of the cloud property is calculated for each bootstrapped set of profiles. From this distribution of bootstrapped samples a confidence interval is constructed for the mean or, in the case of a PDF, each bin.

The proper block length should be large enough that it captures the autocorrelation present in the dataset, but not so large that it creates artificial autocorrelation. Since we are interested in cirrus clouds in this study, the block length we choose should be comparable to the typical horizontal extent of cirrus clouds. For this study we choose 100 km (twenty CALIPSO 5 km profiles) as a block length.

2.5 Comparisons of CALIPSO and Ground-based Lidar Cloud Observations

2.5.1 Cloud Fraction

We derive cloud fraction from the ground-based and CALIPSO observations using the unrestricted datasets. Clouds from all altitudes are considered in this comparison with the exception of clouds with tops below 1 km. These clouds cannot be detected in the ground-based retrieval since the cloud mask is not implemented below 1 km to avoid difficulties in applying the overlap function. To remain consistent, clouds with tops below 1 km are removed from the CALIPSO dataset. The effect of removing these low clouds from the CALIPSO observations has a minimal effect on the cloud fraction—a reduction of less than 2% for all comparisons presented here.

Comparisons of cloud fraction are given in Table 2.1. The cloud fractions derived from the unrestricted observations are shown in the row labeled "5 km" for CALIPSO and "1 or 5 min." for the ground-based observations. CALIPSO observations show a considerably higher cloud fraction ($\sim$ 20%) relative to the ground-based observations. Cloud fraction comparisons are shown separately for the night and day observations in Tables 2.2 and 2.3, respectively. For nighttime only observations agreement improves between the CALIPSO (row labeled "5 km" in Table 2.2) and ground-based (row labeled "1 or 5 min." in Table 2.2) observations. Very large differences are present during the daytime with the ground-based cloud fraction significantly smaller than CALIPSO. This is presumably due to the reduction in the MPL sensitivity during the daytime (section 2.4.2).

Table 2.1: Cloud fraction

	Resolution	Manus	Nauru	Darwin
CALIPSO	5 km	0.871	0.802	0.653
	1 km	0.750	0.574	0.499
	5 km, transparent	0.800	0.763	0.560
ARM	1 or 5 min.	0.692	0.534	0.400
	5 km "pixel"	0.851	0.740	0.652
	1 or 5 min., transparent	0.551	0.429	0.256
	5 km "pixel", transparent	0.709	0.613	0.458

Table 2.2: Cloud fraction, nighttime observations only.

	Resolution	Manus	Nauru	Darwin
CALIPSO	5 km	0.882	0.807	0.677
	1 km	0.765	0.615	0.554
	5 km, transparent	0.833	0.770	0.578
ARM	1 or 5 min.	0.775	0.661	0.501
	5 km “pixel”	0.894	0.833	0.690
	1 or 5 min., transparent	0.724	0.620	0.411
	5 km “pixel”, transparent	0.875	0.818	0.619

Table 2.3: Cloud fraction, daytime observations only.

	Resolution	Manus	Nauru	Darwin
CALIPSO	5 km	0.859	0.796	0.628
	1 km	0.734	0.531	0.443
	5 km, transparent	0.759	0.755	0.543
ARM	1 or 5 min.	0.618	0.436	0.325
	5 km “pixel”	0.799	0.634	0.622
	1 or 5 min., transparent	0.282	0.182	0.111
	5 km “pixel”, transparent	0.493	0.346	0.303

Although we compare two 532 nm backscatter lidars, significant differences exist between the two observations and retrieval algorithms which makes a meaningful comparison difficult. For example, CALIPSO’s space-borne viewpoint provides an advantage for observing high clouds. From a ground-based perspective, the atmosphere below, especially the lower cloud layers, reduces the SNR or even totally blocks the lidar from detecting higher clouds, causing them to go undetected. Therefore one would expect the CALIPSO observations to have a larger cloud fraction at higher altitudes relative to the ground-based observations.

Other factors that influence cloud fraction include spatial resolution, which effects cloud faction in a number of ways. For instance, consider the situation of cloud layers separated in the horizontal by a small clear-air gap. Large enough averaging in the horizontal could merge the signal from the individual cloud layers resulting an increased cloud fraction relative to observations with less horizontal averaging. In addition, under-filled cloud pixels can result in an overestimate of the real cloud fraction. For example, the CALIPSO L2 cloud product contains data on a 5 km horizontal grid. A cloud with an actual horizontal dimension of 2 km (with sufficient backscattering) will be reported in the CALIPSO cloud product as one 5 km cloudy pixel, when the actual cloud fraction in this 5 km region is $\frac{2}{5}$ and not 1. The effect of under-filled cloud pixels is larger for boundary layer clouds since they typically have smaller spatial scales. Our comparison is further complicated by the CALIPSO SIBYL algorithm's high-resolution cloud clearing (Vaughan et al., 2009). It removes boundary layer clouds detected at single-shot ($\frac{1}{3}$ km) resolution from the 5 km cloud product to ensure that the layers identified are homogeneous features. We examine the impact of this process on our cloud fraction comparison in section 2.5.1.3. In the next subsection we focus on eliminating the impact of horizontal resolution on our comparison.

2.5.1.1 Effect of Resolution

The ground-based MPL SNR is improved by averaging over time, 1 minute at night and 5 minutes during the day. The equivalent spatial average can be determined by assessing the advection by wind of atmosphere through the field of view of the MPL. For 5 km of atmosphere to be sampled by the MPL in either 1 or 5 minutes would require an unrealistically large wind speed. Given typical wind speeds at the three TWP sites, 1 and 5 minutes of averaging corresponds to a spatial average significantly less than CALIPSO's 5 km. Therefore the larger cloud fraction in CALIPSO observations may be partially due to differences in resolution due to the effects discussed previously.

Differences in spatial resolution can be accounted for in one of two ways: either reduce the spatial averaging of CALIPSO to better match that of the ground-based data or further average the ground-based observations to 5 km. To achieve the former we can utilize the 1 km CALIPSO cloud product. Cloud fraction derived from the 1 km CALIPSO cloud product is shown in Table 2.1. Comparisons with the ground-based cloud fraction is much improved over the 5 km cloud product. The lower cloud fraction relative to the 5 km data could also be a result of the reduction in CALIPSO's cloud detection capability. Less averaging performed in the 1 km data results in less clouds with sufficient SNR to be detectable. Therefore, the reduction of cloud fraction when using the 1 km CALIPSO cloud product is a result of two convoluted effects: the smaller amount of horizontal averaging and the reduced sensitivity to clouds. In section 2.5.1.1.1 we will examine which factor dominates. Using radiosonde wind data at each TWP site to approximate the equivalent amount of ground-based spatial averaging (not shown, see section 2.5.1.1.1 below) results in an average value of ~ 0.4 km when both night and daytime observations are considered. So the 1 km CALIPSO cloud product still has a larger spatial resolution than the ground-based data.

2.5.1.1.1 Ground-based "pixel" Instead of reducing the horizontal averaging of CALIPSO we can mimic the horizontal average of CALIPSO in the ground-based data. This method is better suited for comparing the two datasets since we do not need to degrade the cloud detection ability of either retrieval. Cloud fraction derived using the ground-based observations which have been modified to mimic the 5 km resolution of the CALIPSO observations are shown in Table 2.1 in the row labeled "5 km "pixel"." The cloud fractions at all three TWP sites agree with the CALIPSO 5 km data to within 0.06. The comparison of cloud fraction during the nighttime (Table 2.2) shows agreement to within 0.03. During the daytime (Table 2.3) the comparison of cloud fraction using either resolution shows larger differences with CALIPSO's cloud fraction being consistently higher. Opposite signs in the differences in cloud fraction between the day and night results in some cancellation of errors when comparing all observations (Table 2.1). Table 2.2 indicates that the differences in cloud fraction between the CALIPSO observations (row labeled "CALIPSO 5 km" in Table 2.1) and the native ground-based observations (row labled "ARM 1 or 5 min.") at nighttime could be caused by the difference in resolution alone. The larger differences during the daytime cloud fraction are further evidence of the limited sensitivity of the MPL during the daytime, although resolution may also partially explain the observed differences.

For the preceding results, the ground-based observations are made to mimic CALIPSO's 5 km horizontal resolution by defining a ground-based "pixel." A "pixel" is a block of consecutive ground-based profiles which are considered approximately equivalent to a 5 km horizontal domain. Collectively the "pixel" of ground-based profiles is meant to approximate the amount of data that CALIPSO would view as a single profile. The number of consecutive profiles to consider as one "pixel" is determined using radiosonde wind data, which is available at least twice a day at all three TWP sites. Individual radiosonde wind profiles are first linearly interpolated to the vertical resolution of the MPL. Monthly mean wind speed profiles are constructed by averaging the u and v wind components separately across each month of data. The monthly mean wind speed profile is then taken as the magnitude of the resulting monthly mean wind vector at each MPL altitude.

The vertical mean of the monthly mean wind speed profiles is taken in four vertical layers: $0-3.5$ km, $3.5-7$ km, $7-14$ km and $14-20$ km. The minimum mean wind speed of these four layers is then used to determine the number of profiles combined to mimic 5 km. Given this mean wind speed, $\overline{U}$, the number of consecutive ground-based profiles is $n = 5\ km/(\overline{U}\Delta t)$. Where Δt is the time average used in the ground-based data (1 minute during the night and 5 minutes during the day). Once the number of ground-based profiles to consider as one "pixel" is determined, the cloud fraction is assessed as follows. If inside this set of profiles there is at least one cloud layer detected then the entire "pixel" is marked as cloudy. Likewise, if no clouds are detected then this is a clear "pixel." The cloud fraction is then derived relative to the total number of "pixels."

This procedure results in an average time of 46 minutes (with a standard deviation of 14 minutes) for each 5 km MPL "pixel". This average (and standard deviation) is derived from all 31 months of data across all three ARM TWP sites. Since the nighttime data is averaged to 1 minute, on average at night a single "pixel" is composed of 46 profiles. During the daytime (5 minute average) this corresponds to 9 profiles per "pixel."

2.5.1.2 Transparent Cloud Fraction

Of particular focus in this study is statistical comparisons of observations in which the lidar signal passed completely through the atmosphere. Before placing significance in any statistical comparisons of this subset of observations, we analyze the cloud occurrences. The transparent cloud fraction is given in Table 2.1. In calculating the cloud fraction using only transparent profiles, profiles in which the lidar becomes fully attenuated are not included. Therefore the cloud fraction becomes the number of transparent cloudy profiles relative to the total number of transparent profiles (i.e. transparent cloudy profiles plus clear profiles).

Differences in the transparent cloud fraction are large and, as discussed above, this may be due to the different spatial resolutions of the two sets of observations. We use the MPL "pixel" method to minimize the uncertainty caused by different horizontal resolutions. A complication arises for determining when a "pixel" is attenuated. Determining this is ambiguous since a "pixel" could be composed of some profiles which are attenuated and some which are completely transparent. Alternatively, one could re-average the original raw backscatter from the MPL to an equivalent spatial average of 5 km and then determine attenuation using this new set of data. However we would not be testing the MPL's cloud occurrence at the 1 and 5 minute averages which are used for all other comparisons in this study. Instead we require that more than half of the profiles composing a "pixel" are transparent in order to consider the entire "pixel" as transparent. Rather than comparing this cloud fraction directly to the CALIPSO observations, we perform a sensitivity test using the ground-based observations alone.

Ground-based observations are first combined into "pixels" using the same method outlined previously. All "pixels" that are composed of more than half opaque profiles are not included in this analysis. The results presented here are not sensitive to the details that determine the fraction of opaque profiles. The remaining "pixels" are then used to calculated two different cloud fractions. The first cloud fraction is derived using the individual 1 or 5 minute profiles which make up each "pixel." The second cloud fraction is derived relative to the total number of "pixels" with a cloudy "pixel" being one which contains at least a single cloud layer. The difference between these two cloud fractions provides an estimate of the effect of spatial resolution on the transparent cloud fraction. This difference can then be used to estimate the true ground-based transparent cloud fraction at an equivalent spatial resolution of 5 km by adding it to the transparent cloud fraction derived using the native 1 and 5 minute profiles (i.e. the row label "1 or 5 min., transparent" in Tables 2.1- 2.3). The resulting cloud fraction is given in Tables 2.1- 2.3 in the row labeled "5 km "pixel", transparent."

The transparent cloud fraction comparisons between CALIPSO and the ground-based observations are more consistent after correcting for the effect of resolution. However, the cloud fraction derived using the full set of CALIPSO observations and the MPL "pixel" are more similar than the transparent-only observations. As with previous nighttime ground-based "pixel" comparisons, cloud fraction from CALIPSO and ground-based observations agree well at all three TWP sites. The CALIPSO daytime transparent cloud fraction, shown in Table 2.3, is significantly larger than that of the ground-based observations even after applying the resolution correction. This suggests that the larger differences in the transparent cloud fraction is due to the MPL's reduced sensitivity during the daytime.

2.5.1.3 Cloud Fraction by Altitude

Previous comparisons of cloud fraction may mask disagreement between CALIPSO and ground-based observations by fortuitous error cancellation in cloud fraction at different altitudes. In addition, no assessment has yet been made of CALIPSO's high resolution-cloud clearing effect on our cloud fraction comparison. Together this motivates the comparison of cloud fraction by altitude shown in Figure 2.4 where cloud fraction is calculated in altitude bins of 0.5 km. We eliminate established discrepancies by only using profiles which are completely transparent to the lidar (to sample similar cloud regimes) and only using nighttime observations (when the sensitivities of each set of observations are more similar). The nighttime transparent cloud fraction profile is shown in Figure 2.4a. To better interpret previous results, the same CALIPSO data is shown in Figures 2.4a and 2.4c with the native ground-based cloud fraction in Figure 2.4a and the ground-based "pixel" cloud fraction in Figure 2.4c. The corresponding difference profiles between ground-based and CALIPSO observations are shown in Figure 2.4b and 2.4d. The method used to calculate the transparent ground-based "pixel" cloud fraction in each altitude bin is analogous to the method used for the total transparent cloud fraction (section 2.5.1.2).

CALIPSO and native ground-based observations of cloud fraction (Figures 2.4a and 2.4b) show significant differences for all three TWP sites. For higher altitudes ($\gtrsim$ 10 km), the CALIPSO cloud fraction is significantly higher with the maximum differences reaching about 0.3. At lower altitudes ($\lesssim$ 7 km), the ground-based cloud fraction is larger with a maximum difference around 0.1. After bringing the two sets of observations onto approximately the same horizontal scale using the ground-based "pixel" method (Figures 2.4c and 2.4d) the majority of altitude bins still contain statistically significant differences. The results presented in Figure 2.4 indicates that the agreement in total cloud fraction between CALIPSO and ground-based ob-

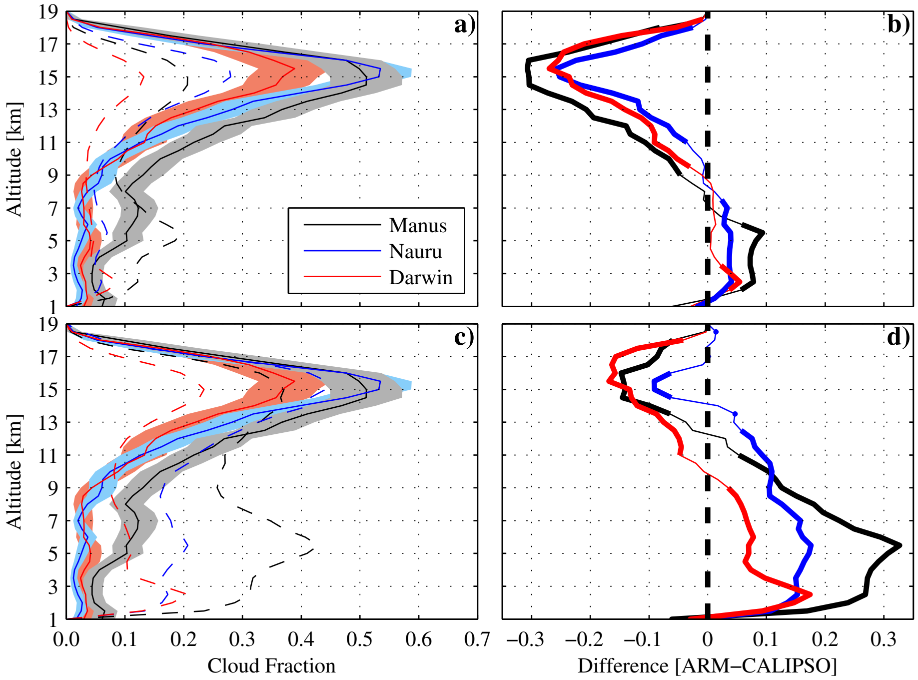

Figure 2.4: Nighttime transparent cloud fraction profiles (panel a and c). CALIPSO cloud fraction (5 km resolution) is given as a solid line for Manus (black), Nauru (blue) and Darwin (red) while the ground-based cloud fraction is given as dashed lines. The shaded regions represent the 95% confidence interval due to CALIPSO's sampling uncertainty. Cloud fraction is shown for (a) the native (1 and 5 minutes averaged) ground-based observation and (c) the cloud fraction derived using the ground-based "pixel" method described in the text. The difference (ground-based minus CALIPSO) in cloud fraction at each altitude bin is shown for (b) the native ground-based observations and (d) the ground-based "pixel" observations. Regions of statistically significantly differences are indicated by a thick line.

servations using the MPL "pixel" method occur by chance, with the difference in cloud fraction changing sign with altitude. Therefore little physical significance is placed in the agreement previously shown for total cloud fraction and, consequently, resolution alone does not explain all of difference in cloud fraction between the two sets of observations.

Figure 2.4 aids to deduce some of the underlying reasons for differences in cloud fraction. The ground-based "pixel" dataset increases the cloud fraction for all altitudes relative to the native ground-based observations. As a result, the difference between CALIPSO and the ground-based observations of high cloud fraction is reduced by about half using the ground-based "pixel" method at Manus and Nauru. The inconsistencies at Darwin are larger which is likely due to poor instrument performance (see section 2.4.3). Thus about half of the difference in high cloud fraction can be explained by resolution. The remaining difference in high cloud fraction may be related to the lower SNR of the ground-based observations at high altitudes. This would particularly become an issue for optically-thin cloud layers.

Comparisons of low cloud fraction between the native ground-based and CALIPSO observations (Figures 2.4a and 2.4b) show that the ground-based cloud fraction is significantly larger than CALIPSO for most altitude bins below about 7 km. This demonstrates that clouds with a horizontal dimension less than 5 km in the CALIPSO observations are not causing CALIPSO to overestimate cloud fraction relative to the ground-based observations as previously suggested. CALIPSO's high-resolution cloud clearing does remove clouds detected at single-shot resolution below 4 km of altitude (Vaughan et al., 2009), which may explain its lower cloud fraction in that altitude range. After applying the "pixel" method to the ground-based data the difference in low cloud fraction becomes even larger (Figures 2.4c and 2.4d). While the impact of CALIPSO's high-resolution cloud clearing could still possibility account for differences below 4 km, significant differences still occur above 4 km. The ground-based "pixel" cloud fraction remains significantly larger than CALIPSO's cloud fraction up until above 10 km, depending on which TWP site is being examined. One explanation is the ground-based observations contain more smaller-scale clouds than the CALIPSO observations. As a consequence, when the ground-based "pixels" are constructed the cloud fraction in these regions of small-scale clouds is greatly enhanced, resulting in an even larger discrepancies between the two set of observations below 10 km.

Precisely quantifying contributions to discrepancies in cloud fraction between the CALIPSO and ground-based observations shown above is not trivial. The effect that CALIPSO's high-resolution cloud clearing has on cloud fraction also warrants more in depth scrutiny. Further dissection of the cloud fraction observations from these two instruments is a worthwhile task, but is beyond the scope of this study.

2.5.2 Cloud Boundaries

CALIPSO and ground-based observations are compared by compiling probability density functions (PDFs) for cloud top height, cloud base height and cloud geometrical thickness for both ice (cloud base > 7 km) and TTL (cloud base > 14 km) clouds. Defined in this manner the TTL cloud observations are a subset of the ice cloud observations. All PDFs are constructed from the restricted datasets. The PDFs of cloud top and cloud base heights are given in Figure 2.5 and cloud geometric thickness in Figure 2.6. The statistics of the distributions are given in Tables 2.4 and 2.5.

Table 2.4: Mean [km] and pseudo-standard deviation (parentheses, km) of ice cloud tops, bases and geometrical thickness. The 95% confidence interval for CALIPSO' sampling uncertainty is given in brackets.

Base		Top		Thickness	
ARM	CALIPSO	ARM	CALIPSO	ARM	CALIPSO
		Manus			
11.99 (2.67)	12.46 (2.34) [12.27, 12.63]	14.11 (2.59)	14.62 (2.28) [14.44, 14.79]	2.12 (1.11)	2.16 (1.38) [2.05, 2.27]
		Nauru			
12.57 (2.20)	12.97 (1.97) [12.82, 13.13]	14.70 (1.93)	15.05 (1.60) [14.90, 15.20]	2.13 (1.09)	2.08 (1.15) [1.98, 2.17]
		Darwin			
12.32 (2.29)	13.04 (2.10) [12.87, 13.22]	14.26 (2.03)	15.17 (1.91) [15.02, 15.33]	1.94 (0.98)	2.13 (1.24) [2.00, 2.27]

Cloud boundaries at Manus and Nauru show good consistency between the ground-based and CALIPSO observations with only a few bins falling outside the confidence intervals. More statistically significant differences, particularly for cloud top heights, are found at Darwin. For ice clouds (Figure 2.5a), the ground-based PDFs of cloud tops and bases are skewed towards lower altitudes relative to the CALIPSO PDFs. Maxima in cloud top and base height occur at higher altitudes in the CALIPSO observations.

Table 2.4 shows the means and pseudo-standard deviations of the cloud top and cloud base

Table 2.5: Same as Table 2.4, but for TTL clouds.

Base		Top		Thickness	
ARM	CALIPSO	ARM	CALIPSO	ARM	CALIPSO
		Manus			
14.89 (0.74)	15.12 (1.07) [15.01, 15.24]	16.48 (0.76)	16.56 (0.93) [16.44, 16.68]	1.59 (0.64)	1.44 (0.67) [1.33, 1.55]
		Nauru			
14.91 (0.73)	14.91 (0.69) [14.82, 15.00]	16.50 (0.76)	16.39 (0.86) [16.29, 16.49]	1.60 (0.67)	1.48 (0.71) [1.40, 1.56]
		Darwin			
14.78 (0.59)	15.04 (0.80) [14.95, 15.13]	16.26 (0.70)	16.50 (0.78) [16.40, 16.60]	1.48 (0.64)	1.46 (0.71) [1.37, 1.54]

height observations used to compile the PDFs in Figure 2.5a. Since distributions of cloud top heights, base heights and geometrical thicknesses are not normally distributed, the width of the distribution is described by the pseudo-standard deviation (Lanzante, 1996). The pseudo-standard deviation is defined as the interquartile range divided by 1.349. The interquartile range is the difference between the third quartile (75th percentile) and the first quartile (25th percentile).

The difference in mean cloud top height and cloud base height are within 0.40 km at Nauru, 0.51 km at Manus and 0.91 km at Darwin. The mean cloud top and base height are higher in the CALIPSO observations and differences are statistically significant at all three TWP sites. The larger discrepancies at Darwin are presumably due to the MPL's reduced output power (section 2.4.3). Pseudo-standard deviations of cloud top and base height distributions are larger in the ground-based observations.

Geometrical thicknesses of ice clouds for the ground-based and CALIPSO observations are shown in Figure 2.6a. Agreement between datasets is consistent across all three TWP sites. Relative to CALIPSO PDFs, ground-based PDFs show less clouds with a thickness below 1 km and more clouds with a thickness from about 1–3 km. The means and pseudo-standard deviations of cloud geometrical thickness are given in Table 2.4. The pseudo-standard deviation is larger in the CALIPSO observations at all three TWP sites. Mean geometrical thickness at Nauru differ by 0.05 km and Manus by 0.04 km, neither difference is statistically significant. At Darwin, the difference is statistically significant with the CALIPSO mean thickness larger by 0.19 km.

PDFs of cloud top height and cloud base height of the subset of ice clouds which reside in the TTL are shown in Figure 2.5b. Like with the ice cloud comparison, cloud top and base heights at Manus and Nauru agree to within the uncertainty intervals for nearly all PDF bins. More significant differences are found at Darwin, especially for cloud top heights. As discussed in section 2.4.3 the MPL at Darwin has below-normal output power during much of our sampling period. It follows that this would have the greatest effect on the detection of cloud top height as signal is lost throughout the cloud layer. Means and pseudo-standard deviations of TTL cloud top and base heights are given in Table 2.5. CALIPSO observations show a higher mean TTL cloud top and base at Manus and Darwin. Nauru TTL mean cloud bases are the same in both sets of observations, cloud tops are higher in the ground-based by 0.11 km. The best cloud top agreement is achieved at Manus (0.08 km) and the mean Darwin cloud top shows the largest difference (0.24 km). Cloud bases heights differ at Darwin by 0.26 km and at Manus by 0.23 km. Differences in the mean TTL cloud base and top height are all statistically significant with the exception of cloud bases at Nauru and cloud tops at Manus. All pseudo-standard deviations except for Nauru cloud bases are larger in the CALIPSO observations.

PDFs of TTL cloud geometrical thicknesses are shown in Figure 2.6b. Differences at Nauru and Darwin are within the confidence interval for nearly every PDF bin. At Manus several PDF bins have statistically significant differences. Table 2.5 given the means and pseudo-standard deviations of the two sets of TTL cloud observations. Ground-based mean TTL geometrical thicknesses are larger than CALIPSO at all three TWP sites. Differences at Darwin are greater by 0.02 km, Nauru by 0.12 km and Manus by 0.15 km. The differences at Nauru and Manus are statistically significant.

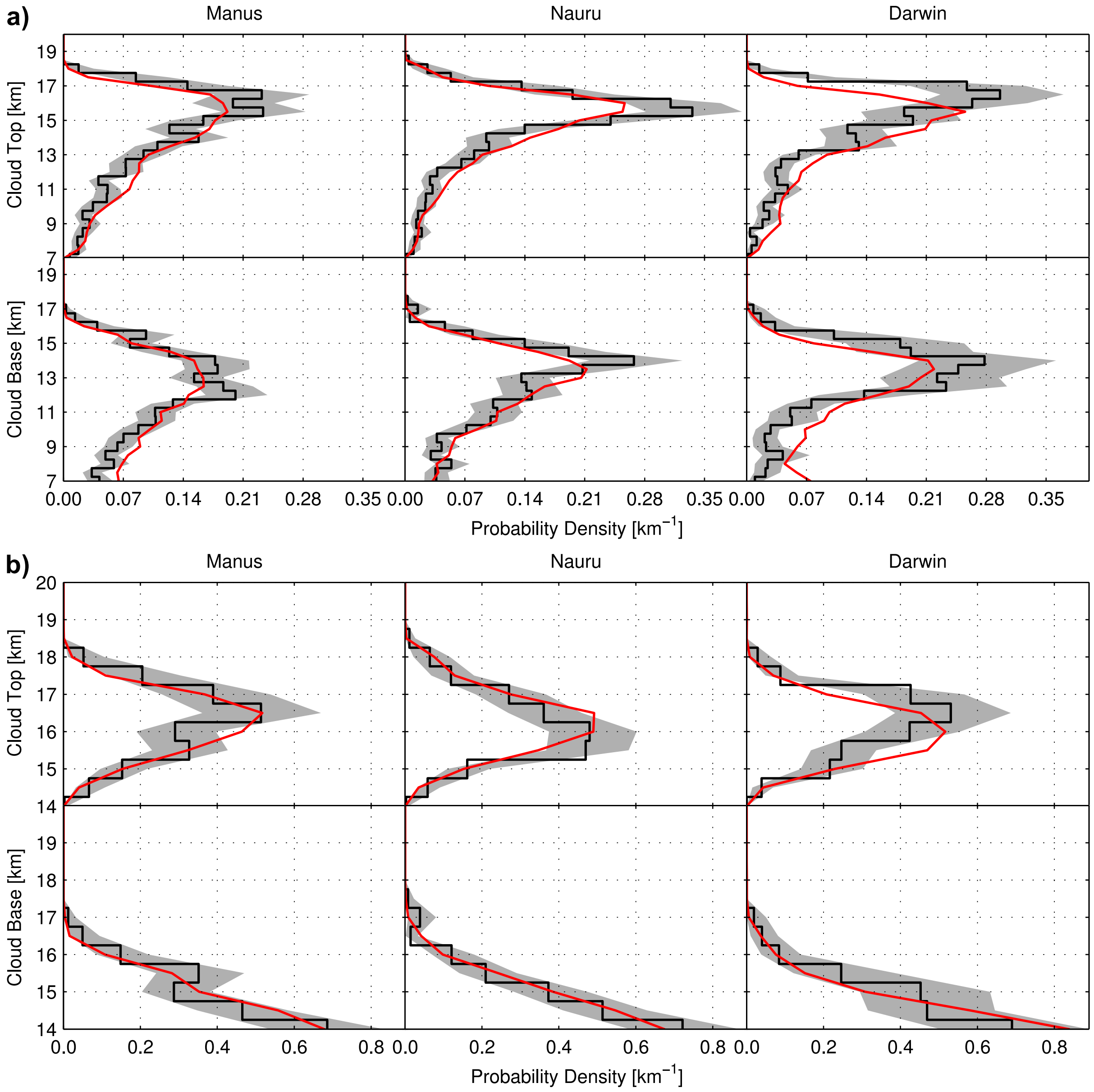

Figure 2.5: PDFs of (a) ice and (b) TTL cloud top heights (top row) and cloud base heights (bottom row) from CALIPSO (black line) and ground-based (red line) datasets. The shaded region represents the 95% confidence interval due to CALIPSO's sampling uncertainty. The three ARM sites are shown (left to right): Manus, Nauru and Darwin.

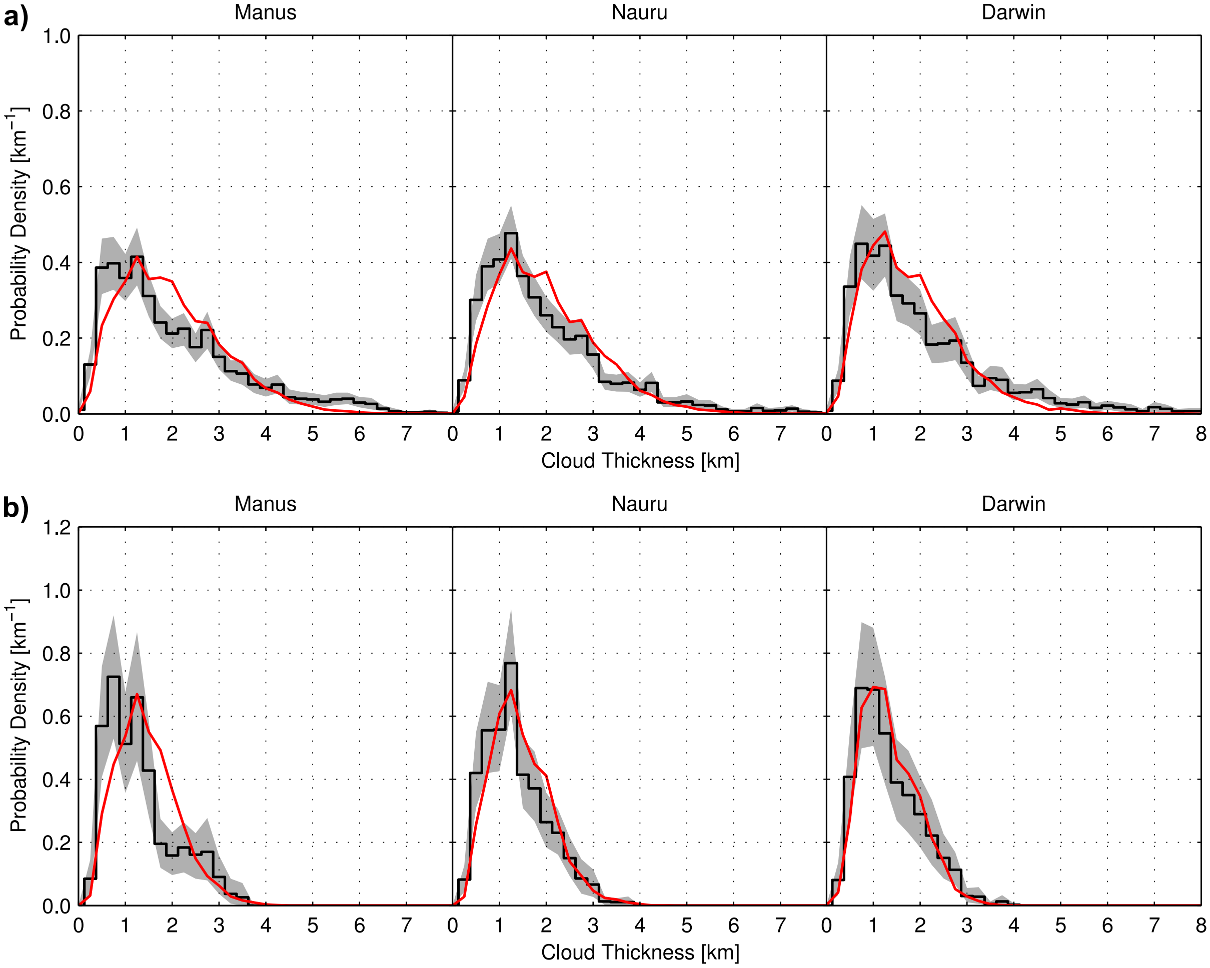

Figure 2.6: PDFs of (a) ice and (b) TTL cloud geometrical thickness from CALIPSO (black line) and ground-based (red line) datasets. The shaded region represents the 95% confidence interval due to CALIPSO's sampling uncertainty. The three ARM sites are shown (left to right): Manus, Nauru and Darwin.

2.5.3 Number of Cloud Layers per Profile

When comparing the number of cloud layers per profile we first transform the ground-based observations to an equivalent spatial resolution of 5 km. This is done since the larger horizontal resolution of CALIPSO will have a better chance of detecting a multi-layer cloud profile than the finer resolution of the ground-based observations. Similar to the procedure for the cloud fraction, a MPL "pixel" is defined using a block of consecutive profiles. Ideally we would like to make a comparison of the number of cloud layers using the restricted datasets. However by constructing MPL "pixels" there is the possibility that some profiles within "pixels" could be opaque to the lidar. To deal with this situation, first only "pixels" where at least half of the profiles are transparent to the lidar signal are considered in this analysis. The number of cloud layers is then determined from this new set of "pixels." To simulate the effect of averaging across each "pixel" cloud layers from adjacent profiles which overlap in the vertical are considered as a single cloud layer. After overlapping cloud layers are combined, the number of cloud layers in each "pixel" is taken as the maximum number of layers from any one profile inside the block. Any opaque profiles which may be present inside a "pixel" are not used for either combining the overlapping cloud layers or for determining the number of cloud layers in each "pixel."

Comparisons of the number of ice cloud layers per profile are shown in Figure 2.7 for CALIPSO data and the unmodified ground-based data. CALIPSO observations have a higher occurrence of multi-layered cloud profiles, as would be expected from a larger amount of horizontal averaging. In Figure 2.7 the number of layers for the ground-based dataset is also derived using the MPL "pixel" that is equivalent to the CALIPSO 5 km horizontal resolution. The only difference which is statistically significant is for profiles which contain two ice cloud layers at Nauru. In this section we do not present a comparison of the number of TTL cloud layers per profiles since the majority ($\sim 97\%$) of profiles contain only a single TTL cloud layer. This result holds true regardless of observation platform or location.

Inhomogeneous cloud features can lead to the detection of multiple, closely-spaced cloud layers. As a consequence, in the retrieval process cloud layers that are considered too close together are merged together. In the ground-based MPL retrieval cloud layers separated by less than 500 m are combined into a single cloud layer. In the CALIPSO cloud product, the process

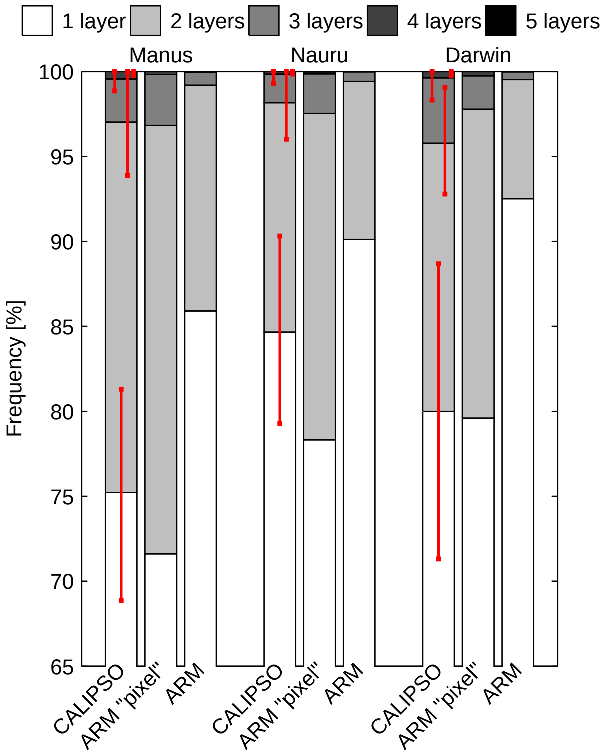

Figure 2.7: Frequency of the number of ice cloud layers per profile from CALIPSO and ground-based datasets for the three ARM TWP sites. The bounds on CALIPSO's 95% confidence interval are given as red lines.

is more complicated. A different minimum separation is specified for each averaging resolution that the CALIPSO data undergoes [*Winker 2011*, personal communication]. Therefore there is no definitive cutoff for a minimum gap but rather any layers separated by less than 1 km have the possibility of being merged together. This complicates our comparison of the number of cloud layers since differences in how each set of observations closes small gaps in between cloud layers may lead to spurious differences or agreement between the datasets. It cannot be ruled out that the overall good agreement in Figure 2.7 may be due to differences in how each retrieval defines a unique cloud layer.

2.5.4 Optical Depth

2.5.4.1 Retrieval Descriptions

Following the lidar equation given by Platt (1973) the layer-integrated attenuated backscatter $\gamma^{'}$ is related to the cloud layer optical depth τ_c by

$$\gamma^{'} = \int_0^{\tau_c} \frac{1}{S} exp(-2\eta\tau) d\tau \tag{2.1}$$

where τ is the visible optical depth, η is the multiple scatter factor which accounts for multiple scattering effects captured by the lidar receiver and S is the lidar ratio which is the ratio of the cloud extinction coefficient to the backscatter coefficient. The retrieval of cloud optical depth from lidar measurements requires the estimation of the lidar ratio and the multiple scattering factor.

The CALIPSO cloud product uses three methods to estimate the lidar ratio: (1) the transmittance method which requires a clear air signal below the cloud layer, (2) the lidar equation using a lidar ratio of 25 sr for ice clouds and 19 sr for water clouds and (3) the lidar equation but with an adjustment of the lidar ratio to avoid unphysical optical depths. In CALIPSO L2 v3.01 the multiple scattering factor is set to a constant value of $\eta = 0.6$ for all retrieval types. [*Winker 2010*, personal communication]. For constrained retrievals Winker et al. (2009) estimates the uncertainty for cloud optical depth to be within a factor of 2 for optical depths less than 5. The large majority ($\sim$ 90% in the restricted ice cloud datasets) of CALIPSO cloud optical depth retrievals use a fixed lidar ratio. In our comparison we consider optical depths derived using any of the three methods for the lidar ratio.

An alternative CALIPSO depth retrieval of Yang et al. (2010) is also considered in our comparison. This retrieval uses a constant multiple scattering factor of 0.5 and a lidar ratio of 34 sr for ice clouds. Optical depth is then calculated using the cloud layer backscatter from the CALIPSO L2 v3.01 cloud product. Using CALIPSO v2.01 data, Yang et al. (2010) estimates a relative uncertainty of 25% in their ice cloud optical depth retrieval.

For the ground-based MPL, extinction is calculated following Comstock and Sassen (2001) with both S and η fixed at 25 sr and 0.8, respectively. Additionally we make comparisons with

η fixed at 0.8 and estimate S for each profile using the backscatter above the cloud layer as described by Comstock and Sassen (2001).

2.5.4.2 Optical Depth Results

PDFs of optical depths are shown in Figure 2.8. Included in this figure is all the optical depth retrievals considered in this study: (1) the official v3.01 CALIPSO retrieval (black line), (2) the CALIPSO retrieval of Yang et al. (2010) (blue line), (3) the ground-based retrieval with $S = 25$ and $\eta = 0.8$ (red line), and (4) the ground-based retrieval with $\eta = 0.8$ and a variable lidar ratio (green line). PDFs are divided into two optical depth ranges: $0.01 \leq \tau < 0.2$ and $0.2 \leq \tau \leq 3$. The mean optical depth in each of these optical depth ranges is denoted with an “x” along the x-axis. The percent of observations which fall within each range are given in the upper-right corner of each plot.

PDFs of ice and TTL cloud optical depth show slight differences between retrieval methods for the same platform. Comparing the two ground-based retrievals, the variable lidar ratio PDF is larger for thicker optical depths, while the fixed lidar ratio PDF is larger in the smaller optical depth bins. For the two CALIPSO retrievals, the Yang et al. (2010) retrieval has less clouds in the thinnest of the optical depth bins relative to the official CALIPSO L2 data.

Examining Figure 2.8a, agreement between retrieval types for ice cloud optical depth varies across all three TWP sites depending on the range of optical depths being examined. Overall we find that all four retrieval types typically agree within uncertainty intervals. In general, the Yang et al. (2010) retrieval agrees best with the ground-based observations for the thick ice clouds ($\tau \geq 0.2$). The Yang et al. (2010) retrieval is more consistent in the thin range ($\tau < 0.2$) with the ground-based variable lidar ratio retrieval at Manus and Darwin, while the CALIPSO L2 and ground-based fixed lidar ratio retrievals agree better for these two sites. Nauru is the exception, where the thin optical depths in the CALIPSO L2 observations agree best with the ground-based variable lidar ratio retrieval.

The percentages in the upper-right corner of the plots in Figure 2.8 gives the distribution of optical depths across the two different ranges. The ground-based fixed lidar ratio retrieval contains the most clouds in the thin optical depth category ($\tau < 0.2$) of the four retrieval types.

For the thick optical depths ($\tau \geq 0.2$) the ground-based variable lidar ratio retrieval contains the most clouds. Comparing the two CALIPSO retrieval types, the retrieval of Yang et al. (2010) contains more clouds in the thick optical depth range while the CALIPSO L2 retrieval contains more clouds in the thin optical depth range.

TTL cloud optical depth comparisons are given in Figures 2.8b. As with the comparisons of ice cloud optical depth, we find that typically all four retrieval types agree to within the uncertainty intervals. In the thin optical depth range ($\tau < 0.2$) the ground-based variable lidar ratio retrieval agrees better to both CALIPSO retrievals. Distributions of the optical depths by range reveal that for all four retrievals and all three TWP sites more than 90% of TTL cloud optical depths fall below 0.2.

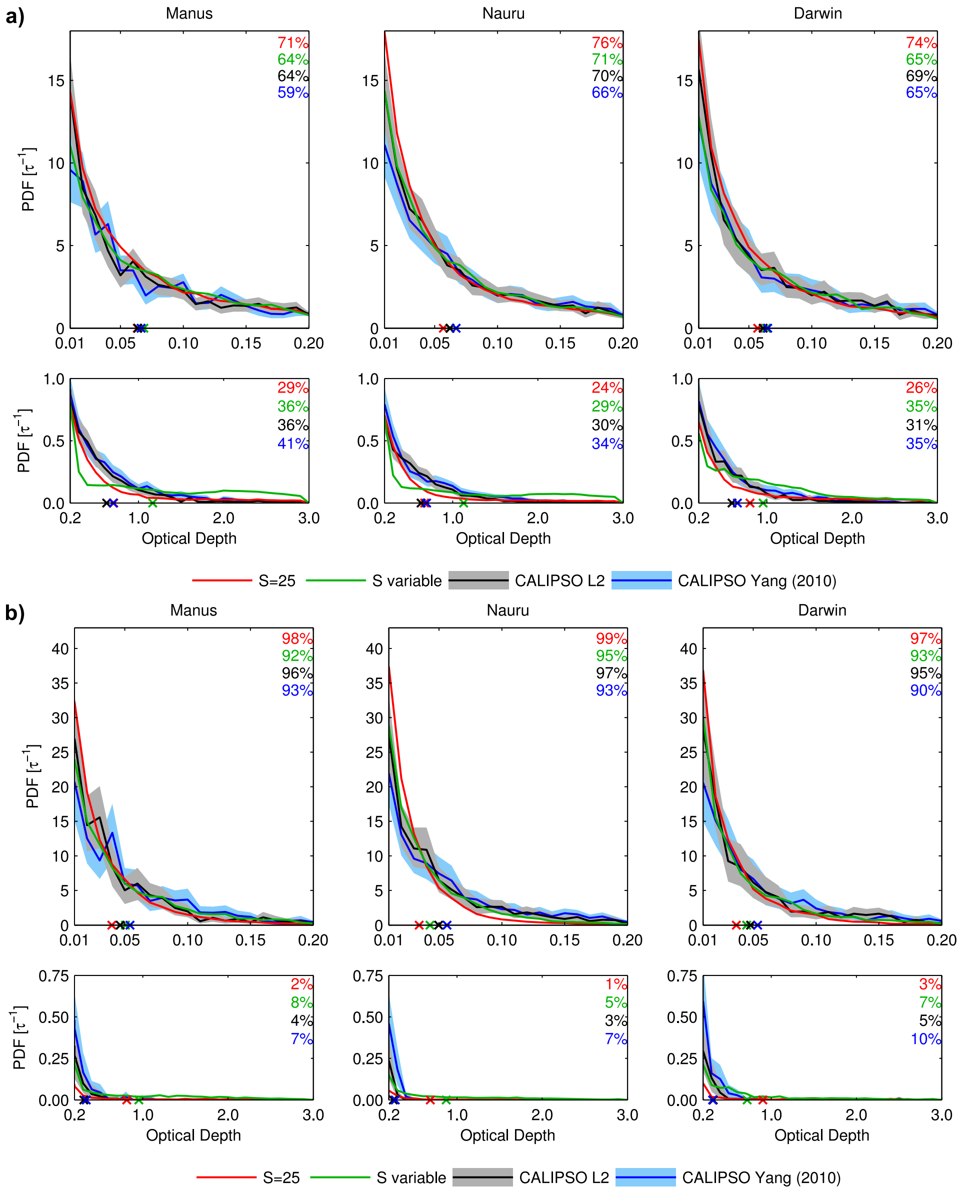

Figure 2.8: PDFs of (a) ice and (b) TTL cloud optical depths from CALIPSO L2 v3.01 cloud product (black line) and the CALIPSO optical depth retrieval of Yang et al. (2010) (blue line). The shaded region on each CALIPSO retrieval represents the 95% confidence interval due to the sampling uncertainty. Ground-based optical depths are shown for the lidar ratio fixed at 25 sr (red line) and the variable lidar ratio retrieval (green line). The three ARM TWP sites are shown (left to right): Manus, Nauru and Darwin. The top row of plots shows the optical depths from $0.01 \leq \tau < 0.2$ and the bottom row shows $0.2 \leq \tau \leq 3$. The upper-right corner of each plot gives the percent of observations which fall within the plotted optical depth range. The mean optical depth within each range is denoted with an “x” along the x-axis.

2.5.5 Diurnal Biases

Observations using lidar become increasingly difficult during the daytime hours due to increased signal noise. As shown in Figure 2.3 daytime MPL observations of cloudy profiles are frequently attenuated, about 70% depending on the month and location. During the nighttime the percentage of MPL profiles which are attenuated is much lower than the daytime. Since many comparisons presented in this study focus on transparent profiles only, the resulting ground-based dataset are biased towards nighttime observations. During the night, both the ground-based and CALIPSO observations have similar fractions of attenuated profiles. The fraction of attenuated profiles during the daytime for CALIPSO observations is typical greater than at night. However, differences between day and night are not as severe as those seen in the ground-based observations. The nighttime bias in the ground-based observations motivates the comparison of cloud properties for night and day separately. Comparisons of night-only restricted datasets provides a set of observations which have a similar fraction of cloudy attenuated profiles. In addition, nighttime-only observations provide a comparison free of retrieval complications due to the solar background. In this analysis we only present results for the ice cloud datasets. The comparisons of the diurnal differences of TTL cloud properties show similar results and conclusions drawn from ice cloud results are also generally applicable to TTL cloud observations. For completeness, we present the night and day-only TTL cloud properties in Appendix B.

Night and day-only ice cloud top and base PDFs are shown in Figure 2.9. Differences between CALIPSO and ground-based nighttime ice cloud PDFs (Figure 2.9a) are similar to comparisons made using observation from all times (Figure 2.5a). Much larger differences exist when comparing daytime observations of ice clouds (Figure 2.9b). During the daytime CALIPSO observations contain more higher ice cloud tops and bases than the ground-based observations. The number of ground-based daytime observations is small enough such that the assumption of insignificant sampling uncertainty may no longer hold true.

Ice cloud PDFs of geometrical thicknesses are given in Figure 2.10. Unlike the cloud top and base heights, both day and night PDFs show similar discrepancies between the two sets of observations as the full set of observations do (Figure 2.6a). Thicker clouds are observed during the night in both the CALIPSO and ground-based datasets. Note that the MPL daytime observations of cloud boundaries are much more severely impacted by the solar background. However, similar differences in cloud thickness between the daytime and nighttime from CALIPSO and MPL observations indicate that both ice and TTL clouds may actually be thicker at night. At the same time, this diurnal cycle of geometrical thickness may also be partly the result of the improvement in the SNR during the nighttime hours. A better detection of the cloud base and cloud top at night would result in a geometrically thicker cloud.

The number of ice cloud layers per profile are given in Figure 2.11 for night and day observations. The MPL "pixel" method described previously is used to calculate the number of ground-based cloud layers. At night the ground-based observations contain more multi-layer ice cloud profiles than CALIPSO. While during the day the opposite is true, CALIPSO observes more multi-layered ice cloud profiles than the ground-based MPL. The diurnal biases negate each other to some degree when we compare observations from both day and night together (Figure 2.7). This results in better agreement in the number of cloud layers between the CALIPSO and ground-based observations when comparing both day and night. As discussed in section 2.5.3 these comparisons may be impacted by differences in how each retrieval defines a unique cloud layer.

Comparisons of daytime and nighttime ice cloud optical depths are given in Figure 2.12. Overall differences between day and night PDFs are similar to those seen using the full sets of observations. The only significant differences are found for the thinnest few ice cloud optical depth bins. There the daytime observations for all four retrieval types, particularly for the ground-based variable lidar ratio retrieval, have less of the very thinnest optical depths relative to the nighttime observations. This indicates that both sets of observations are more sensitive to clouds with the thinnest optical depths at night, as is expected from SNR considerations.

The statistics derived from day and night observations of cloud top height, base height, geometrical thickness and optical depth are not significantly impacted by the MPL's diurnal bias in the restricted datasets. However, this diurnal bias could potentially effect the comparisons of the number of cloud layers per profile. While the full set of ground-based observations is more representative of nighttime cloud properties, the actual diurnal cycle of cirrus clouds as represented by CALIPSO observations is too small for this bias to introduce significant differences.

The TTL cloud observations also support these conclusions and are given in Appendix B.

An additional complication exists for the comparison of daytime data which arises from how attenuation is determined in the two sets of observations. For a CALIPSO profile to be considered completely transparent then a surface return must be identified in the backscatter profile. For the MPL retrieval if the measured backscatter above the cloud layer does not decrease proportional to the molecular backscatter then the profile is assumed to be attenuated. For a cloudy profile viewed by CALIPSO determining attenuation is more clear-cut since a surface return is a relatively large signal compared to an assessment using the molecular scattering above cloud. This makes the attenuation test for the MPL more sensitive to SNR and could lead to an overestimate of the occurrence of attenuated profiles. During the nighttime, SNR is high and this effect should be less significant. However during the daytime, when SNR is low, the MPL restricted dataset could exclude cloud profiles which, if hypothetically viewed by CALIPSO, would be included in the CALIPSO restricted dataset.

Comparing the fraction of attenuated cloud profiles (Figure 2.3) alone gives the impression that this effect could be significant as the fraction of MPL cloud profiles attenuated during the daytime is much larger than CALIPSO's. During the nighttime both sets of observations show a similar fraction of attenuated cloud profiles. Therefore, it is possible that discrepancies in daytime cloud properties are larger due the different attenuation tests. However, this likely does not explain the majority of differences between the two sets of observations during the daytime. Given the same cloud profile, the sensitivity of the MPL attenuation test to lower SNR during the daytime would result in a profile being flagged as attenuated at a thinner optical depth than it would be during the nighttime. This would result in far fewer thicker cloud optical depths in the daytime restricted MPL observations. Examining Figure 2.12 it is evident that this is not the case. Comparing the MPL PDFs from daytime and nighttime observations show that a similar amount of thicker optical depths occur during the nighttime and daytime. In addition the agreement between CALIPSO and MPL optical depth PDFs does not show a striking difference from nighttime to daytime observations.

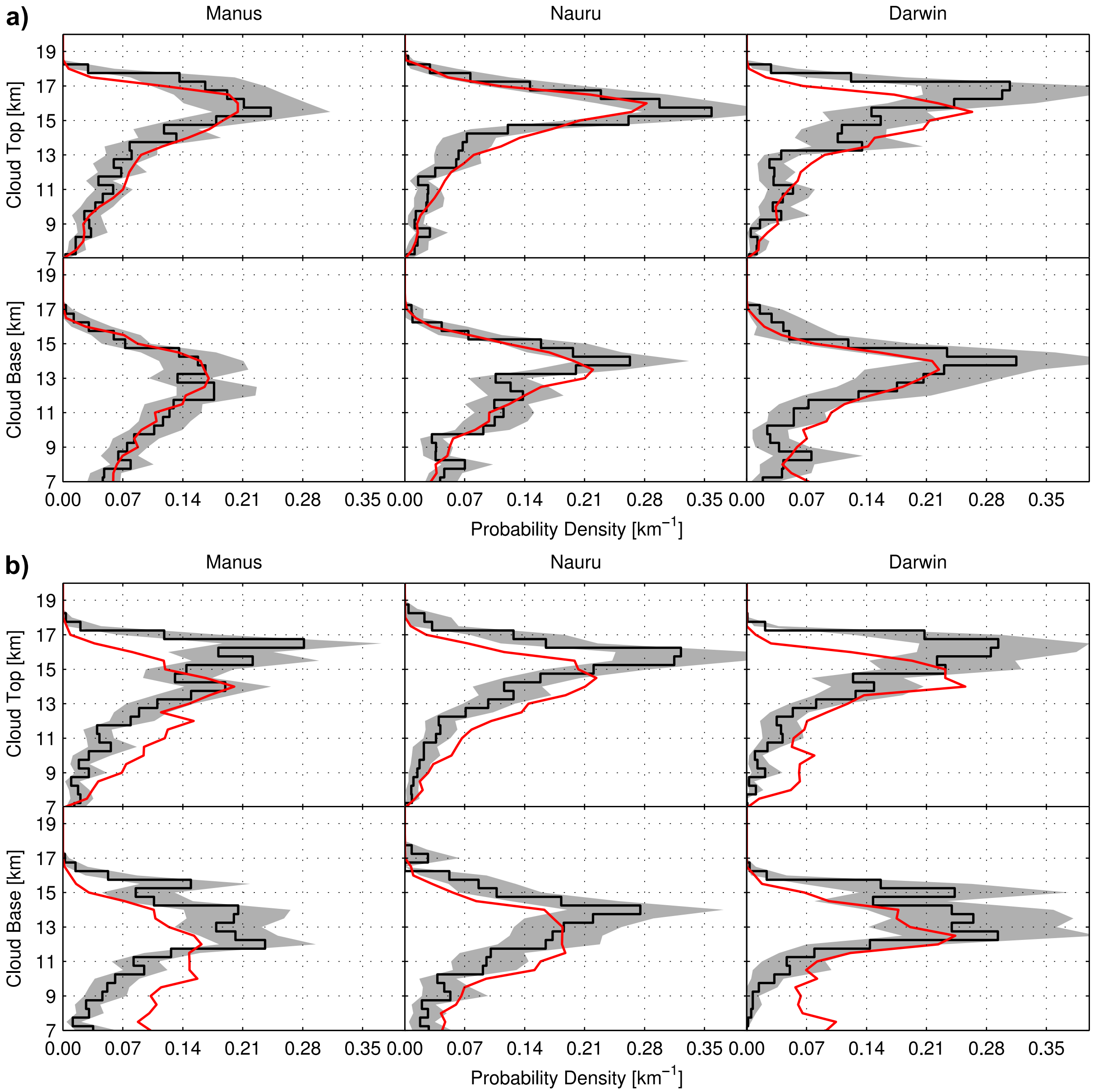

Figure 2.9: PDFs of ice cloud top heights (top row) and cloud base heights (bottom row) from CALIPSO (black line) and ground-based (red line) datasets during the (a) nighttime and (b) daytime. The shaded region represents the 95% confidence interval due to CALIPSO's sampling uncertainty. The three ARM sites are shown (left to right): Manus, Nauru and Darwin.

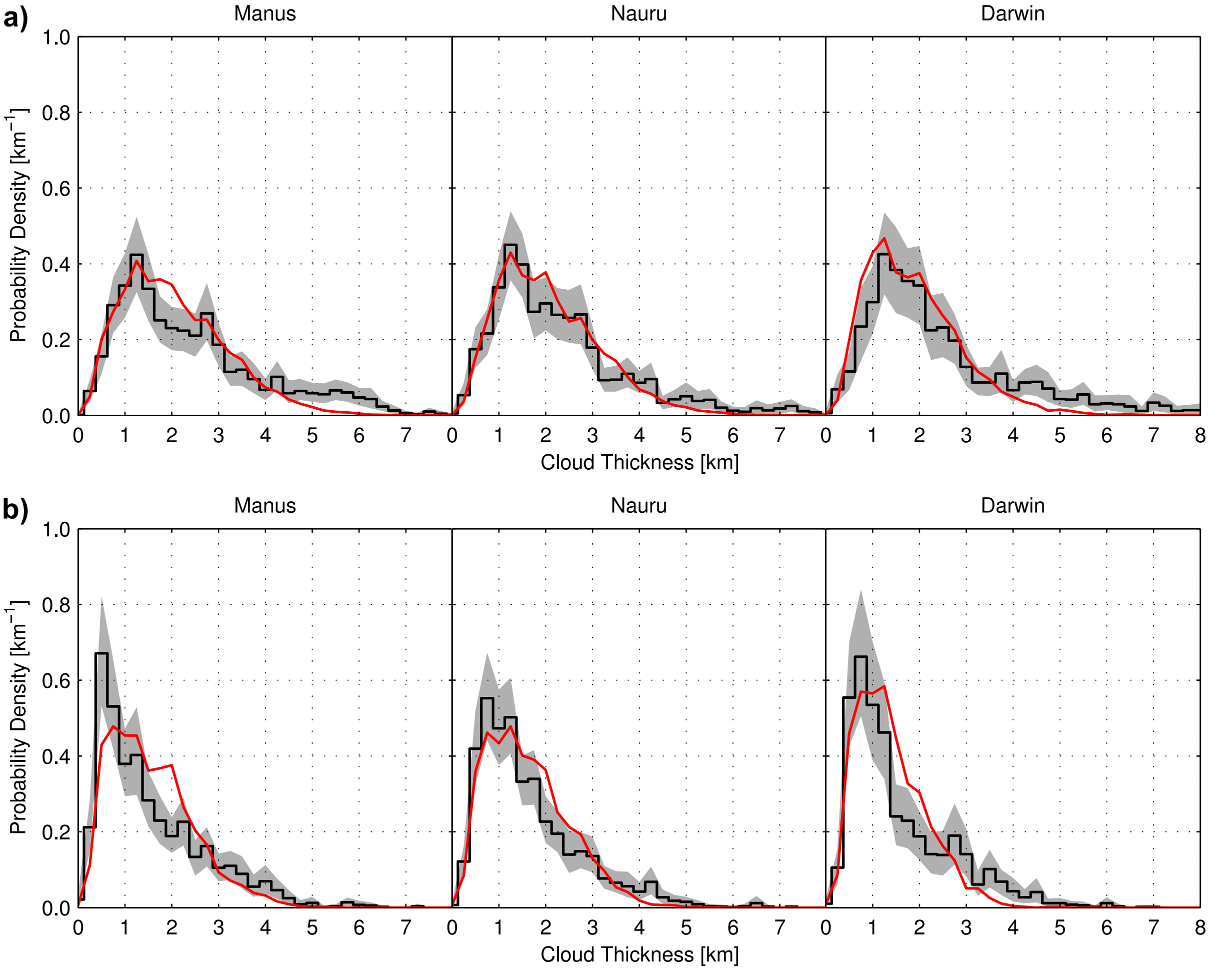

Figure 2.10: PDFs of ice cloud geometrical thickness from CALIPSO (black line) and ground-based (red line) datasets during the (a) nighttime and (b) daytime. The shaded region represents the 95% confidence interval due to CALIPSO's sampling uncertainty. The three ARM sites are shown (left to right): Manus, Nauru and Darwin.

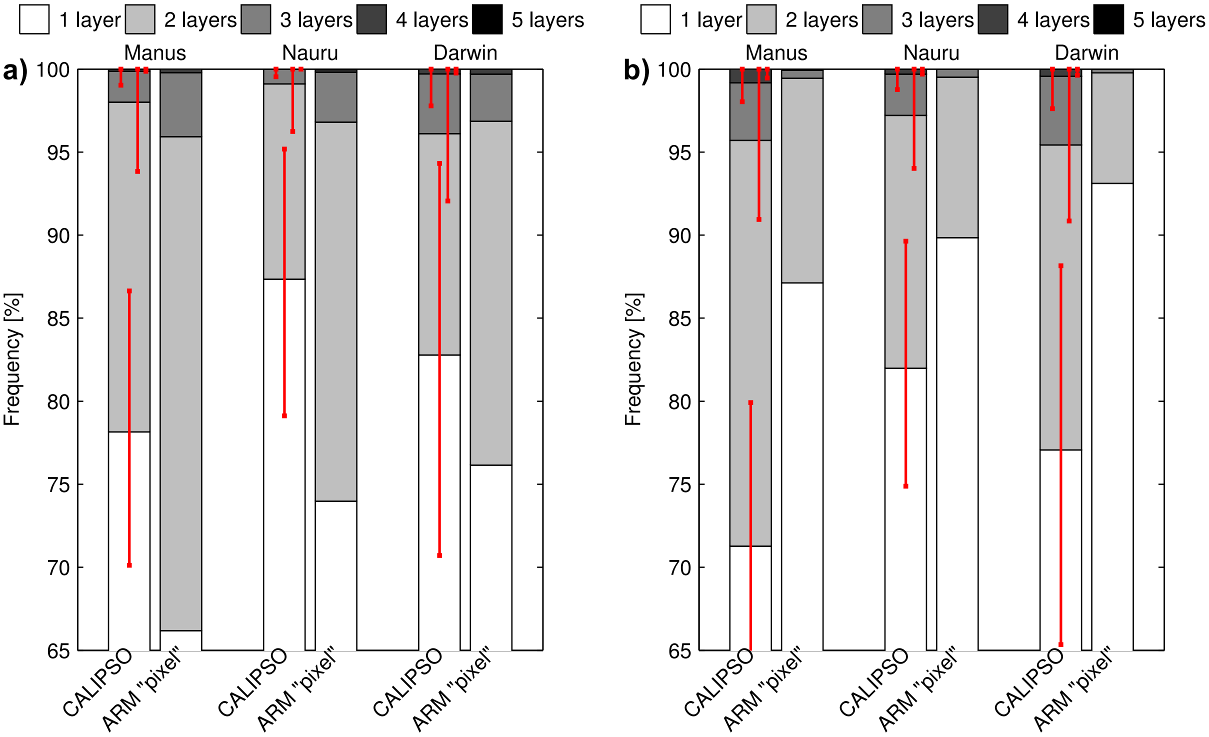

Figure 2.11: Frequency of the number of ice cloud layers per profile during the (a) nighttime and (b) daytime from CALIPSO and ground-based datasets for the three ARM TWP sites. The bounds on CALIPSO's 95% confidence interval are given as red lines. The number of layers in the ground-based data is derived using the MPL "pixel" method, which is described in the text.

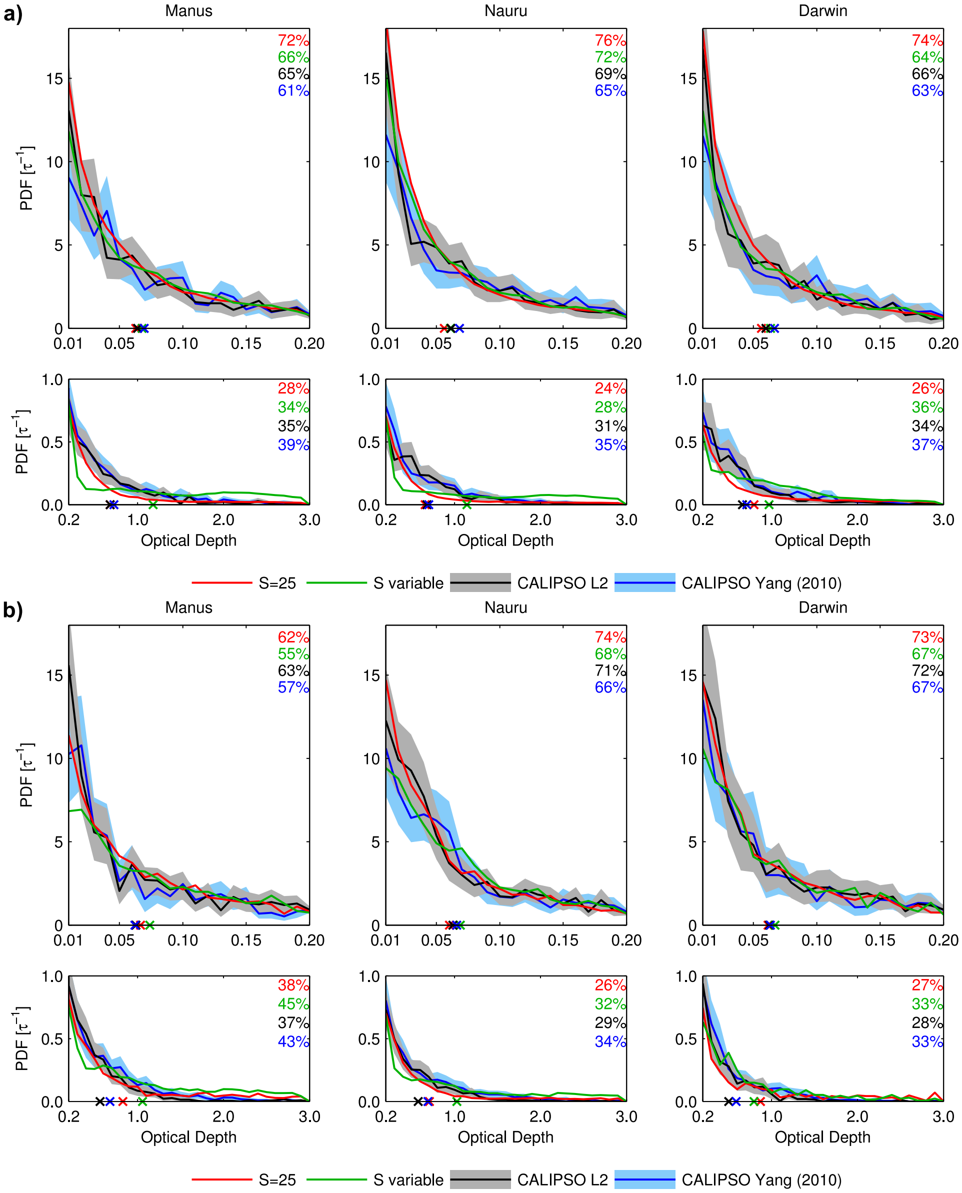

Figure 2.12: PDFs of ice cloud optical depths from CALIPSO L2 v3.01 cloud product (black line) and the CALIPSO optical depth retrieval of Yang et al. (2010) (blue line) during the (a) nighttime and (b) daytime. The shaded region on each CALIPSO retrieval represents the 95% confidence interval due to the sampling uncertainty. Ground-based optical depths are shown for the lidar ratio fixed at 25 sr (red line) and the variable lidar ratio retrieval (green line). The three ARM TWP sites are shown (left to right): Manus, Nauru and Darwin. The top row of plots shows the optical depths from $0.01 \leq \tau < 0.2$ and the bottom row shows $0.2 \leq \tau \leq 3$. The upper-right corner of each plot gives the percent of observations which fall within the plotted optical depth range. The mean optical depth within each range is denoted with an “x” along the x-axis.

2.5.6 Effect of Resolution on PDFs of Cloud Properties

The equivalent spatial resolution of the ground-based MPL is significantly smaller than that of the CALIPSO 5 km observations. This effect was explored when comparing cloud fraction (section 2.5.1). For statistical comparisons of cloud properties CALIPSO's larger spatial average could result in averaging over finer-scale structures of cloud boundaries and variations in optical depth. The higher spatial resolution of the ground-based MPL would capture these finer scale features. Here we perform a similar analysis used for cloud fraction to test the effect of resolution on the PDFs of ice cloud properties.

The effect of resolution is determined using a method analogous to that used for the transparent cloud fraction. Ground-based observations are first combined into "pixels" using mean radiosonde wind profiles as described in section 2.5.1. If more than half of the cloud profiles inside a "pixel" are attenuated then that "pixel" is discarded from the set of observations. Our results are not sensitive to the fraction chosen to determine which "pixels" to keep. Cloud properties are then averaged in each of these "pixels." Since combining multiple cloud layers across profiles in a meaningful way is dubious, we derive column properties. The highest cloud top for each "pixel" is determined by averaging the highest cloud tops from the set of profiles that composes the "pixel." The lowest cloud base in each "pixel" is determined in an analogous manner except by averaging the lowest cloud bases. The "pixel" column optical depth is taken as the average of the column optical depths across the set of profiles inside each "pixel." Figure 2.13 shows the results of this analysis for the highest cloud top heights and lowest cloud base heights. Figure 2.14 gives the results for the column optical depth. The dashed lines in each of these figures represent the ground-based set of observations which have been averaged into "pixels." The solid lines shows the column properties derived from the restricted set of CALIPSO and unmodified ground-based observations.

Differences between the ground-based and the averaged ground-based PDFs for the highest ice cloud top and lowest ice cloud base are typically quite small. These small differences between the ground-based PDFs relative to the much larger differences seen when comparing either one of the ground-based PDFs to the CALIPSO PDFs in Figure 2.13 indicate that resolution alone can not explain the majority of the discrepancies in cloud top and base height. Therefore

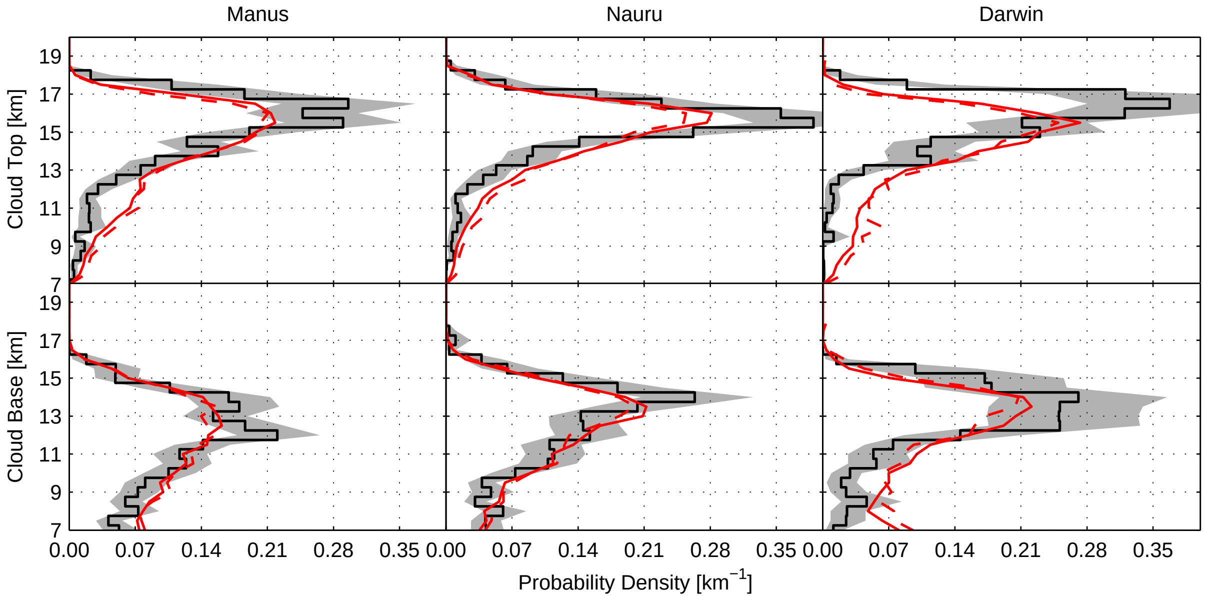

Figure 2.13: PDFs of the highest cloud top heights (top row) and lowest cloud base heights (bottom row) from CALIPSO (black line) and ground-based (red line) ice cloud datasets. The dashed line gives the ground-based ice cloud PDF for the datasets which has been averaged to an equivalent spatial resolution of 5 km. The shaded region represents the 95% confidence interval due to CALIPSO's sampling uncertainty. The three ARM sites are shown (left to right): Manus, Nauru and Darwin.

we conclude that comparisons of cloud top and base height PDFs presented in this study are not significantly impacted by the different spatial resolutions. Physically this means that CALIPSO's larger amount of horizontal averaging is not large enough to significantly mask variations in ice cloud boundaries. The sensitivity of TTL cloud boundaries was also tested but is not shown here. The results are similar to what is shown for the ice cloud observations.

Column optical depths in Figure 2.14 include comparisons for all four retrievals considered in this study— the ground-based with a fixed lidar ratio, a variable lidar ratio, the official CALIPSO L2 retrieval, and the CALIPSO retrieval of Yang et al. (2010). Comparisons of the TTL cloud observations show little change after averaging the ground-based data and are not shown. Discrepancies between the ground-based and the averaged ground-based ice cloud PDFs are prevalent in a few particular areas. Both retrieval types tend to have slightly less clouds with optical depths in the very thinnest bins ($\tau \lesssim 0.03$). Most significant is for thicker ice cloud optical depths ($\tau \gtrsim 0.3$) for the variable lidar ratio retrieval. We expect the spatial averaging to play a larger role for the variable lidar ratio since estimating the lidar ratio for each cloud profile results in a greater variability of optical depth from profile to profile. Averaging the fixed lidar ratio retrieval results in a smaller difference when compared with the original ground-based observations. Since the CALIPSO retrieval of Yang et al. (2010) uses a fixed lidar ratio and the majority of clouds in the CALIPSO L2 retrieval use a fixed lidar ratio we can conclude that CALIPSO optical depth PDFs are not significantly affected by spatial resolution. However, in comparing with the ground-based variable lidar ratio retrieval the results shown in Figure 2.14 need to be taken into consideration. We showed in section 2.5.4 that the PDFs for thicker optical depth disagreed the most for the variable lidar ratio retrieval. The analysis here suggest that this may be an artifact of the finer spatial resolution of the ground-based observations. For the thinnest of optical depths we showed that the ground-based variable lidar ratio retrieval agreed best to either of the two CALIPSO retrievals. Given that the disagreement at thicker optical depth is a result of different resolutions we can conclude that optical depths are most similar between CALIPSO and the variable lidar ratio ground-based retrieval.

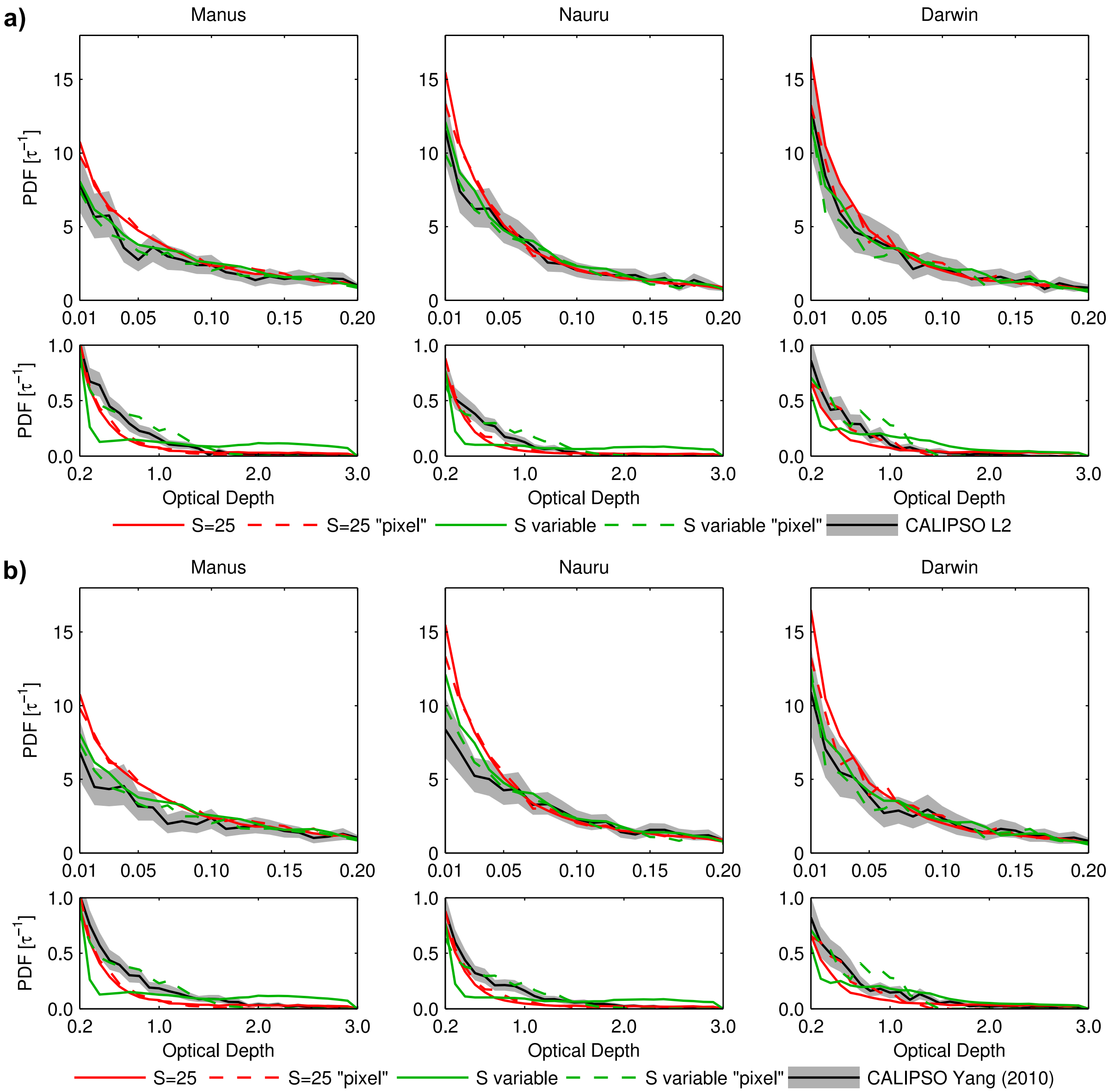

Figure 2.14: PDFs of ice cloud column optical depths from (a) CALIPSO L2 v3.01 cloud product (black line) and (b) the CALIPSO optical depth retrieval of Yang et al. (2010) (black line). The shaded region represents the 95% confidence interval due to CALIPSO's sampling uncertainty. Ground-based ice cloud column optical depths are shown for the lidar ratio fixed at 25 sr (red line) and the variable lidar ratio retrieval (green line). The dashed lines give the ground-based column optical depths for datasets which have been averaged to an equivalent spatial resolution of 5 km. The three ARM TWP sites are shown (left to right): Manus, Nauru and Darwin. The top row of plots shows the optical depths from $0.01 \leq \tau < 0.2$ and the bottom row shows $0.2 \leq \tau \leq 3$.

2.6 Summary

Statistics of CALIPSO and ground-based lidar observations are compared over a 31 month period. Ground-based lidar observations are taken from the MPLs at the three ARM TWP sites: Manus, Nauru and Darwin. CALIPSO's sampling uncertainty is nontrivial for the sampling period chosen and is assessed using the moving block bootstrap resampling method. Analyzed for consistency is cloud fraction, top height, base height, geometrical thickness, optical depth and the number of cloud layers per profile. Besides cloud fraction, cloud properties are compared for ice clouds only, which we define as a cloud with a base greater than 7 km. Also compared are the subset of ice clouds which reside in the TTL, defined by a cloud base greater than 14 km. Applications of MPL or CALIPSO observations to asses atmospheric processes, for instance the delicate radiative balance of the TTL, requires consideration of the strengths and weakness of each dataset outlined in this study.

The cloud fraction derived from the CALIPSO observations showed a significantly higher cloud fraction— by up to 0.27— than the native ground-based observations. After accounting for the difference in resolution using the ground-based "pixel" method the total cloud fraction agrees to within 0.06 at all three TWP sites. During the nighttime, total cloud fraction agrees even better. This is also the case for the assessment of the occurrence of transparent cloud profiles. The overall good agreement in total cloud fraction between CALIPSO and ground-based observations with a similar horizontal resolution is revealed to be caused by a fortuitous cancellation of errors from cloud fraction at different altitudes. For higher altitudes ($\gtrsim$ 10 km), the CALIPSO cloud fraction is significantly larger while at lower altitudes ($\lesssim$ 7 km), the ground-based cloud fraction is significantly larger. CALIPSO's high-resolution cloud clearing does remove clouds detected at single-shot resolution below 4 km of altitude, which may explain it's lower cloud fraction in that altitude range. However, significant differences still occur above 4 km. It is possible that the ground-based observations contain more smaller-scale clouds than the CALIPSO observations. Differences become even larger when the ground-based "pixels" are constructed as the cloud fraction in these regions of small-scale clouds is greatly enhanced. For cloud fraction at higher altitudes, approximately half of the difference can be explained by the difference in spatial resolution. Even after correcting for resolution differences the CALIPSO cloud fraction remains larger at high altitudes. This may be an indication that the MPL is not as sensitive to high clouds during both the nighttime and daytime. All comparisons of daytime cloud fraction show significantly larger differences.

Comparisons of cloud top and base heights show that CALIPSO places clouds at higher altitudes relative to the ground-based observations. The only exception is at Nauru where the mean ground-based TTL cloud top falls just outside the upper bound of CALIPSO's confidence interval. Mean TTL cloud top and base heights differ by less than 0.23 km at Manus and 0.11 km at Nauru. Mean ice cloud tops and bases are lower in the ground-based observations by 0.51 km at Manus and 0.47 km at Nauru. Discrepancies in cloud top and base height are larger at Darwin, particular cloud top heights, due to a reduction in the MPL output power during much of our sampling period. At Darwin the ground-based mean cloud top is lower by 0.91 km for ice clouds. We find both in terms of mean and PDFs of cloud top and base heights that the CALIPSO observations are placed at higher altitudes relative to the ground-based observations. This systematic difference can be explained by the different viewpoints of each instrument. Besides the amount of noise, cloud detection is limited by in-cloud attenuation of the lidar beam making the cloud boundary furthest from the lidar more difficult to detect accurately. Measurements with a space-borne lidar are likely to overestimate the cloud base, that is place the cloud base at a higher altitude than it should be. Conversely, the same cloud viewed from a ground-based lidar is likely to underestimate the cloud top, that is place the cloud top at a lower altitude than the actual cloud top. Therefore when comparing the ground-based MPL and space-borne CALIPSO lidar the net of these two effects is that clouds boundaries are shifted to higher altitudes in the CALIPSO observations relative to the ground-based observations. We also determine that CALIPSO's larger amount of horizontal averaging does not effect comparisons of cloud top and base heights.

All three MPLs have a large fraction of attenuated profiles during the daytime. Therefore the ground-based statistics derived from the restricted datasets are more representative of the characteristics of nighttime clouds. We find that comparisons of cloud top and base heights using observations from both day and night are not affected by the MPL's diurnal bias. While the full set of ground-based observations is more representative of nighttime cloud properties, the diurnal cycle of cirrus clouds as represented by CALIPSO observations is too small for this to introduce significant differences. During the daytime cloud top and base heights are considerably lower relative to CALIPSO observations.

Mean ice cloud geometrical thicknesses differ significantly only at Darwin where CALIPSO is thicker by 0.19 km. For TTL cloud geometrical thicknesses we find statistically significant differences of 0.15 km at Manus and 0.12 km at Nauru. Geometrical thickness is unaffected by the diurnal bias of the MPL. Day and night observations show similar agreement to the entire sets of observations. CALIPSO and ground-based observations both show the same diurnal cycle with geometrically thicker ice and TTL clouds during the nighttime hours. Given that both instruments have the same diurnal cycle lends credibility that this is a real effect, although it may be partially due to improved SNR at night, which allows for better detection of cloud top and base and therefore a thicker cloud.

The number of ice cloud layers per profile agree well after the effects of resolution is considered. Breaking the datasets into day and night reveals that some of this agreement may be due to different diurnal cycles in each set of observations. The ground-based observations contain more multi-layer ice clouds during the nighttime while CALIPSO observations show more during the daytime. Differences between observations in these diurnal comparisons are small and not always statistically significant. The comparison of the number of cloud layers per profile may be impacted by differences in how each retrieval defines a unique cloud layer.

Agreement in ice cloud optical depth varies between the four retrieval types depending on the range of optical depth and TWP site being examined. However, for the majority of the PDF bins all four retrievals agree to within the 95% confidence level. The vast majority of TTL cloud optical depths are less than 0.2, regardless of retrieval type and location. In this optical depth range, the ground-based variable lidar ratio retrieval agrees best with either of the two CALIPSO retrievals. The ground-based fixed lidar ratio retrieval has statistically significant differences in the very thinnest of the optical depth bins. All retrieval types for both sets of observations show slightly more of the very thinnest ice clouds during the nighttime. This is presumably due to an increase in SNR, allowing for the easier detection of optically thin clouds.

Overall, for the thin ($\tau < 0.2$) ice and TTL clouds, both CALIPSO retrievals tend to agree better to the ground-based variable lidar ratio retrieval rather than the fixed lidar ratio. The opposite is true for thick ice clouds ($\tau \geq 0.2$), with better agreement between either CALIPSO retrieval when using the ground-based fixed lidar ratio retrieval. However, the ground-based variable lidar ratio retrieval PDF is sensitive to the resolution particularly for thicker ($\tau \gtrsim 0.3$) optical depths. Differences between the PDFs for thicker optical depths may be an artifact of the difference in spatial resolution.

Appendix

2.A Merging CALIPSO's Multi-resolution Layers

Cloud layers in the CALIPSO 5 km products are identified using a multi-resolution averaging algorithm called the selective, iterated boundary location (SIBYL) algorithm. SIBYL allows CALIPSO to achieve a balance between the highest possible spatial resolution and a sufficient SNR to accurately retrieve layer properties. Details of CALIPSO's detection of cloud and aerosol layers are given in Vaughan et al. (2009). Multiple passes are made through the data and the amount of horizontal averaging increases with each pass. After cloud layers are identified at a particular horizontal resolution they are removed before moving on to further averaging. In the 5 km L2 v3.01 cloud product three horizontal averages are considered: 5, 20 and 80 km. In the first pass the data is averaged to 5 km and cloud layers are identified by comparing to a threshold. The signal associated with cloud layers identified at 5 km are then removed before moving on to further averaged. This step creates a backscatter profile as if the detected cloud layers where never present. Then a second pass is made by averaging the data to 20 km and layer detection and removal is repeated. The process is repeated one last time with the data averaged to 80 km.

Interpreting the layer properties resulting from SIBYL requires an understanding of the output of a multi-scale averaging algorithm. Figure 2.15 gives a schematic of retrieved cloud boundaries from the 5 km cloud product. This artificial scene shows cloud layers detected at resolutions of 5 km (red, feature A), 20 km (green, features B1, B2 and B3) and 80 km (blue, feature C). Hashing indicates that the region was identified as cloud at more than one horizontal resolution. The CALIPSO 5 km cloud product would report layer properties for each 5 km column and for each feature: A, B1, B2, B3 and C. For example in column 5 the number of cloud layers reported would be three with the properties retrieved from feature A, B1 and C. The boundaries reported from these three layers would overlap in the vertical. It is apparent in column 5 that there is only a single cloud layer but the SIBYL algorithm has caused it to be detected at three different horizontal resolutions. In order to compare to the ground-based data, which performs cloud detection at a single resolution, we combined cloud layers which overlap in the vertical into a single cloud layer. The merged single-layer cloud top is taken as the highest cloud top in the set of overlapping CALIPSO cloud layers (i.e. 9.48 km is column 5 in Figure 2.15). Likewise, the merged single-layer cloud base is taken as the lowest cloud base in the set of overlapping CALIPSO cloud layers (i.e. 9 km in column 5 in Figure 2.15). After obtaining the cloud top and base height of the merged single-cloud layer the geometrical thickness becomes the difference between the merged layer's cloud top and base. The optical depth of a merged single-cloud layer is the sum of all the overlapping CALIPSO cloud layers. Summing the individual optical depths is appropriate since the signal associated with each detected feature is removed before moving on to larger horizontal averages.

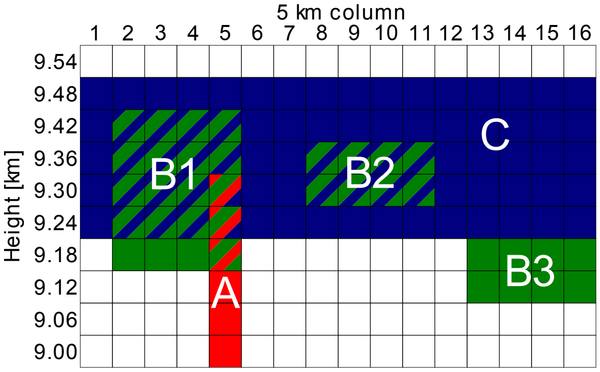

Figure 2.15: A fictitious schematic of CALIPSO's multi-resolution cloud layer detection. Colors represent cloud layers found at 5 km (red), 20 km (green) and 80 km (blue) of horizontal averaging. Hashing indicates a cloud layer being identified at multiple horizontal resolutions. White represents regions of clear air.

In addition to overlapping cloud layers, situations can also arise where the CALIPSO 5 km cloud product produces cloud layers which appear immediately adjacent to each other. Figure 2.15 shows this situation occurring in columns 13 through 16 where feature B3, detected at 20 km, is adjacent to feature C, detected at 80 km. Columns containing such cloud layers are also merged together as outlined above. It is also possible for cloud layers to be completely contained inside other clouds layers. This situation is shown in columns 8 through 11 in Figure 2.15 where feature B2, detected at 20 km, is completely contained inside feature C, detected at 80 km. These two layers are also merged into single layers in our CALIPSO dataset.

Ignorance of the CALIPSO 5 km cloud product's multi-resolution retrieval can result in spurious scientific conclusions. To illustrate this point Figure 2.16 shows the number of ice cloud layers per profile calculated by using the cloud layers reported in the 5 km cloud product at face value. This is in contrast to Figure 2.7 which uses the merged CALIPSO ice cloud layers. Merging the overlapping cloud layers results in the reduction of the occurrence of multi-layer ice cloud profiles by $\sim 5\%$.

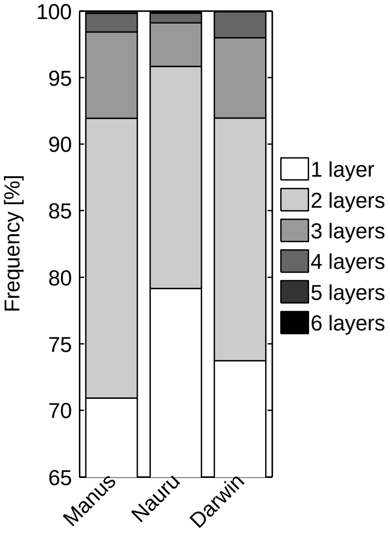

Figure 2.16: Frequency of the number of ice cloud layers per profile from the CALIPSO 5 km cloud product for the three ARM TWP sites. Overlapping and adjacent layers are not merged together.

While we have focused on the detection of cloud layers at multiple resolutions here, this method is also used to identify aerosol layers in the CALIPSO 5 km aerosol product. Therefore the same considerations are applicable to the aerosol layers in the CALIPSO 5 km aerosol product.

2.B TTL Cloud Diurnal Biases

The analysis of the diurnal variations of ice cloud properties presented in section 2.5.5 is repeated here but for TTL cloud properties. Observations using lidar become increasingly difficult during the daytime hours due to increased signal noise. Nighttime-only observations provide a comparison free of retrieval complications due to the solar background. In addition during the night both the ground-based and CALIPSO observations have similar fractions of attenuated profiles (see section 2.4.2). While during the daytime MPL cloud profiles are frequently attenuated which results in the restricted ground-based datasets being biased towards nighttime observations. By comparison, a much smaller fraction of CALIPSO daytime cloud profiles are attenuated although the fraction of attenuated profiles during the daytime is typical greater than at night.

Observations of TTL cloud top and base heights for nighttime and daytime observations are given in Figure 2.17. Analogous to the ice cloud comparisons in section 2.5.5, nighttime observations of TTL clouds show similar differences between CALIPSO and the ground-based datasets as the PDFs using both day and night together (Figure 2.5b). Larger differences exist in daytime-only observations but are less striking than for the ice cloud comparisons. Of interest is Nauru, whose daytime observations agree almost as well as the nighttime observations.

TTL cloud PDFs of geometrical thicknesses are given in Figure 2.18. Unlike the cloud top and base heights, both day and night PDFs show similar agreement between the two sets of observations as the full set of observations do (Figure 2.6b). Thicker TTL clouds are observed during the night in both the CALIPSO and ground-based datasets. As discussed in section 2.5.5 this diurnal cycle is likely part real and partly due to the improved SNR at night.

Comparisons of daytime and nighttime TTL cloud optical depths are given in Figure 2.19. Overall differences between day and night PDFs are similar to those seen using the full sets of observations. As with the ice cloud observations the daytime observations for all four retrieval types typically have less optical depths in the very thinnest bins during the daytime. This result is expected since lidar observations will be more sensitive to clouds with thin optical depths during the nighttime due to increased SNR.

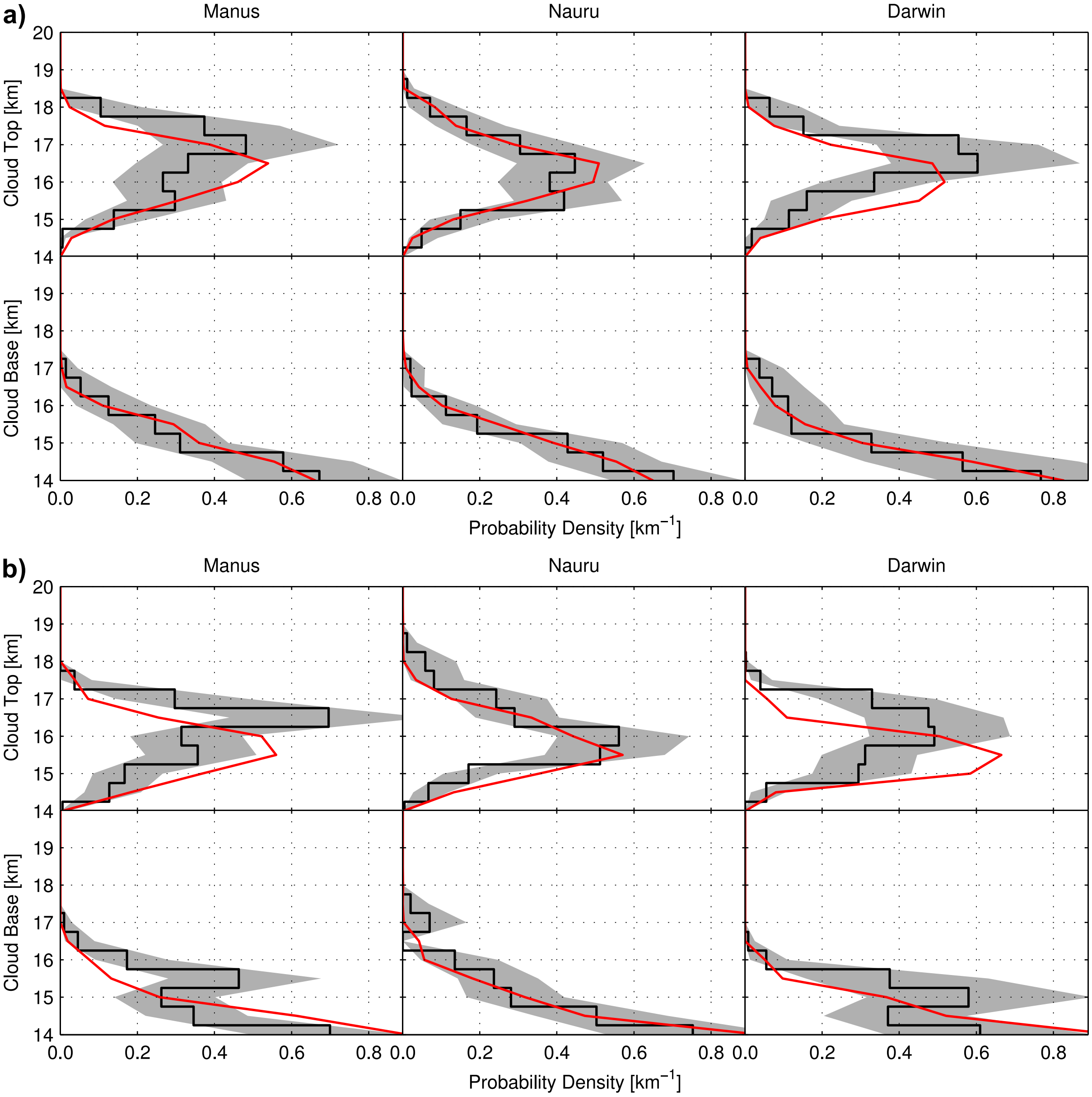

Figure 2.17: PDFs of TTL cloud top heights (top row) and cloud base heights (bottom row) from CALIPSO (black line) and ground-based (red line) datasets during the (a) nighttime and (b) daytime. The shaded region represents the 95% confidence interval due to CALIPSO's sampling uncertainty. The three ARM sites are shown (left to right): Manus, Nauru and Darwin.

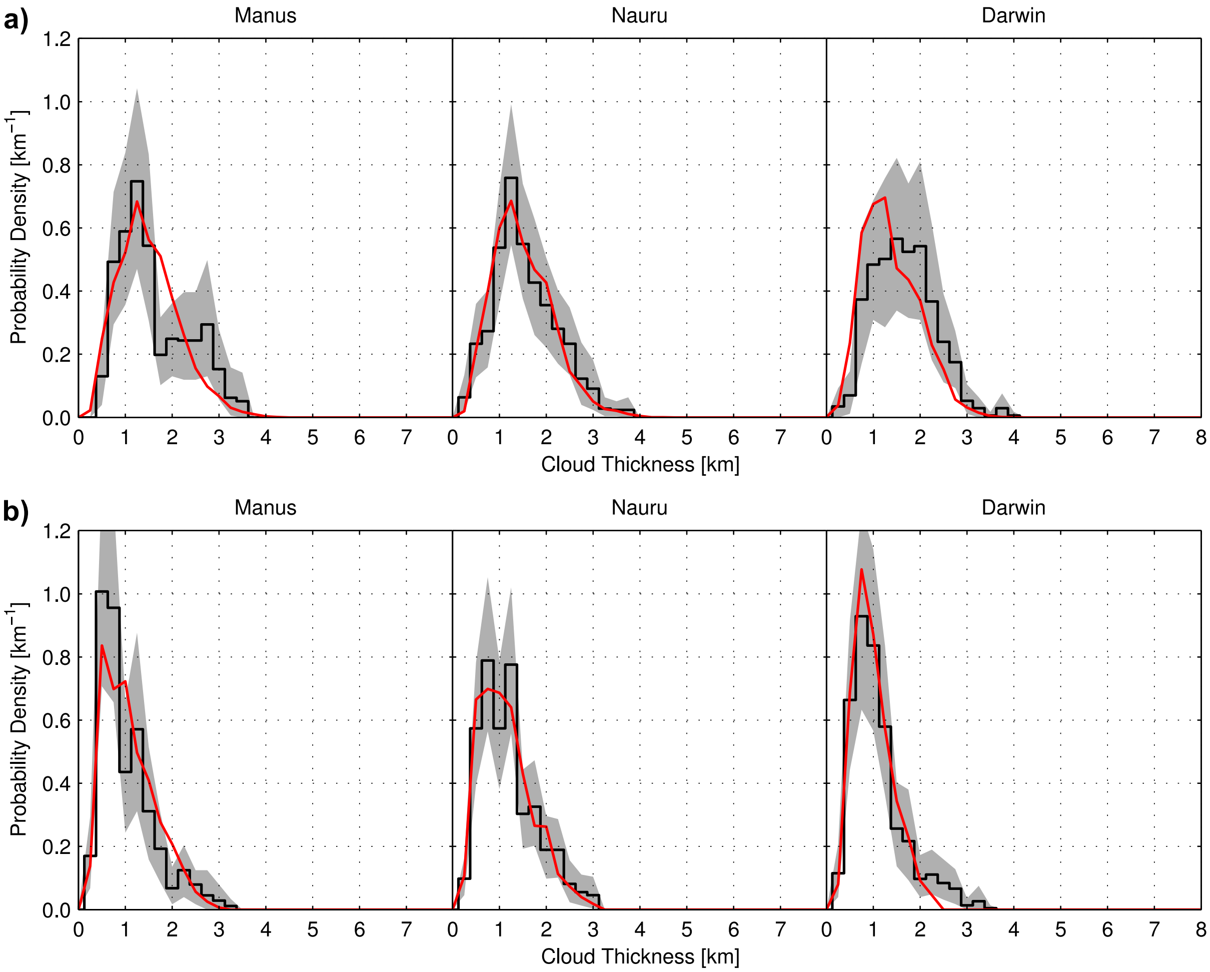

Figure 2.18: PDFs of TTL cloud geometrical thickness from CALIPSO (black line) and ground-based (red line) datasets during the (a) nighttime and (b) daytime. The shaded region represents the 95% confidence interval due to CALIPSO's sampling uncertainty. The three ARM sites are shown (left to right): Manus, Nauru and Darwin.

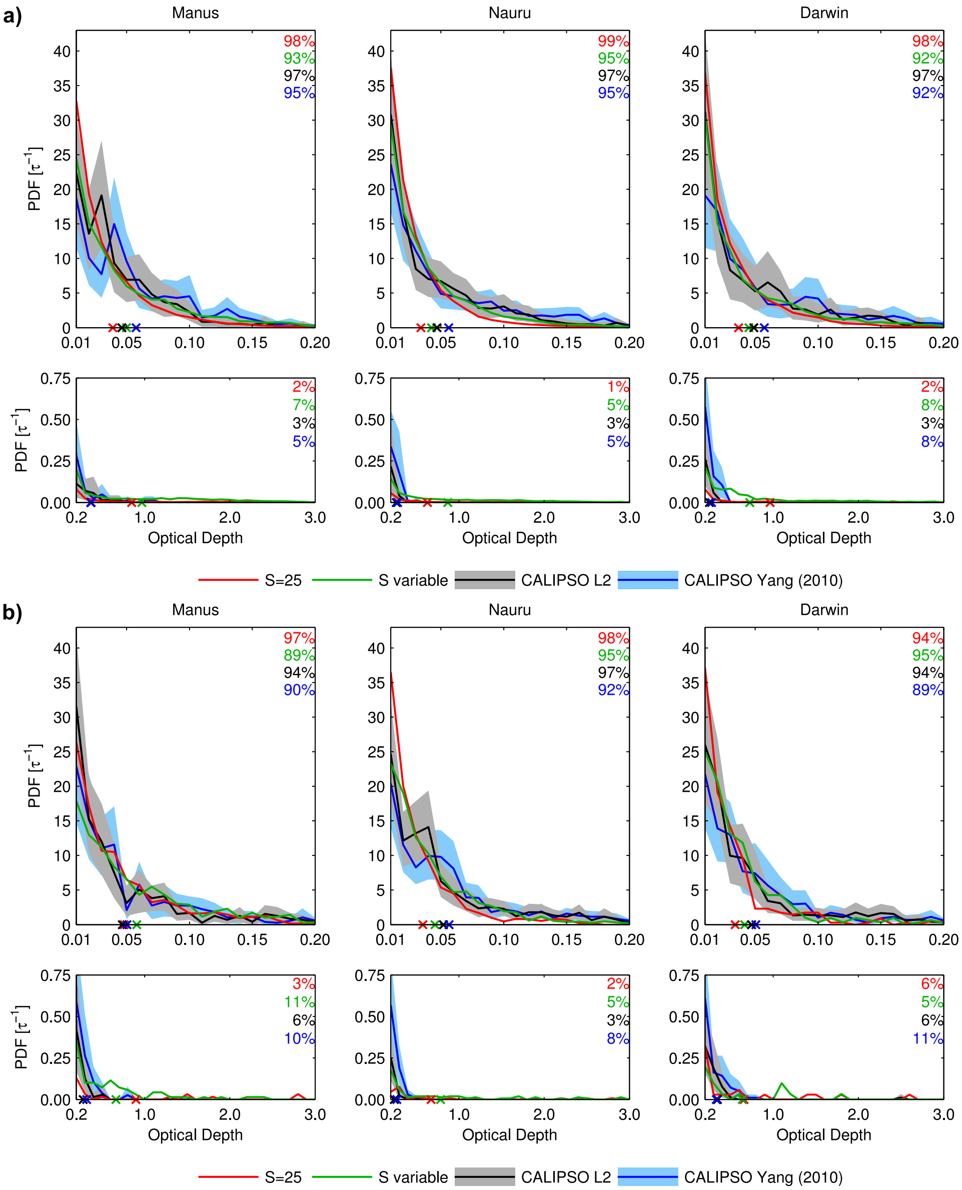

Figure 2.19: PDFs of TTL cloud optical depths from CALIPSO L2 v3.01 cloud product (black line) and the CALIPSO optical depth retrieval of Yang et al. (2010) (blue line) during the (a) nighttime and (b) daytime. The shaded region on each CALIPSO retrieval represents the 95% confidence interval due to the sampling uncertainty. Ground-based optical depths are shown for the lidar ratio fixed at 25 sr (red line) and the variable lidar ratio retrieval (green line). The three ARM TWP sites are shown (left to right): Manus, Nauru and Darwin. The top row of plots shows the optical depths from $0.01 \leq \tau < 0.2$ and the bottom row shows $0.2 \leq \tau \leq 3$. The upper-right corner of each plot gives the percent of observations which fall within the plotted optical depth range. The mean optical depth within each range is denoted with an “x” along the x-axis.

Chapter 3

CLOUD EFFECTS ON RADIATIVE HEATING RATE PROFILES OVER DARWIN USING ARM AND A-TRAIN RADAR/LIDAR OBSERVATIONS

The contents of this chapter are reproduced from: Thorsen, T. J., Q. Fu, and J. Comstock, 2013, J. Geophys. Res., 118 (11), 5637–5654, doi: 10.1002/jgrd.50476. The Introduction and Summary sections have been revised from their original form and minor modifications have been made throughout the text.

3.1 Introduction

The vertical distribution of radiative heating plays an important role in determining atmospheric dynamic processes and is strongly influenced by clouds. Profiles of radiative heating are typically not observed directly, but rather are calculated using a radiative transfer model. This requires a specification of the atmospheric state including profiles of temperature, water vapor, ozone, aerosol and cloud properties. Investigating the impact of clouds on the radiative heating profile, which is the focus of this chapter, will therefore require detailed information about the cloud vertical structure. Observations from passive satellite sensors, such as the MODerate resolution Imaging Spectroradiometer (MODIS) (Barnes et al., 1998; Platnick et al., 2003; Ackerman et al., 2008) and the International Satellite Cloud Climatology Project (ISSCP) (Rossow and Schiffer, 1999) provide macrophysical and microphysical properties on a global scale, but only provide limited information on the cloud vertical structure (Zhang et al., 2004). Only active remote sensors, such as cloud radars and lidars, can provide detailed information on the vertical structure of clouds necessary to calculate profiles of radiative heating.

The U.S. Department of Energy Atmospheric Radiation Measurement program (ARM; Ackerman and Stokes, 2003) operates a millimeter cloud radar (MMCR) and a micropulse lidar (MPL) providing continuous observations of cloud vertical structure at three sites in the tropics: Manus, Nauru and Darwin. Cloud properties derived using the MMCRs at Manus and

Nauru have been used to document the effect of clouds on the vertical structure of radiative heating (Fueglistaler and Fu, 2006; Mather et al., 2007; McFarlane et al., 2007; Mather and McFarlane, 2009). The ARM sites provide a valuable continuous time series of cloud observations with high temporal resolution.

Cloud radar and lidar observations as part of the A-train satellite constellation (Stephens et al., 2002) provide near-global observations with a sun-synchronous orbit allowing observations at approximately 0130 and 1330 local time. Analogous to the ARM MMCR and MPL, the A-train contains the CloudSat cloud radar and the Cloud-Aerosol Lidar Infrared Pathfinder Satellite Observations (CALIPSO) lidar. As part of the CloudSat mission, vertical profiles of cloud microphysical properties are routinely produced (Austin et al., 2009) and used as input for the 2B-FLXHR product which calculates total-sky radiative heating rate and flux profiles (L'Ecuyer et al., 2008). An additional CloudSat product, 2B-FLXHR-LIDAR, incorporates clouds detected by CALIPSO only into the inputs for calculating the flux and heating rate profiles (Henderson et al., 2011). The 2B-FLXHR and the 2B-FLXHR-LIDAR products provide users with a convenient way to investigate radiative processes (e.g., Feldman et al., 2008; Haladay and Stephens, 2009). An alternative A-train-based radiative flux profile product is produced as part of the Clouds and the Earth's Radiant Energy System (CERES) mission. CALIPSO and CloudSat cloud profiles are merged inside the footprint of the CERES instrument on the Aqua satellite to create the CCCM (CALIPSO-CloudSat-CERES-MODIS) data product (Kato et al., 2010). Radiative fluxes are calculated using the merged cloud profiles. CCCM has been used to help improve CERES estimates of the global radiation budget and to improve uncertainty estimates (Kato et al., 2011, 2012). Work by Yang et al. (2010) also used multiple instruments to investigate the radiation budget in the TTL by combining CALIPSO and ISCCP cloud optical depths along with CloudSat cloud boundaries.

Depending on the atmospheric process being studied either the ARM or A-train observations or both may be appropriate given their relative temporal and spatial coverages. Therefore we perform a detailed comparison between the two sets of observations. In this study we focus on comparing statistics of retrieved cloud properties and their impact on radiative heating profiles. We seek to determine whether both sets of instruments are well suited for inferring the radiative effect of clouds and to document specific advantages and disadvantages to each.

Previous studies documenting radiative heating in the tropics using either ARM or A-train observations have used cloud inputs from radar only (Fueglistaler and Fu, 2006; Mather et al., 2007; McFarlane et al., 2007; Mather and McFarlane, 2009; L'Ecuyer et al., 2008) or have used merged radar and lidar cloud inputs (L'Ecuyer et al., 2008; Haladay and Stephens, 2009; Kato et al., 2010; Yang et al., 2010). In the current study we compare cloud radiative effects between ARM and A-train observations using more accurate combined radar/lidar retrievals for ice clouds. We will particularly pay attention to the impact of lidar on the cloud radiative forcing since high, optical thin clouds in the upper troposphere frequently go undetected by radar (e.g., Comstock et al., 2002). Details of the cloud retrievals, atmospheric profiles and other radiative transfer model inputs are discussed in section 3.2. Mean ARM and A-train heating rate and cloud radiative forcing profiles are compared in section 3.3 along with the retrieved cloud properties. In section 3.4 we quantify the individual effects of cloud inputs on the cloud radiative forcing profiles and provide concluding remarks in section 3.5.

3.2 Data and Methodology

Observations from multiple instruments are taken from the Darwin, Australia ARM site ($12.325°S$, $130.891°E$) from July 2006 through December 2010. For A-train data, observations are taken from a $2.5° \times 2.5°$ latitude-by-longitude box centered on the Darwin site. The ARM observations are limited to times within ± 2 hours of the A-train overpasses through the spatial domain, which occur approximately at 0130 and 1330 local time. Only times when all four primary instruments used in this study— the MMCR, MPL, CloudSat and CALIPSO— are producing quality data are considered for comparison. After screening for data quality and the collocation of the observations in space and time we are able to compare 27405 ARM profiles (at 2 minute resolution) and 34053 A-train profiles (at 1.1 km resolution).

The evaluation of each dataset is performed statistically including comparisons of mean profiles and two-dimensional probability density functions (PDFs). Therefore discussions in the study include whether or not differences between observations are statistical significant. Statistical significance at the 95% level is determined using the moving-block bootstrap technique (Efron, 1982; Wilks, 1997). In this study, the block lengths are set by the collocation criterion for each dataset— entire A-train passes through the spatial domain and ARM profiles within ±2 hours of these overpasses are considered as single blocks. More details on the use of this method for the comparison of ground-based and A-train data can be found in Thorsen et al. (2011) (and in Chapter 2) and Liu et al. (2010a).

3.2.1 ARM

The ARM sites are equipped with multiple, collocated instruments capable of collecting detailed information about the atmospheric state. We derived profiles of the quantities necessary for input into a radiative transfer model from various instruments including radiosondes, surface meteorology instruments, a microwave radiometer (MWR), the MMCR and MPL at the Darwin site. The MWR measures downwelling radiation at 23.8 and 31.4 GHz allowing simultaneous retrievals of the integrated amount of water vapor and liquid water (Liljegren and Lesht, 1996). The MMCR is a vertically-pointing Doppler cloud radar operating at 35 GHz in four different modes to achieve different sensitivities and vertical resolutions (Clothiaux et al., 1999). The MPL is a vertically-pointing, polarization-sensitive 532 nm backscatter lidar (Campbell et al., 2002).

3.2.1.1 Cloud Retrievals

Cloud microphysical properties are computed using the Combined Retrieval (CombRet; Comstock et al., 2013) which combines MMCR, MPL and MWR measurements. The CombRet cloud mask applies the cloud detection algorithm of Wang and Sassen (2001) to the MPL data and combines this with the best-estimate MMCR cloud mask from the Active Remote Sensing of Clouds (ARSCL) value-added product (VAP; Clothiaux et al., 2000). Cloud phase is determined following Shupe (2007) utilizing the lidar backscatter and radar Doppler moments (reflectivity, spectral width, and Doppler velocity) with parameters adjusted for tropical regimes.

The CombRet liquid cloud radar retrieval is essentially the same algorithm as the ARM MICROBASE VAP (Miller et al., 2005) with a modification to the assumed total number density of water droplets which is assumed to be 100 cm^{-3} (Mather et al., 2007). Liquid clouds detected by lidar only are assumed to have a small 5 μm effective radius since the particle size must be too small for the radar to detect. The LWC for these lidar only liquid clouds is calculated from the empirical relationship of Slingo (1989) using the retrieved lidar extinction (α_e; Comstock and Sassen, 2001). For layers identified as drizzle or rain, the rain water content (RWC) and effective radius are taken from an assumed Marshall-Palmer distribution computed using the rain rate following Wood (2005). When drizzle or rain is not present in the profile, the cloud liquid water path (LWP) retrieved from the radar and lidar is scaled to match the LWP from the MWR.

Ice cloud microphysical properties are determined conditionally depending on available measurements. When both radar and lidar detect a cloud layer, the algorithm of Wang and Sassen (2002) is applied to the radar reflectivity (Z_e) and α_e to retrieval the ice water content (IWC) and generalized effective diameter (D_{ge}). When only lidar detects cloud, the method of Heymsfield et al. (2005) is applied to α_e and temperature (T) to calculate IWC. D_{ge} can then be computed using Fu (1996), which is also used in the Wang and Sassen (2002) combined radar and lidar portion of CombRet. For radar only ice clouds, the Z_e-IWC-T relationship of Hogan et al. (2006a) is used to retrieve the microphysical properties. Additionally no lidar data is used when the lidar is severely attenuated— defined as times when the highest radar cloud top height exceeds the highest lidar cloud top height by more than 1 km.

After the retrieval is run for a given profile, it is run again with the radar reflectivity corrected for attenuation by water drops (Lhermitte, 1990). The MPL backscatter is averaged to 2 minutes to improve the signal-to-noise ratio prior to its use in CombRet. CombRet retrieves profiles every 2 minutes at a 60 m vertical resolution.

3.2.1.2 Other Data

Besides cloud properties, the calculation of radiative heating requires profiles of pressure, temperature, water vapor, ozone and several other trace gases. In this study we do not consider aerosol impacts on the radiative heating profiles. Radiosondes at the ARM sites are typically launched twice daily providing profiles of pressure, temperature and humidity. Humidity corrections of Miloshevich et al. (2004, 2009) are applied to each radiosonde profile to account for the known dry bias and time lag of the radiosonde humidity sensor. The column-integrated water vapor, as measured by the MWR, is used to scale the corrected humidity profile (Turner et al., 2003). Since ARM sites do not make ozone measurements, monthly-mean ozone profiles are taken from the near-by Southern Hemisphere ADditional OZonesondes (SHADOZ; Thompson et al., 2003) Watukosek, Java site ($7.6°S$, $112.7°E$).

ARM radiosonde and SHADOZ observations are typically available up to ~ 25 km. Above this altitude we supplement these balloon-borne observations with temperature data from the UKMO stratospheric analysis (Swinbank and O'Neill, 1994), and water vapor and ozone observations from the HALOE instrument on-board the UARS satellite (Russell et al., 1993). Monthly-mean upper-air climatological profiles are derived from ten years (1995-2005) of data from both the UKMO and HALOE datasets. Individual radiosonde/ozonesonde profiles are blended to these upper-air climatologies using a linear function following Hollars (2004). While the balloon-borne profiles of temperature are used up to their highest altitude, radiosonde-based water vapor measurements are only used up to 19 km to avoid large errors that occur in very dry conditions.

Profiles of pressure, temperature and water vapor are then linearly interpolated to the times of the CombRet cloud retrieval. Profiles are then either linearly (temperature, ozone) or logarithmically (pressure, water vapor) interpolated in height to the CombRet resolution of 60 m. Above 21 km in altitude, the vertical resolution is decreased to 100 m (21.1 to 25 km), 1 km (26 to 50 km) and 5 km (55 to 70 km). Above 50 km the standard tropical profile is used (McClatchey et al., 1972). ARM one minute surface meteorology observations are used to weight the interpolated profiles up to 600 m following Hollars (2004).

3.2.2 A-train

The A-train constellation of satellites allows for near-coincident measurements from multiple remote sensing instruments. CALIPSO (Winker et al., 2010) and CloudSat (Stephens et al., 2002) both joined the A-train constellation in April 2006 and started collecting data in June 2006. CloudSat is a 94 GHz nadar-viewing cloud radar and CALIPSO is equipped with CALIOP (Cloud-Aerosol Lidar with Orthogonal Polarization), a 532 and 1064 nm polarization-sensitive backscatter lidar. Similar to the ARM retrievals, a combined radar/lidar method is used to retrieve ice cloud microphysical properties while liquid cloud properties are retrieved using a single instrument. Profiles are derived at the same vertical resolution as the ARM profiles. Other qualities besides cloud properties (i.e. pressure, temperature, water vapor and ozone) are taken from the ECMWF (European Centre for Medium-range Weather Forecasts) ERA-Interim daily data (Dee et al., 2011) that are linearly interpolated to the time, latitude/longitude and altitude of each profile layer. The standard tropical profile (McClatchey et al., 1972) is used above 1 mb to complete the profiles up to 70 km.

The A-train cloud mask and phase determination used in this study is part of the DARDAR (raDAR/liDAR) project (DARDAR-MASK, version 1.14) the details of which are given in Delanoë and Hogan (2010). The DARDAR-MASK merges CloudSat reflectivity from the 2B-GEOPROF product (release 4; Marchand et al., 2008) and CALIPSO backscatter from the Level 1B product (version 3; Anselmo et al., 2006) by horizontally averaging lidar beams that fall within each CloudSat footprint (1.1 km). The reflectivity and backscatter are re-gridded to 60 m in the vertical. A cloud mask is determined by combining the CloudSat 2B-GEOPROF product with the CALIPSO Vertical Feature Mask (VFM; Vaughan et al., 2009) as described in Delanoë and Hogan (2010). In DARDAR-MASK, the high-resolution CALIPSO backscatter is used to refine the VFM mask and remove the effect of larger amounts of averaging [J. Delanoë, personal communication, 2012]. Therefore, unlike the official CALIPSO VFM product, DARDAR-MASK only contains CALIPSO clouds identified using at a single averaging interval of 1.1 km. Cloud phase is determined using the method of Hogan and O'Connor (2004).

Ice cloud microphysical properties are taken from the DARDAR-CLOUD product (version 2.1 Delanoë and Hogan, 2010). DARDAR applies a variational retrieval algorithm (Varcloud; Delanoë and Hogan, 2008) to lidar and radar data. In the algorithm's forward model, radar reflectivity is derived using the T-matrix approach and lidar backscatter is derived from the multiple-scattering model of Hogan (2006). When only the radar signal is available, the retrieval tends toward $Z_e - IWC - T$ relationships (e.g.; Liu and Illingworth, 2000; Hogan et al., 2006a; Protat et al., 2007). When only the lidar signal is available the visible extinction is retrieved (Delanoë and Hogan, 2008). Portions of a cloud detected by both radar and lidar, when available, are used to adjust the a priori estimates for radar only and lidar only retrievals.

Microphysical properties of liquid clouds identified in the DARDAR-MASK product are taken from 2B-CWC-RVOD (Austin et al., 2009) and 2C-RAIN-PROFILE (Lebsock and L'Ecuyer,

2011) from release 4 of the CloudSat data products. For rain layers identified by DARDAR-MASK we use the 2C-RAIN-PROFILE product when possible; otherwise, the retrieval of LWC from the 2B-CWC-RVOD product is taken as the rain water content. Both 2B-CWC-RVOD and 2C-RAIN-PROFILE retrievals are performed at CloudSat's 240 m vertical resolution. The liquid microphysical properties for the 60 m DARDAR-MASK bins are taken from the closest 240 m bin in the CloudSat products. Visible extinction of liquid clouds detected by CALIPSO only is calculated following Young and Vaughan (2009) using an assumed lidar ratio of 18 sr and a multiple scattering factor of 0.6. The effective radius for these lidar only liquid clouds is assumed to be 10 μm.

3.2.3 Radiative Transfer Model

The aforementioned cloud and atmospheric profiles are inputed into the NASA-Langley Fu-Liou radiative transfer model (Fu and Liou, 1992, 1993; Fu, 1996; Fu et al., 1998; Rose and Charlock, 2002). The delta-four-stream method is used for both the shortwave and longwave spectra (Liou et al., 1988; Fu and Liou, 1993). Gaseous absorption due to H_2O, CO_2, O_3, N_2O, and CH_4 is parameterized using the correlated k-distribution method (Fu and Liou, 1992). Additionally absorption by CO_2 and CFCs in the window region is considered (Kratz and Rose, 1999). H_2O continuum absorption in the thermal spectra is accounted for using the CKD 2.4 (Tobin et al., 1999). The parameterizations of Fu (1996) and Fu et al. (1998) are used for the single-scattering properties of nonspherical ice particles. The infrared single-scattering properties of ice particles with D_{ge} less than 15 μm are parameterized following Robinson (2007). The single-scattering properties of water clouds are parameterized based on Mie calculations using the liquid water content and mean effective radius (Slingo, 1989). For rain, single-scattering properties are based on Mie calculations and the assumed size distribution of Manton and Cotton (1977).

The surface albedo is set to 0.05 (typical for an ocean surface) and trace gas concentrations (CO_2, N_2O, CH_4 CO_2 and CFCs) are taken from annual global-mean National Oceanic and Atmospheric Administration (NOAA) Earth System Research Laboratory (ESRL) observations. Both ARM and A-train cloud phase algorithms classify mixed phase clouds; however, in this study only the radiative transfer due to the liquid portion of these clouds is considered as we expect the liquid to dominate the radiative flux in that cloud layer. In this study we calculate instantaneous radiative fluxes by determining the solar zenith angle for each profile's time and location.

3.3 Comparison of ARM and A-train Cloud and Radiative Heating Profiles

In this section we present the comparison of ARM and A-train derived heating rates and cloud radiative forcing profiles. Also examined are cloud fraction profiles and probability distributions of the retrieved microphysical cloud properties. Throughout this paper the following terminology is used to delineate cloud layers by the instrument they are detected by (see Figure 3.1 for an example):

1. "radar only": Clouds detected only by radar, not lidar (red in Figure 3.1).
2. "lidar only": Clouds detected only by lidar, not radar (green in Figure 3.1).
3. "both radar and lidar": Clouds detected by both radar and lidar (teal in Figure 3.1).
4. "radar": Clouds detected by "radar only" or "both radar and lidar" (red and teal in Figure 3.1).
5. "lidar": Clouds detected by "lidar only" or "both radar and lidar" (green and teal in Figure 3.1).
6. "combined radar and lidar": All clouds that are detected, by either radar only or lidar only or both radar and lidar. We also use "radar+lidar" to represent this category. When no specification is made, the quantity being analyzed falls into this category (red, green, and teal in Figure 3.1).

3.3.1 Radiative Heating Profiles

The mean ARM and A-train clear-sky radiative heating rate profiles are shown in Figure 3.2. In these mean profiles, the maximum (mean) differences are 0.25 (0.06), 0.10 (0.03) and 0.27

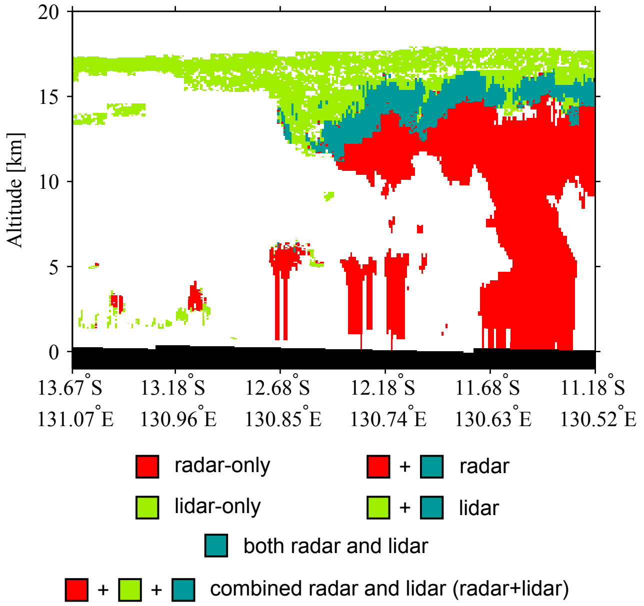

Figure 3.1: CloudSat and CALIPSO cloud mask from the DARDAR-MASK product on 25 December 2010. The legend gives the terminology used in this study when delineating clouds by lidar/radar instrument(s).

(0.07) K/day for the net, shortwave and longwave, respectively. For comparison, the maximum difference in the mean net radiative heating rate profiles for total-sky conditions is 1.47 K/day (not shown). While the differences in mean clear-sky heating rate profiles in Figure 3.2 are statistically insignificant, attributing the heating rate differences to the differences in inputs (i.e. ARM observation-based versus A-train reanalysis-based pressure, temperature, water vapor and ozone) is a worthwhile task, but will not be addressed further here. Given the large differences in the total-sky radiative heating rate, we instead focus our efforts on resolving the impact of cloud inputs on the mean radiative heating rate profiles. Instead of comparing the total-sky heating rate, the impact of clouds are isolated by comparing the mean cloud radiative forcing profile defined as:

$$CF(z,i) = Q_{R,\text{total}-\text{sky}}(z,i) - Q_{R,\text{clear}-\text{sky}}(z,i), \tag{3.1}$$

where $Q_{R,\text{total}-\text{sky}}$ is the total-sky radiative heating rate and $Q_{R,\text{clear}-\text{sky}}$ is the radiative heating rate for clear-sky conditions for profile i and layer z.

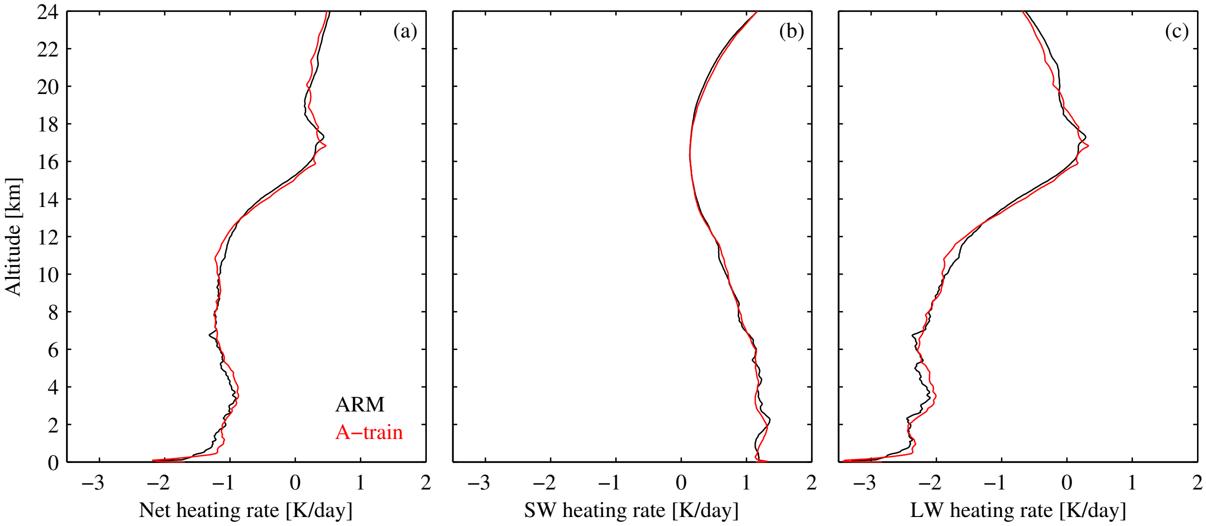

Figure 3.2: Vertical profiles of the mean ARM (black line) and A-train (red line) (a) net, (b) shortwave, and (c) longwave clear-sky heating rate.

Mean cloud radiative forcing profiles are given in Figure 3.3 (solid lines). Large differences exist, particularly in the longwave, with the A-train cloud radiative forcing significantly larger from around 12 to 17 km. Over this range of altitudes the difference in cloud radiative forcing reaches a maximum of 1.43, 0.28 and 1.27 K/day in the net, shortwave and longwave, respectively. Below about 8 km ARM cloud radiative forcing shows that clouds at some altitudes cause a mean longwave cooling, while in the A-train data the longwave cloud radiative forcing is consistently positive. These differences at lower altitudes are smaller reaching a maximum of 0.51, 0.17 and 0.54 K/day in the net, shortwave and longwave, respectively. The results in Figure 3.3 suggest that very large differences exist in either the retrieved microphysical cloud properties and/or the vertical profile of cloud fraction, particularly for ice clouds.

3.3.2 Cloud Fraction

Vertical profiles of combined radar and lidar cloud fraction are shown in Figure 3.4 (solid lines) along with the radar (dashed lines) and lidar (dotted lines) cloud fraction. In Figure 3.4a the comparison between ARM and A-train cloud fraction demonstrates close agreement below about 12 km and very poor agreement above. Above 12 km, the A-train cloud fraction is

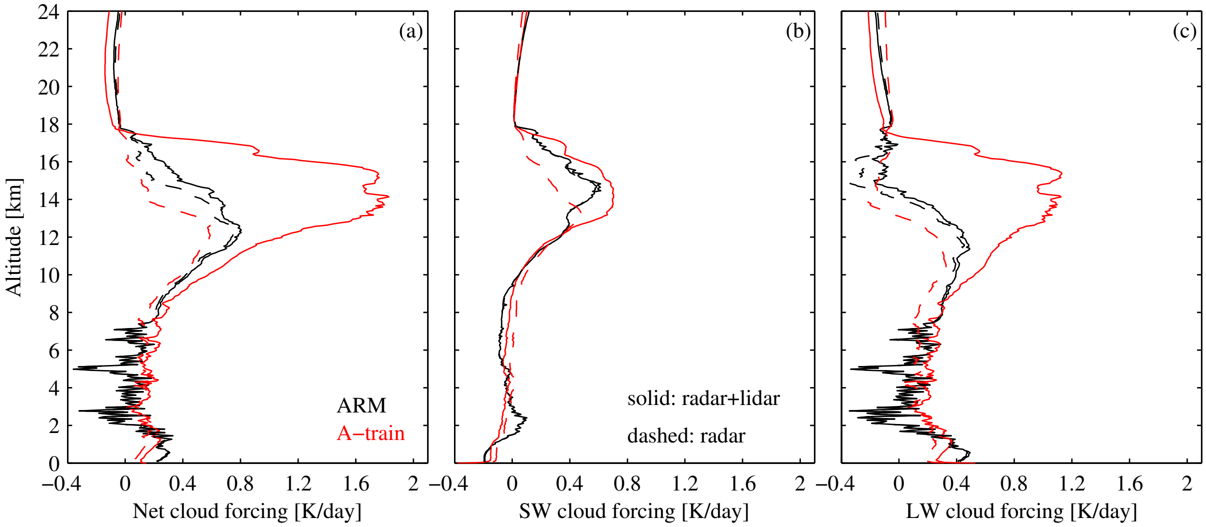

Figure 3.3: Vertical profiles of the mean ARM (black) and A-train (red) (a) net, (b) shortwave, and (c) longwave cloud radiative forcing calculated using clouds detected by radar (dashed line) and clouds detected by the combination of radar and lidar (solid line).

much larger than ARM reaching a maximum difference of 0.25 at ∼ 16 km. After examining Figure 3.4b, it is evident that the large differences at higher altitudes is due mainly to the difference between the MPL and CALIPSO cloud fraction profiles. It is worth noting that the altitude ranges where the lidar cloud fraction differs the most in Figure 3.4b is similar to the altitudes in Figure 3.3 where the cloud forcing shows large disagreement. This suggests that at least part of the difference in cloud radiative forcing may be due to differences in the lidar cloud fraction. Agreement between MMCR and CloudSat cloud fraction is reasonably good (no differences are statistically significant) although the MMCR has a larger cloud fraction at higher altitudes (above about 11 km). This may be due to the MMCR's higher sensitivity (-35 to -48 dBZ at 11 km; Clothiaux et al., 1999) compared to CloudSat (-30 dBZ; Tanelli et al., 2008) allowing the MMCR to detect more thin cirrus clouds.

3.3.3 Impact of Lidar Observations

Figure 3.3 shows the cloud radiative forcing for combined radar and lidar (solid lines) and radar (dashed lines) observations. The comparison of ARM and A-train radar cloud forcing in

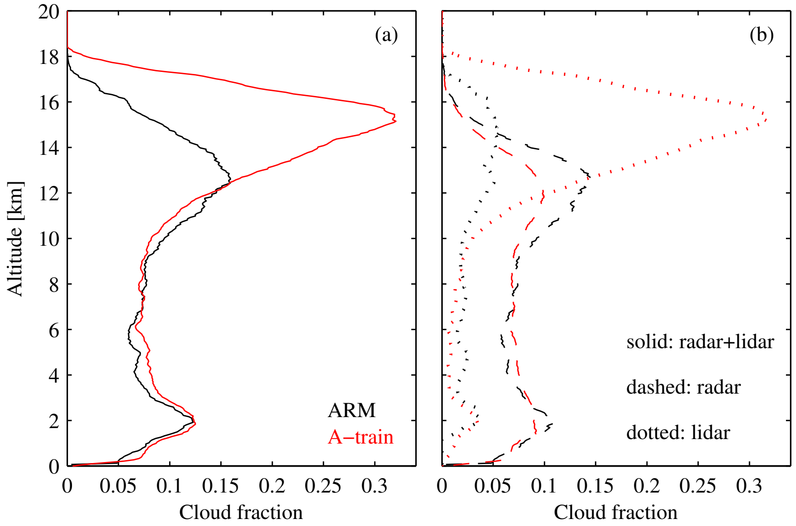

Figure 3.4: Vertical cloud fraction profiles of (a) combined radar and lidar observations (solid line) and (b) radar (dashed line) and lidar (dotted line) observations for the ARM (black) and A-train (red) datasets.

Figure 3.3 (dashed lines) exhibits better agreement than the combined radar and lidar cloud radiative forcing (solid lines). The large differences from 12 to 17 km are reduced by using radar clouds to 0.39, 0.29 and 0.33 K/day for the net, shortwave and longwave cloud radiative forcing, respectively. Cloud forcing calculated using clouds detected by radar also slightly improves the agreement at lower altitudes.

The cloud radiative forcing for the combined radar and lidar observations (solid lines in Figure 3.3) show that for the ARM observations, additional clouds detected by the MPL have almost no impact on the shortwave cloud forcing but add some longwave heating at upper altitudes (above about 12 km). However, in the A-train dataset additional clouds detected by CALIPSO have a much larger impact on the cloud radiative forcing in both the shortwave and the longwave. This leads to different conclusions on the addition of lidar to radar observations. For ARM observations, the MMCR observations alone result in a similar cloud radiative forcing profile to the combination of the MMCR and MPL. But for A-train observations, the CloudSat observations alone do not produce an accurate representation of the cloud radiative forcing due to the large number of clouds detected by CALIPSO only. For the ARM observations, the smaller effect of MPL only clouds is likely due to a smaller cloud fraction than CALIPSO (Figure 3.4), and also partially due to the higher sensitivity of ground-based radar to high clouds (Figure 3.4b). This large discrepancy in the impact the lidars have in these ARM and A-train observations illustrates the importance of quality lidar observations in regions with frequent high clouds. Quantifying the impact cloud fraction has on cloud radiative forcing profiles is explored in detail in section 3.4.

3.3.4 Retrieved Cloud Extinction

The cloud visible extinction coefficient retrieved from the ARM and A-train data are shown in Figure 3.5 including the mean in-cloud vertical profiles of ARM (brown line) and A-train (red line) extinction. Also given in Figure 3.5 is the height-dependant probability density functions (HPDF, colors; Protat et al., 2010). HPDFs are two-dimensional PDFs where the normalization is made separately by the total number of points in each altitude bin. The statistics of the retrieved extinction show large differences between the ARM and A-train observations with ARM extinction larger at lower altitudes (below about 5 km) and at higher altitudes (above about 12 km).

The difference at lower altitudes corresponds to altitudes where clouds are typically liquid water. Both sets of observations show a bi-modal HPDF for liquid clouds where the contribution to the lower mode is mainly due to drizzle/rain layers and the mode at higher values of extinction is mainly due to clouds. This cloud mode of extinction is less pronounced in the A-train observations, causing the mean A-train extinction profile to be less than the ARM profile below about 5 km. Relative to ice cloud retrievals, both datasets use simpler and less accurate retrievals of liquid cloud properties possibly causing this discrepancy in the retrieved liquid cloud extinction. Another possibility could be due to a bug in the CloudSat CWC-RVOD product used in this study, which causes an underestimate in the retrieved LWC and effective radius when the radar reflectivity is high [N. Wood, personal communication, 2012]. Regardless of the reason for the differences in retrieved liquid cloud extinction in Figure 3.5, the cloud radiative forcing at lower altitudes in Figure 3.3 doesn't show particularly large differences relative to higher altitudes. In Figure 3.3 only a few layers below 5 km exhibit statistically significant

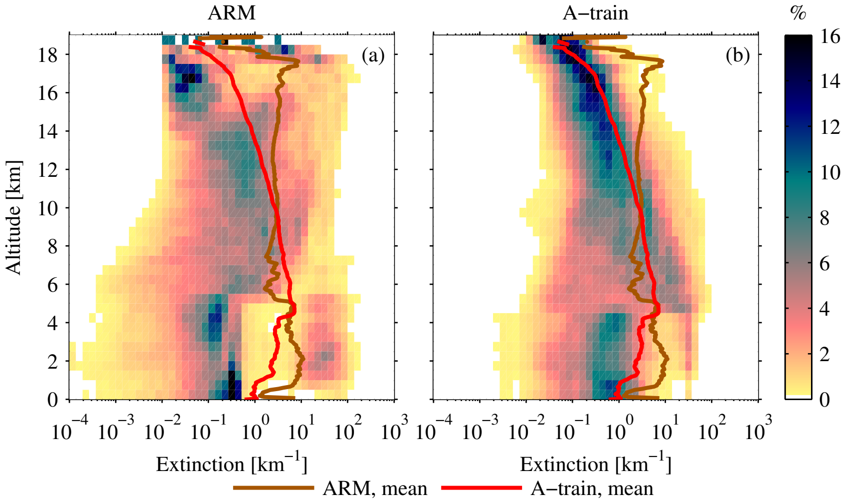

Figure 3.5: Height dependant probability density functions (HPDFs) of cloud visible extinction (colors) derived from (a) ARM and (b) A-train observations. Also given are the mean in-cloud profiles of cloud visible extinction derived from ARM (brown line) and A-train (red line) observations. For HPDFs, altitude is divided into 1 km bins and extinction into 50 logarithmically-space bins from 10^{-4} to 10^{3} km^{-1}.

differences.

Mean ARM extinction at higher altitudes (Figure 3.5) is also larger than A-train with the ARM HPDF skewed towards larger values of extinction. The extinction differences occur above about 10 km, similar to where the A-train cloud fraction begins to become larger than ARM (Figure 3.4) and where the cloud radiative forcing shows its largest disagreement (Figure 3.3). The comparison of extinction in Figure 3.5 is influenced by the cloud that can be detected. For example, at high altitudes, where much more thin cirrus clouds are detected by CALIPSO than the MPL, the A-train statistics of extinction will have more influence from thin cirrus clouds than ARM statistics. Therefore differences in the extinction shown in Figure 3.5 are a combination of both the differences in the retrieval methods and the vertical occurrence of clouds that can be detected.

A more direct comparison can be made by separating the comparison of cloud properties derived from radar, lidar, and both radar and lidar. In this manner the comparisons become roughly separated by cloud type. Such a comparison of ice cloud microphysical properties is given in Appendix 3.A where it is shown that ice cloud properties agree better than is implied by Figure 3.5. But, notable disagreement still exists in the retrieved cloud property statistics.

3.4 Attribution of Cloud Radiative Forcing Differences

In the previous section we outlined the differences between ARM and A-train profiles of cloud fraction and retrieved cloud properties, which cumulate in some manner to produce large differences in cloud radiative forcing profiles, particularly from 12 to 17 km. In this section we quantify the impact of retrieved cloud properties and cloud fraction on the difference in cloud radiative forcing. We also examine the possible reasons for the large discrepancies between the MPL and CALIPSO: whether sensitivity, attenuation, or the amount of averaging performed is responsible.

3.4.1 Lidar Signal Averaging

Lidar observations are typically averaged to improve the signal-to-noise ratio and thereby improve the detection of cloud boundaries and the retrieval of extinction profiles. As more averaging is applied to a lidar signal, cloud fraction can artificially increase as clouds become smeared in the horizontal. Therefore two different lidar datasets may have cloud fraction differences due to the amount of averaging applied. In this study, the ARM MPL backscatter is averaged to 2 minutes and the CALIPSO backscatter is averaged to the within each CloudSat footprint of 1.1 km (typically 3 CALIPSO beams). Note that CALIPSO's averaging differs from the official level 2 cloud products which use multiple amounts of horizontal averaging from 333 m to 80 km (Vaughan et al., 2009). Thorsen et al. (2011) (Chapter 2), comparing the official CALIPSO L2 cloud layer product and ARM TWP MPL observations, showed CALIPSO's larger cloud fraction to be partially explained by CALIPSO's larger amount of horizontal averaging. We perform an analysis similar to Thorsen et al. (2011) to determine if 2 minutes of temporal averaging applied to the MPL data is approximately equivalent to a 1.1 km spatial average applied to the CALIPSO data.

To convert the time average of the MPL data into a spatial one we use the wind speed to determine the amount of atmosphere advected above the MPL in a 2 minute period. The mean

MPL horizontal sampling is:

$$\bar{x}(z) = \bar{u}(z)\Delta t, \tag{3.2}$$

where $\bar{u}$ is the mean wind speed profile taken from radiosonde observations during our sampling period and Δt is the time average of the MPL, 2 minutes. The MPL horizontal sampling profile is shown in Figure 3.6. While exact agreement with the amount of CALIPSO horizontal sampling varies with height, the MPL horizontal sampling remains similar to CALIPSO. Therefore, we don't expect the amount of lidar averaging to explain any significant portion of the difference in cloud fraction (Figure 3.4).

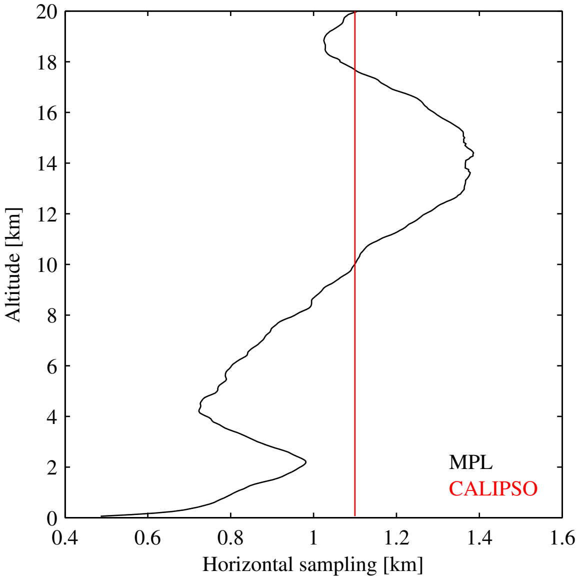

Figure 3.6: MPL (black line) and CALIPSO (red line) horizontal sampling imposed by the amount of averaging of the lidar signal.

3.4.2 Cloud Fraction Profiles

The A-train cloud fraction above 12 km is significantly larger due to the larger amount of clouds detected by CALIPSO relative to the MPL (Figure 3.4). To assess the impact this discrepancy has we remove the impact of the frequency of occurrence of clouds on the comparison of cloud radiative forcing by forcing the combined radar and lidar cloud fraction profiles to match each other. This is accomplished through a Monte-Carlo method which creates two new datasets with clouds removed at altitudes where the cloud fraction is larger than the other dataset. Clouds are removed until the dataset with the larger cloud fraction matches the dataset with the smaller cloud fraction at each altitude. Physically this removal of clouds can be considered as an A-train set of observations degraded to the sensitivity of the combination of the MPL and MMCR. The removal of clouds is determined randomly with the probability following

$$P_{ARM}(z) = \frac{\overline{cf}_{ARM}(z) - \overline{cf}_{Atrain}(z)}{\overline{cf}_{ARM}(z)}, \tag{3.3}$$

and

$$P_{Atrain}(z) = \frac{\overline{cf}_{Atrain}(z) - \overline{cf}_{ARM}(z)}{\overline{cf}_{Atrain}(z)}, \tag{3.4}$$

where $\overline{cf}_{ARM}(z)$ and $\overline{cf}_{Atrain}(z)$ are the mean ARM and A-train cloud fraction profiles. Separate probability profiles are calculated for day and night. Cloud layers are only removed, not added, therefore negative probabilities are not considered:

$$P'_D(z) = \begin{cases} P_D(z), & \text{if } P_D(z) > 0 \\ 0, & \text{if } P_D(z) \leq 0 \end{cases} \tag{3.5}$$

where D represents either the ARM or A-train dataset. For each ARM and A-train profile, i, we chose a uniformly distributed random number (r) between 0 and 1. Cloud layers are removed to create a new set of cloud profiles:

$$Y_D(z,i) = \begin{cases} X_D(z,i), & \text{if } P'_D(z) \leq r(i) \\ 0, & \text{if } P'_D(z) > r(i) \end{cases} \tag{3.6}$$

where X_D is the original set of cloud property profiles and zero represents the removal of cloud properties from a layer (i.e. the layer is considered as clear-sky). This process leads to two entirely new cloud properties datasets (Y_{ARM} and Y_{Atrain}) which have the same mean cloud fraction profiles. We repeat this process 500 times to create 500 new sets of profiles for both ARM and A-train observations. The value of interest is calculated by taking the mean over all iterations. The maximum and minimum cloud radiative forcing at each altitude over all iterations are used to estimate the range of possible solutions. The distribution of A-train, as well as ARM, retrieved cloud properties (Figures 3.10, 3.11 and 3.12 in appendix 3.A) do not change significantly after cloud layers are removed (not shown).

The mean cloud radiative forcing profiles for the ARM and A-train datasets with the same combined radar and lidar cloud fraction profiles are shown in Figure 3.7 . Also plotted in Figure 3.7 is the mean cloud radiative forcing profiles from the unmodified ARM and A-train observations (duplicated from Figure 3.3). The shading on the Y_D profiles (purple/orange in Figure 3.7) represents the maximum and minimum mean cloud forcing from the 500 datasets created using the cloud layer removal process. The difference between cloud forcing calculated using Y_{ARM} (purple) and X_{ARM} (black) is small since only a relatively small number of cloud layers are removed from the original observations. At higher altitudes changes to the A-train mean cloud forcing profile are more drastic with a large number of cloud layers being removed. This significantly reduces the cloud forcing at these altitudes. Relative to the unmodified datasets, matching the combined radar and lidar cloud fraction vastly improves the agreement for the net and longwave cloud forcing reducing the maximum differences above 12 km to 0.28 (net) and 0.40 (longwave) K/day. Therefore we conclude that much of the difference in cloud radiative forcing profiles at higher altitudes is due to the difference in cloud fraction between the ARM and A-train observations. For the shortwave cloud forcing, differences increase at some altitudes with a maximum difference of 0.41 K/day above 12 km. The longwave cloud forcing profiles still show non-trivial differences especially from 14 to 16 km with differences of about 0.3 K/day. Since we have eliminated cloud fraction differences, these remaining cloud forcing differences are somehow related the difference in the retrieved cloud properties and/or differences in cloud sampling. Further resolution of the cloud forcing differences is explored in section 3.4.3. We also note that at lower altitudes agreement is only slightly improved, which is expected considering profiles are hardly modified at those altitudes.

In appendix 3.B these modified datasets are used to partition missing clouds due to MPL attenuation and the MPL's relative lack of sensitivity. The largest amount of missing clouds is due to complete attenuation of the MPL signal by lower clouds, which occurs about twice as often compared to CALIPSO. In addition, a non-trivial amount of ice clouds are not detected

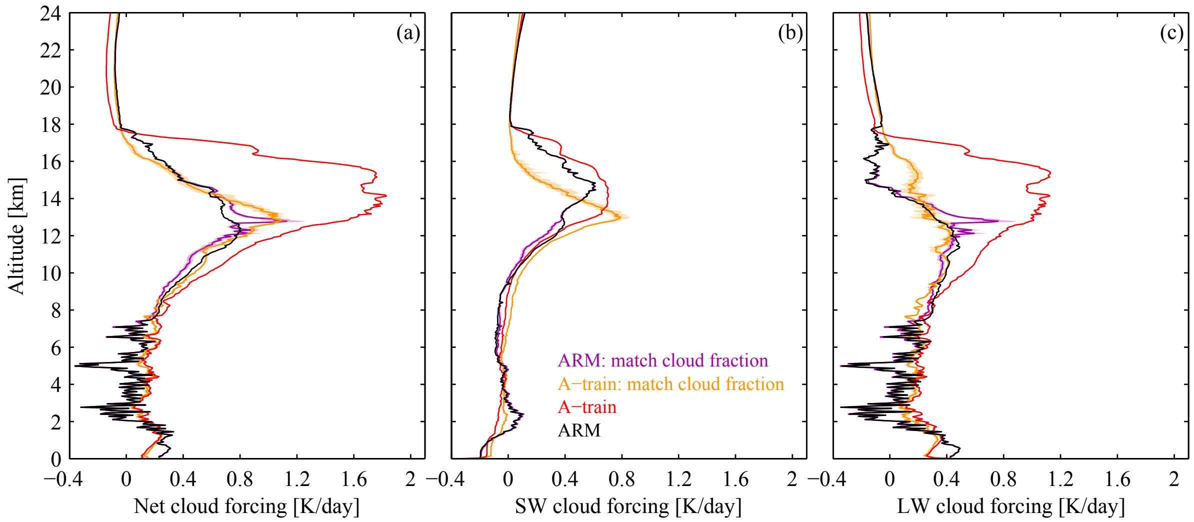

Figure 3.7: Vertical profiles of the mean (a) net, (b) shortwave, and (c) longwave cloud radiative forcing. Shown is the ARM (purple line) and A-train (orange line) observations which are forced to have the same mean combined radar and lidar cloud fraction profiles. The shading indicates the maximum and minimum cloud forcing from all iterations. The mean cloud radiative forcing profiles derived from the unmodified ARM (black line) and A-train (red line) observations are also given.

by the MPL even for profiles determined to be transparent to the MPL beam. This includes profiles identified as clear-sky, i.e. the MPL observations have a significant number of clear-sky profiles which likely have cirrus clouds present.

3.4.3 Retrieved Cloud Properties

After we force the mean combined radar and lidar cloud fraction profiles to be identical the remaining cloud radiative forcing differences between the modified datasets in Figure 3.7 are related to the differences in retrieved cloud properties and a sampling difference which is illustrated in Figure 3.8. Figure 3.8 shows cloud fraction profiles for cloud layers detected by radar only, lidar only, and both radar and lidar in the unmodified datasets (black and red lines in Figure 3.8) and the datasets with the combined radar and lidar cloud fraction forced to match (purple and orange lines in Figure 3.8). We partition the cloud fraction this way because the type of clouds being sampled varies depending on the instrument(s) the cloud is detected by. For example, the clouds detected by lidar only are optically thin. In addition, the retrieval method and accuracy varies depending on which instrument(s) detected the cloud layer. Therefore, despite forcing the combined radar and lidar cloud fraction profiles to be the same, the remaining differences in Figure 3.7 are still partially due to different occurrences of radar only, lidar only, and both radar and lidar cloud layers (Figure 3.8, orange and purple lines) and partially due to differences in the retrieved cloud properties.

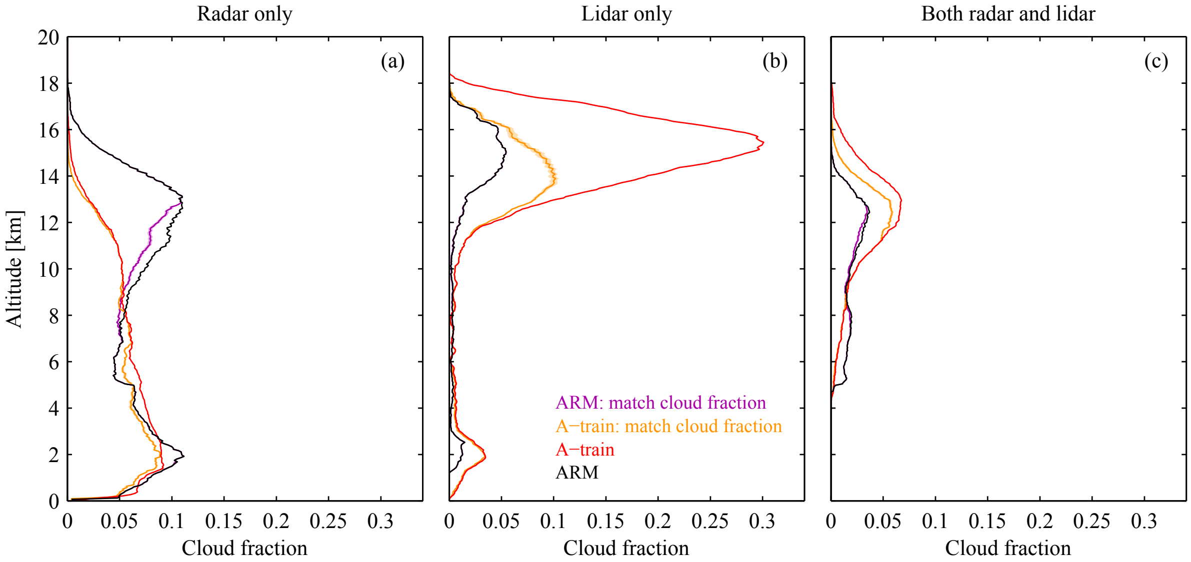

Figure 3.8: Vertical cloud fraction profiles of (a) clouds detected by radar only, (b) clouds detected by lidar only and (c) cloud detected by both radar and lidar. Shown is the ARM (purple line) and A-train (orange line) observations which are forced to have the same mean combined radar and lidar cloud fraction profiles. The shading indicates the maximum and minimum cloud fraction from all iterations. The cloud fraction profiles derived from the unmodified ARM (black line) and A-train (red line) observations are also given.

Figure 3.8 shows that for high clouds, above about 12 km, the ARM observations (black line) contain more radar only clouds relative to A-train (red line) while A-train contains more lidar only, and both radar and lidar clouds. This is also the case when comparing the ARM (purple line) and A-train (orange line) observations with the same mean combined radar and lidar cloud fraction, although the lidar only A-train cloud amount is reduced greatly. The ARM observations do show more cloud layers detected by both radar and lidar below 8 km but there are relatively few ice clouds at those altitudes. Note that while there are a portion of liquid clouds detected by both radar and lidar, they are not shown in Figure 3.8c since these cloud properties are retrieved using radar only measurements.

The ARM data's heavier reliance on the MMCR for ice cloud detection is partially due to the poorer performance of the MPL. However, even if both sets of instruments performed exactly the same, a spaceborne viewpoint will allow for more cloud layers to utilize the more accurate retrievals which use both radar and lidar due to attenuation considerations alone. This is because relative to a ground based viewpoint, where attenuation can completely mask high clouds (appendix 3.B), CALIPSO, when attenuated, is able to observe at least a portion of the ice clouds in the profile. This allows for more lidar only retrievals and both radar and lidar retrievals for ice clouds (Figure 3.8b/c). Therefore, all else being equal, a spaceborne combined radar and lidar ice cloud retrieval may be more accurate than a ground-based one solely due to lidar attenuation.

We now determine how much of the remaining discrepancies in A-train and ARM cloud radiative forcing profiles (Figure 3.7, orange and purple lines) is due to the retrieved cloud microphysical properties. Ideally, a comparison of cloud retrievals should be performed using the same cloud mask (radar only, lidar only, both radar and lidar) and cloud phase identification. This allows the difference between datasets to be interpreted as solely due to retrieval methods and assumptions. As a proxy for this, we apply the method outlined in section 3.4.2 to match the radar only, lidar only, and both radar and lidar cloud fraction profiles (Figure 3.8, red and black lines). The result of this is two idealized datasets which, in the mean, have the same occurrence of radar only, lidar only, and both radar and lidar cloud layers.

Figure 3.9 shows the cloud radiative forcing profiles for the ARM and A-train observations which have been forced to have the same mean cloud fraction profiles of radar only, lidar only, and both radar and lidar cloud layers. Comparing these results to those when only the combined radar and lidar cloud fraction is forced to be the same (Figure 3.7) we see that the agreement in the net cloud forcing is similar at most altitudes and the maximum difference above 12 km is reduced to 0.13 K/day. Both the shortwave and longwave cloud forcing agreement show improvement when each dataset has the same radar only/lidar only/ both radar and lidar cloud fraction with maximum differences above 12 km reducing to 0.20 and 0.17 K/day, respectively.

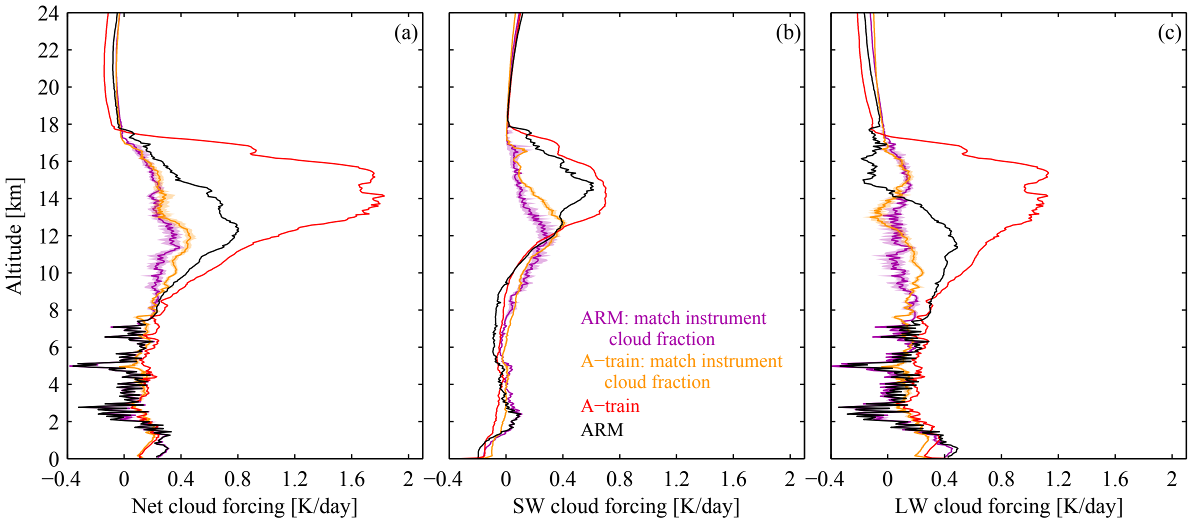

Figure 3.9: Vertical profiles of the mean (a) net, (b) shortwave, and (c) longwave cloud radiative forcing. Shown is the ARM (purple line) and A-train (orange line) observations which are forced to have the same mean radar only/lidar only/ both radar and lidar cloud fraction profiles. The shading indicates the maximum and minimum cloud forcing from all iterations. The mean cloud radiative forcing profiles derived from the unmodified ARM (black line) and A-train (red line) observations are also given.

After cloud layers are removed to either match the combined radar and lidar cloud fraction profiles or to match the radar only/lidar only/both radar and lidar cloud fraction we find better agreement in the cloud radiative forcing. However, some of the reduction of differences relative to the unmodified datasets may be due to the reduction in the number of clouds. To examine this, we scale the differences in cloud radiative forcing in these modified datasets by the ratio of the unmodified A-train cloud fraction to the modified combined radar and lidar cloud fraction profile. After doing so, the maximum difference in the cloud radiative forcing profiles due to the combination of sampling and retrieval discrepancies (Figure 3.7) remains similar with 0.32, 0.42 and 0.43 K/day differences in the net, shortwave and longwave, respectively. After scaling to the A-train cloud fraction profile, the maximum difference due to retrieval differences alone (Figure 3.9) increases to 0.43, 0.61, 0.56 K/day in the net, shortwave and longwave, respectively. These larger differences indicate that there is some cancellation of errors between the retrieval and sampling differences. To isolate the differences due to sampling alone we take the difference between the scaled error profile due to the combination of sampling and retrieval discrepancies and the scaled error profile due to the retrieval discrepancies alone. This shows that the maximum differences due to sampling alone are 0.23, 0.35 and 0.31 K/day in the net, shortwave and longwave, respectively, comparable to those due to retrieval differences alone. Note that even after scaling, the sampling and retrieval differences remain smaller than the impact the cloud fraction differences has on the comparison of ARM and A-train cloud radiative forcing.

Forcing the radar only/lidar only/both radar and lidar cloud fraction to be the same is not meant to be a thorough comparison of the CombRet and DARDAR ice cloud retrievals. In these modified datasets some altitudes show significant changes to the distribution of the retrieved cloud properties, an indication that this idealized comparison excludes certain cloudy situations. A more direct comparison of DARDAR and CombRet retrieval methods requires the application of both retrieval algorithms to the same set of instruments (i.e. identical inputs) as was performed by Comstock et al. (2013) using ARM data at Darwin. Comparisons in the Comstock et al. (2013) study of cloud radiative forcing profiles showed Varcloud (the variational algorithm that produces the DARDAR product) to have more heating in both the shortwave and longwave than CombRet. However, in the context of this study, such retrieval errors are small in comparison to the impact of cloud fraction differences.

3.5 Summary

Spatially and temporally collocated ARM and A-train observations of clouds and atmospheric state are used to compute radiative heating and cloud radiative forcing profiles from July 2006 through December 2010 at the Darwin ARM site. Both ARM and A-train datasets use combined radar/lidar ice cloud retrievals and radar only or lidar only retrievals for liquid clouds.

Very large, statistically significant differences (up to 1.43 K/day) exist between the mean ARM and A-train net cloud radiative forcing profiles. The largest differences occur over an altitude of about 12 to 17 km where the A-train data showed a larger cloud forcing. At the same altitudes, A-train observations had a larger cloud fraction, reaching a maximum difference of 0.25 at $\sim$ 16 km. Cloud fraction profiles show good agreement below 12 km. Examining the cloud fraction profiles separated by instrument showed that the large difference at higher altitudes was due to a discrepancy in the lidar cloud fractions— above 12 km the CALIPSO cloud fraction is significantly larger than the MPL. For ARM observations, the MMCR observations alone result in a similar cloud radiative forcing profile to the combination of the MMCR and MPL. But for A-train observations, the CloudSat observations alone do not produce an accurate representation of the cloud radiative forcing due to the large number of clouds detected by CALIPSO only. When only using clouds detectable by radar, profiles of cloud radiative forcing showed better, although not perfect, agreement; with the difference in cloud radiative forcing from 12 to 17 km reduced to 0.39 K/day.

To remove the influence of cloud fraction differences on the cloud radiative forcing comparison, we used a Monte-Carlo method to create new ARM and A-train datasets which have the same mean combined radar and lidar cloud fraction profiles. The agreement between cloud radiative forcing profiles using these modified datasets showed a vast improvement— the A-train cloud forcing was significantly reduced from 12 to 17 km. The maximum difference in net cloud forcing reduced from 1.43 to 0.28 K/day at these altitudes. Therefore the majority of the difference in cloud radiative forcing profiles is due to the difference in ARM and A-train cloud fraction.

After matching the mean combined radar and lidar cloud fraction profiles, the occurrence of cloud layers detected by radar only, lidar only, and both radar and lidar still do not agree. This means that the ARM and A-train datasets contain a different sampling of cloud types. In order to remove the effect of the different sampling of cloud types we create idealized datasets which have matching mean lidar only, radar only, and both radar and lidar cloud fraction profiles. In these idealized datasets, the differences in cloud radiative forcing profiles are due to differences in the retrieved microphysical properties alone. After accounting for the reduced cloud occurrence in the modified datasets, we show that the impact of the different cloud microphysical retrievals and the effect of sampling cause comparable differences in the cloud radiative forcing. However, even after scaling, the sampling and retrieval differences remain smaller than the impact the cloud fraction differences has on the comparison of ARM and A-train cloud radiative forcing.

Appendix

3.A Retrieved Ice Cloud Properties

Figures 3.10, 3.11 and 3.12 show HPDFs and mean in-cloud profiles of ice visible extinction, ice water content and ice effective radius, respectively. The cloud properties in each of these figures are shown separately for cloud layers detected by radar, lidar, and both radar and lidar. Compared in this manner the comparisons become roughly separated by cloud type. This is done to avoid differences due to differences in the vertical occurrence of clouds that can be detected (see section 3.3.4).

The definition of the ice effective radius used in DARDAR is that of Foot (1988):

$$r_e = \frac{3}{4\rho_i}\frac{IWC}{A_c}, \tag{3.7}$$

where ρ_i is the density of solid ice and A_c is total cross sectional area of the ice particles per unit volume. In contrast, the ARM CombRet retrieves generalized effective diameter which is related to the Foot (1988) effective radius by (Fu, 1996, equation 3.12)

$$r_e = \frac{3(3)^{1/2}}{8}D_{ge}. \tag{3.8}$$

The above the relationship to convert the CombRet D_{ge} to r_e to compare retrieved ice particle sizes in this section.

Comparing the extinction in Figure 3.5 to Figure 3.10 we see that the agreement improves above 12 km. When separating cloud properties by instrument the statistics of ice water content is also improved (statistics of combined radar and lidar ice water content not shown). For effective radius comparisons, the improvement is minimal (statistics of combined radar and lidar ice effective radius not shown). Separated in this manner, the cloud properties from when both radar and lidar detect the cloud layer would be the most accurate portion of their respective retrievals. The cloud properties for cloud layers detected by radar or lidar will be less accurate, being some combination of both radar and lidar retrievals and radar only or lidar only retrievals.

While agreement in ice water content and extinction improves when we examine the distribution of cloud properties separated by instrument, differences still exist. The most obvious differences occur when comparing clouds detected by both radar and lidar above $\sim$ 14 km (panels (e) and (f) in Figures 3.10, 3.11 and 3.12). The ARM observations show no clouds above 16 km and very poor sampling above 15 km. The A-train distributions have clouds above these altitudes which have relatively large extinction, ice water content and effective radius suggesting that these are thick clouds. This discrepancy is due to the difference in platform—A-train's spaceborne viewpoint allows thick cloud layers to be detected by both radar and lidar near the cloud top before CALIPSO becomes attenuated. The same thick clouds viewed from a ground-based perspective would completely attenuate the MPL before it could be used to detect/retrieve cloud properties near the cloud top.

Another notable area where clouds are present in one set of observations but not the other occurs near the melting level (about 5–6 km). Here the ARM distributions of cloud properties show optically thin clouds with small ice water contents while the A-train observations have no clouds in these smaller bins.

ARM lidar clouds at higher altitudes are optically thinner (Figure 3.10c) and have smaller ice water contents (Figure 3.11c) than A-train lidar clouds (Figures 3.10d and 3.11d). The ARM HPDF and mean profiles tend to be noisy above about 16.5 km due to the MPL's poor sampling. Both ARM and A-train HPDFs and mean profiles of lidar cloud effective radius agree well at all altitudes (Figure 3.12c/d).

ARM and A-train radar clouds have similar ice water content distributions above about 10 km (Figure 3.11a/b) while at the same altitudes A-train clouds are optically thinner (Figure 3.10a/b). Therefore we expect the A-train effective radius above 10 km to be larger for radar clouds. This is shown to be the case in Figure 3.12a/b where A-train radar cloud effective radius is biased to larger sizes at all altitudes. The A-train radar cloud effective radius also have a wider HPDF, particularly at higher altitudes.

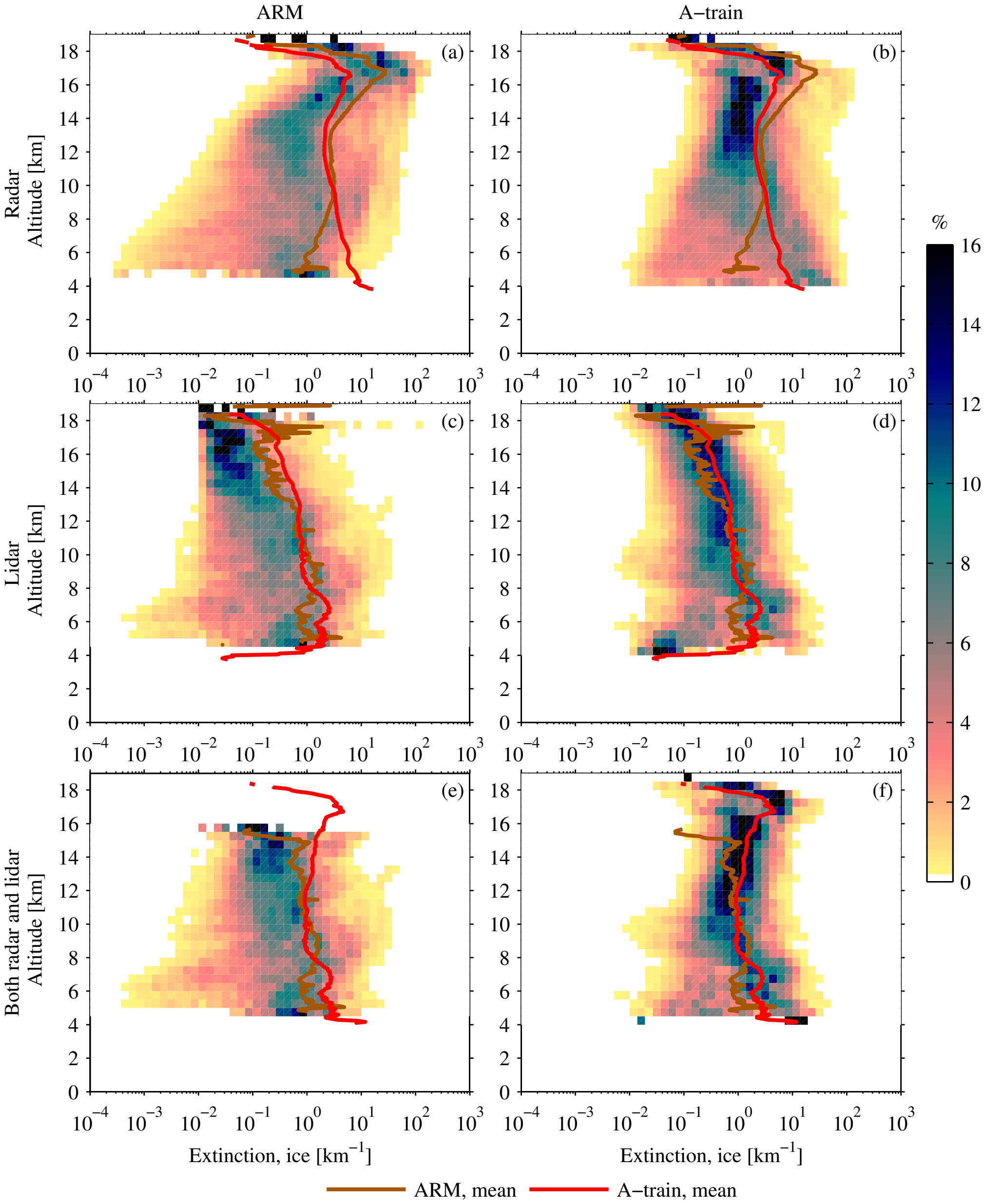

Figure 3.10: Height dependant probability density functions (HPDFs) of ice cloud visible extinction (colors) derived from ARM (left column: a,c,e) and A-train (right column: b,d,f) observations. Also given are the mean in-cloud profiles of ice cloud visible extinction derived from ARM (brown line) and A-train (red line) observations. The HPDFs and mean profiles are shown separately for the cloud layers detected by radar (top row: a,b), lidar (middle row: c,d) and both radar and lidar (bottom row: e,f). For HPDFs, altitude is divided into 1 km bins and extinction into 50 logarithmically-space bins from 10^{-4} to 10^{3} km^{-1}.

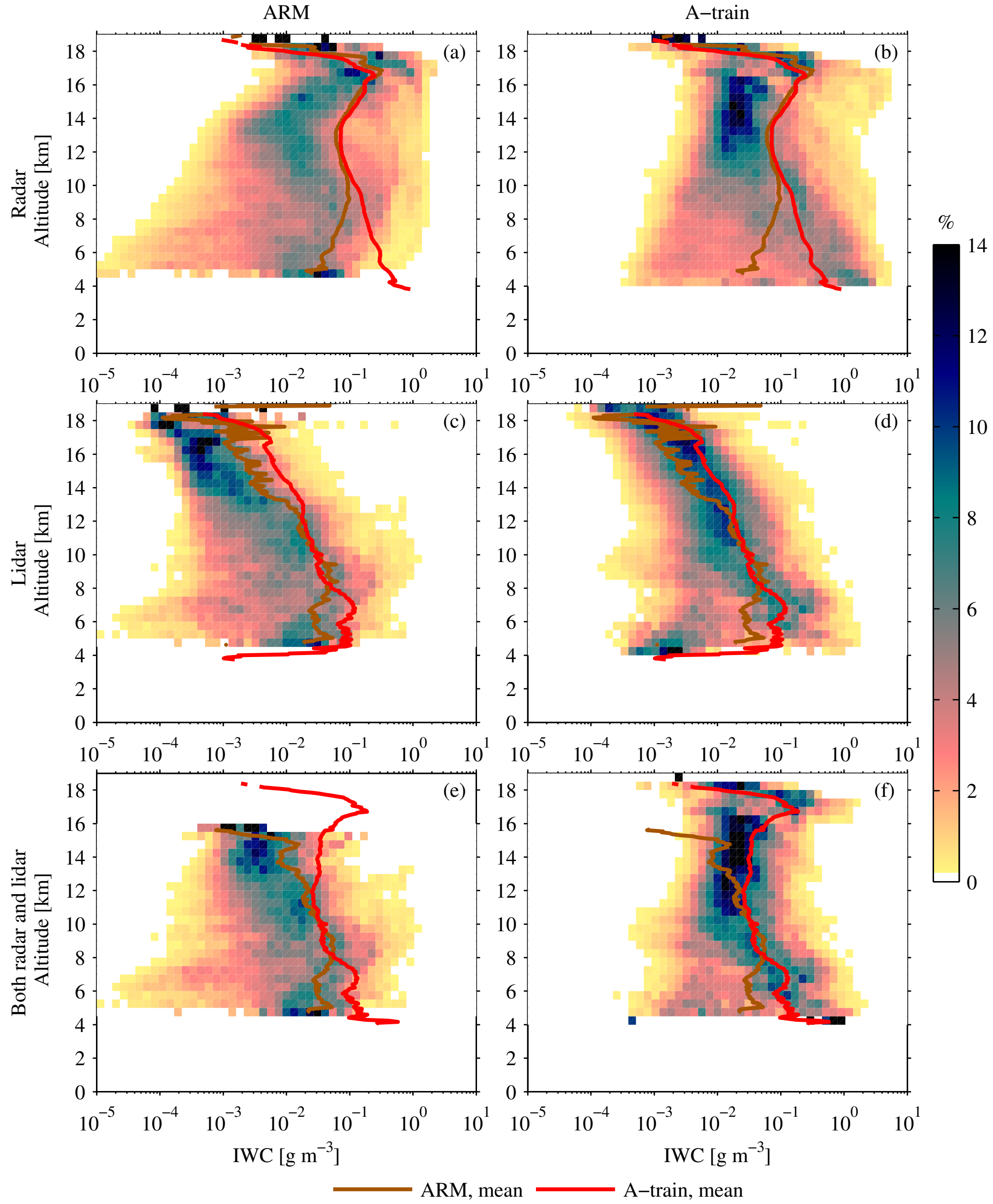

Figure 3.11: Same as Figure 3.10, but for ice water content in 50 logarithmically-space bins from 10^{-5} to 10^{1} $g\ m^{-3}$.

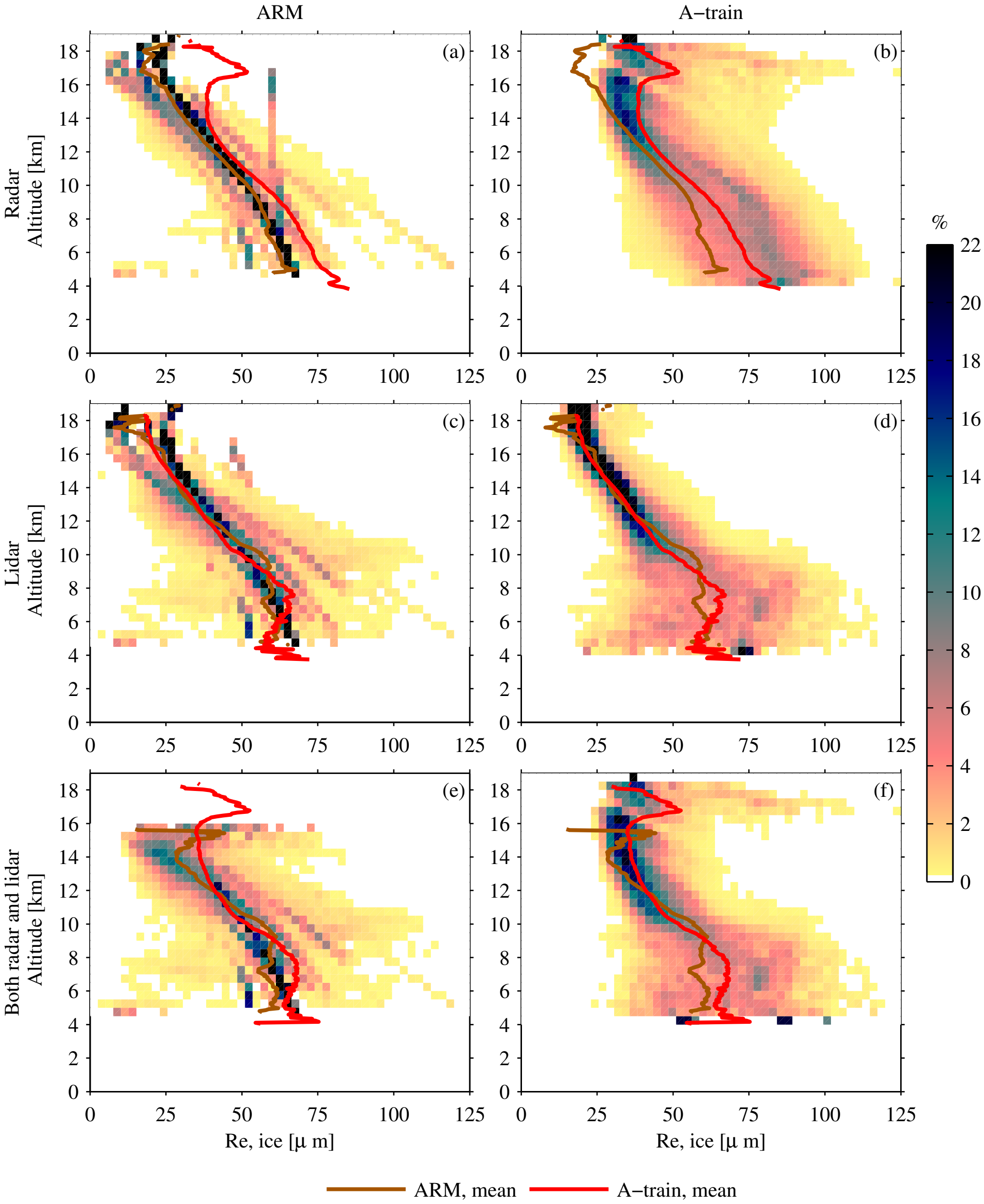

Figure 3.12: Same as Figure 3.10, but for ice particle effective radius in 2.5 μm bins.

3.B Impact of MPL Attenuation and Sensitivity on Cloud Fraction

When creating datasets with the same combined radar and lidar cloud fraction profile (section 3.4.2), many cloud layers are removed from the A-train observations since the ARM cloud fraction is much smaller at higher altitudes. Here we examine the A-train profiles where clouds have been removed by the Monte-Carlo method described in section 3.4.2 to determine the scenarios in which ARM observations have a relative lack of clouds. We interpret differences in the overall cloud fraction as differences in the frequency of cloud detected by the lidars since this accounts for the majority of cloud fraction differences at higher altitudes. To do so we begin by defining a binary representation of cloud occurrence:

$$C_{X,D}(z,i) = \begin{cases} 1, & \text{if } X_D(z,i) > 0 \\ 0, & \text{if } X_D(z,i) = 0 \end{cases} \tag{3.9}$$

where D represents either the ARM or A-train dataset and X_D is the original set of cloud property profiles (i) with zero representing a clear layer and greater than zero indicating a cloud layer. Likewise for the set of cloud properties which have had cloud layers removed (Y_D):

$$C_{Y,D}(z,i) = \begin{cases} 1, & \text{if } Y_D(z,i) > 0 \\ 0, & \text{if } Y_D(z,i) = 0 \end{cases} \tag{3.10}$$

We then determine the similarity between each pair of ARM profiles (j) and A-train profiles (k) which have had cloud layers removed by calculating the phi coefficient

$$\phi(j,k) = corr\left[C_{Y,ARM}(z,j),\ C_{Y,Atrain}(z,k)\right] \tag{3.11}$$

where *corr* denotes the calculation of the phi coefficient which is a special case of the Pearson correlation coefficient for the association between two binary variables. The set of A-train profiles (M) with clouds at similar altitudes to each ARM profile (j) is defined by

$$M(j) = \{k : \phi(j,k) > 0.57\}. \tag{3.12}$$

We require the profiles to have a correlation coefficient greater than 0.57. This cutoff ensures at least one matching profile for more than 99% of the ARM profiles across all 500 iterations. The matching of profiles is performed separately for day and night profiles. The median number of A-train cloudy profiles matching each ARM cloudy profile using this method is 278 during the daytime and 264 during the nighttime. The mean correlation coefficient in these matching sets of cloud profiles is 0.69 for both the day and night.

We then estimate the difference in cloud fraction for a given ARM profile relative to what A-train would observe as:

$$\Delta cf(z,j) = \frac{\displaystyle\sum_{n\in M(j)} C_{X,Atrain}(z,n)}{|M(j)|} - \frac{\displaystyle\sum_{n\in M(j)} C_{Y,Atrain}(z,n)}{|M(j)|} \tag{3.13}$$

where $|M(j)|$ is the number of members in the set $M(j)$. In equation 3.13 the first term on the right hand side is the mean cloud fraction profile for the original A-train data (X_{Atrain}) for the profiles in set $M(j)$. The second term is the mean cloud fraction profile for the A-train data where cloud layers have been removed (Y_{Atrain}) for the profiles in the set $M(j)$. The evaluation of equation 3.13 estimates the difference in cloud fraction for each ARM profile if that profile was hypothetically viewed using the A-train.

The original set of ARM data (X_{ARM}) is divided into three categories based on the state of the MPL: (1) clear-sky profiles (2) profiles with clouds transparent to the MPL and (3) profiles with clouds which severely attenuate the MPL. As discussed in section 3.2.1.1 profiles where the MMCR highest cloud top is more than 1 km above the MPL highest cloud top are considered completely attenuated and MPL data is not used in the retrieval. While we refer to profiles matching this criteria as attenuated, it is likely that there is some attenuated profiles not identified by this method. For example, it is possible that the MPL could be partially attenuated by lower clouds, and then become completely attenuated in a thin high cloud that is undetectable by the MMCR. In such a case, the MPL would be considered transparent in the ARM dataset.

For each ARM profile in the three categories, we calculate the mean difference in cloud fraction using equation 3.13 across all 500 sets of profiles created by the method described in section 3.4.2. Figure 3.13 shows the mean difference in cloud fraction for the three categories for the daytime (Figure 3.13a) and nighttime (Figure 3.13b) along with the difference expressed as a percent of the total cloud fraction difference ($cf_{ARM} - cf_{Atrain}$; Figure 3.13c/d). Figure 3.13 only shows these differences above 10 km where the A-train cloud fraction is much larger than ARM. This comparison reveals that in addition to attenuation blocking the MPL's view of high clouds, the MPL is also much less sensitive than CALIPSO. This is illustrated by the non-trivial amount of cloud fraction differences due to the MPL completely missing high clouds in otherwise clear profiles (teal line in Figure 3.13). This lack of sensitivity also translates to missing clouds in profiles considered transparent to the MPL (red line in Figure 3.13). Even without considering the effect of attenuation, the MPL performance is inferior to CALIPSO which causes a significant difference in the cloud fraction and cloud radiative forcing profiles above about 12 km.

The MPL signal is completely attenuated for 69% of cloudy daytime profiles and 41% of cloudy nighttime profiles. The fraction of cloudy profiles that completely attenuate the CALIPSO signal is smaller— 27% of daytime profiles and 29% of nighttime profiles. It is shown in Figure 3.13 that during the daytime the majority of the difference in cloud fraction at all altitudes is due to complete attenuation of the MPL signal. This is also the case during the nighttime below 16 km; above that the MPL is missing clouds mainly due to partial attenuation of the signal by lower clouds. While differences in platform (i.e spaceborne versus ground-based viewpoint) impacts the ability to observe high clouds when the lidar signal is attenuated, the effect on the fraction of attenuated cloudy profiles should be smaller. This is because complete attenuation of the lidar signal is determined by the integrated optical thickness of clouds in the column. The MPL's larger occurrence of attenuated profiles indicates that it has more difficultly penetrating through all cloud layers than CALIPSO. This further exacerbates the difficultly of observing high clouds from a ground-based lidar. The impact of MPL attenuation is more pronounced during the daytime with the MPL more than twice as likely to be attenuated relative to CALIPSO.

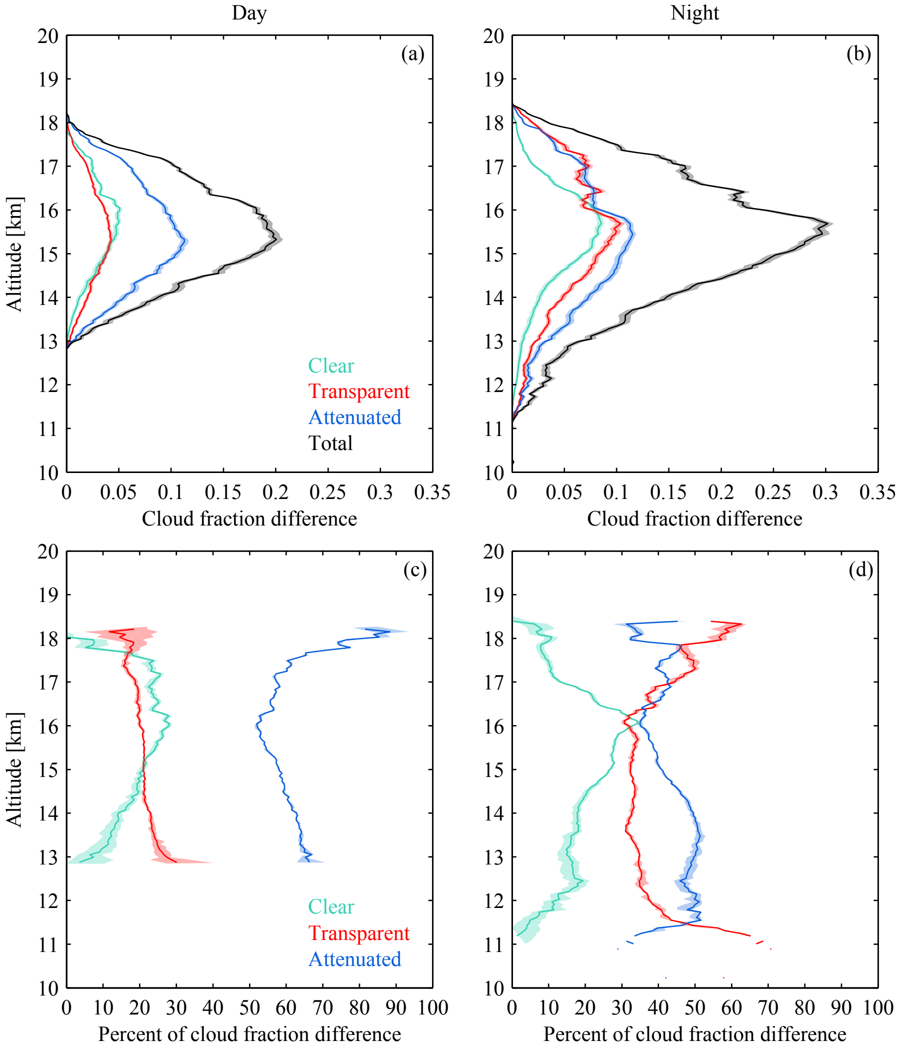

Figure 3.13: Vertical profiles of the difference in daytime (left column: a,c) and nighttime (right column: b,d) cloud fraction between the unmodified A-train observations and the A-train observations where the mean combined radar and lidar cloud fraction profiles has been forced to match (see text). Differences (top row: a,b) are taken for three categories of ARM profiles: clear-sky (teal line), profiles with clouds transparent to the MPL (red line) and profiles with clouds which completely attenuate the MPL (blue line). The total difference (black line) is also given. The differences in these three categories are also shown as a percentage of the total cloud fraction difference (bottom row: c,d). The shading indicates the maximum and minimum differences from all iterations.

Chapter 4

MACROPHYSICAL PROPERTIES OF TROPICAL CIRRUS CLOUDS FROM THE CALIPSO SATELLITE AND FROM GROUND-BASED MICROPULSE AND RAMAN LIDARS

The contents of this chapter are reproduced from: Thorsen, T. J., Q. Fu, J. M. Comstock, C. Sivaraman, M. A. Vaughan, D. M. Winker, and D. D. Turner, 2013, J. Geophys. Res., 118 (16), 9209–9220, doi: 10.1002/jgrd.50691. The Introduction and Summary sections have been revised from their original form and minor modifications have been made throughout the text.

4.1 Introduction

In this chapter, comparisons are made of macrophysical properties of tropical cirrus clouds as observed by three different lidar systems over the Department of Energy Atmospheric Radiation Measurement (ARM) program's Darwin, Australia site (Ackerman and Stokes, 2003): (1) the Cloud-Aerosol LIdar with Orthogonal Polarization (CALIOP) instrument on board the Cloud-Aerosol Lidar and Infrared Pathfinder Satellite Observations (CALIPSO) (Winker et al., 2009, 2010), (2) the ground-based ARM micropulse lidar (MPL; Campbell et al., 2002), and (3) the ground-based ARM Raman lidar (RL; Goldsmith et al., 1998; Turner et al., 2002).

The comparison of CALIPSO to ground-based lidars provides a way to evaluate each of the instruments and understand their relative strengths and weaknesses. In one such comparison of the ARM MPL and CALIPSO, Thorsen et al. (2011) (Chapter 2 found that statistics of cloud properties in profiles where the lidar beam was not fully attenuated typically agreed well, particularly at night. However, the frequency of occurrence of cirrus clouds in the MPL observations is significantly less than CALIPSO, suggesting that the MPL is less sensitive than CALIPSO. As part of the current study, we perform a similar comparison but with the addition of the relatively new ARM RL at Darwin (deployed in December 2010), which transmits a more powerful laser beam than either CALIPSO or the MPL. We seek to determine if the RL can provide better observations of tropical cirrus clouds compared to the MPL and thereby provide a more useful tool for comparisons to CALIPSO.

Both the MPL and CALIPSO lasers operate at 532 nm, which is in a region of maximum solar energy. Therefore daytime MPL and CALIPSO observations must contend with a large amount of additional noise during the daytime which may cause biases. Unlike the MPL and CALIPSO, the RL elastic channel operates at a wavelength of 355 nm where the sun emits less energy. Therefore the smaller impact of daytime noise, which is explicitly quantified in this study, on RL observations provides an opportunity to determine the effects of daytime noise on both MPL and CALIPSO observations of cirrus clouds.

Thorsen et al. (2011) (Chapter 2) documented diurnal cycles in tropical cirrus cloud that occurred in both MPL and CALIPSO observations— during the daytime, cirrus clouds occur less frequently and are geometrically thinner. While it is possible that the observed diurnal cycles could indicate real geophysical phenomena, they could also be due to increased noise during the daytime associated with the solar background. Noise will prevent the detection of optically thinner clouds, causing less cloud to be detected relative to the nighttime. Noise may also prevent the detection of the more tenuous cloud top and/or base, causing geometrically thinner clouds during the daytime. We use the RL to examine these diurnal cycles and determine if they are physical or an artifact of noise.

Details of the RL, MPL and CALIPSO datasets are given in section 4.2 and the comparison methods used are discussed in section 4.3. The increased amount of daytime noise in each lidar system is quantified and compared in section 4.4.1 along with the signal-to-noise ratios in section 4.4.2. Vertical profiles of cirrus cloud fraction are compared in sections 4.4.3 and 4.4.4 along with the diurnal cycles in each set of observations. Finally, cirrus layer geometrical thickness and its diurnal cycle is compared in section 4.4.5 with concluding remarks given in section 4.5.

4.2 Datasets

4.2.1 MPL

The ARM MPL (Campbell et al., 2002; Coulter, 2012) transmits $6-8$ μJ pulses of 532 nm light with a pulse repetition frequency (PRF) of 2500 Hz. Backscattered light is collected by a 20 cm telescope using a 0.1 mrad field-of-view (FOV) at a vertical resolution of 30 m. Data is averaged to 2 min to improve the signal-to-noise ratio (SNR). A cloud mask is applied to the backscattered signal following Wang and Sassen (2001). The Wang and Sassen (2001) algorithm is a slope method which examines the relative change in the returned signal power for strong negative and positive slopes which occur in the presence of clouds/aerosols. Complete attenuation of the lidar beam is determined following Lo et al. (2006) whereby the vertical gradient of the measured backscatter signal above the cloud layer is compared to that expected from pure molecular scattering. Individual cloud layers separated by less than 500 m are merged into single cloud layers. Times when the data quality are questionable are not considered in this study. A shutter covers the telescope around solar noon to prevent direct sunlight from damaging the system during which no backscatter data is available.

The lower-level *mplpolavg* value added product (VAP), containing raw MPL signals at a 30 s averaging interval and a 30 m vertical resolution, is also used in this study for the comparison of background noise among the three lidars.

4.2.2 RL

The ARM RL (Goldsmith et al., 1998; Turner et al., 2002; Newsom, 2009) operates with a PRF of 30 Hz with 300-350 mJ pulses of light at 355 nm. A 61 cm telescope collects elastic backscatter (355 nm) as well as Raman scattered light from nitrogen (387 nm) and water vapor (408 nm) using both a narrow FOV (NFOV, 0.3 mrad) and wide FOV (WFOV, 2 mrad). The signals in these channels are detected at a vertical resolution of 7.5 m. The WFOV signal is too noisy to be useful for cirrus cloud observations; therefore, we only use signal collected in the elastic NFOV channel, which is split into copolarized and cross-polarized signals. Like the MPL, the RL uses a shutter to prevent damage from direct sunlight. The amount of time the shutter is in place varies with season from remaining completely open during the winter to being closed for up to 4 hours a day during the summer.

Raw RL data is used to produce several higher-level VAPs available from the ARM data archive. These include the aerosol scattering ratio (ASR), and total linear depolarization ratio products (DEP): both include a cloud mask. Visual inspection of these clouds mask reveal that they perform well in identifying low clouds, but miss a significant amount of high clouds (up to $\sim$ 50%) particularly ones with weak backscatter signals. Therefore in this study we created our own cloud mask that is more sensitive to cirrus. We use the depolarization ratio from the DEP product, whose data is averaged to 2 min and 30 m, to create a cloud mask during times when the RL is producing good-quality data.

A cloud mask is determined by first applying a median filter to the total linear depolarization ratio (i.e. the Rayleigh component is not removed) using a moving window of 150 m by 10 min. Since the clear-sky depolarization ratio is calibrated to 2% (Turner et al., 2002), clouds are identified as a depolarization ratio greater than 3% with a random error less than 20%. Individual cloud layers separated by less than 500 m are combined into single cloud layers. Complete attenuation is determined by examining the mean clear-sky depolarization ratio from 18.5 to 19 km in each profile. When the mean depolarization ratio in this altitude range differs by more than 30% from the expected clear-sky value (2%) the lidar beam is considered completely attenuated.

Lower-level data is used in the comparison of background noise among the three lidars. For the RL, we use the *rlprofmerge* VAP (Newsom et al., 2009) available from the ARM data archive which contains merged analog and photon counting profiles at a resolution of 10 s and 7.5 m.

4.2.3 CALIPSO

The CALIPSO satellite (Winker et al., 2009, 2010) was launched in April 2006 into a sun-synchronous orbit as part of the A-Train satellite constellation (L'Ecuyer and Jiang, 2010) providing near global observations at approximately 0130 and 1330 (local time) for a fixed point. The main instrument on board is CALIOP, a 2 wavelength (532 nm and 1064 nm) polarization sensitive lidar with a PRF of 20 Hz and 110 mJ pulses of light (Hunt et al., 2009). Backscattered light is collected with a 1 m telescope using a 0.13 mrad FOV. In this study we utilize the CALIPSO L2 v3 5 km cloud layer (CLay) product whose vertical resolution is 30 m from the surface to 8.2 km and 60 m from 8.2 to 20.2 km. The description of the algorithm used to identify cloud (and aerosol) layers is given in Vaughan et al. (2009). The Vaughan et al. (2009) algorithm is a threshold method where portions of the measured backscatter signal profile which exceed the backscatter expected from clear-sky only are identified as clouds/aerosols. The CLay product includes an opacity flag that identifies profiles where the lidar beam has become completely attenuated. The flag is determined by examining the profile for the presence of signal return from the surface. Only layers identified with "high confidence", that is layer with a Cloud-and-Aerosol Discrimination (CAD) score (Liu et al., 2009) of 70–100, are included in our analysis. In the CLay product, cloud layers are identified using a nested multigrid averaging scheme using horizontal averages of 5, 20 or 80 km. The method can result in a single cloud layer being reported as multiple layers that appear to overlap in the vertical. In such cases, we merge the cloud boundaries to create a single cloud layer. The minimum gap allowed between cloud layers varies with each horizontal resolution applied to the data making it possible for any cloud layers separated by less than 1 km to be combined into a single cloud layer. For cloud layers separated by less than 1 km we find the mean amount of clear-sky between layers to be 497 m. Therefore the mean effect of CALIPSO's gap closing technique is approximately equivalent to that used for the MPL and RL data— both allow a minimum gap of 500 m.

The CALIPSO L2 v3 5 km cloud profile (CPro) product is also utilized which has a uniform vertical resolution of 60 m. Thresholds are applied to the CPro profiles to estimate the effect of CALIPSO's different daytime and nighttime detection limits. The detection limit of CALIPSO data averaged to 5 km, in terms of extinction (α), is 0.0016 km^{-1} at night and varies between 0.0035 to 0.0061 km^{-1} during the day at 15 km (Chepfer et al., 2012). In addition to the official CPro data we consider two other modified datasets with (1) extinction is greater than 0.0061 km^{-1} (the high threshold), (2) extinction greater than 0.0035 km^{-1} (the low threshold). After removing cloudy bins which fall below the extinction threshold, is it possible that small gaps will be created in between clouds layers. In CALIPSO's retrieval of cloud layers, such small gaps would be removed as the multiple layers are merged into a single layer. Since we cannot exactly replicate CALIPSO's process of gap closing, we instead merge layers in these thresholded profiles separated by less than 500 m. This is approximately the mean minimum gap allowed in the official CALIPSO data and is consistent with the minimum gap allowed in the MPL and RL datasets. Note that applying the daytime threshold only approximately estimates what a nighttime cloud layer would be viewed as during the daytime. This is because the retrieval of extinction is dependant on the detection of all cloudy portions of the profile so the signal can be corrected for in-cloud attenuation (Young and Vaughan, 2009). Since portions of cloudy layers may go undetected during the daytime it is difficult to make strict comparisons of nighttime and daytime extinction coefficients. Therefore the thresholded datasets are used secondarily to the comparisons to the RL and MPL as a method to understand day and night differences.

Comparisons of signal quality (background noise and SNR) are made using the CALIPSO L1B v3 profile product which contains backscatter profiles at a horizontal resolution of up 1/3 km and a vertical resolution of up to 30 m.

4.3 Comparison Method

Statistics of cirrus macrophysical properties are compared during two time periods dictated by the availability of data: (1) June 2006 through August 2011 and (2) December 2010 through December 2012. The first time period is used to compare CALIPSO (which began in June 2006) with the MPL (which was removed from the Darwin site in August 2011) which we refer to as the "MPL sampling period". The second time period is used to compare CALIPSO with the RL (which began operating in December 2010) which we refer to as the "RL sampling period". While the RL sampling period spans two years, the RL data is only available 46% of the time due to frequent periods of downtime. There is a period of time (December 2010 through August 2011) when data from all three lidars is available. However, during these 9 months the period when collocated CALIPSO, MPL and RL observations can be compared amounts to less than 2 weeks of continuous ground-based data. Therefore, we don't present results from this time period since the small sample size greatly increases the uncertainty and noise in the derived statistics. Since we don't consider a period to directly compare the MPL and RL and since CALIPSO's sensitivity is similar during the two sampling periods (section 4.4.2), CALIPSO is used as an intermediary to discuss differences between the three lidars.

CALIPSO data is taken from a 5° × 5° latitude-by-longitude box centered on the ARM

Darwin site ($12.325°S$, $130.891°E$). In the chosen spatial domain, CALIPSO makes 2 passes (1 day and 1 night) about every 5 days. Two different sets of ground-based data are considered: (1) profiles within ±4 hours of CALIPSO overpasses and (2) all available profiles. We particularly focus our comparisons on the former, ground-based data collocated in time to CALIPSO, reducing the number of ground-based profiles by about an order of magnitude. Our relatively large collocation criteria was chosen to reduce sampling uncertainty for the CALIPSO and RL comparison period. Reducing CALIPSO's spatial domain to a $2.5° \times 2.5°$ latitude-by-longitude box and the ground-based collocation time to ±2 hours results in statistically identical results for both time periods. However, during the CALIPSO and RL comparison period these smaller collocation windows result in noisy statistics with very large statistical uncertainties, particular during the daytime (when the RL shutter is closed for up to 4 hours). Therefore we chose to analyze data using the larger spatial and temporal collocation criteria. Note that in all of the comparisons presented in this study there is uncertainty associated with these spatial/temporal collocation criteria which is not explicitly quantified. However, we do not expect this uncertainty to adversely impact our conclusions since, compared to other cloud types, cirrus are relatively homogeneous with large horizontal scales— typically around 100 km (Massie et al., 2010).

Statistical significance for all quantities is determined using the moving-block bootstrap technique (Efron, 1982; Wilks, 1997). The moving-block bootstrap technique estimates sampling uncertainty through a large number of resamplings (10000 in this study) of the original data. To preserve the autocorrelation inherent in atmospheric variables, sets of consecutive profiles (blocks) are resampled. CALIPSO blocks are defined as whole passes through the spatial domain and the ground-based data block length is taken as 4 hours.

The main focus in this study is on the subset of profiles transparent to the lidar beam and cirrus clouds— defined as a cloud layer with a base above 7 km. For CALIPSO and the MPL, whose cloud masks are defined using backscatter, water and mixed phase clouds may also be identified since these clouds can occur above 7 km in the tropics (e.g. Zhang et al., 2010). However, these clouds are typically optically thick and therefore should be excluded from the set of transparent profiles. We verified this by examining the CALIPSO CLay product's assessment of cloud phase (Hu et al., 2009). In transparent CALIPSO profiles, 0% of cloud layers with bases above 7 km are identified as containing liquid water and 0.1% are of unknown phase. Since the depolarization ratio is used to construct the RL cloud mask all cloud layers identified are composed of ice. For consistency, the 7 km cloud base requirement is still applied the RL data which excludes about 1% of cloud layers from the transparent profiles.

It is possible that the RL cloud mask may miss horizontally oriented ice crystals since they induce a small depolarization signal. However, since horizontally oriented ice crystals occur in environments with weak updrafts (Magono, 1953; Ono, 1969), we don't expect horizontally oriented ice crystals to frequently occur at a tropical location like Darwin. To confirm this we examine CALIPSO's identification of horizontally oriented ice particles (Hu et al., 2009) which shows that less than 4% of cloud layers are identified as containing horizontally oriented ice particles. While possible that this subset of cloud layers are missed by the RL's depolarization threshold, such layers are easily identifiable by their very strong backscattered signal. The ARM data archive's ASR and DEP products apply a cloud mask to the backscattered signal and, as discuss in section 4.2.2, are able to identify strongly scattering cirrus. Therefore we use these ASR/DEP cloud masks to supplement the clouds identified using the depolarization ratio (section 4.2.2). We find that a negligible amount of clouds are not identified using our cloud mask method. Therefore we conclude that the presence of horizontal oriented ice crystals will not impact the comparisons presented in this study.

4.4 Results

4.4.1 Solar Background

Accurate lidar measurements during the daytime are challenging due to the noise present from the solar background. We anticipate the solar background to have a smaller impact on the RL than either CALIPSO or the MPL due to the different operating wavelengths. However, the magnitude of the solar background is also determined by other characteristics of the lidar system besides wavelength. Reduction of the solar background in lidar systems is achieved through the use of a narrow FOV and narrowband interference filters to only allow light from the desired direction and wavelength. The factors that determine the amount of solar background present in a given lidar profile also depend on viewing platform. For example, a profile containing an optically thick cloud viewed from a ground-based lidar would have a low solar background since the cloud obscures the sun above. The same profile view from space would have a high solar background due to reflection from the top of the optically thick cloud. In this section we examine the impact the solar background has on the MPL, RL and CALIPSO signal.

Random error in lidar measurements from background noise is due to solar radiation, detector dark current and thermal noise. Daytime background noise is much higher due to the presence of the solar background. The larger daytime random error makes the detection of cloud layers more difficult and increases uncertainty in retrievals. Since this study examines diurnal cycles of cirrus cloud properties (sections 4.4.3 and 4.4.5), we examine the enhancement of the background noise during daytime to determine the likelihood that observed diurnal cycles are the consequence of noise differences.

The background root mean square (RMS) noise is computed for each profile using the standard deviation of the lidar signal in a region where the backscattered signal is negligible:

$$N_{BG} = \sqrt{\frac{1}{n}\sum_{i=1}^{n}\left(S_{BR}(i) - \overline{S}_{BR}\right)^2} \tag{4.1}$$

where S_{BR} is the signal in a background region of n samples. For the RL, the background RMS noise is computed from the signal before the laser fires, that is from -2.4 to -0.23 km in the *rlprofmerge* VAP. The MPL background RMS noise is given in the *mplpolavg* VAP and is computed using the signal from 45-55 km. CALIPSO background RMS noise is reported in the L1B product and computed using samples from 65-80 km. All of the background RMS noise is calculated from data with a finer temporal/spatial resolution than the higher-level data used for cloud macrophysical retrievals. Therefore, the background RMS noise is averaged to the temporal/spatial resolution of their respective higher-level datasets using

$$\overline{N_{BG}} = \sqrt{\frac{1}{m}\sum_{i=1}^{m}\left(N_{BG}\right)^2} \tag{4.2}$$

where m is the number of profiles being averaged.

The ratios of the median daytime background RMS noise to the median nighttime background RMS noise are given in Table 4.1. The ratio of day to night represents the relative contribution of the solar background to the noise present in each lidar measurement. The ratios are derived using only profiles transparent to the lidar since this subset of profiles are used for the comparison of cloud properties. The solar background noise has the smallest impact on the RL observations with only about factor of 2 increase in the noise during the daytime. CALIPSO experiences about a factor of 10 increase in noise during the daytime which, compared to data collocated in time, is about 4 times more than the RL. The MPL performs the poorest with a factor about 25-30 more noise during the daytime— about 3 times more than CALIPSO and 12 times more than the RL. Therefore we conclude that the solar background will have the smallest impact on the cloud properties retrieved from RL measurements. Accordingly, subsequent comparisons of cloud properties will treat the RL observations as relatively unaffected by the solar background.

Table 4.1: Ratio of the median daytime background RMS noise to that at night for profiles transparent to the lidar.

Jun. 2006 - Aug. 2011		Dec. 2010 - Dec. 2012	
CALIPSO	9.3	CALIPSO	10.0
MPL	25.3	RL	2.1
MPL, ± 4 h	28.9	RL, ± 4 h	2.4

4.4.2 Signal-to-Noise Ratio (SNR)

To further compare the signal quality among the three lidars we examine the SNR. SNR is calculated from the quantity used for retrieving the cloud mask for each lidar, i.e. backscatter for CALIPSO (from the L1B product) and the MPL, and the depolarization ratio for the RL. CALIPSO L1B backscatter profiles are averaged to the primary horizontal resolution of the L2 CLay product (5 km) before calculating SNR. All three lidar retrievals perform some smoothing before determining the cloud mask. However for this comparison no smoothing is performed so that the comparison of signal quality is independent of the processing performed during the retrievals.

Two comparisons of SNR are made: (1) using approximately the same horizontal and vertical averaging for all three lidars and (2) using the signal averaged to its respective amount of horizontal and vertical averaging used for deriving the cloud mask. The former allows the comparison of SNR among the three lidars independent of the amount of averaging performed. Examination of the mean radiosonde wind speed profiles at Darwin show that the 2 min RL/MPL averaging interval samples less atmosphere than CALIPSO's 5 km of horizontal averaging. Using the mean wind speed from 7 to 19 km we find that 10 min of averaging (during both the MPL and RL sampling period) is approximately equivalent to a 5 km spatial average. Therefore we use the MPL and RL data averaged to 10 min for this comparison along with same vertical averaging, 60 m, for all three lidar datasets. The SNR is calculated using a rolling window of 50 min for the ground-based lidars and 25 km for CALIPSO. The mean divided by the standard deviation in this window is defined as the SNR.

The MPL, RL and CALIPSO profiles of the median SNR in the clear-sky portion of transparent profiles using the same horizontal and vertical averaging are given as dashed lines in Figure 4.1. Profiles are shown separately for the day (Figure 4.1a) and night (Figure 4.1b). Only the ground-based data collocated in time to CALIPSO overpasses are shown. Note that in this comparison the CALIPSO SNR only differs from its native amount of averaging (shown as a solid line in Figure 4.1) below 8.2 km. During the daytime the MPL SNR is very poor with median values below 1 above 8 km. Above about 17 km, the median MPL SNR becomes negative and is not shown in Figure 4.1a. The CALIPSO SNR is around 1 during the daytime and increases to about 2-3 during the nightime. The MPL SNR is greatly improved during the nighttime and larger than CALIPSO at all altitudes. The RL SNR is much larger than the other two lidars with little difference between the day and night profiles.

The second comparison of SNR, using the signals averaged to the horizontal and vertical resolutions of the respective cloud detection schemes, are given as solid lines in Figure 4.1. The SNR in this comparison is calculated using a rolling window of 10 min for the ground-based lidars and 25 km for CALIPSO. The mean divided by the standard deviation in this window is defined as the SNR. The CALIPSO SNR profiles only differ from the previous comparison below 8.2 km below which the SNR suddenly decreases due to the amount of vertical averaging decreasing from 60 m to 30 m. For CALIPSO two lines are shown, one for the MPL (black in Figure 4.1) and one for the RL (blue in Figure 4.1) sampling periods. During the two different

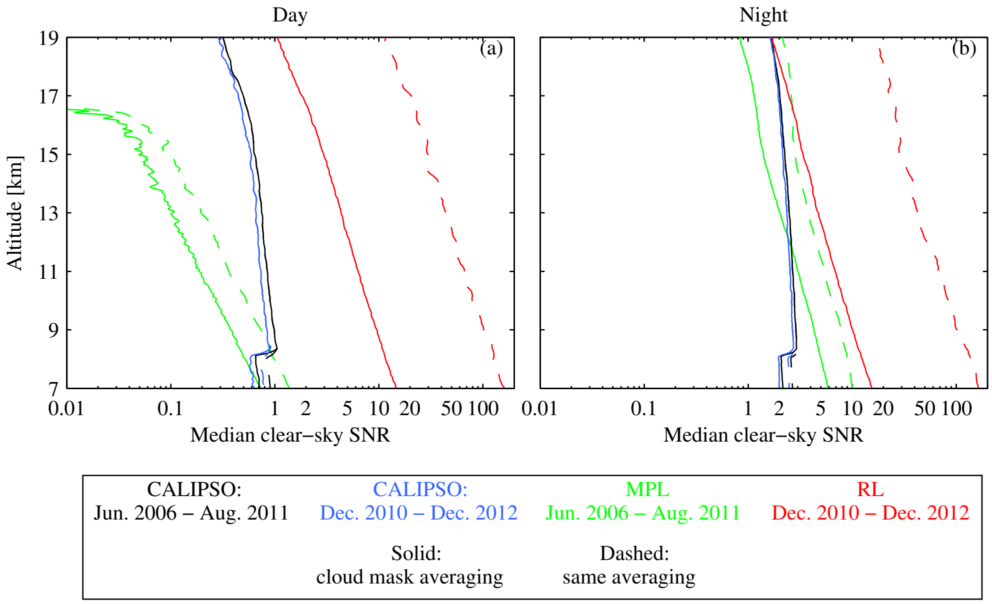

Figure 4.1: Median signal-to-noise ratio (SNR) in the clear-sky portion of profiles transparent to the lidar derived from the CALIPSO observations during the MPL sampling period (black), CALIPSO observations from the RL sampling period (blue), MPL observations (green) and RL observations (red). Profiles are shown separately for daytime (a) and nighttime (b). SNR profiles depicted as solid lines are calculated using the signals averaged to their respective amount of horizontal and vertical averaging used for deriving the cloud masks. Profiles depicted as dashed lines are calculated using approximately the same horizontal and vertical averaging for all three lidars. RL and MPL observations are collocated in time (± 4 hours) to CALIPSO overpasses.

sampling periods CALIPSO's SNR is very similar with SNR during the RL sampling period slightly smaller. The good agreement in SNR during the two sampling periods justifies our comparison strategy of using CALIPSO as an intermediary to discuss differences between the three lidars. Daytime SNR for the MPL is very small with median values less than 1 at all altitudes. The MPL's SNR is larger during the nighttime and more comparable to CALIPSO with larger SNR than CALIPSO below about 11 km and lower above. The RL SNR is the largest of the three lidars at all altitudes during both the day and night. Unlike the MPL and CALIPSO, the SNR is similar between the day and night, which is consistent with the conclusion from the previous section.

4.4.3 Transparent Cloud Fraction

Profiles of cirrus cloud fraction are compared for the transparent MPL, RL and CALIPSO profiles in Figure 4.2. The MPL detects significantly less cirrus than CALIPSO (Figure 4.2a-c). The difference is more striking during the daytime (Figure 4.2b), when the MPL detects very little cirrus clouds. Given the relatively large amount of noise caused by the solar background and the resulting poor SNR during the daytime (sections 4.4.1 and 4.4.2) the lack of cirrus detected by the MPL is unsurprising. During the nighttime (Figure 4.2c) the MPL performs better, detecting more cirrus but still significantly less than CALIPSO above about 11 km. Below 11 km at night CALIPSO and the MPL agree better with the MPL detecting slightly more cirrus at lower altitudes. The agreement at night mirrors the SNR comparison (Figure 4.1) where the MPL SNR is smaller than CALIPSO's above about 11 km and larger below. During the RL and MPL sampling periods CALIPSO cloud fraction profiles are very similar. Unlike the MPL, the RL and CALIPSO transparent cirrus cloud fraction profiles (Figure 4.2d-f) show excellent agreement— when all profiles are considered (Figure 4.2d) no statistically significant differences exist. When the comparison of the RL and CALIPSO is separated into day (Figure 4.2e) and night (Figure 4.2f) some significant differences are found particularly at night below about 12 km where the RL observes significantly fewer cirrus clouds than CALIPSO. Compared to the MPL, the RL considerably improves ground-based cirrus observations at the ARM Darwin site and agrees well with CALIPSO observations.

A comparison of cloud fraction profiles may be impacted by the different amount of averaging performed in each set of observations. For example, a larger amount of horizontal/temporal averaging can smear clouds and artificially increase the reported cloud fraction. Considering typical wind speeds at Darwin, the ground-based lidars' time averages sample less atmosphere than CALIPSO's spatial average so that the CALIPSO cloud fraction is larger due to spatial averaging alone. To test this effect we follow Thorsen et al. (2011) (Chapter 2) and used monthly-mean radiosonde wind speed profiles to convert the 2 min MPL data into larger averages that approximate a 5 km sample. After correcting for spatial averaging differences, the MPL's cloud fraction increases; however, the MPL still shows significantly fewer cirrus clouds than CALIPSO. When this process is repeated for the RL data the resolution difference with

CALIPSO has a negligible impact. The contrasting effect of converting MPL and RL cloud mask to 5 km is apparent after a visual inspection of the cloud masks. The larger increase in the MPL cloud fraction is due the presence of cloud layers that appear broken in time (i.e. the horizontal). When the 2 min data is converted to 5 km the gaps in the cloud disappear, increasing the MPL cloud fraction. The same cloud layer viewed with the RL, with its superior performance, appear as a continuous, unbroken cloud layer so when a larger averaging is considered the cloud fraction remains relatively the same. Therefore we can conclude that the comparison of the RL and CALIPSO in Figure 4.2 is unaffected by the difference in horizontal resolution.

The diurnal cycle of transparent cloud fraction—that is the mean nighttime transparent cloud fraction minus the mean daytime transparent cloud fraction — is shown in Figure 4.3. For the MPL and CALIPSO, both sets of observations show the same diurnal cycle with more cirrus during the nighttime at all altitudes. This diurnal difference is larger for the MPL observations (Figure 4.3, green line) and also occurs in the full set of MPL data (Figure 4.3, dashed green line). Given the increased noise during the daytime, which prevents the detection of optically thin clouds, it is not clear how much, if any, of this diurnal cycle is physical. For further insight we examine the CALIPSO and RL sampling period, where CALIPSO shows a similar mean diurnal cycle as in the MPL sampling period. Unlike in the longer MPL sampling period, the CALIPSO diurnal cycle during RL sampling period is not significantly different from zero above about 15 km, which is likely just due to the reduced sample size. The RL diurnal cycle is statistically different than zero only below about 11 km but with an opposite sign (i.e. less cirrus during the nighttime) from the CALIPSO observations. Therefore, if we take the RL observations as a reference, then the CALIPSO and MPL decreased cirrus occurrence during daytime below about 11 km appears to be the result of increased daytime noise. The diurnal cycle from the RL observations is not statistically different from CALIPSO's diurnal cycle above about 14 km but is also not significantly different than zero. Therefore a larger sample size of collocated RL observations is required to make statistically significant conclusions above 14 km where the MPL and CALIPSO observations show significantly less cirrus during the daytime.

Also examined was the changes to the CALIPSO diurnal cycle caused by applying the daytime extinction thresholds to the CPro data. Relative to the unmodified CPro data, the enforcement of the either high or low daytime thresholds reduces the magnitude of the diurnal cycle, but cirrus clouds are still less frequent during the daytime at all altitudes (not shown). Neither of the thresholded datasets shows the diurnal cycle as the RL observes.

When all RL data (Figure 4.3, dashed red line) is considered the diurnal cycle is close to zero with slightly more daytime cirrus at most altitudes. This suggests that CALIPSO's diurnal cycle could be due to it's particular sampling time of day and night (approximately 0130 and 1330). If so, the collocated RL observations may not adequately capture this since the RL shutter is closed around solar noon by up 4 hours during the summer. This reduces the number of profiles closely coincident with daytime CALIPSO overpasses. Ideally, seasonal observations would be useful since the RL shutter remains open all day during the winter; however, the small amount RL data prohibits this.

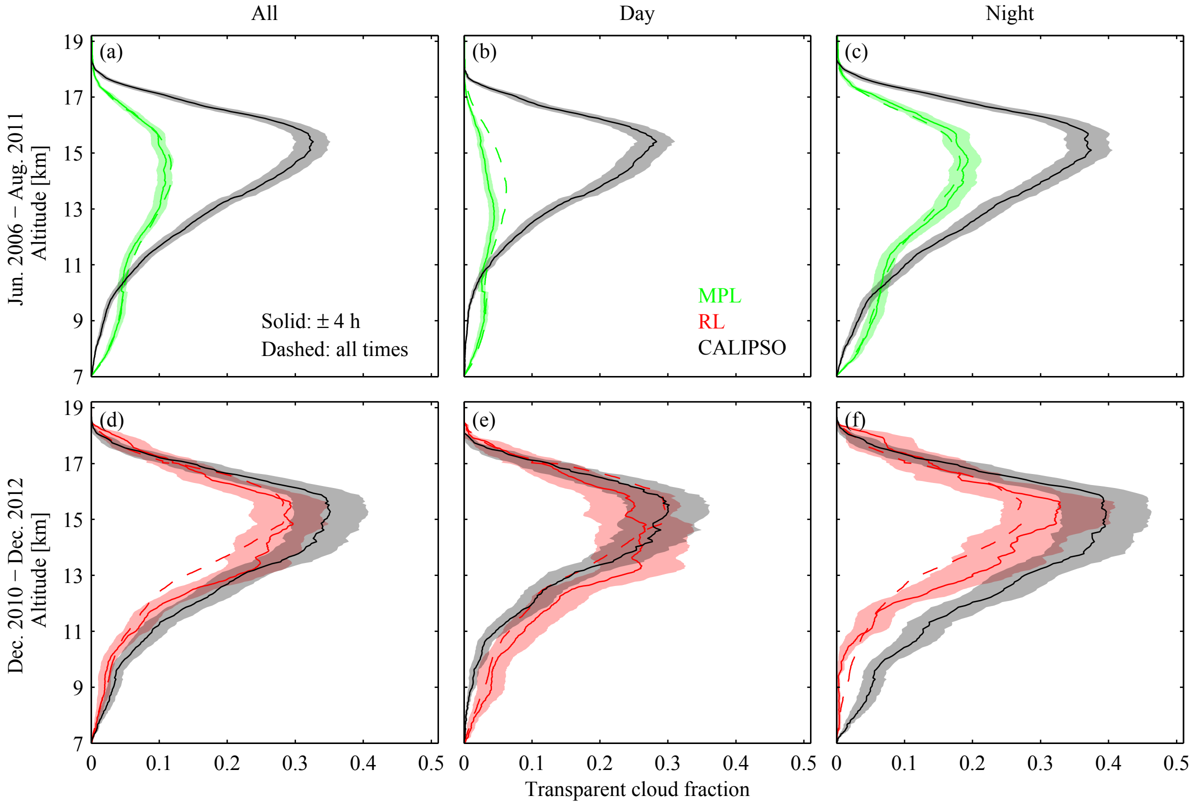

Figure 4.2: Transparent cirrus cloud fraction profiles for MPL (green), RL (red) and CALIPSO (black) observations from June 2006 through August 2011 (a-c) and December 2010 through December 2012 (d-f). Profiles are shown separately for observations from all times (a/d), only daytime (b/e) and only nighttime (c/f). MPL and RL observations collocated in time (± 4 hours) to CALIPSO overpasses are depicted as solid lines. The shading on each line represents the 95% confidence interval due to statistical uncertainty. Dashed lines denote MPL and RL profiles derived using all available data.

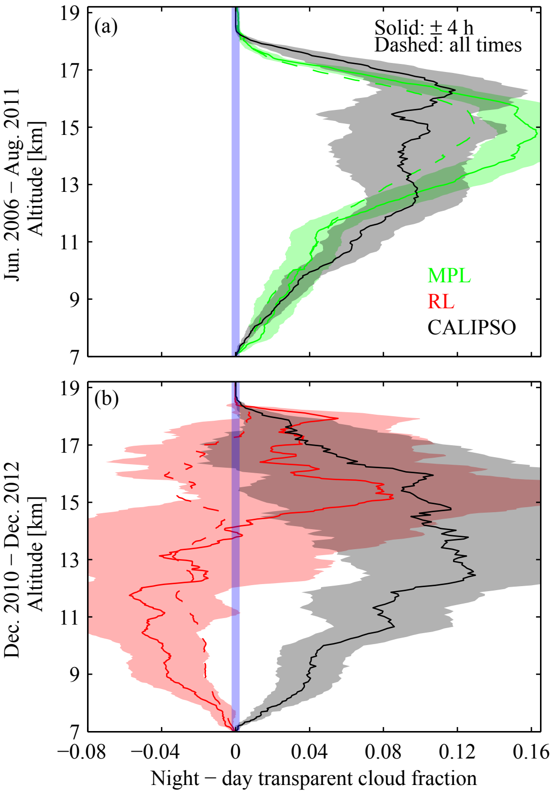

Figure 4.3: The difference between the day and night mean transparent cirrus cloud fraction profiles for MPL (green), RL (red) and CALIPSO (black) observations from June 2006 through August 2011 (a) and December 2010 through December 2012 (b). MPL and RL observations collocated in time (± 4 hours) to CALIPSO overpasses are depicted as solid lines. The shading on each line represents the 95% confidence interval due to statistical uncertainty. Dashed lines denote MPL and RL profiles derived using all available data.

4.4.4 Total Cloud Fraction

The RL and CALIPSO comparison in the previous section portrayed excellent agreement in the subset of profiles transparent to the lidar beam. Unfortunately, complete attenuation of a lidar beam is not uncommon and in these cases cloud layers beyond the point of the lidar beam's extinguishment are unobservable. The total (both transparent and attenuated profiles) CALIPSO and RL ice cloud fraction is given in Figure 4.4. For this comparison it is possible for the CALIPSO observations to contain mixed phase cloud layers or layers of supercooled water (see section 4.3). Therefore to compare fairly to the RL observations, whose cloud mask identifies only ice clouds, CALIPSO's cloud phase information in the CLay product is used to remove any liquid cloud layers. In this section the cloud fraction profiles are no longer composed solely of cirrus clouds since the inclusion of attenuated cases may include thicker ice clouds such as anvil clouds. We therefore refer to the cloud fraction as the ice cloud fraction.

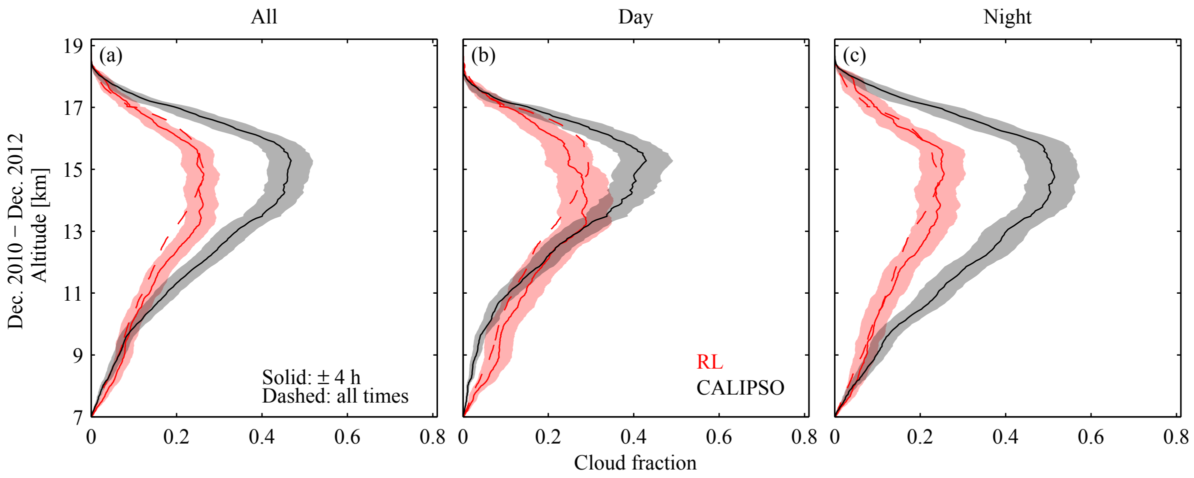

Figure 4.4: Total ice cloud fraction profiles for RL (red) and CALIPSO (black) observations from December 2010 through December 2012. Profiles are shown separately for observations from all times (a), only daytime (b) and only nighttime (c). RL observations collocated in time (± 4 hours) to CALIPSO overpasses are depicted as solid lines. The shading on each line represents the 95% confidence interval due to statistical uncertainty. Dashed lines denote RL profiles derived using all available data.

Ice cloud fraction profiles in Figure 4.4a show the RL observations to have significantly less clouds above about 12 km. During the day (Figure 4.4b) and night (Figure 4.4c) the RL observations have significantly less clouds above about 15 km and 10 km, respectively. Since transparent cloud fraction agreed well (Figure 4.2d-f), the differences in Figure 4.4 are mostly occurring in attenuated profiles. During this sampling period, the fraction of attenuated RL profiles, 44%, is significantly larger than CALIPSO, 34%. The larger amount of RL profiles that are completely attenuated is perhaps due to the difference in wavelengths of the two lidar system. At the RL's shorter wavelength (355 nm), the optical depth due to molecular scattering is about 5 larger than at CALIPSO's wavelength (532 nm).

CALIPSO has two distinct advantages in attenuated profiles which allows it to observed more cirrus clouds than the RL. The first is due to its spaceborne platform. In a profile containing an ice cloud layer, the ground-based RL signal must first penetrate through any lower liquid cloud layers present, which rapidly and possibly completely extinguishes the lidar signal. Profiles viewed from CALIPSO's spaceborne platform have the advantage of observing the ice layer first before encountering any thick liquid cloud layers. The second advantage is due to multiple scattering which is a function of the particle properties, the lidar FOV and the distance to the scattering target (Eloranta, 1998). While the RL FOV is larger, the large distance between CALIPSO and it's target allows for a more significant contribution from multiple scattering. This allows CALIPSO to penetrate further into opaque layers (e.g. Yorks et al., 2011) and therefore detect more clouds than the RL in these cases. Figure 4.4 proves these advantages to be significant since at most altitudes CALIPSO cloud fraction is larger.

4.4.5 Geometrical Thickness

Probability density functions (PDFs) of cirrus cloud layer geometrical thicknesses in transparent profiles are given in Figure 4.5. Table 4.2 shows the median cirrus cloud layer thickness for each comparison.

Figure 4.5 shows that overall agreement of PDFs is good during the MPL sampling period. Only a few bins have significant differences; namely the day and night CALIPSO and MPL comparison for thicknesses larger than 3 km. During the RL sampling period, CALIPSO and RL PDFs agree well when all times are considered and during the nighttime. During the day, the RL PDF is shifted towards larger thicknesses relative to CALIPSO. Both CALIPSO

Table 4.2: Median cirrus cloud layer geometrical thicknesses (km) in transparent profiles. Bold values indicate that the difference between day and night is statistically significant.

Jun. 2006 - Aug. 2011				Dec. 2010 - Dec. 2012			
	All	Day	Night		All	Day	Night
CALIPSO	1.44	**1.14**	**1.80**	CALIPSO	1.50	**1.26**	**1.68**
MPL	1.50	**1.23**	**1.68**	RL	1.47	1.53	1.44
MPL, ± 4 h	1.44	**1.14**	**1.62**	RL, ± 4 h	1.65	1.83	1.56

and MPL PDFs shift towards lower thickness during the day relative to at night. This is also apparent when comparing the median cirrus thicknesses (Table 4.2) where the MPL and CALIPSO cirrus layers are 0.48 km and 0.66 km thinner during the daytime, respectively. Both these differences are statistically significant. When all daytime and all nighttime MPL data are considered (Figure 4.5a-c, dashed green line; Table 4.2) cirrus are also thinner during the daytime. CALIPSO observations during the RL sampling period (Figure 4.5d-f and Table 4.2) also have a similar significant diurnal cycle with cirrus layers 0.42 km thinner during the daytime. In contrast to the MPL and CALIPSO observations, RL observations show non-significant differences in PDFs and median cloud thicknesses between the day and nighttime with cloud layers thicker during the daytime by 0.27 km. Median cloud thickness in Table 4.2 show that cirrus cloud thickness agrees better among all three sets of observations during the nighttime while during the day both CALIPSO and the MPL are significantly thinner than the RL. The RL observations imply that thinner daytime CALIPSO and MPL clouds are the result of increased noise. The larger amount of noise during the daytime could cause thinner cloud layers due to the difficultly in detecting the tenuous top and base of the cloud. This would result in a geometrically thinner cloud layer than if it was observed at night.

The diurnal cycle of cirrus cloud thickness is more closely examined in Figure 4.6 which shows the hourly anomaly of the median cirrus cloud thickness relative to the median nighttime thickness. A portion of the RL observations are plotted with a dotted line to indicate hours with relatively poor sampling due to the protective shutter being closed (hours 10-13). In addition to poor sampling, the RL observations during these times are biased to winter-time cirrus when the shutter is kept open all day. The MPL also has fewer samples around noon, but its sample size is not as severely reduced as the RL. Both the RL and MPL fully sample the diurnal cycle making it natural to compare their results directly. However, spurious agreement or disagreement may be due to the different time periods they sample. To better compare the MPL data to the RL data we force the monthly sampling of the MPL data to match the RL. This is accomplished using a Monte-Carlo method whereby random MPL profiles are added or removed from the native MPL dataset in order to match the RL monthly sampling. This creates a modified MPL dataset used to recalculate the hourly cirrus thickness. Many (1000) modified MPL datasets are created and the hourly cirrus thicknesses recalculated. The mean of these 1000 iterations are used to approximate a MPL dataset with the same monthly sampling as the RL. This process is also performed for the CALIPSO data from the MPL sampling period. The datasets forced to have the same RL monthly sampling are denoted with pluses in Figure 4.6. Compared to their respective native datasets, both the MPL and CALIPSO diurnal cycles are similar when the RL monthly sampling is imposed.

Figure 4.6 shows the hourly thickness for the daytime MPL observations are highly correlated with the progression of the sun with clouds becoming thinner as the sun rises and thicker as the sun sets. And, as shown previously, the daytime CALIPSO observations have thinner clouds than the nighttime observations. The RL cloud thickness in Figure 4.6 remains similar throughout the day which implies that the diurnal cycle of the CALIPSO and MPL observations is mostly due to increased noise during the daytime causing clouds layers to be thinner.

In addition to using the RL observations as a reference, diurnal cirrus cloud thickness differences with thresholds applied to the transparent CALIPSO CPro data are used to determine if daytime noise is responsible for CALIPSO observing thinner cloud layers. While this comparison uses only CALIPSO data, the observations are still collocated to the MPL and RL observations during their respective sampling periods. Since cloud layers separated by less than 500 m in the threshold datasets are merged together (section 4.2.3), the same criterion is applied to the unmodified dataset for comparison purposes. The median cirrus cloud layer thickness derived from extinction profiles in the CPro product is shown in Table 4.3. Since we merge layers separated by less than 500 m, both day and night cloud layers derived from the unmodified CPro product (Table 4.3) are thicker than those taken from the official CLay product (Table 4.2). However, cloud layers do remain significantly thinner during the daytime by approximately the same amount.

Table 4.3: CALIPSO cirrus cloud layer median geometrical thicknesses (km) derived from the L2 CPro product in transparent profiles. Layer thickness is also derived after applying two different extinction (α) thresholds to the data. Bold values indicate that the difference between day and night is statistically significant.

Jun. 2006 - Aug. 2011			Dec. 2010 - Dec. 2012		
	Day	Night		Day	Night
CALIPSO	**1.26**	**1.86**	CALIPSO	**1.44**	**1.86**
CALIPSO, $\alpha > 0.0061$ km^{-1}	**1.20**	**1.38**	CALIPSO, $\alpha > 0.0061$ km^{-1}	1.38	1.32
CALIPSO, $\alpha > 0.0035$ km^{-1}	**1.26**	**1.56**	CALIPSO, $\alpha > 0.0035$ km^{-1}	1.44	1.50

The median cirrus cloud layer thickness from the unmodified CALIPSO CPro product, the dataset with the high daytime extinction threshold applied and the dataset with the low daytime extinction threshold applied are shown in Table 4.3. During the RL sampling period, the application of the either the high or low threshold eliminates the significant difference between day and night cirrus layer thicknesses. For the MPL sampling period, daytime cirrus layers remain significantly thinner after applying either the high or low threshold. However, the magnitude of the diurnal cycle is reduced by approximately a factor of 3.5 and 2 for the high and low thresholded data, respectively. The application of this simple range of thresholds to the CALIPSO data indicates that it is possible for the different detection limits to cause cirrus cloud layers to be thinner during the daytime which is consistent with the conclusions determined using the comparisons to RL observations.

Comparisons of the shift in the daytime median cloud top and base heights relative to the nighttime are used to determine whether inaccurate cloud top, base or both is the dominate cause of thinner daytime CALIPSO and MPL cirrus cloud layers. For the RL observations, both cloud top and base heights shift towards lower altitudes during the daytime by 0.33 km and 0.66 km, respectively. The slightly larger shift downward in cloud base height results in slightly thicker RL cirrus cloud layers during the daytime (Table 4.2). The CALIPSO observed cloud tops also shift to lower altitudes by 0.24 km, which is a similar amount as shift in the RL observed cloud top. However, unlike the RL, the CALIPSO cloud bases shift to higher altitudes by 0.54 km during the day resulting in thinner cloud layers (Table 4.2). Therefore the thinner daytime CALIPSO cirrus is primary due to premature cloud base identification. For the MPL, the severe lack of high clouds in the daytime observations results in larges shifts to lower altitudes in both cloud top (2.07 km) and base (1.29 km) during the daytime. The shift in MPL cloud top heights is 0.78 km larger, implying that the dominate cause of thinner daytime MPL cirrus layers is poor identification of cloud top location.

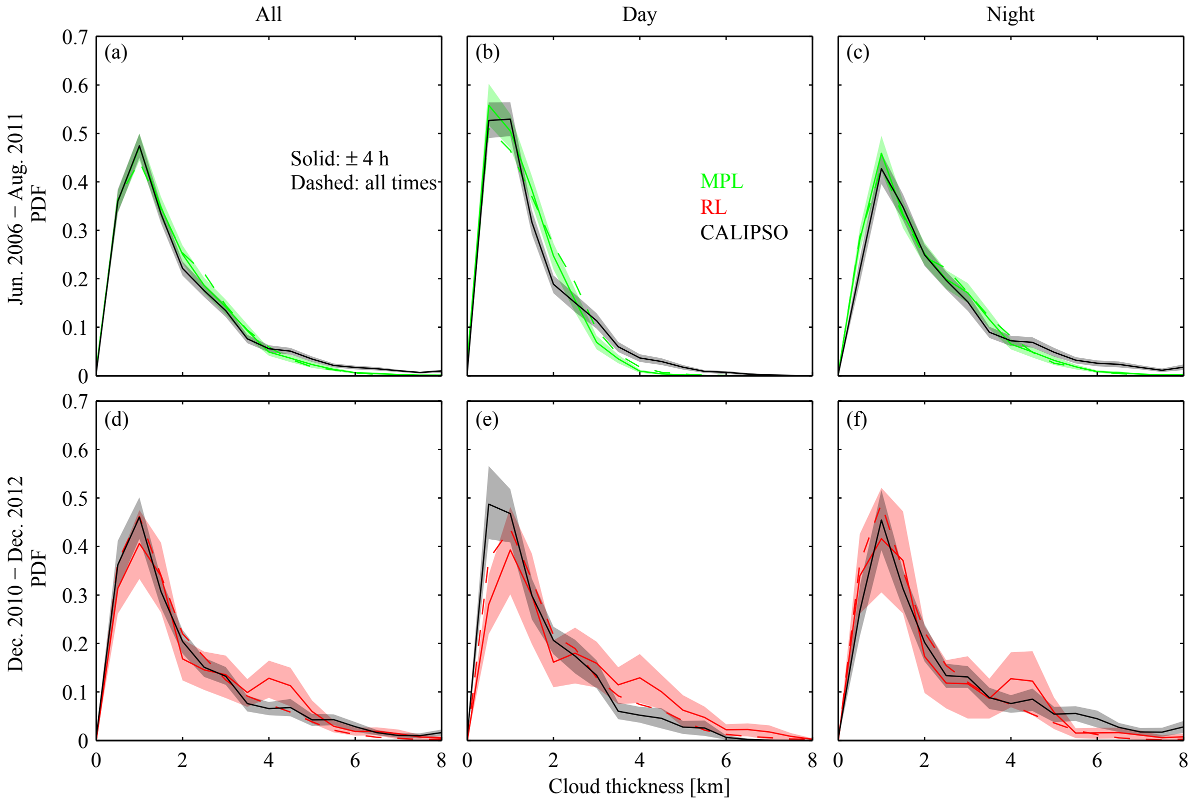

Figure 4.5: Probability density functions (PDFs) of cirrus cloud layer geometrical thickness in profiles transparent to the lidar for MPL (green), RL (red) and CALIPSO (black) observations from June 2006 through August 2011 (a-c) and December 2010 through December 2012 (d-f). Profiles are shown separately for observations from all times (a/d), only daytime (b/e) and only nighttime (c/f). MPL and RL observations collocated in time (± 4 hours) to CALIPSO overpasses are depicted as solid lines. The shading on each line represents the 95% confidence interval due to statistical uncertainty. Dashed lines denote MPL and RL profiles derived using all available data. Bin size for the PDFs is 0.5 km.

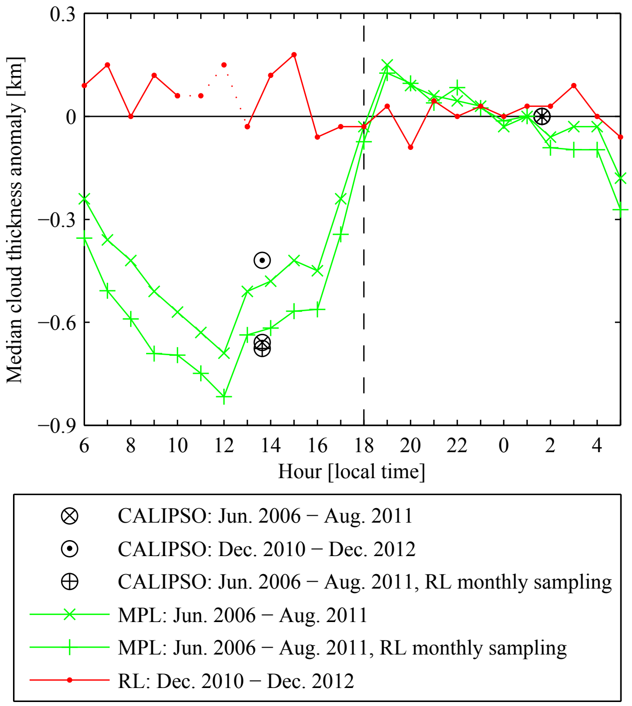

Figure 4.6: Hourly median cloud thickness anomaly relative to the median nighttime thickness for MPL (green 'x'), RL (red dot) and CALIPSO (black circle) observations. CALIPSO observations are shown for the June 2006 through August 2011 (black 'x' inside circle) and December 2010 through December 2012 (black dot inside circle) sampling periods. CALIPSO (black plus inside circle) and MPL (green cross) data from June 2006 through August 2011 forced to match RL's monthly sampling is also shown. Times when the RL sample size is poor are connected using a dotted line. Sunrise occurs at approximately 6 and sunset at 18.

4.5 Summary

Cirrus cloud macrophysical properties from the RL, MPL and CALIPSO are compared over two sampling periods: (1) June 2006 through August 2011 and (2) December 2010 through December 2012. The RL observations are shown to have the smallest increase in noise due to the solar background with approximately a factor of 2 increase— about 4 times less than CALIPSO and 12 times less than the MPL. Therefore the RL observations are considered relatively unaffected by the solar background and are used as a reference for examining the diurnal cycle of cirrus cloud properties.

The impact of the solar background on the MPL is evident by a very low daytime SNR, severely reducing its ability to detect cirrus. Even during nighttime, the MPL SNR is too low at the altitudes where cirrus most frequently occur (above 11 km), causing it to miss a significant amount of cirrus compared to CALIPSO. In contrast, the RL and CALIPSO show excellent agreement at all altitudes when day and night observations are considered together. The CALIPSO observations have a lower SNR and higher solar background relative to the RL, but the good agreement with the RL suggests that CALIPSO's measurement quality is sufficient to detect a similar amount of cirrus at Darwin.

CALIPSO and MPL PDFs of cirrus cloud geometrical thickness in transparent profiles agree well. CALIPSO and RL PDFs show good agreement, particularly during the nighttime. Both CALIPSO and MPL PDFs and median layer thicknesses shift towards lower thicknesses during the daytime relative to at night. The RL observations do not show this diurnal cycle but instead show similar statistics for the day and night observations. In terms of median layer thickness the RL, MPL and CALIPSO agree best at night while during the day both the MPL and CALIPSO cirrus layers are significantly thinner than the RL. When comparing hourly median cirrus layer thickness the RL observations show little variation throughout the day while the MPL cloud layers are correlated with the sun— becoming thinner as the sun rises and thicker as the sun sets. Furthermore, the application of the approximate daytime detection limits to all CALIPSO data eliminates or reduces the differences between day and night cloud layer thicknesses. All this evidence insinuates that the diurnal cycle of the MPL and CALIPSO is caused mainly due to increased daytime noise. Users of CALIPSO and MPL data should be aware that observations of cirrus clouds are biased towards smaller geometrical thicknesses during the daytime.

Chapter 5

AUTOMATED RETRIEVAL OF CLOUD AND AEROSOL PROPERTIES FROM THE ARM RAMAN LIDAR, PART 1: FEATURE DETECTION

The contents of this chapter are reproduced from a manuscript currently in review: Thorsen, T. J., Q. Fu, R. K. Newsom, D. D. Turner, and J. M. Comstock, 2014, J. Atmos. Oceanic Technol. The Introduction and Summary sections have been revised from their original form and minor modifications have been made throughout the text.

5.1 Introduction

Here we develop an algorithm for a Raman lidar to objectively determine the vertical extent of clouds and aerosols (particulates). The algorithm falls into the general category of a threshold method where an estimate of a clear-sky signal is made and significant returns above that are considered to be particulates. Variations of threshold methods have been widely used in the analysis of elastic lidar signals (e.g. Winker and Vaughan, 1994; Clothiaux et al., 1998; Campbell et al., 2002; Vaughan et al., 2009). Raman lidars (RL; e.g. Goldsmith et al., 1998; Matthais et al., 2004) and high spectral resolution lidars (HSRL; e.g Hair et al., 2008; Grund and Eloranta, 1991) are more advanced lidars that can intrinsically separate returns from molecules and particulates. This work presents a threshold method developed for the Atmospheric Radiation Measurement (ARM) program's Raman lidars which operate at the ARM Southern Great Plains (SGP) site near Lamont, Oklahoma and the Tropical Western Pacific (TWP) Darwin, Australia site.

The ARM Raman lidar was originally conceived to meet the ARM program's goal of measuring water vapor profiles at a high temporal and spatial resolution. Since the RL was designed to be a continuously operated instrument, automated algorithms were designed to process the data in a timely fashion (Turner et al., 2002) with a focus on the retrieval of water vapor and aerosol extinction profiles in the lower part of the atmosphere. While cloud observations were originally considered of secondary importance for this system, Thorsen et al. (2013b) (Chapter 4) and Dupont et al. (2011) showed that the RL provides far superior observations of clouds compared to the ARM program's primary lidar, the micropulse lidar (MPL; Campbell et al., 2002; Coulter, 2012). However, the identification of clouds is treated in a simple manner in current ARM RL data products and many clouds, especially cirrus, are not identified (Thorsen et al., 2013b, Chapter 4).

In order to fully realize the potential of the ARM RL, we develop an automated algorithm for Feature detection and EXtinction retrieval (FEX). The FEX algorithm objectively identifies features (i.e. clouds and aerosols) and retrieves their extinction profiles over the full extend of the troposphere. Complete details of the retrieval of extinction profiles is given in part 2 of this series of papers (Thorsen and Fu, 2014, Chapter 6), while part 1 here focuses on feature identification. The intent is to run FEX operationally within the ARM Data Management Facility (DMF) with the output being made available to the general user community via the ARM website (http://www.arm.gov/).

5.2 The ARM Raman lidar

The RL at the SGP site has been in near-continuous operation since 1998 and its basic design is described in Goldsmith et al. (1998). This original system has since evolved through various upgrades and modifications (Ferrare et al., 2006; Newsom, 2009). In December of 2010 a second ARM RL was deployed at the Darwin TWP facility with nearly the same design as the SGP RL. Specifications of the ARM RL system and the detection channels used in this work are given in Table 5.1. The system contains channels for detection of elastic as well as Raman scattered light from nitrogen, water vapor and two temperature channels. Only the elastic and nitrogen channels are used for this work; details concerning retrieval of water vapor are given in Turner et al. (2002) and temperature in Newsom et al. (2013). Backscattered returns are collected using both a narrow FOV (NFOV; here after referred to as the "high channels") and wide FOV (WFOV, here after referred to as the "low channels") at a vertical resolution of 7.5 m. The high elastic channel signal is split into copolarized and cross-polarized signals. For convenience, throughout this paper the prefix "high" is dropped when referring to the high channel signals; although the prefix "low" will be included when referring to low channel signals.

Table 5.1: Specifications of the ARM RL transmitter and receiver channels used for feature detection in this study.

Transmitter	
Laser	Frequency-tripled Nd:YAG
Wavelength	355 nm
Pulse energy	$\sim$ 300 mJ
Pulse width	$\sim$ 5 ns
Pulse repetition frequency	30 Hz
Beam divergence	0.1 mrad
Receiver	
Telescope	61 cm
FOV (wide)	2 mrad
FOV (narrow)	0.3 mrad
Data acquisition	Simultaneous analog and photon counting
Pulse accumulation time	10 s
Range resolution	7.5 m
Channels (0.3 nm bandpass filters)	
High elastic parallel ($S_{\lambda_0,\parallel}$)	355 nm copolarized, narrow FOV
High elastic perpendicular ($S_{\lambda_0,\perp}$)	355 nm cross-polarized, narrow FOV
High nitrogen ($S_{\lambda_{N_2}}$)	387 nm, narrow FOV
Low elastic (S_{L,λ_0})	355 nm, wide FOV
Low nitrogen ($S_{L,\lambda_{N_2}}$)	387 nm, wide FOV

5.3 Feature detection algorithm

Feature detection in FEX centers around the application of signal detection theory (e.g. Kingston, 1978). In the presence of noise, the problem of determining if a signal contains a contribution from particulates becomes one of comparing two probability distributions. This is shown schematically in Fig. 5.1 where an expected molecular signal (m) with noise σ_m is given in blue and the measured signal (S) with noise σ_S is given in red. In the presence of noise the detection threshold (T) is set at a value larger than what we expect a purely molecular signal to be— in this case one standard deviation away from the expected molecular signal. In addition to setting a threshold, an important consideration is the identification and removal of false detections. In this work, the possibility of a false detection is assessed by quantifying the overlap between the P_m and P_S probability distributions: i.e. the purple region P_o in Fig. 5.1. The essential components of feature detection are all given in Fig. 5.1— given the signal measured by the lidar we need to determine: (1) the noise in the measured signal, (2) the expected molecular signal and (3) the noise in the expected molecular signal. From this we can set a threshold and assess whether a true feature was detected. In the following sections (5.3.1–5.3.4), details of the algorithm are given accompanied by examples from the Darwin, Australia ARM RL to illustrate the method.

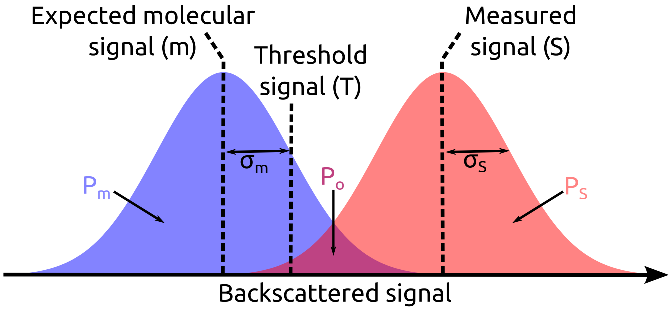

Figure 5.1: Schematic comparing the expected molecular signal (left) to the signal measured by the lidar (right).

5.3.1 Initial processing

The main input into our feature detection algorithm is the MERGE product (Newsom et al., 2009) routinely produced as part of the ARM archive (http://www.archive.arm.gov). MERGE applies deadtime corrections and combines raw analog voltages and deadtime-corrected photon counting data signals into a single signal by converting the analog signals to an equivalent photon count rate. These photon count rate profiles are then converted to photon counts for the channels listed in Table 5.1. Photon counts from the native 10 s and 7.5 m resolution in the MERGE data are then accumulated by FEX into their desired time and height bins— in this study we primarily use 2 min and 30 m— to improve the signal-to-noise ratio (SNR).

Noise in lidar signals are contributed from two main sources: (1) background noise due to solar radiation, detector dark current and thermal noise and (2) shot noise. Background noise is range-independent and measured by the ARM RL system by using pre-trigger samples— i.e. samples taken for $\sim 15\mu s$ (~300 samples) before the laser fires. Shot noise is the uncertainty associated with the arrival of photons on the detector due to the discrete nature of the incident light. The uncertainty due to shot noise is well described by a Poisson distribution (Oliver, 1965), making it straightforward to calculate since the standard deviation is equal to the square root of the signal intensity. While possible that excess noise beyond background and shot noise may be present, no attempt is made to determine its potential impact. Using the RL at SGP, Wulfmeyer et al. (2010) found this assumption to be a reasonable one since various methods to retrieve water vapor mixing ratio noise profiles agreed well with those estimated using Poisson statistics.

The MERGE pre-trigger samples, at the native 10 s and 7.5 m resolution, are used to determine the background signal in the 2 min and 30 m data:

$$B_i = \frac{n_h}{n_B} \sum_{j=1}^{n_B} \sum_{k=1}^{n_t} S_i^{pt}(j,k) \tag{5.1}$$

where S^{pt} are the MERGE pre-trigger signals, n_h is the number of height bins accumulated ($n_h = 4$), n_t is the number of time bins accumulated ($n_t = 12$) and n_B is the number of pre-trigger samples. The subscript i throughout this paper is used to denote the channels considered in Table 5.1. These background signals are subtracted from each channel. The range-independent background noise for each 10 s MERGE profile k is computed as the standard deviation of the pre-trigger samples

$$\theta_i(k) = \sqrt{\frac{1}{n_B} \sum_{j=1}^{n_B} \left(S_i^{pt}(j,k) - \overline{S_i^{pt}(j,k)} \right)^2} \tag{5.2}$$

where the overbar denotes the mean over all pre-trigger samples. Equation (5.2) is then used to calculate the background noise in data accumulated to 2 min and 30 m

$$\sigma_{B,i} = \sqrt{n_h \sum_{k=1}^{n_t} \theta_i^2(k)}. \tag{5.3}$$

The range-dependent shot noise is then calculated in each channel

$$\sigma_{s,i}(z) = \sqrt{S_i(z) + B_i} \tag{5.4}$$

where S is the background-subtracted photon counts in the 2 min and 30 m data. Finally, the total noise can then be determined by adding the shot and background noise in quadrature

$$\sigma_i(z) = \sqrt{\sigma_{s,i}^2(z) + \sigma_{B,i}^2}. \tag{5.5}$$

5.3.2 Scattering and depolarization ratios

Following the development by Measures (1984) the lidar equation for a background-subtracted signal due to elastic backscattering can be written as

$$S_{\lambda_0}(z) = \nu_{\lambda_0}\frac{S_0}{z^2}O_{\lambda_0}(z)\left[\beta_{m,\lambda_0}(z) + \beta_{p,\lambda_0}(z)\right]T_{m,\lambda_0}^2(0,z)T_{p,\lambda_0}^2(0,z), \tag{5.6}$$

where $S_{\lambda_0}(z)$ is the number of photons received from height z, ν_{λ_0} is the system constant incorporating all the lidar parameters which describe the characteristics of the optics and detectors, S_0 is the number of transmitted photons and $O(z)$ is the overlap function which describes overlap between the laser beam and receiver's FOV. $\beta_{m,\lambda_0}(z)$ and $\beta_{p,\lambda_0}(z)$ are the molecular and particulate backscatter coefficients, respectively. $T_{m,\lambda_0}(0,z)$ and $T_{p,\lambda_0}(0,z)$ are the transmission due to molecules and particulates which, for a zenith pointing lidar like the ARM RL, are

$$T_{m,\lambda_0}(0,z) = \exp\left[-\int_0^z \alpha_{m,\lambda_0}(z^{'})dz^{'}\right] \tag{5.7}$$

and

$$T_{p,\lambda_0}(0,z) = \exp\left[-\int_0^z \alpha_{p,\lambda_0}(z^{'})dz^{'}\right] \tag{5.8}$$

where $\alpha_{m,\lambda_0}(z)$ and $\alpha_{p,\lambda_0}(z)$ are the molecular and particulate extinction coefficients, respectively. For the signal in the nitrogen Raman channels, which only contains backscatter due to nitrogen molecules, the lidar equation can be written as

$$S_{\lambda_{N_2}}(z) = \nu_{\lambda_{N_2}} \frac{S_0}{z^2} O_{\lambda_{N_2}}(z) \beta_{N_2,\lambda_{N_2}}(z) T_{m,\lambda_0}(0,z) T_{p,\lambda_0}(0,z) T_{m,\lambda_{N_2}}(0,z) T_{p,\lambda_{N_2}}(0,z). \tag{5.9}$$

Compared to Eq. (5.6), extra transmission terms are needed to account for the different wavelength of the return signal. In Eqs. (5.6) and (5.9), the molecular backscatter terms, $\beta_{m,\lambda_0}(z)$ and $\beta_{N_2,\lambda_{N_2}}(z)$, can be expressed in terms of the molecular number concentration:

$$\beta_{m,\lambda_0}(z) = N(z) \frac{d\sigma_{Ra}}{d\Omega_\pi} \tag{5.10}$$

and

$$\beta_{N_2,\lambda_{N_2}}(z) = w_{N_2} N(z) \frac{d\sigma_{Rm}}{d\Omega_\pi} \tag{5.11}$$

where $N(z)$ is the molecular number profile, w_{N_2} is the nitrogen mixing ratio, $d\sigma_{Ra}/d\Omega_\pi$ and $d\sigma_{Rm}/d\Omega_\pi$ are the differential backscatter cross sections for Rayleigh and nitrogen Raman scattering, respectively, at the laser wavelength λ_0. Equations (5.10) and (5.11) ignore the temperature dependence of the Rayleigh and nitrogen Raman backscattering as it is very small for the narrow filter widths of the RL and a laser wavelength of 355 nm (Whiteman, 2003). The influence of multiple scattering is also not accounted for, i.e. Eqs. (5.10) and (5.11) assume that the transmitted photons and the atmosphere undergo a single interaction. Although FEX does explicitly consider multiple scattering, the details of this are discussed in part 2 of this work (Thorsen and Fu, 2014, Chapter 6).

In order to identify signals above that expected from clear-sky, we use the scattering ratio

$$SR(z) = \frac{\beta_{p,\lambda_0}(z) + \beta_{m,\lambda_0}(z)}{\beta_{m,\lambda_0}(z)}. \tag{5.12}$$

The scattering ratio is thus the ratio of the total (molecular and particulate) backscatter to the backscatter from just molecules. Since the elastic channel signal contains contributions from both molecular and particulate scattering and the nitrogen channel signal is a function of molecular scattering only, a scattering ratio can be formed by using Eq. (5.6) and (5.9) (Cooney et al., 1969; Melfi, 1972). The expression for this scattering ratio using the high channels can be written as

$$SR_{E,N_2}(z) = C_{E,N_2} \frac{O_{\lambda_{N_2}}(z)}{O_{\lambda_0}(z)} \frac{T_{m,\lambda_{N_2}}(0,z)}{T_{m,\lambda_0}(0,z)} \frac{S_{\lambda_0,\perp}(z) + S_{\lambda_0,\parallel}(z)}{S_{\lambda_{N_2}}(z)} \times \exp\left\{ \int_0^z \alpha_{p,\lambda_0}(z^{'}) \left[1 - \left(\frac{\lambda_0}{\lambda_{N_2}} \right)^{a(z^{'})} \right] dz^{'} \right\} \quad (5.13)$$

where $S_{\lambda_0,\perp}$ and $S_{\lambda_0,\parallel}$ are the signals in the high perpendicular and parallel channels, respectively, and a is the Angstrom exponent. The subscript E, N_2 is used to denote that this scattering ratio is derived by using both the elastic and nitrogen channel signals. C_{E,N_2} is a calibration constant:

$$C_{E,N_2} = \left(w_{N_2} \frac{d\sigma_{Rm}}{d\Omega_\pi} \nu_{\lambda_{N_2}} \right) / \left(\frac{d\sigma_{Ra}}{d\Omega_\pi} \nu_{\lambda_0} \right). \quad (5.14)$$

An example of this scattering ratio derived using the elastic and nitrogen channels is given in Fig. 5.2a for the high channel signals. Note that separate system constants are not used for the high parallel and perpendicular channels because any difference between the two channels has already been accounted for as shown in Appendix A. Separate overlap functions are not derived for the high parallel and perpendicular channels either as discussed in section 5.3.3. The exponential term accounts for the differential particulate transmission between the elastic and nitrogen channels where the wavelength dependence has been rewritten in terms of the Angstrom exponent a. For cloud layers, this term is 1 since $a = 0$ for this small difference in wavelength. However, the same cannot be assumed for aerosols; therefore we use collocated CIMEL sun photometer data (Holben et al., 1998) to determine the aerosol Angstrom exponent. Using multiple years of data (1996–2007 at SGP and 2004–2007 at Darwin) we find the median Angstrom exponent to be 1.35 between 340 and 380 nm at both the SGP and Darwin site. Similarly, the differential transmission due to molecules must also be taken into account in calculating this scattering ratio. These molecular transmission terms are calculated following Bucholtz (1995) using pressure and temperature profiles from radiosondes, which are launched at least twice daily at all ARM facilities and are linearly interpolated to the heights and times of the lidar profiles.

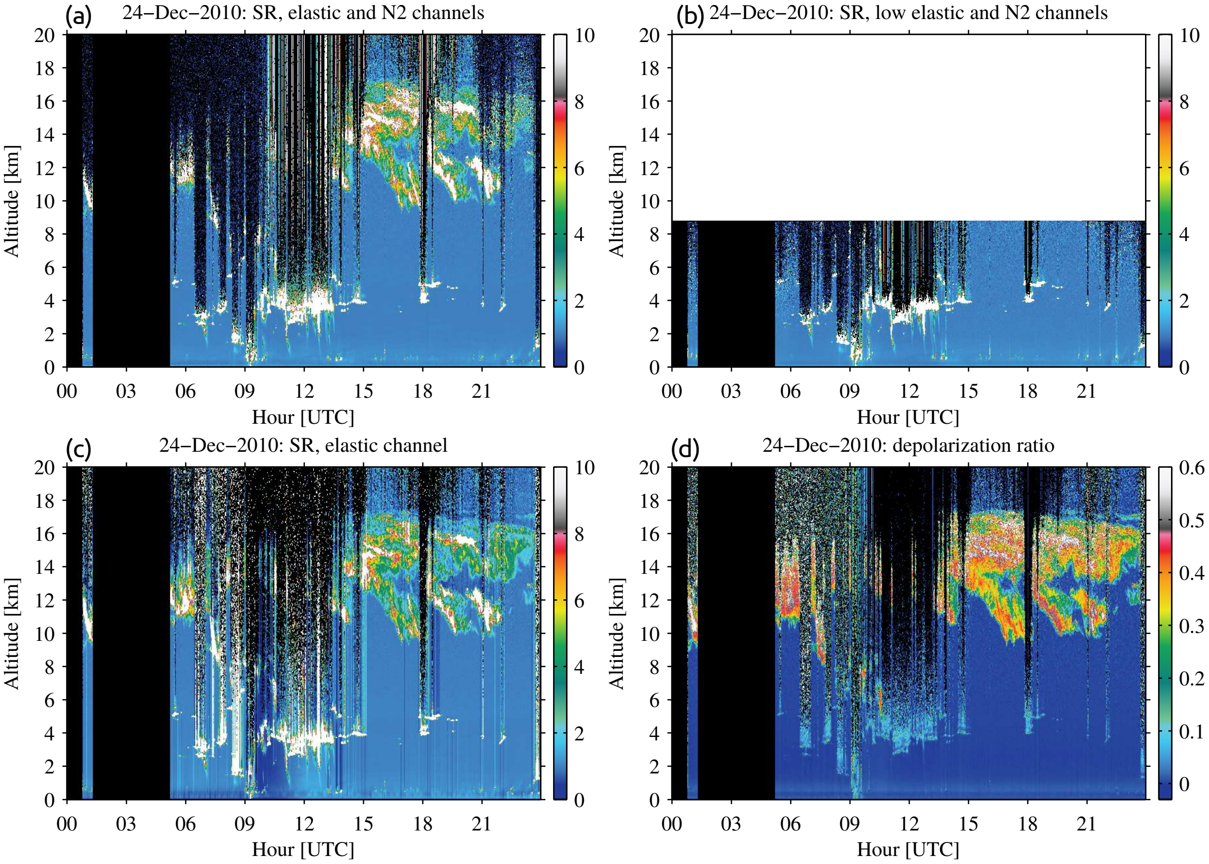

Figure 5.2: (a) Scattering ratio derived using the elastic and nitrogen channels, (b) scattering ratio derived using the low elastic and nitrogen channels, (c) scattering ratio derived using only the elastic channel, and (d) depolarization ratio after the final iteration of FEX for December 24, 2010 at Darwin.

Similarly we can construct a scattering ratio using the low elastic and nitrogen channels

$$SR^L_{E,N_2}(z) = C^L_{E,N_2}\frac{O^L_{\lambda_{N_2}}(z)}{O^L_{\lambda_0}(z)}\frac{T_{m,\lambda_{N_2}}(0,z)}{T_{m,\lambda_0}(0,z)}\frac{S^L_{\lambda_0}(z)}{S^L_{\lambda_{N_2}}(z)} \times \exp\left\{\int_0^z \alpha_{p,\lambda_0}(z^{'})\left[1-\left(\frac{\lambda_0}{\lambda_{N_2}}\right)^{a(z^{'})}\right]dz^{'}\right\} \quad (5.15)$$

where the superscript L is used to denote the low channel. Figure 5.2b gives an example of this scattering ratio below 9 km since the ARM RL doesn't record low channel signals above that height. At the expense of increased noise, using the low channel signals has the benefit of achieving complete overlap sooner (i.e. at a lower altitude above the system), allowing for a more accurate scattering ratio in the near-field than the high channels. For the ARM RL the high channels achieve complete overlap by 5 km and the low channels by 800 m (Goldsmith et al., 1998).

After determining the calibration factors and overlap corrections (section 5.3.3), we can derive the scattering ratio using Eqs. (5.13) and (5.15). An advantage of deriving a scattering ratio using both the elastic and nitrogen channel signals is that taking the ratio of the two overlap functions helps reduce the impact of incomplete overlap. While the differential molecular transmission is straightforward to account for using radiosonde observations, determining the differential aerosol transmission term requires both identifying aerosol and retrieving extinction. Its is fortunate that the differential aerosol transmission term is not very sensitive to aerosol extinction properties (Whiteman et al., 1992). For the Darwin RL we find mean corrections for differential aerosol transmission ranging from 0% to 2% from 0–18 km. The more accurately constrained correction for differential molecular transmission ranges from 0% to 18% from 0–18 km. As is shown in section 5.4, the main limitation of using SR_{E,N_2} and SR^L_{E,N_2} for feature detection is that Raman scattering is a relatively weak process compared to elastic scattering. Therefore, detecting features will be limited by the amount of noise in the nitrogen channel especially during the day when the Raman backscatter must compete with the solar background.

To produce a quantity with the smallest amount of noise possible, the scattering ratio can also be derived using only the elastic channel signal. This is commonly done for single channel elastic backscatter lidars for the purpose of feature detection (e.g. Winker and Vaughan, 1994; Campbell et al., 2002; Vaughan et al., 2009) since Rayleigh scattering can be accurately modeled (e.g. Bucholtz, 1995). The elastic signal due to just molecular scattering can be determined by setting $\beta_{p,\lambda_0} = 0$ in Eq. 5.6. From this, the scattering ratio using only the elastic channel can be written as

$$SR_E(z) = C_E \frac{S_{\lambda_0,\perp}(z) + S_{\lambda_0,\parallel}(z)}{\frac{S_0}{z^2} O_{\lambda_0}(z) N(z) T^2_{m,\lambda_0}(0,z) T^2_{p,\lambda_0}(0,z)}. \tag{5.16}$$

where

$$C_E = 1/\left(\frac{d\sigma_{Ra}}{d\Omega_\pi}\nu_{\lambda_0}\right). \tag{5.17}$$

An example of the scattering ratio derived using only the elastic channel is shown in Fig. 5.2c. An accurate estimate of the full profile of cloud and aerosol extinction coefficients is crucial in determining the scattering ratio in this way. In addition there is no cancellation of overlap effects as occurs if both the elastic and nitrogen channels are used to derive the scattering ratio. Despite these limitations, deriving the scattering ratio using only the elastic channel has a better SNR for identifying features, especially considering solar background only adds a small amount of noise to daytime measurements in the ARM RL's elastic channels (Thorsen et al., 2013b, Chapter 4). This is apparent when comparing SR_E in Fig. 5.2c to SR_{E,N_2} in Fig. 5.2a where the upper portion of the daytime cirrus layer after 21 UTC becomes overwhelmed by noise in SR_{E,N_2} but is clearly visible in the SR_E image. Note that we do not derive the scattering ratio using only the low elastic channel as doing so identified few additional cloud or aerosol layers.

With the ARM RL it is also possible to identify features using the linear volume depolarization ratio

$$\delta(z) = \frac{S_{\lambda_0,\perp}(z)}{S_{\lambda_0,\parallel}(z)}. \tag{5.18}$$

An example false-color image of depolarization is given in Fig. 5.2d. Depolarization has the benefit of not depending on extinction as well as only using the elastic channel signals. But it is limited to identifying particulates which induce a depolarization, i.e. non-spherical particles like ice and some aerosols (Sassen, 1991; Gobbi, 1998; Murayama et al., 2001; Sassen, 2002) and layers which induce a significant amount of multiple scattering (Carswell and Pal, 1980; Sassen, 1991).

The four ratios given in Eqs. (5.13), (5.15), (5.16) and (5.18) (Fig. 5.2) are used for identifying features in FEX and, as discussed above, each quantity has specific advantages and disadvantages. Therefore the approach is to analyze each quantity separately with the expectation that taken as a whole they will be complementary and provide a more complete description of the vertical extent of clouds and aerosols. To calculate these ratios, calibration constants must be determined using clear-sky regions where the ratios have known values. One can readily see that the problem at hand is circular since clear-sky must be used to calibrate these quantities, but clear-sky cannot be identified without the calibrated quantities themselves. In addition we also require the particulate extinction coefficients, but we first must identify where the particulates are. Therefore FEX is an iterative algorithm as illustrated in Fig. 5.3: going through the process of calibration and determining overlap functions (section 5.3.3), calculating the expected molecular signals and identifying features (section 5.3.4), retrieving extinction (described in Thorsen and Fu (2014) and Chapter 6) and finally re-calculating the ratios (this section). The process is iterated over as depicted in Fig. 5.3 until less than 0.1% of all pixels in the feature mask change relative to the previous iteration (typically 5-6 iterations).

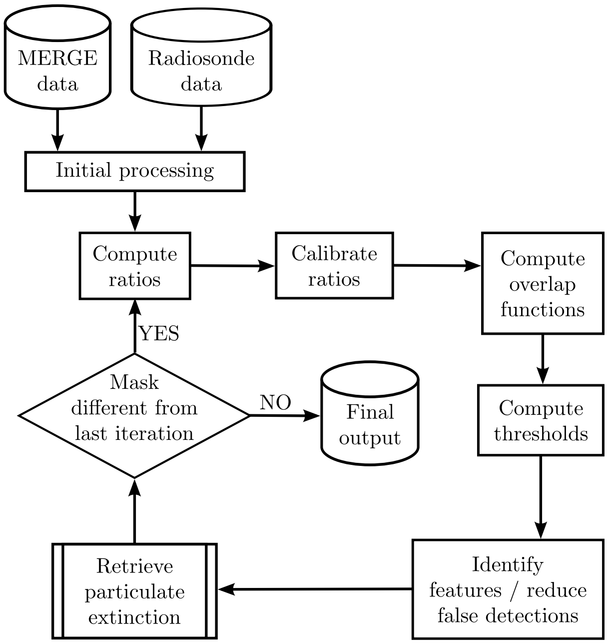

Figure 5.3: Flow diagram for feature detection in the FEX algorithm.

5.3.3 Calibration and overlap functions

Calibration constants and overlap functions are determined by similar methods as Turner et al. (2002) with some improvements. We establish a quality requirement for the signals used to calculate calibration constants and overlap functions in terms of SNR

$$\mathrm{SNR}_i(z) = \frac{S_i(z)}{\sigma_i(z)} \tag{5.19}$$

where a SNR of greater than 3 is flagged as a "good" signal. Using "good" signals from clear-sky regions calibration constants are determined for the scattering ratios by solving for the respective constants in Eqs. (5.13), (5.15) and (5.16). An additional calibration constant, $C^L_{\lambda_0}$, is calculated to match the low elastic channel signal to the high elastic channel signal. For $C^L_{\lambda_0}$, in addition to clear-sky signals, signals anywhere the scattering ratio is less than 2 are used since we expect the low and high channel signals to be proportional anywhere without significant multiple scattering. All constants are determined at varying degrees of frequency. At the coarsest level, constants are determined for each day being processed. Any automated or manual alignment "tweaks" made are noted from the instrument log files (automated alignment tweaks (Turner et al., 2002) were only performed prior to an upgrade in 2007 (Newsom, 2009)) and separate calibrations constants are determined per-tweak period. More finely-resolved calibration constants are also determined per-profile which are then used to obtain other per-profile constants by interpolating. A summary of the altitude regions and rules used to determine when each type of calibration type is performed is given in Table 5.2. When no suitable signals exist to derive any type of calibration constant, a database of historical values are used to determine the mean constant over the previous 7 days.

Table 5.3 gives the percentage of profiles for the ARM Darwin RL from December 2010 through December 2013 by calibration type: per-tweak, per-profile, interpolated or default (per-day or historical). For both high channel scattering ratios, a default calibration is only needed for 2% of profiles and the majority of profiles, 77%–80%, are able to use a per-profile calibration constant. For C_{E,N_2}, the uncertainty in the per-tweak and per-profile derived values are about 6%. A similar uncertainty (~5%) exists in the per-profile calculation of C_E. However, when C_E is determined per-tweak the uncertainty is larger (~16%). This larger per-tweak uncertainty is due to the additional uncertainty from the particulate transmission in each profile below the altitudes used for calibrations. When a per-profile calibration is made, any bias in the transmission below is absorbed by the calibration constant. For calibration constants which use

Table 5.2: Hierarchy of calibration types and altitude regions used by FEX. Calibrations constants are taken as the median over all samples and interpolated constants are obtained using a cubic spline interpolant. The 2–9 km and 5–9 km altitude regions are not used for deriving $C^L_{\lambda_0}$ and C^L_{E,N_2}, respectively. Also given is the multiplicative factor use to modify the probability P used by the spatial filter to reduce false detections.

Preference ranking	Altitude region	Type	Requirements	Spatial filter factor
1 2	5–9 km 2–9 km	per-profile	2 km of bins in profile	1
3 4	5–9 km 2–9 km	interpolated	gap smaller than 3 hours in per-profile constants	1
5 6	5–9 km 2–9 km	per-tweak	number of bins > 2 km × 25% of profiles in tweak period	1
7 8	5–9 km 2–9 km	per-day	number of bins > 2 km × 25% of profiles in day	10^{-5}
9	N/A	historical	N/A	10^{-5}

low channel signals, the larger amount of noise in the low channel signals results in relying more on default calibrations (used for 9–20% of profiles) and larger uncertainties for both calibrations derived per-tweak and per-profile (ranging from about 11% to 16%).

A single estimate for the low channel overlap functions are derived offline. These low channel signals are then calibrated to their respective high channel signals using $C^L_{\lambda_0}$, for the elastic channels, and $C^L_{\lambda_{N_2}}$, for the nitrogen channels which can be expressed as

$$C^L_{\lambda_{N_2}} = \frac{C_{E,N_2} C^L_{\lambda_0}}{C^L_{E,N_2}}. \tag{5.20}$$

These calibrated, overlap-corrected low channels signals are used to derive the high channel overlap functions by taking the median value of the ratio between them in each height bin. Only “good” signals where the scattering ratio is less than 2 are used. High channel overlap functions

Table 5.3: The calibration type used in each profile (percent). The relative uncertainties (in percents) are given in parentheses for the per-tweak and per-profile calibration constants. The standard deviation is determined in each per-tweak or per-profile region and the relative uncertainties are added in quadrature to obtain the uncertainties given in this table. The frequency of default calibrations includes the use of either per-day or historical calibrations.

	Per-tweak	Per-profile	Interpolated	Default
C_{E,N_2}	4 (5.5)	80 (5.5)	14	2
C_E	4 (15.7)	77 (4.6)	17	2
C^L_{E,N_2}	29 (12.1)	47 (11.3)	15	9
$C^L_{\lambda_0}$	10 (15.6)	43 (13.7)	27	20

are determined per-tweak period for each height bin where suitable signals exists in at least 10% of the profiles. Per-day values are used for height bins failing to meet this requirement. When per-days values cannot be used, a historical database is used to determine the mean overlap function from the previous 7 days. Note since separate polarization components are not measured in the low channels, the same overlap function is used for both the high parallel and perpendicular channels.

5.3.4 Feature identification and example performance

To determine if a feature is present in the four ratios given in the previous section we must determine what we expect the ratio and its noise to be in clear-sky as illustrated in Fig. 5.1. The expected clear-sky ratio is straightforward since, after calibration, we expect a scattering ratio of 1 and a depolarization of 0.4% (see Appendix A). For the clear-sky noise in each of the ratios, the rules of error propagation (Bevington and Robinson, 2002) need to be applied. The ratios in Eqs. (5.13), (5.15), (5.16) and (5.18) follow the general form

$$r(z) = A(z)\frac{S_1(z) + S_2(z)}{S_3(z)} \tag{5.21}$$

where $S_i(z)$ represents the signal in channel i needed to form the various ratios (i.e. $S_{\lambda_0,\perp}$, $S_{\lambda_0,\|}$, $S^L_{\lambda_0}$, $S_{\lambda_{N_2}}$ and $S^L_{\lambda_{N_2}}$) and A(z) contains all other terms which are assumed to have negligible noise. By propagation of uncertainty, the noise in Eq. (5.21) is

$$\sigma_r(z) = r(z)\sqrt{\frac{\sigma^2_{S_1}(z) + \sigma^2_{S_2}(z)}{[S_1(z) + S_2(z)]^2} + \frac{\sigma^2_{S_3}(z)}{S^2_3(z)}}. \tag{5.22}$$

Therefore, to determine $\sigma_r(z)$, the expected number of photon counts $S_i(z)$ and the expected noise in each channel $\sigma_{S_i}(z)$ due to molecular scattering is needed. The expected number of photon counts $S_i(z)$ are calculated from each channel's respective lidar equation (Eqs. (5.6) and (5.9)). The product of all constants needed for each channel's lidar equation (i.e. ν, w_{N_2}, $d\sigma/d\Omega_\pi$) can be determined from the previously determined calibration constants (C_{E,N_2}, C^L_{E,N_2}, C_E, C_{L,λ_0}). Then the expected noise in each channel is determined by

$$\sigma_{S_i}(z) = \sqrt{\sigma^2_{B,i} + [S_i(z) + B_i]}, \tag{5.23}$$

where $\sigma_{B,i}$ is the background noise measured by the RL (Eq. (5.3)) and $\sqrt{S_i(z) + B_i}$ is the expected shot noise for a purely molecular signal. A threshold profile is then defined for each ratio

$$T(z) = r(z) + \sigma_r(z). \tag{5.24}$$

Portions of the ratio profiles which exceed the threshold profile $T(z)$ are identified as features—that is values greater than one standard deviation from the expected clear-sky ratio are considered to potentially contain a feature.

An example application of these threshold profiles for SR_E and δ is given in Fig. 5.4a and Fig. 5.4b, respectively, for the profile at 19:58:00 UTC in Fig. 5.2. For SR_E, the need for an accurate estimate of particulate extinction can be seen by comparing the initial profile of SR_E (gray line) with the final profile of SR_E (black line). In the initial profile, where no extinction estimate is available, the value of SR_E falls well below the expected clear-sky value of 1 once the cirrus layer above 10 km is encountered. As indicated by the color bar in Fig. 5.4a this causes portions of the cirrus layers to go undetected since SR_E falls below the threshold profile (dashed blue). By the final iteration, when an extinction estimate exists, SR_E doesn't rapidly decrease above 10km and the full extent of the cirrus layer is detected. Particulate extinction also impacts the threshold itself which is particularly apparent in Fig. 5.4b. The value of δ

remains unchanged from the initial to final iterations since it doesn't depend on extinction. Above ∼16 km, δ exceeds the initial threshold (dashed blue) at many altitudes although it is apparent that this is just noise. The threshold on the final iteration (solid blue) increases relative to the initial threshold above the cirrus layer base at 10 km due to the influence of extinction. This final iteration is more accurate since above ∼16 km the threshold follows the envelope of the noise well.

The need for an iterative process is illustrated by the initial poor calibration for SR_E in Fig. 5.4a. Examining the clear-sky portion of the profile below 10 km one can see that the initial profile of SR_E is biased high (by about 5%), causing a large portion of the profile in the region to be identified as containing a feature. By the final iteration the calibration of SR_E is improved and much of the falsely-detected features are gone. However on the final iteration there still exists portions of the SR_E profile exceeding the threshold which are obviously just excursions above the threshold due to noise. This is expected since, if the noise is assumed to be Gaussian distributed, there is up to a ∼16% probability that a measured ratio will be above a one standard deviation threshold solely due to noise and is therefore a false detection.

To reduce the rate of false detections the overlap between the expected molecular signal and measured signal, i.e. the purple regions in Fig. 5.1, is used. In establishing the threshold profile, the expected ratio and noise in a molecular signal has already been determined (Eq. (5.21) and (5.22)). The noise in the measured ratio is calculated by propagation of uncertainty similar to that given in Eq. (5.22) except that the measured signal is used in place of the expected molecular signal. Assuming the noise is Gaussian distributed, the overlap probability can then be determined

$$P_o(z) = \frac{1}{\sqrt{2\pi}} \int_{-\infty}^{+\infty} \min \left\{ \frac{\exp\left[-\frac{[x-R_M(z)]^2}{2\sigma_{R_M}^2(z)}\right]}{\sigma_{R_M}(z)} ; \ \frac{\exp\left[-\frac{[x-R_S(z)]^2}{2\sigma_{R_S}^2(z)}\right]}{\sigma_{R_S}(z)} \right\} dx \qquad (5.25)$$

where R_M and σ_{R_M} are the expected clear-sky ratio and estimated noise associated with it, respectively, R_S is the measured ratio, σ_{R_S} is the noise in the measured ratio and min indicates using the minimum value of the two probability density functions. $P_o(z)$ is used to construct a spatial filter to reduce the amount of false detections. We expect feature occurrence to be highly spatially correlated over a 90 m by 6 minute window (3 range bins by 3 time bins) centered on the feature bin. Assuming the noise is independent in each range and time bin, the overlap probability in this window is

$$P = \prod_{i=1}^{9} P_o(i). \tag{5.26}$$

If a true feature is present we expect the surrounding bins in this box to also contain a feature and therefore the probability P in this 90 m by 6 min box should be low. For pixels identified as features, if $P > 10^{-4}$ then the pixel is changed to clear-sky. This threshold is lowered to $P > 10^{-8}$ for bins below the altitude where complete overlap is achieved in order to compensate for potential biases in the overlap functions. These initial values of P are also modified depending of the type of calibration performed by the multiplicative factors given in Table 5.2. P is also decreased by an addition factor of 10^5 for high channel bins which use a historical overlap function.

After the application of the spatial filter to each of the four masks separately, the masks are then further checked for false detections by comparing with each other. The SR_E mask is most likely to be troublesome since its accuracy depends strongly on the ability to correctly determine the overlap function and particulate extinction. In addition, biases may exist in the depolarization ratio at lower altitudes since separate overlap functions are not determined for the high parallel and perpendicular elastic channels. To catch any potential false positives in the SR_E and δ masks, regions of high-confidence clear-sky are identified using the SR_{E,N_2} and SR^L_{E,N_2} masks. Pixels where the low nitrogen channel SNR is greater than 10 and the SR^L_{E,N_2} mask is clear are considered to be high-confidence clear-sky. Where the low nitrogen channel SNR is less than 10, the SR_{E,N_2} mask is used with high-confidence clear-sky being defined as pixels where the SR_{E,N_2} mask is clear and the high nitrogen channel SNR is greater than 10. Any features that occur in the δ mask below 1 km, or at any altitude in the SR_E mask in these regions of high-confidence clear-sky are considered false detections and are removed.

A final check for false detections is made when a per-day or historical calibration constant is used for a profile. In these cases, it is possible for the calibration constant to contain a significant bias. Therefore, when a default calibration constant is used for a ratio, at least one other ratio must also detect the feature. Otherwise the feature is remove from the mask.

The identification of false detections is illustrated in the example profiles in Fig 5.4 where the color bar indicates when the ratio is above the threshold value (blue or yellow) and when the algorithm has identified a false detection (yellow). Small excursions above the threshold due to noise, like those seen in the depolarization profile (Fig. 5.4b), are typically identified by the spatial filter. More egregious errors can be caused by a poor calibration as seen in the initial profile of SR_E in Fig. 5.4a below 10 km. Since the noise is expected to be small at these altitudes, as indicated by how close the threshold is to one, this calibration bias causes SR_E to exceed the threshold by a large enough amount that the spatial filter cannot identify these as false detections. This demonstrates the importance of the additional checks made to the feature mask which serves to both improve the accuracy of FEX and reduce the number of iterations needed to converge to a final feature mask. In this case the SR_{E,N_2} mask identifies this region from 2–10 km as clear-sky so the SR_E features in Fig. 5.4a are considered false detections. On the algorithm's next iteration, this clear-sky region is then used to derive a SR_E calibration constant and correct the initial bias.

Figure 5.5 shows the feature mask after the final iteration but before (Fig. 5.5a) and after (Fig. 5.5b) removing false detections using the four ratios given in Fig. 5.2. Even after achieving the best possible calibration constants, overlap functions and extinction estimates, numerous false detections exist in Fig. 5.5a which are effectively identified and removed using the logic outlined in this section resulting in the final mask in Fig. 5.5b. Comparing Fig. 5.5b to Fig. 5.2 demonstrates the typically good performance of the algorithm. All major features are detected, including many small isolated cumulus throughout the day below 6 km, the thick and at times multi-layered cirrus from 10–17 km, the very thin cirrus layer at 17 km that exist after 21 UTC and a very weakly-scattering layer of aerosols in the boundary layer. From about 6 to 15 UTC numerous optically-thick water clouds exist which total attenuated the RL's signal, although small glimpses of the upper-level cirrus deck are still possible during this period.

A second example of FEX's feature detection is given in Fig. 5.6 for May 10, 2013 over Darwin. During this day there exists some scattered low clouds and two distinct layers of cirrus: an optically thicker layer from about 11–14 km and a very thin tropical tropopause layer (TTL) cirrus from about 15–17 km. The TTL cirrus layer is more clearly discerned using the depolarization ratio (Fig. 5.6d), i.e. the contrast between the clear-sky and in-cloud values is larger than for the scattering ratios. This is reflected in the feature mask (Fig. 5.6e) where the TTL cirrus is captured best in the depolarization mask. The ubiquitousness of the depolarization ratio to more easily detect thin cirrus is explored further in section 5.4.

The separate colors in Fig. 5.5b and 5.6e depict which combination of the four ratios identified the feature. The rainbow of color in these figures illustrates the strength of the algorithms approach in that all four mask taken together produces a more accurate feature mask than any single quantity. While care was taken by the algorithm to remove false positives, a similar effort is not made to reduce the rate of missed detections. Instead we rely on the noise characteristics and any errors in the ratios to be different enough not to cause missed detections at the same pixels. In both Fig. 5.5b and 5.6e, and in general, we find this to be the case as small gaps in the feature mask for any one ratio are typically filled by other ratio's masks. For example, this gap filling can be seen in Fig. 5.5b in the thick cirrus layer from 15–24 UTC as well in the cirrus present in Fig. 5.6e.

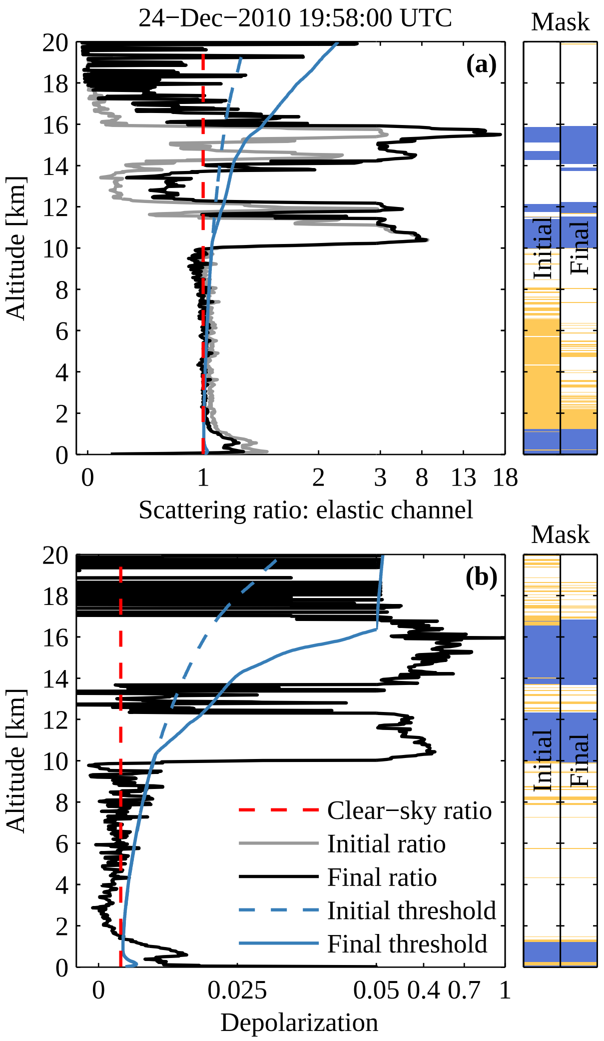

Figure 5.4: The initial threshold (dashed blue) and final threshold (solid blue) for the profile at 19:58:00 UTC in Fig. 5.2 for the (a) scattering ratio derived using only the elastic channel and (b) depolarization ratio. For the scattering ratio derived using only the elastic channel, the initial profile (gray line) and final profile (black line) is given. Features identified in these ratios on the initial and final iteration are noted by the color in the bars on the right hand side of each panel— features which have been determined to be false detections are denoted by yellow and true feature denoted by blue. For reference, the expected clear-sky ratio is given as a dashed red line.

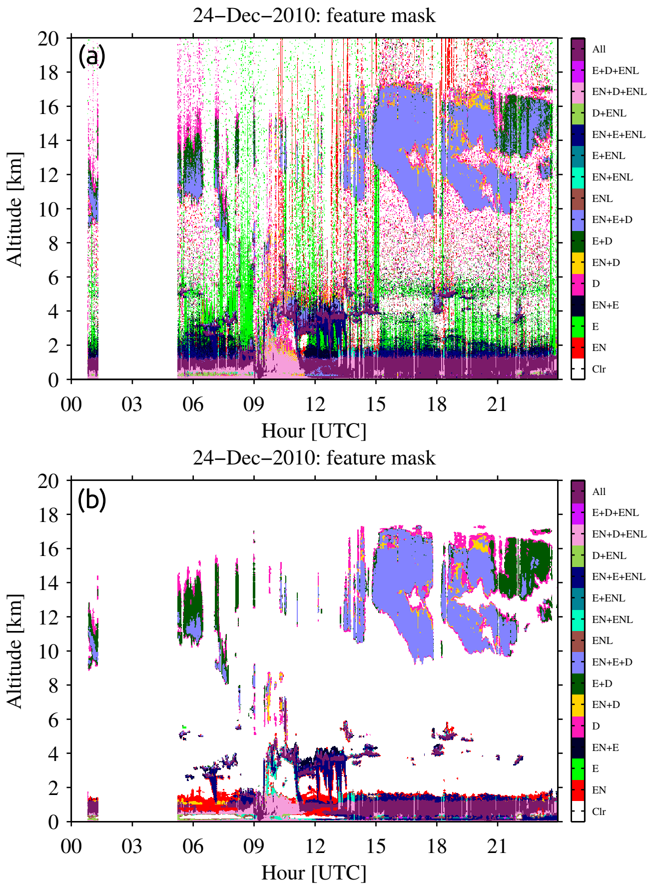

Figure 5.5: Feature mask on the final iteration of FEX for the ratios given in Fig. 5.2. Each color represents a different combination of the four ratios— scattering ratio derived using the elastic and nitrogen channels (EN), scattering ratio derived using the low elastic and nitrogen channels (ENL), scattering ratio derived using only the elastic channel (E), and depolarization ratio (D)— which detected the feature. Panel (a) shows the feature mask before any attempt was made to remove false detections. Panel (b) gives the final mask, which has had false detections removed.

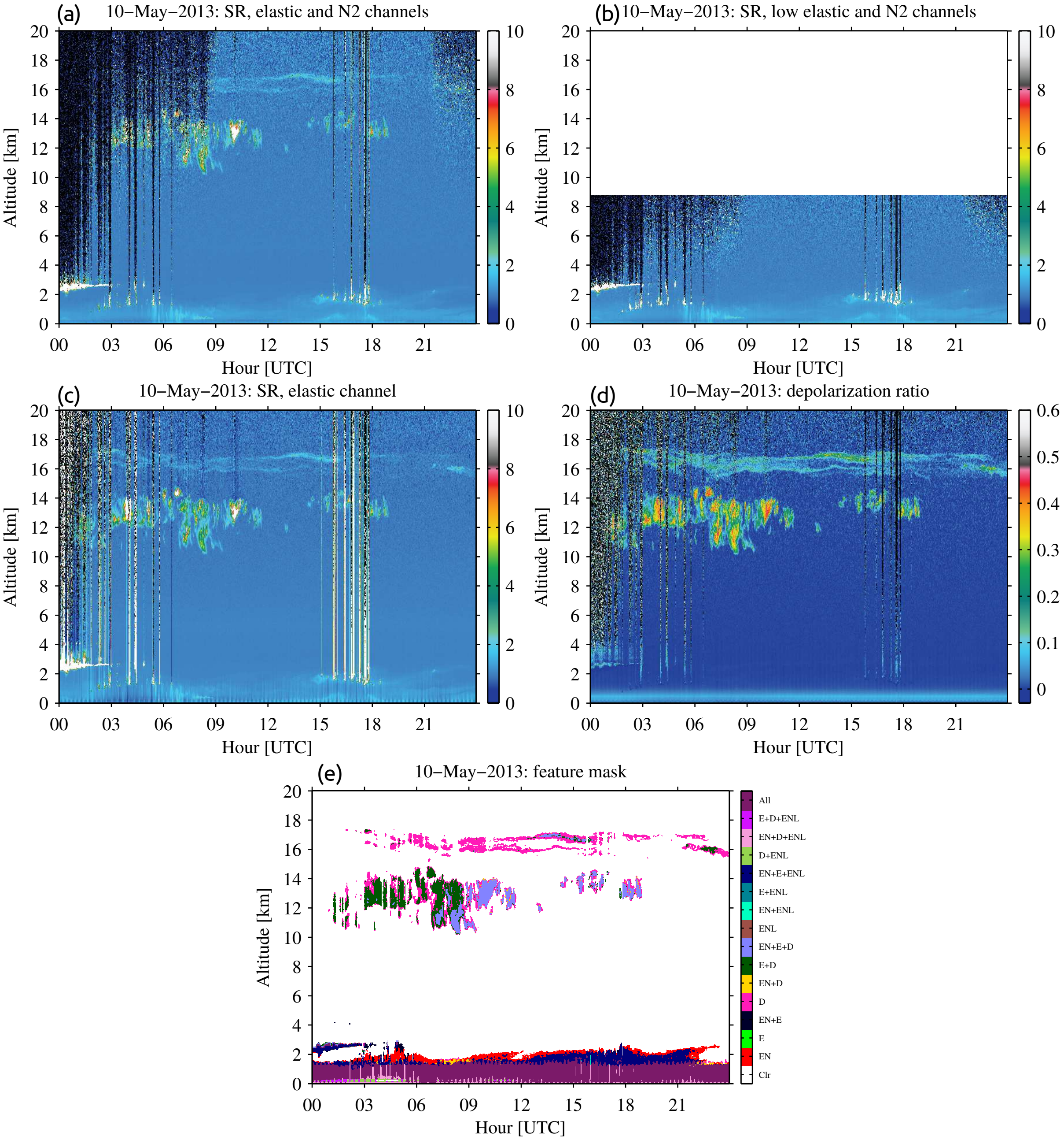

Figure 5.6: (a) Scattering ratio derived using the elastic and nitrogen channels, (b) scattering ratio derived using the low elastic and nitrogen channels, (c) scattering ratio derived using only the elastic channel, and (d) depolarization ratio after the final iteration of FEX for May 10, 2013 at Darwin. (e) Feature mask where each color represents a different combination of the four ratios which detected the feature: scattering ratio derived using the elastic and nitrogen channels (EN), scattering ratio derived using the low elastic and nitrogen channels (ENL), scattering ratio derived using only the elastic channel (E), and depolarization ratio (D).

5.4 Feature discrimination

Figure 5.7 shows the cloud occurrence profile obtained from FEX for December 2010 through December 2013 at Darwin for daytime (a) and nighttime (b) profiles. The overall cloud occurrence profile (gray line) are separated into the occurrence of clouds in each ratio: the scattering ratios from the low elastic and nitrogen channels (red line), from the elastic and nitrogen channels (green line), from only the elastic channel (blue line), and depolarization ratio (brown line). Note that a similar analysis of aerosol occurrence profiles was also performed, but is not given here since the mean occurrence profiles for all four ratios are more similar and don't show any large diurnal variations.

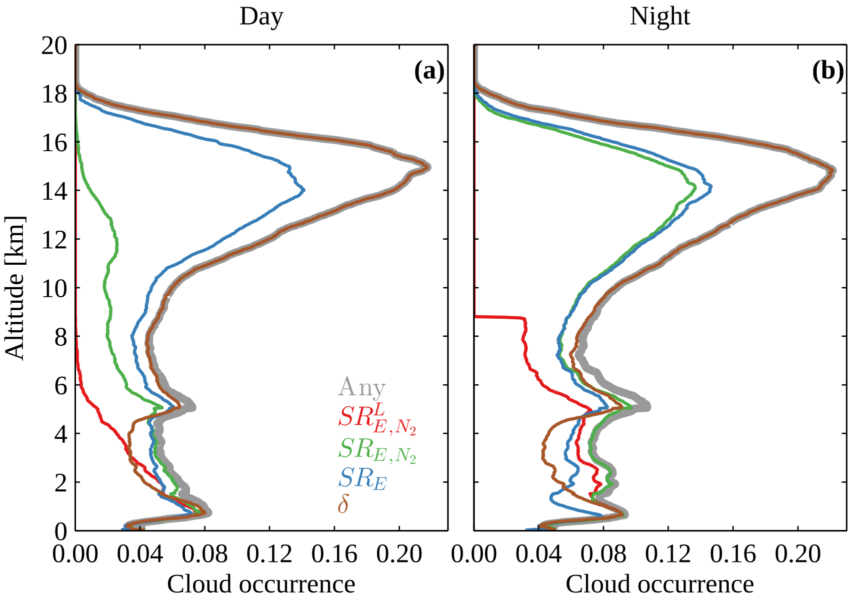

Figure 5.7: The (a) daytime and (b) nighttime cloud occurrence profiles for cloud detected by any ratio (gray), the scattering ratio derived using the low elastic and nitrogen channels (red), the scattering ratio derived using the elastic and nitrogen channels (green), the scattering ratio derived using only the elastic channel (blue), and the depolarization ratio (brown) at Darwin from December 2010 through December 2013.

Distinct diurnal differences can be seen in the scattering ratios derived using both the elastic and nitrogen channels which detect significantly less clouds during the daytime. Most altitudes also have less cloud during the daytime in the SR_E and δ mask, although the diurnal difference is much smaller. Below about 8 km, no single ratio quite matches the total occurrence of clouds; an indication that a better estimate of the mean occurrence of clouds is obtained by the use of all four ratios. Above about 8 km, any cloud present is almost always detected by the depolarization ratio method. The SR_E mask is the second most sensitive method at these higher altitudes, but consistently detects fewer clouds than the depolarization. Since both of these ratios are constructed from elastic channel signals one would expect the amount of noise, and perhaps the amount of cloud detected, to be similar. SR_E may detect less clouds since we are more aggressive at removing potential false detections in its mask. For better insight into this difference, and the diurnal variations in Fig. 5.7, the ability of FEX to discriminate a feature from a clear-sky signal is examined in more detail. That is, we seek to quantify how the distribution thresholds at each altitude differs from the distribution of the in-feature values of the ratios themselves.

Figure 5.8 shows the median thresholds (red) and median in-feature (blue) ratios at Darwin from December 2010 through December 2013. The shaded region encompasses the 5^{th} to 95^{th} percentile of the distribution of thresholds and in-feature ratios at each altitude. The top and bottom most bin of feature layers are not included in calculating these distributions since we assume these bins are some mixture of feature and clear-sky; therefore, some overlap between threshold and feature distributions is expected. Each distribution of feature ratios is determined using only points where the respective ratio detected a feature. The calculation of threshold distributions includes all points where the laser beam has not been completely attenuated—defined as a high parallel elastic channel SNR greater than 1.

The influence of the solar background can be determined from the lower bound (i.e. the 5^{th} percentile) on the threshold profiles in Fig. 5.8. The lower bound represents points where the particulate extinction at lower altitudes is small to non-existent. In addition, we expect the shot noise to be similar between day and night at a fixed altitude. Therefore diurnal differences in the lower bound of this threshold can be attributed to differences in the background signal, i.e. the solar background. Making this comparison of the lower bound on the threshold distribution in Fig. 5.8 the impact of the solar background is clearly discernible for the both SR_{E,N_2} and SR^L_{E,N_2}, which have higher thresholds during the daytime. In the SR_E threshold almost no difference exists between day and night. A slight increase can be seen in the δ threshold above about 17 km; however, there are very little clouds at those altitudes. Therefore the diurnal difference in the Fig. 5.7, where less clouds are detected during the day at most altitudes, is due to the solar background for SR_{E,N_2} and SR^{L}_{E,N_2}. However, the same smaller difference in the overall occurrence can be taken as a true physical phenomena since the solar background doesn't bias detections by either SR_E or δ. The increased cloud occurrence at night is reflected in the increase upper bound of the δ and S_E thresholds since the increased particulate extinction necessitates an increased threshold.

The higher amount of cloud occurrence in the δ mask compared to SR_E can be explained by comparing their respective threshold distributions to their feature distributions. During both day and night, the feature distribution of δ has less overlap with its threshold distribution compared to SR_E at higher altitudes. In other words, the contrast between typical in-cloud depolarization values and the clear-sky value of 0.004 is greater than typical in-cloud scattering ratios and the clear-sky value of 1. This higher contrast can be seen in the example ratios and feature mask given in Fig. 5.6, particularly for the TTL cirrus layer. In terms of median values in Fig. 5.8, the ratio of feature to threshold is typically 3-4 times larger above 8 km for δ than SR_E. This allows for an easier detection using the depolarization ratio. However, this does not imply that a feature mask constructed using only a scattering ratio cannot detect tenuous features, just that it would require more averaging to do so than needed for the depolarization ratio.

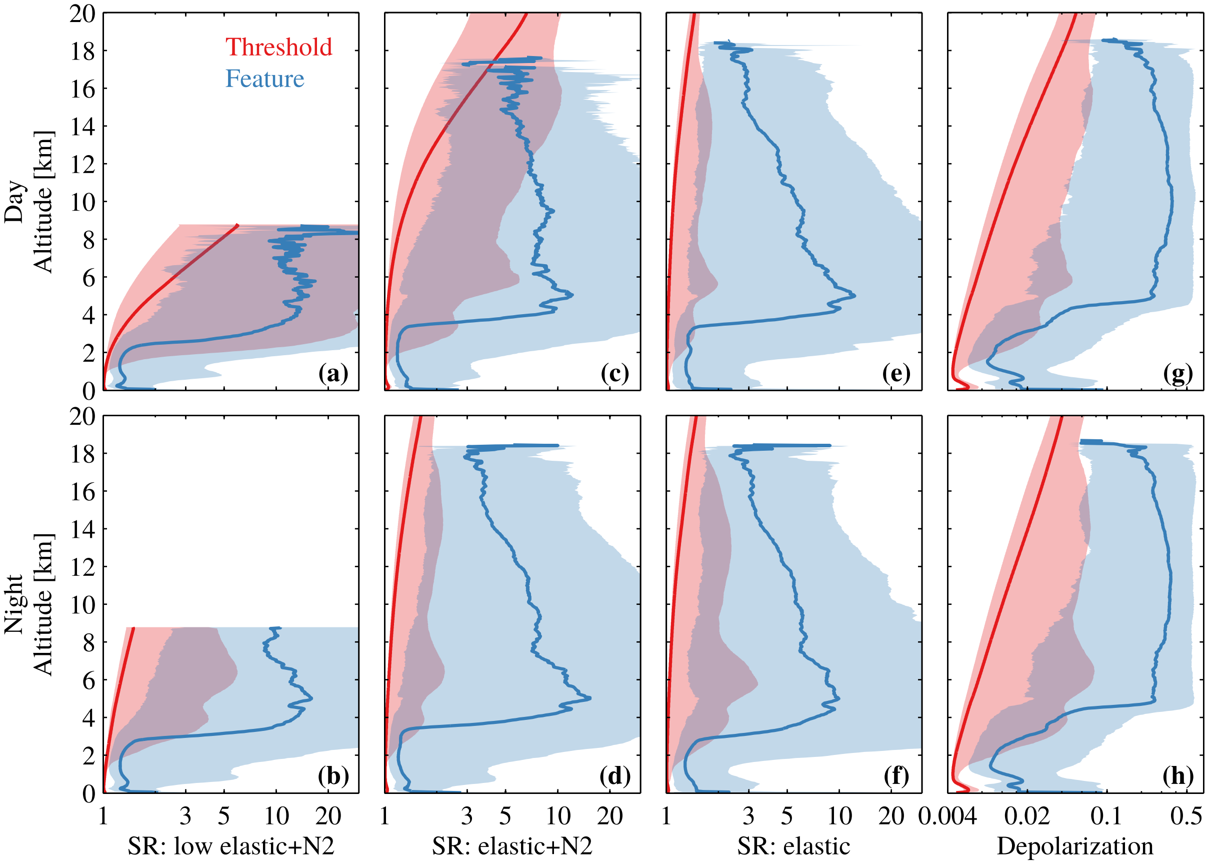

Figure 5.8: The median threshold profiles (red) for points where the laser beam has not been completely attenuated and the median ratio value (blue) for points where that ratio detected a feature. Separate panels are shown for each ratio— (a,b) the scattering ratio derived using the low elastic and nitrogen channels, (c,d) the scattering ratio derived using the elastic and nitrogen channels, (e,f) the scattering ratio derived using only the elastic channel, and (g,h) depolarization ratio — and for (top row: a,c,e,g) daytime and (bottom row: b,d,f,h) nighttime profiles. The shaded region on both the threshold and ratio profiles encompasses the 5th to 95th percentiles from their respective distributions.

5.5 Performance assessments

Assessing FEX's performance is inherently difficult since we have no underlying truth for the physical world. Therefore much of the testing during the development of this algorithm was qualitative: comparing the algorithm's mask to the features identified by an expert observer looking at an image of the data. By this measure, the algorithm performance is satisfactory with acceptably low rates of false and missed detections. More quantitative assessments of performance are made for cloud detection at the ARM Darwin site here. A tropical site like Darwin presents a challenge for a lidar due to the high levels of solar background noise and the high altitude of the tropopause, near which very optically thin cirrus frequently occur (e.g. Winker and Trepte, 1998; Wang et al., 1998; Fu et al., 2007; Dessler and Yang, 2003; Massie et al., 2010).

One of the motivations for this work was to improve the cloud mask in the current generation of ARM RL products. Figure 5.9 shows the profile of cloud occurrence profile from the ARM depolarization (DEP) product. The DEP product applies static thresholds to the depolarization and scattering ratio (calculated using the nitrogen and elastic channels) to identify cloud layers: defined as where depolarization is greater than 0.05 or the scattering ratio is greater than 1.5. The comparison of the cloud occurrence profile from the DEP product to FEX is given in Fig. 5.9. While reasonable agreement exists below 5 km, FEX detects more clouds at high altitudes. The increased detection is most striking for altitudes above 12 km where up to twice as many clouds are detected. A visual comparison of the two cloud masks revealed that the DEP product has not only missed detections but also have numerous false positives. This is reflected in the amount of cloud that exists in the DEP product from 18–20 km, a region where we expect almost no clouds to occur. It is of no surprise that the simple static thresholds used in the original ARM RL cloud mask are outperformed by our more rigorous threshold algorithm. Since there is such a stark difference in complexity between these two approaches, we seek to provide better assessments of our algorithm's performance by comparing to other lidar observations in the following sections.

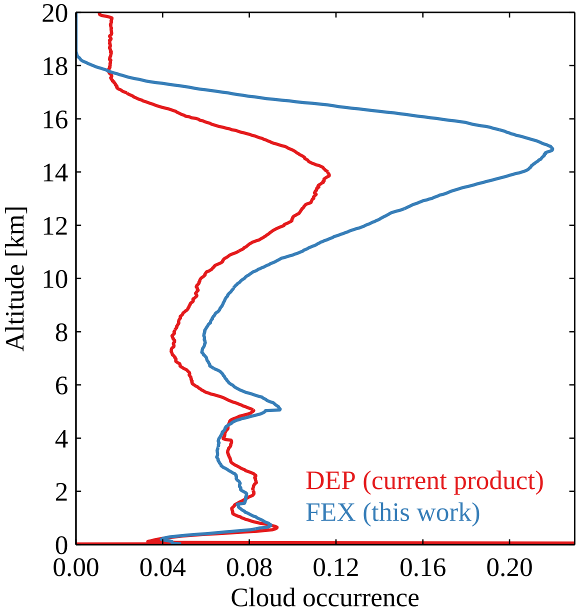

Figure 5.9: The cloud occurrence profile from the ARM DEP product (red) and from the new FEX algorithm (blue) described in this work at Darwin from December 2010 through December 2013.

5.5.1 MPL comparison

The ARM Darwin site is also equipped with a micropulse lidar (MPL; Campbell et al., 2002; Coulter, 2012) which transmits $6-8$ μJ of 532 nm light with a PRF of 2500 Hz. Data is averaged to 2 min and 30 m, the same averaging used for the RL. The cloud mask of Wang and Sassen (2001) is applied to the backscattered signal. The Wang and Sassen (2001) algorithm is a slope method which examines the relative change in the returned signal power for strong negative and positive slopes which occur in the presence of clouds. The Wang and Sassen (2001) algorithm has been widely used in the analysis of MPL signals (e.g. Comstock et al., 2002; Luo et al., 2008; Thorsen et al., 2011; Comstock et al., 2013; Riihimaki et al., 2012).

We compare the MPL cloud mask (Wang and Sassen, 2001) to that of FEX at Darwin from December 2010 through August 2011, a period when both instruments were operating. While the RL was not operating for a significant portion of this period, we are still left with over 80000 coincident profiles to compare. Figure 5.10a compares the cloud occurrence profiles during this period. Good agreement exists from about 5 to 10 km. Below 5 km, the MPL detects more clouds at some altitudes and less at others than the RL. Below 5 km differences can be due to several things beyond the methods used for cloud detection. Like the RL high channels, the MPL doesn't achieve complete overlap until 5 km, so uncertainties in overlap functions may contribute to differences in Fig. 5.10a. The MPL data has a single generic overlap correction applied to all the data and, because of increased uncertainty in this generic correction at lower altitudes, no cloud mask is determined below 1 km. In addition, the different methods used to identify rain/virga may contribute to discrepancies at lower altitudes. The mask of Wang and Sassen (2001) separates the base of rain/virga from the cloud base by comparing the increase in slope between the two. In FEX, the identification of rain is based on the retrieved lidar ratio (Thorsen and Fu, 2014, Chapter 6). Above 10 km, the MPL detects significantly less clouds due to its larger amount of noise (Thorsen et al., 2013b, Chapter 4).

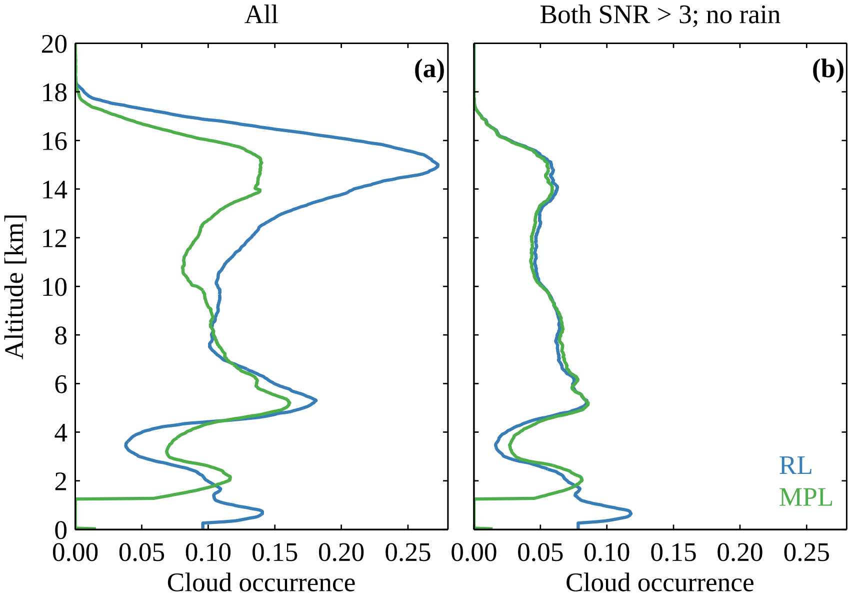

Figure 5.10: The cloud occurrence profile from the MPL cloud mask (Wang and Sassen, 2001) (green) and RL-FEX cloud mask (blue) from December 2010 through August 2011 for (a) all pixels and (b) only pixels where both the MPL and RL SNR is greater than 3 in profiles where no rain was detected.

In order to provide a more direct comparison of the detection algorithms themselves, only profiles without rain (as determined by FEX) and only pixels where both the MPL and RL SNR is greater than 3 are used to calculate the cloud occurrence profile in Fig. 5.10b. The MPL SNR is calculated in the same way as is done for the RL (Eq. 5.19 and section 5.3.1) except that background noise is inferred from high altitude (45–55 km) signals where the contribution from molecular scattering is negligible. About 60% of RL pixels where the SNR is greater than 3 also have the MPL SNR greater than 3. In this more limited comparison (Fig. 5.10b) the MPL still lacks clouds below 2 km, an indication that its cloud mask is adversely effected by the uncertainty in its overlap function. However, above 2 km the MPL and RL agree very well. To ensure that this agreement is not due to some fortuitous cancellation of errors, the error matrix for this comparison is shown in Table 5.4 for pixels above 2 km. When the SNR for both instruments is greater than 3, the two algorithms show good agreement with the MPL detecting cloud for only ~2% of the pixels label by the RL as clear. The opposite error, when RL pixels determined to be cloudy are marked as clear by the MPL, has a slightly larger error rate of ~9%. This is likely an indication of the higher SNR required for a slope method versus a threshold method since taking the slope increases the signal noise. If we make the same comparison for a higher MPL SNR, e.g. compare the subset of pixels where the MPL SNR is greater than 6 and the RL SNR is greater than 3, this error is reduced to 7%. Overall we find reasonable agreement between the RL-FEX and Wang and Sassen (2001)'s MPL cloud mask when both instruments have sufficient SNR.

Table 5.4: Comparison between RL-FEX and MPL cloud detection (which uses the algorithm of Wang and Sassen (2001)) at Darwin from December 2010 through August 2011. Only the subset of pixels where both the RL and MPL SNR is greater than 3 are compared. Percentages are given relative to the detection of RL-FEX.

	MPL Clear	MPL Cloud
RL Clear	98.1	1.9
RL Cloud	9.2	90.8

5.5.2 CALIPSO comparison

The CALIPSO satellite (Winker et al., 2009, 2010) was launched in April 2006 into a sun-synchronous orbit providing near global observations at approximately 0130 and 1330 (local time) for a fixed point. We use the CALIPSO L2 v3 5 km vertical feature mask (VFM) product (Vaughan et al., 2009) which, like FEX, is based on a threshold method. Since CALIPSO and the ARM RL don't make coincident measurement only a statistical comparison can be made. CALIPSO VFM profiles that fall within 200 km of the Darwin site are compared to RL profiles from December 2010 through December 2013. The RL data are limited to times within ±2 hours of CALIPSO overpasses. In order to fairly compare a space-borne platform with a ground-based one, the profiles are further limited to those where the lidar beam passes through all layers unattenuated, i.e. transparent profiles. For CALIPSO, transparent profiles are defined as those with the presence of a signal return from the surface. For the RL, transparent profiles are defined as those where the high elastic channel SNR is greater than 1 at 18.5 km.

Figure 5.11 shows the cloud occurrence in transparent profiles from the RL (blue line) and CALIPSO (red line). Large differences exist with the RL detecting more low clouds and CALIPSO more high clouds. CALIPSO must perform significantly more averaging than a ground-based lidar to obtain a SNR suitable for feature detection. The occurrence of clouds is dependent on averaging since more averaging allows for smaller cloud optical thicknesses to be detected. For example, given in Fig. 5.12 is the FEX cloud mask for the ratios in Fig. 5.6 but for 9 min of averaging instead of 2 min. With 9 min of averaging, more of the thin TTL cirrus from 16–18 km can be detected. However, larger amounts of averaging can smear clouds, artificially increasing the reported cloud occurrence. This can be seen in the lower layer of cirrus (11–14 km) in Fig. 5.12. Small gaps that appear in this layer at 2 min of averaging (Fig. 5.6e) are smeared-out at 9 min of averaging (Fig. 5.12). The opposite effect, a decrease in the reported cloud occurrence, can occur for clouds with small spatial scales as larger amounts of averaging can mix in clear-sky signals causing the cloud to go undetected. This effect can been seen for the two small cumulus clouds at 4 km from 0-3 UTC in Fig. 5.6 which don't exist in the mask when 9 min of averaging is used in Fig. 5.12. Furthermore, our comparison is composed of transparent profiles which also depends on averaging. Larger amounts of averaging increases the likelihood that enough laser shots penetrate through the feature thereby reducing the occurrence of complete attenuation. To avoid all these complications, we create a RL-FEX dataset with a temporal and height average which is approximately equal to CALIPSO's spatial average.

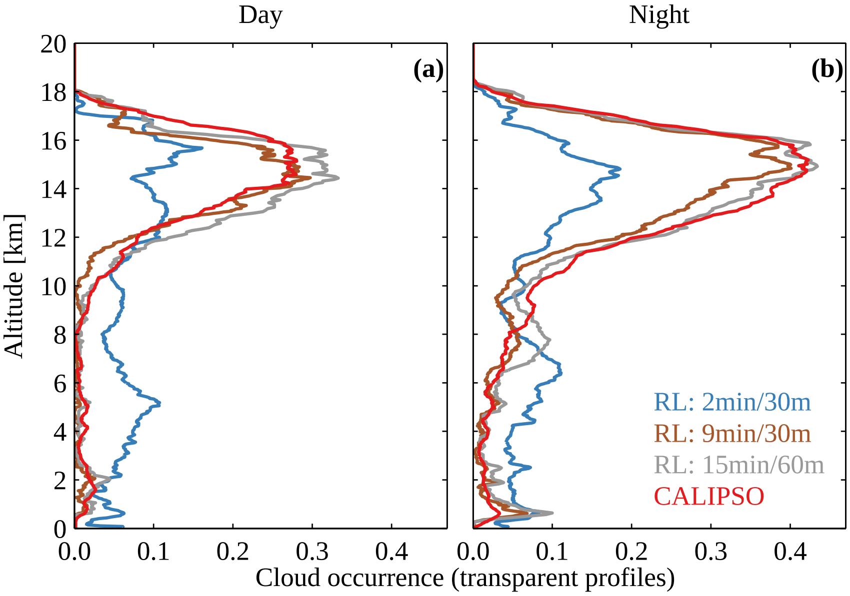

Figure 5.11: The cloud occurrence in transparent profiles from the RL at 2 min and 30 m of averaging (blue) and from the CALIPSO VFM product (red). The profile from the RL data averaged to 9 min and 30 m, which is approximately equivalent to CALIPSO's averaging below 8.2 km, is given in brown. The profile from the RL data averaged to 15 min and 60 m, which is approximately equivalent to CALIPSO's averaging above 8.2 km, is given in gray. Profiles are shown separately for the (a) daytime and (b) nighttime observations. This comparison includes CALIPSO profiles that fall within 200 km of the Darwin site from December 2010 through December 2013. The RL data are limited to times within ±2 hours of CALIPSO overpasses.

The mean amount of horizontal averaging used by CALIPSO is determined from the reported amounts for each cloudy pixel in the VFM product. Since advection determines the amount of cloud which passes through the RL FOV, the mean wind speed is obtain from the collocated radiosonde profiles at Darwin. Dividing the profile of mean horizontal averaging by the profile of mean wind speed gives the equivalent temporal average for the RL: a mean of 9 min for altitudes less than 8.2 km and 15 min for those above. Since above 8.2 km CALIPSO's vertical averaging increases to 60 m, the same vertical averaging is used for the RL in the 15 min data.

Figure 5.11 shows the RL cloud occurrence profile for 9 min and 30 m of averaging (brown line) and 15 min and 60 m of averaging (gray line). For nighttime profiles in Fig. 5.11b, nearly all the difference between the 2min/30min RL and CALIPSO profiles can be attributed to averaging since the 15min/60m RL profile agrees well with CALIPSO above 8.2 km and the 9min/30 RL

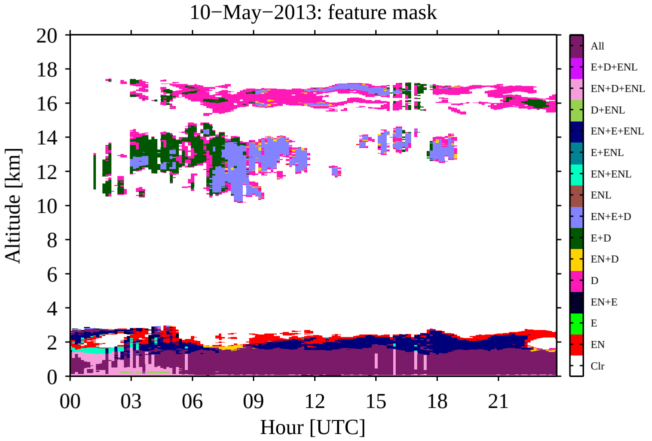

Figure 5.12: FEX feature mask for May 10, 2013 at Darwin when 9 min and 30 m of averaging is performed. Each color represents a different combination of the four ratios which detected the feature: scattering ratio derived using the elastic and nitrogen channels (EN), scattering ratio derived using the low elastic and nitrogen channels (ENL), scattering ratio derived using only the elastic channel (E), and depolarization ratio (D).

profile agrees well below. Making the same comparison for daytime profile (Fig. 5.11a), the 15min/60m RL data detection more clouds from about 11–16 km. This suggests the increased solar background may cause some thin cirrus to go undetected by CALIPSO, although this difference is not statistically significant. Overall, when approximately the same amount of averaging is used, we find good agreement between RL-FEX and the CALIPSO VFM product.

The agreement between the RL and CALIPSO in Fig. 5.11 is similar to that found by Thorsen et al. (2013b) (Chapter 4). However, unlike the current study, agreement between CALIPSO and the RL was found by Thorsen et al. (2013b) when the RL data was averaged to 2 min and 30 m. The reason for this discrepancy is that the Thorsen et al. (2013b) study applied a median filter to the depolarization ratio, which was used to identify cirrus, with a moving window of 150 m by 10 min. This filter essentially created a dataset with an effective resolution of 10 min, which we show here to be approximately equivalent to CALIPSO's horizontal averaging.

5.6 Summary

We have presented an automated method for the detection of features in ARM RL measurements which is part 1 of the Feature detection and EXtinction retrieval (FEX) algorithm. While the detection of features in FEX requires an estimate of particulate extinction, this work focused on the aspects most pertinent to feature detection. The retrieval of particulate extinction in FEX is given in part 2 on this work (Thorsen and Fu, 2014, Chapter 6). The intent is to run FEX operationally within the ARM Data Management Facility (DMF) with the output being made available to the general user community via the ARM website (http://www.arm.gov/). The feature detection approach used in FEX is to analyze multiple quantities— scattering ratios derived using elastic and nitrogen channel signals from two FOVs, the scattering ratio derived using only the elastic channel, and the total volume depolarization ratio— for the presence of features. Range-dependent detection thresholds are determined for each profile separately by calculating the expected noise in a clear-sky signal. We show that the approach of using multiple quantities provides a complementary description of the vertical and temporal extent of clouds and aerosols. Using multiple quantities also allows for additional consistency checks on the feature mask which reduces the rate of false detections and improves the efficiency of the algorithm.

The performance of FEX's feature detection is illustrated by the application of the algorithm to 3 years of ARM RL data over Darwin, Australia. The feature detection in FEX is found to be robust across the diurnal cycle as no bias exists in the elastic channel detection thresholds. Sufficiently small noise in the depolarization ratio and the strong contrast between molecular and typical in-cloud values allows for the depolarization ratio to be the most effective for the detection of thin cirrus for the ARM RL system. We also presented the improvement of FEX's cloud mask relative to the cloud mask used in the current operational ARM products. Quantitative evaluations of FEX's cloud detection were made by comparing to a collocated MPL and to observations from the CALIPSO satellite, which used independent methods for identifying clouds. RL-FEX detects more clouds than the MPL due to the RL's superior SNR. However, when the comparison is limited to when both instruments SNR was above 3 good agreement was found. Comparisons to CALIPSO also agreed well for transparent profiles when similar amounts of signal averaging are used, particularly for nighttime profiles.

Appendix

5.A Depolarization calibration

The ARM RL separates the high elastic signal into parallel and perpendicular components. To prevent saturation of the detector, an extra neutral density filter exists in the parallel channel. Therefore, to determine the total elastic signal and the depolarization, the difference in gain between the parallel and perpendicular channels must be taken into account. In addition, the accuracy of the depolarization measurements are effected by possible misalignment of the polarizing beamsplitter to that of the transmitted beam. This misalignment induces cross talk into the signal— some portion of the perpendicular signal ends up in the parallel channel and vice versa. The relationship between the observed or apparent signals and the true signals is given by (Alvarez et al., 2006)

$$S_{\parallel}^{'} = \frac{1}{G}\left(S_{\parallel}\cos^2\phi + S_{\perp}\sin^2\phi\right) \tag{5.27}$$

and

$$S_{\perp}^{'} = \left(S_{\parallel}\sin^2\phi + S_{\perp}\cos^2\phi\right) \tag{5.28}$$

where $S_{\parallel}^{'}$ and $S_{\perp}^{'}$ are the observed signals in the parallel and perpendicular channels, respectively. $S_{\parallel}$ and $S_{\perp}$ are the true parallel and perpendicular signals, respectively. The factor G represents the relative gain; that is, the reduction in signal by the extra neutral density filter in the parallel channel relative to the perpendicular channel. The angle ϕ is the misalignment angle between the transmitter and receiver polarization planes.

The relative gain G is taken as the ratio of daytime perpendicular to parallel channel background signal during the presence of optically-thick liquid water clouds. In these situations the true depolarization is 1 since multiply-scattered sunlight through the clouds will be randomly polarized and, by using the background signals, any misalignment between the transmitter and receiver polarization planes is irrelevant. Times of optically thick liquid water clouds are identified using collocated microwave radiometer (MWR) observations (Liljegren and Lesht, 1996)—

defined as times when the liquid water path exceeded 75 gm^{-2}. Multiple years of collocated RL and MWR data are used calculate a mean G offline. Given the offline estimate of G, the misalignment angle ϕ is then determined from backscattered signals in clear-sky. Forming a ratio of Eqs. (5.28) to (5.27) and solving for ϕ gives

$$\phi = \arctan\left(\sqrt{\frac{\delta_m G - \delta'}{\delta_m \delta' - G}}\right) \tag{5.29}$$

where δ' is the observed depolarization, i.e. $\delta' = S'_\perp / S'_\|$, and δ_m is the true depolarization due to molecular scattering, i.e. $\delta_m = S_\perp / S_\|$. The true molecular depolarization is calculated using the model of Behrendt and Nakamura (2002) and for the RL's interference filter's bandpass we find a value $\delta_m = 0.004$. Since we need to identify clear-sky signals, the calculation of ϕ using Eq. (5.29) is performed as an addition step in the iterative portion of FEX using the same tactics as is done for the other calibration constants (section 5.3.3). The breakdown of when ϕ is determined per-tweak, per-profile, interpolated or a default value is used is given in Table A1 along with the associated uncertainties which are about 4%.

Note that in this paper the calculation of signal noise detailed in section 5.3.1 is performed using the observed signals (i.e. $S'_\|$ and $S'_\perp$). However, for the purpose of feature detection the true signals are used (i.e. $S_\|$ and $S_\perp$). Therefore in practice, propagation of uncertainty is applied to Eqs. (5.27) and (5.28) to determine the noise in these true signals.

Table 5.5: Same as Table 5.3, but for the depolarization misalignment angle.

	Per-tweak	Per-profile	Interpolated	Default
ϕ	4 (3.7)	81 (4.1)	13	2

Chapter 6

AUTOMATED RETRIEVAL OF CLOUD AND AEROSOL PROPERTIES FROM THE ARM RAMAN LIDAR, PART 2: EXTINCTION

The contents of this chapter are reproduced from a manuscript currently in review: Thorsen, T. J., and Q. Fu, 2014, J. Atmos. Oceanic Technol. The Introduction and Summary sections have been revised from their original form and minor modifications have been made throughout the text.

6.1 Introduction

Lidars have the capability to provide unparalleled range-resolved observations of particulate extinction. However, lidars fundamentally measure backscattered energy, not extinction, and for widely prevalent single-channel elastic backscatter lidars (e.g. Campbell et al., 2002; Winker et al., 2010) extinction must be obtained by assuming the ratio of extinction to backscatter known as the lidar ratio (Klett, 1981; Fernald, 1984). High spectral resolution lidars (HSRL; e.g Hair et al., 2008; Grund and Eloranta, 1991) and Raman lidars (RL; e.g. Goldsmith et al., 1998; Matthais et al., 2004) are more advanced lidars that can intrinsically separate signals from molecules and particulates allowing for directly retrieved particulate backscatter and extinction coefficients. These advanced lidars also provide observations of the lidar ratio which is an indicator of the target's microphysical properties (e.g. Burton et al., 2014) and helps improve retrievals for elastic-backscatter lidars.

The work here centers around developing an automated extinction retrieval algorithm for the Atmospheric Radiation Measurement (ARM; Ackerman and Stokes, 2003) program's Raman lidars (Goldsmith et al., 1998) which operate at the ARM southern Great Plains (SGP) site near Lamont, Oklahoma and the Darwin, Australia Tropical Western Pacific (TWP) site. As discussed in Chapter 5, the ARM RL was originally designed to measure water vapor and aerosol properties (Turner et al., 2002). Therefore the main goal of this series of papers is to develop a new automated algorithm for Feature detection and EXtinction retrieval (FEX) in order to fully realize the potential of the ARM RL. The FEX algorithm objectively identifies features (i.e. clouds and aerosols) and retrieves their extinction and backscatter profiles over the full extent of the troposphere. Complete details of feature detection is given in part 1 of this series of papers (Thorsen et al., 2014, Chapter 5), while part 2 presented here focuses on the retrieval of particulate extinction. The intent is to run FEX operationally within the ARM Data Management Facility (DMF) with the output being made available to the general user community through the ARM website (http://www.arm.gov/).

A description of the ARM RL system and a review of methods for inverting the elastic and Raman lidar equations are given in sections 6.2 and 6.3, respectively. The retrieval methodology is given in section 6.4 with extinction being retrieved by FEX directly using the Raman method in addition to other methods developed for elastic backscatter lidars to obtain the best possible extinction estimate for all detected features. In support of an accurate extinction retrieval, a classification of feature type is made and multiple scattering effects are explicitly considered. In section 6.5 multiple years of data at both the SGP and TWP sites are analyzed. Presented is the frequency of feature types at these sites and the frequency with which different types of retrievals are performed. The need to correct for multiple scattering effects is justified *a posteriori* by presenting the errors introduced by ignoring its effects. The retrieval of aerosol optical depth is validated against collocated sun photometers. Finally, a summary is given in section 6.6.

6.2 The ARM Raman lidar

Table 5.1 describes the ARM RL and the detection channels used in this work. The basic design is given in Goldsmith et al. (1998), although the original system has since evolved through various upgrades and modifications (Ferrare et al., 2006; Newsom, 2009). The RL at the ARM SGP site has been in near-continuous operation since 1998 and in December of 2010 a second ARM RL with nearly the same design was deployed at the Darwin TWP facility. While the ARM RL contains temperature (Newsom et al., 2013) and water vapor (Turner et al., 2002) channels, only the elastic and nitrogen channels are used for this work. Backscattered returns are collected using both a narrow FOV (here after referred to as the "high channels") and wide FOV (here after referred to as the "low channels"). Throughout this paper the prefix "high" is dropped when referring to the high channel; while the prefix "low" will be included when referring to low channel signals.

6.3 Inversion of the elastic and Raman lidar equations

The lidar equation for the background-subtracted signal received in the elastic channel can be written as (Measures, 1984)

$$S_{\lambda_0}(z) = \nu_{\lambda_0}\frac{S_0}{z^2}O_{\lambda_0}(z)F_{\lambda_0}(z)\left[\beta_{m,\lambda_0}(z)+\beta_{p,\lambda_0}(z)\right]T^2_{m,\lambda_0}(0,z)T^2_{p,\lambda_0}(0,z), \tag{6.1}$$

where $S_{\lambda_0}(z)$ is the number of photons received from height z, ν_{λ_0} is the system constant incorporating all the lidar parameters which describe the characteristics of the optics and detectors, S_0 is the number of transmitted photons and $O(z)$ is the overlap function which describes overlap between the laser beam and receiver's FOV. $\beta_{m,\lambda_0}(z)$ and $\beta_{p,\lambda_0}(z)$ are the molecular and particulate backscatter coefficients, respectively. $T^2_{m,\lambda_0}(0,z)$ and $T^2_{p,\lambda_0}(0,z)$ are the transmission due to molecules and particulates which, for a zenith pointing lidar like the ARM RL, are

$$T_{m,\lambda_0}(0,z) = \exp\left[-\int_0^z \alpha_{m,\lambda_0}(z^{'})dz^{'}\right] \tag{6.2}$$

and

$$T_{p,\lambda_0}(0,z) = \exp\left[-\int_0^z \alpha_{p,\lambda_0}(z^{'})dz^{'}\right] \tag{6.3}$$

where $\alpha_{m,\lambda_0}(z)$ and $\alpha_{p,\lambda_0}(z)$ are the molecular and particulate extinction coefficients, respectively. $F_{\lambda_0}(z)$ is the multiple scattering function which describes the enhancement in the received signal caused by multiple scattering, that is

$$S_{\lambda_0}(z) = F_{\lambda_0}(z)S^1_{\lambda_0}(z) \tag{6.4}$$

where $S^1_{\lambda_0}(z)$ is single scattering signal, i.e. the received signal expected from a single scattering interaction between the transmitted photons and the atmosphere.

Numerous iterative numerical methods (e.g. Young and Vaughan, 2009; Platt, 1973) and analytical solutions (e.g. Klett, 1981; Fernald, 1984) have been developed to invert the elastic lidar equation. In this work we use solution of Fernald (1984) who showed that

$$\beta_{p,\lambda_0}(z) = \frac{S^1_{\lambda_0}(z)\exp\left\{-2\int_{z_0}^{z}\left[S_{p,\lambda_0}(z^{'}) + S_m\right]\beta_{m,\lambda_0}(z^{'})dz^{'}\right\}}{\frac{S^1_{\lambda_0}(z_0)}{\beta_{p,\lambda_0}(z_0)+\beta_{m,\lambda_0}(z_0)} - 2\int_{z_0}^{z} S_{p,\lambda_0}(z^{'})S^1_{\lambda_0}(z^{'})T(z_0,z)dz^{'}} \tag{6.5}$$

with

$$T(z_0,z) = \exp\left\{-2\int_{z_0}^{z}\left[S_p(z^{''}) + S_m\right]\beta_{m,\lambda_0}(z^{''})dz^{''}\right\} \tag{6.6}$$

where $S_p(z)$ is the lidar ratio, that is the ratio of the particulate extinction to particulate backscatter

$$S_{p,\lambda_0}(z) = \frac{\alpha_{p,\lambda_0}(z)}{\beta_{p,\lambda_0}(z)}, \tag{6.7}$$

S_m is the ratio of molecular extinction to its backscatter which from Rayleigh theory is $8\pi/3$ and z_0 is a boundary condition. The single scattering signal used here ($S^1_{\lambda_0}$) is related to the measured signal by Eq. (6.4). Equation 6.5 illustrates the problem with all solutions to the elastic lidar equation: there exists 2 unknowns, particulate extinction and backscatter, but only one equation.

This significant limitation of elastic backscatter lidars is alleviated by the use either a HSRL or a Raman lidar: both measure a signal independent of the particulate backscatter. For the signal in the Raman nitrogen channel, which only contains backscatter due to nitrogen molecules, the lidar equation can be written as

$$S_{\lambda_{N_2}}(z) = \nu_{\lambda_{N_2}}\frac{S_0}{z^2}O_{\lambda_{N_2}}(z)F_{\lambda_{N_2}}(z)\beta_{N_2,\lambda_{N_2}}(z)T_{m,\lambda_0}(0,z)T_{p,\lambda_0}(0,z)T_{m,\lambda_{N_2}}(0,z)T_{p,\lambda_{N_2}}(0,z). \tag{6.8}$$

Compared to Eq. (6.1), extra transmission terms are needed to account for the different wavelength of the return signal. Since there is no dependence on the particulate backscatter in Eq. (6.8) the particulate extinction can be explicitly solved for (Ansmann et al., 1990)

$$\alpha_{p,\lambda_0}(z) = \frac{\frac{d}{dz}\left[\ln\frac{O_{\lambda_{N_2}}(z)N(z)}{z^2S^1_{\lambda_{N_2}}(z)}\right] - \alpha_{m,\lambda_0}(z) - \alpha_{m,\lambda_{N_2}}(z)}{1 + \left(\frac{\lambda_0}{\lambda_{N_2}}\right)^{a(z)}} \tag{6.9}$$

where $N(z)$ is the number concentration of nitrogen molecules, $a(z)$ is the Angstrom exponent used to describe the wavelength dependence of the extinction. The single scattering signal is related to the measured signal by

$$S_{\lambda_{N_2}}(z) = F_{\lambda_{N_2}}(z) S^1_{\lambda_{N_2}}(z). \tag{6.10}$$

Furthermore with a RL, the particulate backscatter can be directly obtained

$$\beta_{p,\lambda_0}(z) = \left[SR_{E,N_2}(z) - 1 \right] \beta_{m,\lambda_0}(z) \tag{6.11}$$

where $SR_{E,N_2}(z)$ is a scattering ratio (Thorsen et al., 2014, Chapter 5), i.e. the ratio of total (particulate and molecular) backscattering to just molecular backscattering at λ_0, derived from both the elastic and nitrogen channels

$$\begin{aligned} SR_{E,N_2}(z) = C_{E,N_2} \frac{O_{\lambda_{N_2}}(z)}{O_{\lambda_0}(z)} \frac{T_{m,\lambda_{N_2}}(0,z)}{T_{m,\lambda_0}(0,z)} \frac{S^1_{\lambda_0}(z)}{S^1_{\lambda_{N_2}}(z)} \\ \times \exp\left\{ \int_0^z \alpha_{p,\lambda_0}(z^{'}) \left[1 - \left(\frac{\lambda_0}{\lambda_{N_2}} \right)^{a(z^{'})} \right] dz^{'} \right\} \end{aligned} \tag{6.12}$$

which is obtained by combining Eqs. 6.1 and 6.8 (Cooney et al., 1969; Melfi, 1972; Thorsen et al., 2014) where C_{E,N_2} is a calibration constant. Via Eqs. (6.9) and (6.11) a Raman lidar can directly retrieve profiles of the particulate extinction and backscatter— we refer to this as the Raman method. However, the application of the Raman method is limited by the relatively weak strength of Raman scattering relative to elastic scattering. Noise is particularly an issue for the extinction retrieval since in Eq. (6.9) the slope of the signal is needed, which greatly amplifies the noise.

Using only the elastic channel signal, the layer-average lidar ratio can be determined using the transmission-loss method (e.g. Spinhirne et al., 1996; Comstock and Sassen, 2001; Chen et al., 2002; Young, 1995). By taking the ratio of the elastic signal (Eq. (6.1)) in clear-sky above a feature (at $z = z_t$) to that below it (at $z = z_b$) the optical depth of the layer can be solved for

$$\tau_\ell(z_b, z_t) = \frac{1}{2}\ln\left[\frac{S_{\lambda_0}(z_b)z_b^2 O_{\lambda_0}(z_t)\beta_{m,\lambda_0}(z_t)T^2_{m,\lambda_0}(0, z_t)}{S_{\lambda_0}(z_t)z_t^2 O_{\lambda_0}(z_b)\beta_{m,\lambda_0}(z_b)T^2_{m,\lambda_0}(0, z_b)}\right] \tag{6.13}$$

where the optical depth is the integral of the extinction coefficients which is

$$\tau_\ell(z_b, z_t) = \bar{S}_{p,\lambda_0}\int_{z_b}^{z_t}\beta_{p,\lambda_0}(z^{'})dz^{'}. \tag{6.14}$$

By iterating, Eqs. (6.5) and (6.14) can be used to solve for a layer-averaged lidar ratio. In situations when the lidar ratio cannot be determined using Eq. (6.13) as a constraint, retrievals using only the elastic channel signal must assume a lidar ratio profile. In these situations FEX attempts to infer the lidar ratios from other regions where a direct-retrieval was made otherwise climatological values are used.

The retrieval of particulate extinction and backscatter in this work is performed for both FOVs of the ARM RL. At the expense of increased noise, using the low channel signals has the benefit of achieving complete overlap sooner (i.e. at a lower altitude above the system), allowing for a more accurate retrievals in the near-field than the high channels. For the ARM RL the high channels achieve complete overlap by 5 km and the low channels by 800 m (Goldsmith et al., 1998). Quantities retrieved from low channel signals are denoted by a superscript L, e.g. S^L_{p,λ_0}, β^L_{p,λ_0}, α^L_{p,λ_0}, while those retrieved from high channel signals have no superscript.

6.4 Retrieval algorithm

Part 1 in this series (Thorsen et al., 2014, Chapter 5) describes in full detail the initial processing, determining calibration constants and the detection of features. In summary, photon counting profiles from the MERGE product (Newsom et al., 2009) are accumulated to their desired time and height bins— here we use 2 min and 30 m. Random signal uncertainty in each accumulated photon counting profile is also calculated along with the signal-to-noise ratio (SNR). Molecular scattering terms (e.g. β_{m,λ_0} and α_{m,λ_0}) are determined following Bucholtz (1995) using radiosonde observations. Climatological values of the aerosol Angstrom exponent ($a(z)$) are obtained from collocated CIMEL sun photometer data (Holben et al., 1998). Overlap functions (e.g. $O_{\lambda_0}(z)$) are determined, along with all calibrations constants (e.g. C_{E,N_2}). Features are identified using range-dependent thresholds applied to multiple quantities. Of these quantities, the scattering ratio profile from the high elastic and nitrogen channels (Eq. (6.12)) and from the low elastic and nitrogen channels (SR^L_{E,N_2}) are needed along with the high channel volume depolarization ratio (δ).

The FEX extinction retrieval is summarized in Fig. 6.1 as a flow chart and is fully described in this section. The approach is to obtain an estimate of the particulate backscatter and lidar ratio profiles for all features using multiple retrieval methods and combine these into a single best-estimate. The extinction retrieval is iterative since both the feature classification and the multiple scattering model requires knowledge of the extinction profile itself.

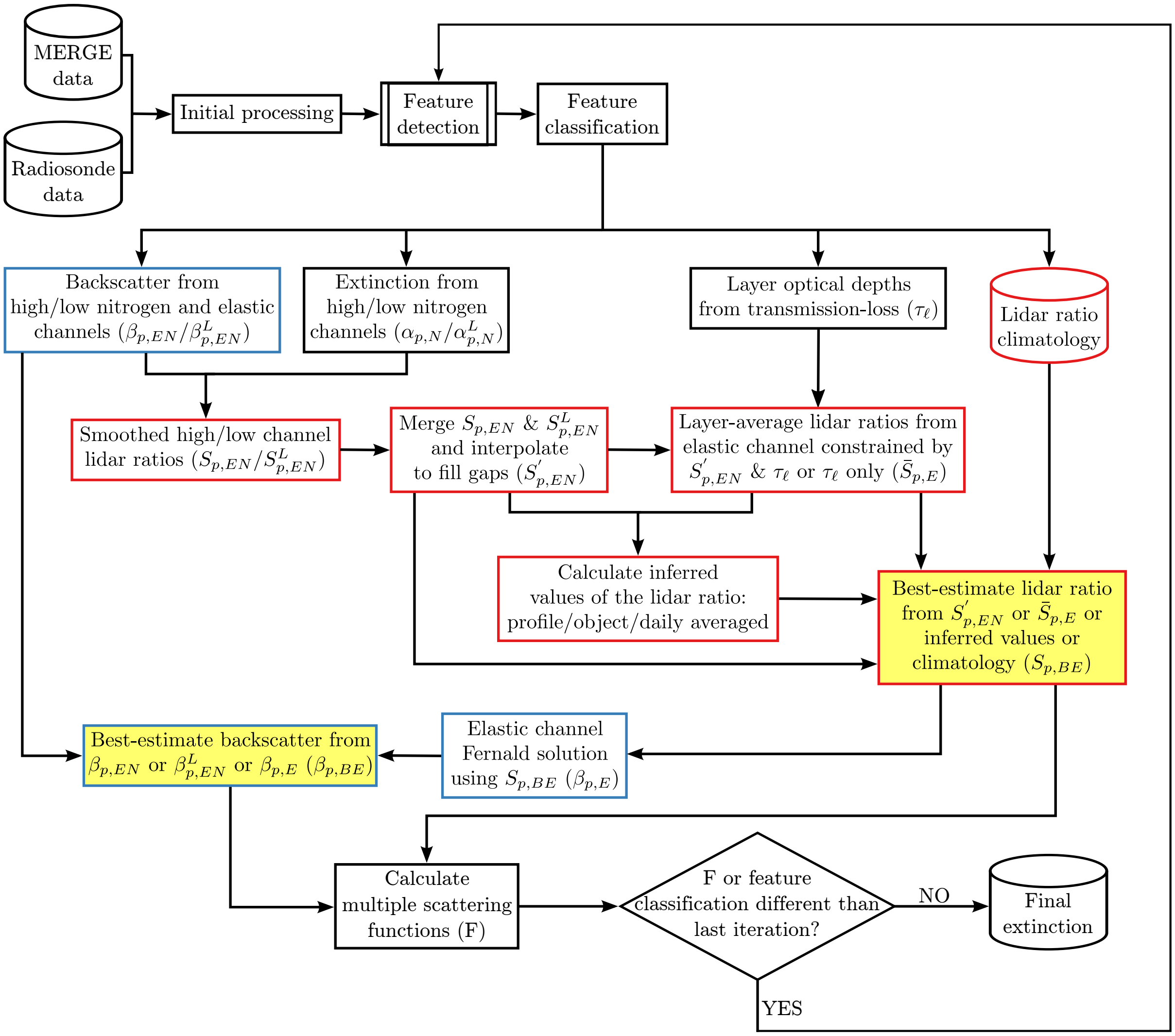

Figure 6.1: Flow diagram for the extinction retrieval in the FEX algorithm. Blue and red boxes denote the retrievals of particulate backscatter coefficient and lidar ratio, respectively. The best-estimate calculations occur in boxes with yellow backgrounds. Both the lidar ratio and particulate backscatter coefficient are retrieved at the laser wavelength $\lambda_0 = 355$ nm. The second subscripts given indicate the channels used to derive each quantity with E denoting the elastic channel, N denoting the nitrogen channel, EN denoting that both the elastic and nitrogen channels are used, and BE denoting a best-estimate derived from the combination of several quantities.

6.4.1 Feature classification

Each pixel where a feature is detected by FEX is classified as aerosol, rain (including virga), water cloud, ice cloud, or horizontally oriented ice (HOI) cloud. In addition to providing essential information about the target, this classification serves several practical purposes for the algorithm itself. Separating clouds from aerosols allows for the correct Angstrom exponent profile to be used in Eq. (6.8). For the purpose of particulate extinction retrieval, this classification provides a guide for the appropriate lidar ratio to be inferred or assumed from a climatology when no direct retrieval can be made (section 6.4.2.2). Since the retrieval of lidar ratio using the Raman method relies on smoothing to overcome insufficient SNR, feature classification allows different feature types to be smoothed separately. Finally, knowledge of the feature type is important for modeling multiple scattering (section 6.4.2.3) to both determine the appropriate particle size and backscatter phase function. Although a more accurate determination of feature type could be made by incorporating other remote sensors, such as cloud radar and/or microwave radiometer (e.g. Shupe, 2007), we have chosen here to design a scheme which relies only on temperature and humidity profiles from radiosondes in addition to the RL measurements. In lieu of more advance classification schemes, such as those based on neural networks (e.g. Bankert, 1994; Miller and Emery, 1997) or probabilistic methods (e.g. Baum et al., 1997; Hu et al., 2009; Liu et al., 2009), the classification here is based on a set of rules and thresholds determined empirically and guided by established literature. The same set of rules/thresholds is used for both the SGP and TWP sites. Fixed thresholds are applied to temperature, wet bulb temperature, the depolarization ratio (δ), the best-estimate particulate backscatter ($\beta_{p,BE}$, see section 6.4.2.1), directly-retrieved lidar ratios using the Raman method ($S'_{p,EN}$, see section 6.4.2.2). Temperature is taken from radiosonde profiles interpolated to the RL heights/times. The wet bulb temperature is calculated using the interpolated radiosonde temperature and relative humidity profiles following Stull (2011).

Clouds and aerosol are partitioned with δ and $\beta_{p,BE}$ using the thresholds depicted in Fig. 6.2a. These thresholds are the result of comparisons between the multiple runs of the FEX algorithm and classifications performed manually by a human observer. While qualitative, designing an automated classification in this manner is commonplace. For example, the separation of clouds and aerosols used by the Cloud-Aerosol Lidar and Infrared Pathfinder Satellite Observations (CALIPSO) satellite algorithms is based on a manual classification of one day of data (Liu et al., 2009). Aerosols in Fig. 6.2a are those features with relatively small backscatter and small depolarization ratios. At a tropical site like TWP, high-altitude thin cirrus clouds can also have low backscatter coefficients and depolarization ratios therefore, to avoid misidentifying them as aerosol, it is assumed that all TWP features at pressures lower than 400 mb are clouds. The thresholds in 6.2a also have the potential to misidentify pure dust, which has larger backscatter and depolarization ratios, as cloud. Currently in FEX this possibility is not considered since pure dust is nearly non-existent over the TWP and SGP sites (Omar et al., 2009). However, if FEX were applied to other lidars in regions where pure dust is prevalent the lidar ratio could be used to identify pure dust. Modeling calculations and lidar observations have shown that typical lidar ratios of pure dust vary between 40–70 sr (Sakai et al., 2002; Liu et al., 2002; Murayama, 2003; Anderson, 2003; De Tomasi et al., 2003; Amiridis et al., 2005; Dubovik et al., 2006; Müller et al., 2007), larger than expected from liquid or ice clouds (section 6.4.2.2). Since the presence of pure dust is not expected at either ARM site, the maximum allowable aerosol depolarization ratio is dictated by polluted dust shown by Omar et al. (2009) to have δ less than 0.15. In Fig. 6.2a, the maximum allowed aerosol δ is set at 0.09. This lower threshold value is used since sensitivity tests show that using an increased threshold increases the rate of aerosol false positives and very little true aerosol has large depolarization ratios. At both SGP and TWP 97% of aerosol identified by FEX has $\delta < 0.08$; therefore a threshold of $\delta = 0.09$ is expected to be a reasonable maximum to expect. The lower aerosol depolarization ratios found in this work compared to Omar et al. (2009) are perhaps due to wavelength difference between CALIPSO and the RL (532 nm versus 355 nm). The maximum backscatter allowed from aerosols is set at a value which is more aggressive in the identification of aerosol than cloud. Strictly applying the threshold in Fig. 6.2a can result in parts of clouds, typically the edges, to be falsely identified as aerosol. To remedy this, several steps are taken. First, two-dimensional feature "objects" are determined and are defined as regions of connected pixels in the current day being processed. Connectivity is defined using an eight pixel neighborhood: i.e. a pixel is consider connected to another pixel when any one of its eight neighbors— either the pixel in the next higher or lower height bin, the pixel in the preceding or following time bin, or the four pixels on the diagonals— contain a feature. If the majority of pixels in a feature object are identified as cloud, then all pixels in the object are changed to cloud. In addition, any aerosol objects completely surround by cloudy pixels are also changed to cloudy pixels. None of the preceding criteria used to identify aerosol false positives are applied to the boundary layer aerosol: defined aerosol objects with at least one pixel below 400 m. The boundary layer aerosol as originally identified using the thresholds in Fig. 6.2a is preserved since clouds are commonly found embedded in boundary layer aerosol. Such cases would be identified as a single feature object and, if enough pixels are cloudy, the entire object could be erroneously changed to cloud.

Rain is identified using the lidar ratio. The presence of rain is allowed when the wet bulb temperature is greater than $0°C$; therefore, since ice cannot exist at these temperature, rain needs to be separated from aerosol and liquid clouds. Figure 6.3 shows the theoretical lidar ratio from Mie theory (Wiscombe, 1980) for a wavelength of 355 nm and an index of refraction of $1.357 + i2.416 \times 10^{-9}$ (Segelstein, 1981). The theoretical lidar ratios in Fig. 6.3 are given as a function of the median volume radius used in an assumed normalized gamma size distribution (e.g. Bringi and Chandrasekar, 2001) for multiple values of the shape parameter μ. The variation of the lidar ratio with μ and median radii in Fig. 6.3 embodies a wide-range of observed distributions of liquid clouds and rain (Miles et al., 2000; Bringi et al., 2003). Also shown in Fig. 6.3 is the median lidar ratios retrieved from liquid clouds from the SGP and TWP RL (section 6.4.2.2). These retrieved values of the lidar ratio agree well to the theoretical values considering that the median droplet radius of most liquid clouds lies between 2–13 μm (Miles et al., 2000). When the median radius becomes larger than about 500 μm the lidar ratio begins to decrease with increasing droplet size. This decrease in the lidar ratio is used to identify the presence of rain in FEX: bins with $S'_{p,EN} < 12$ sr are initially considered to be rain. The median rain lidar ratio retrieved by FEX using the SGP and TWP RL shown in Fig. 6.3 is lower than predicted from Mie theory. This is likely because the assumption of spherical drops, and therefore Mie theory, is not valid for drops above a radius of 0.5 mm (Beard, 1976). Less restrictive scattering calculations are needed to validate the retrieved values of the lidar ratio for rain, but such work is beyond the scope of this study. After the initial identification of rain is made where $S'_{p,EN} < 12$ sr, several requirements must be met to avoid falsely identifying aerosol as rain. Layers of rain, i.e. consecutive range bins containing rain, must occur immediately below a cloud layer that fully attenuates the lidar signal or the rain itself must completely attenuate the lidar signal (full attenuation is defined as when the high elastic channel SNR $<$ 1). If these requirements are not met, the initial rain bins are re-classified as cloud or aerosol using the thresholds in Fig. 6.2a. Finally, any cloud layers immediately below rain layers are changed to rain and if rain occurs in the lowest bin where a retrieval of $S'_{p,EN}$ using the high channel signals is made, i.e. 1.5 km (see section 6.4.2.2), then the remainder of features at lower altitudes are assumed to also be rain.

The phase of cloudy pixels is then determined using the temperature and wet-bulb temperature which provide definitive constraints: only ice can exist at temperatures below the level of homogeneous freezing of $-40°$C and only liquid can exist when the wet-bulb temperature is above 0°C. In the intermediate temperature range, either liquid or ice can exist and its phase is determined using the depolarization and best-estimate particulate backscatter thresholds in Fig. 6.2b. Depolarization is especially useful as only non-spherical particles like ice induce a depolarization (Sassen, 1991). The depolarization ratio due to randomly-oriented ice is expected to be larger than 0.03 (Sassen, 1991) as reflected by the thresholds in Fig. 6.2b. However multiple scattering in liquid clouds also causes depolarization (Carswell and Pal, 1980; Sassen, 1991). The δ and $\beta_{p,BE}$ thresholds defined in Fig. 6.2b are based on an examination of the distribution of their values in pixels identified as cloud (excluding rain and HOI) shown in Fig. 6.4. Clouds form two distinct distributions with ice clouds associated with lower backscatter and higher depolarization and visa versa for liquid clouds. The black line in Fig. 6.4 denotes the thresholds defined to separate liquid from ice where the allowable depolarization for a liquid pixel increases with increasing backscatter to allow for multiple scattering effects. Note a similar analysis with TWP data shows the same thresholds to be appropriate (not shown). After applying the thresholds in Fig. 6.2b, the classification of cloud phase is finalized by applying a filter to only the cloudy pixels to reduce speckle. For each pixel, the phase is replaced by the most common phase in the surrounding 8 time bins by 8 height bins box.

HOI particles are also identified by FEX. The beam angle for the TWP RL is about 4–5° off-zenith and the SGP RL is about 1–2° off-zenith (David Turner, personal communication, 2013). This near-zenith geometry makes it possible for some portion of the laser beam to be scattered perpendicular to the surface of HOI. Scattering from HOI particles have fundamentally different properties than randomly oriented ice (ROI); namely, for HOI, the polarization of the incident beam is preserved. Therefore, when the liquid/ice thresholds in Fig. 6.2b are applied, HOI will commonly be falsely identified as liquid. In addition to small values of depolarization, Platt (1978) showed using theoretical calculations that the lidar ratio can reach a minimum of 0.0013 if all plates in the volume perfectly aligned horizontally. Therefore $S'_{p,EN}$ is used to distinguish between HOI and liquid. As shown above, a lidar ratio threshold of 12 sr falls below all theoretical values that occur in liquid clouds; therefore, like with rain identification, pixels with $S'_{p,EN} < 12$ sr are classified as HOI. However, unlike rain, HOI only exists when the wet-bulb temperature is below $0°C$ and $\beta_{p,BE}$ must be relatively large. The HOI backscatter and depolarization requirements defined in Fig. 6.2b are similar to the limits found by Noel and Chepfer (2010). HOI is also not allowed to exist below temperatures of $-40°C$ in this classification scheme as both models and observations show HOI is very infrequently at these low temperatures (Noel and Chepfer, 2010; Zhou et al., 2012). FEX's HOI threshold of 12 sr corresponds with identifying volumes with ice crystals tilted to within 12° or less of the horizontal (Platt, 1978) which should be sufficient for detecting HOI since previous lidar observation have shown that the majority of ice crystals wobble within 2.5° from the horizontal plane (Sassen, 1991; Sassen and Comstock, 2001).

Fig. 6.5 gives the inputs into and result of FEX's feature classification for August 10, 2009 at the SGP site. All feature categories identified by FEX are present in this example. A layer of boundary layer aerosol exists throughout the day that is at times topped by liquid clouds. During the first half of the day, a thick upper level cloud exists that is composed mostly of ice; however, from about 6–10 UTC this cloud also contains HOI and some liquid water. Several periods of rain occur during the second half of this day. The stark contrast in the lidar ratio (Fig. 6.5c) exploited by FEX to identify HOI and rain is clearly visible in this example.

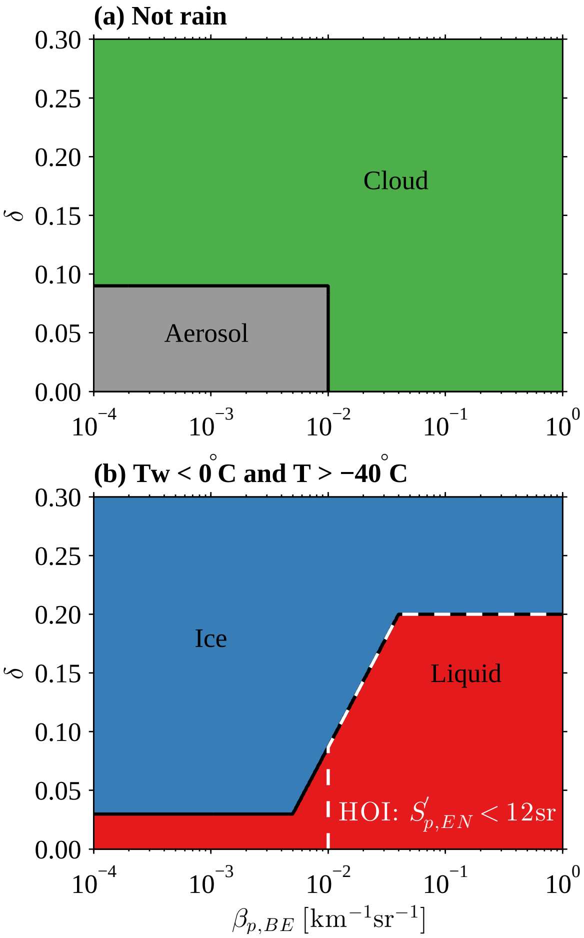

Figure 6.2: Feature classification thresholds using depolarization (δ) and particulate backscatter ($\beta_{p,BE}$) for (a) separating clouds and aerosol for bins without rain (see section 6.4.1) and (b) determining the cloud phase in the mixed phase temperature regime, i.e. a wet-bulb temperature (T_w) less than 0°C and a temperature (T) greater than −40°C. In panel (b), the horizontally oriented ice (HOI) thresholds are identified by a white dashed line and are only applied when the lidar ratio ($S^{'}_{p,EN}$) is less than 12 sr.

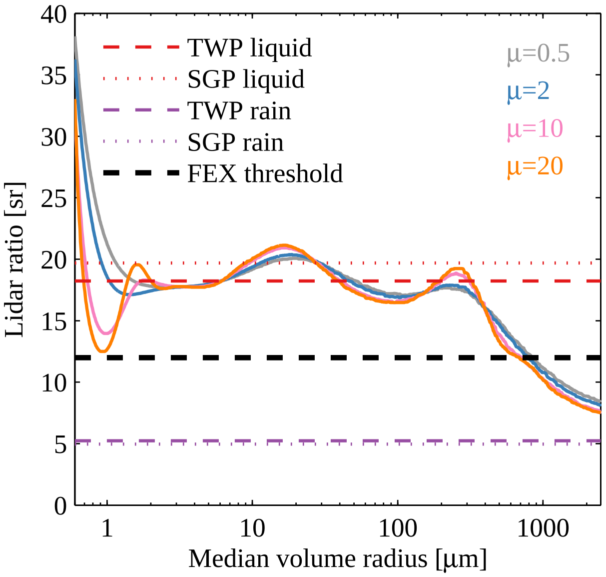

Figure 6.3: Theoretical lidar ratio at 355 nm as a function of median volume radius (solid lines) for gamma droplet size distributions with $\mu = 0.5$ (gray), $\mu = 2$ (blue), $\mu = 10$ (pink), $\mu = 20$ (orange). Also shown is the median liquid cloud (red) and rain (purple) lidar ratios directly retrieved by FEX (Table 6.2). Values from the TWP and SGP RL are given as dashed and dotted lines, respectively. The lidar ratio threshold used by FEX to identify rain and horizontally oriented ice (HOI) is depicted as a dashed black line.

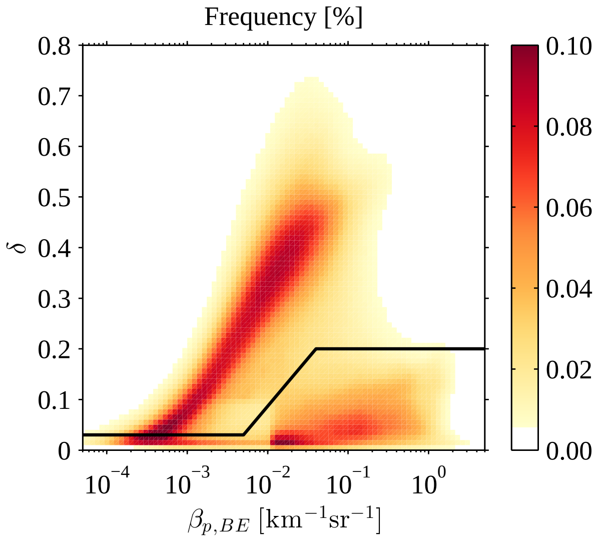

Figure 6.4: Distributions of depolarization (δ) and best-estimate particulate backscatter ($\beta_{p,BE}$) of pixels identified as clouds from August 2008 through July 2013 at the SGP site. The thresholds used to separate liquid from ice clouds (Fig. 6.2) are given as a black line with the upper left region for ice and the lower right region for liquid.

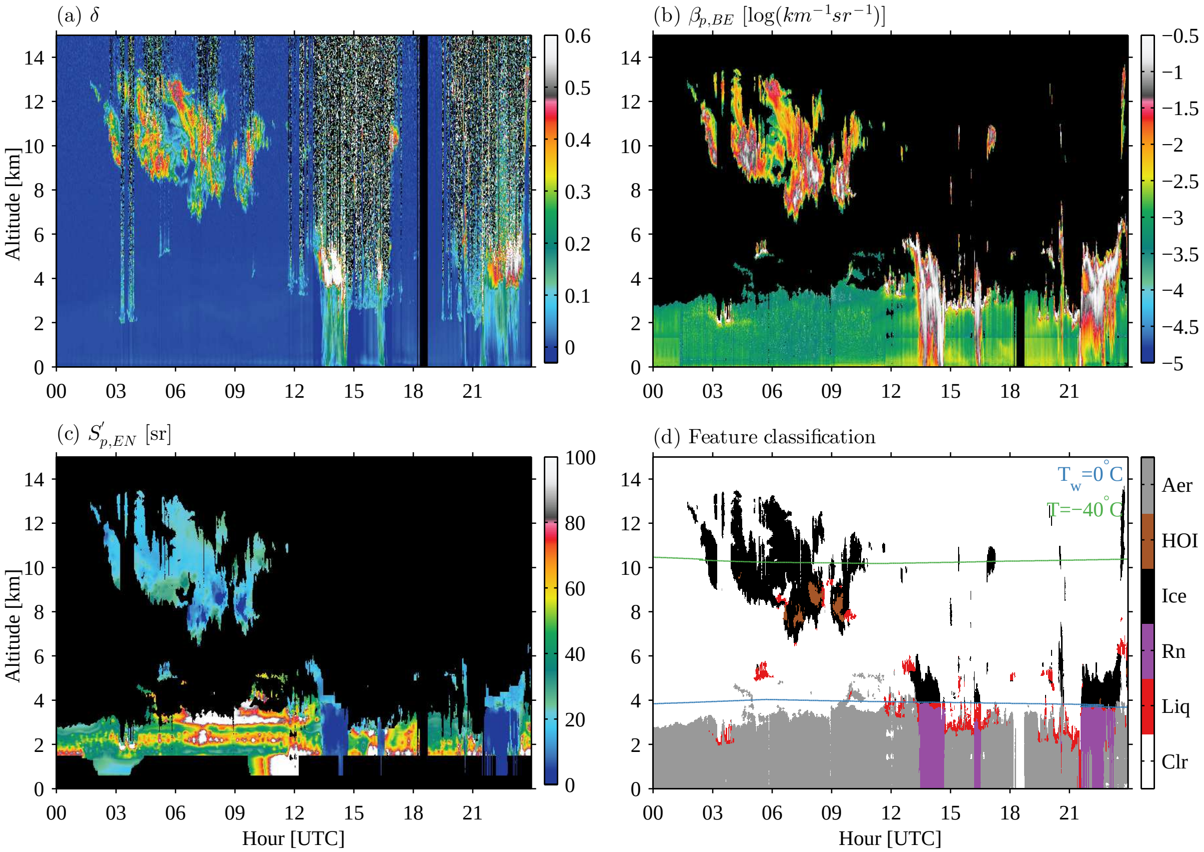

Figure 6.5: Feature classification for August 10, 2009 at the SGP site. Shown is the inputs used by the classification scheme: (a) depolarization ratio (δ), (b) particulate backscatter ($\beta_{p,BE}$) and (c) lidar ratio ($S'_{p,EN}$). The resulting classification is given in panel (d) with pixels classified as either liquid cloud (red), rain (purple), ice (black), horizontally oriented ice (HOI; brown) or aerosol (gray). The 0°C contour of wet bulb temperature (T_w; blue line) and −40°C contour of temperature (T, green line) are also shown in panel (d).

6.4.2 Extinction

An extinction retrieval with high accuracy is achieved by using the nitrogen channel signal to obtain the extinction and backscatter coefficients at the expense of less precision due to the larger amount of signal noise. On the other hand, retrievals using only the elastic channel give more precise values but with less accuracy due to the uncertainty in specifying the lidar ratio profile. Therefore FEX seeks to create a best-estimate using the methodology discussed in this section with the aim of creating a balance between precision and accuracy. At the same time, FEX also provides values and their uncertainties from all retrieval methods so researchers can tailor a best-estimate to their requirements if need be. Specifically the processing works towards retrieving the lidar ratio profile and the particulate backscatter coefficient as depicted in Fig. 6.1.

Both the lidar ratio and particulate backscatter coefficient are retrieved at $\lambda_0 = 355$ nm although in Fig. 6.1 and in the following sections the subscript λ_0 is omitted from all symbols. Instead the subscripts given indicate the channels used to derive each quantity with E denoting the elastic channel, N denoting the nitrogen channel, EN denoting that both the elastic and nitrogen channels are used, and BE denoting a best-estimate.

6.4.2.1 Particulate backscatter

The particulate backscatter coefficient can be directly obtained from the scattering ratio using both the elastic and nitrogen channels (Eq. (6.11)) for both the high ($\beta_{p,EN}$) and low ($\beta^L_{p,EN}$) channel signals. For the best-estimate ($\beta_{p,BE}$), $\beta^L_{p,EN}$ is used where the low nitrogen channel SNR is greater than 10, otherwise $\beta_{p,EN}$ is used. When the high nitrogen channel SNR is less than 3, the best-estimate is taken from the Fernald method (Eq. (6.5); $\beta_{p,E}$) using the lidar ratio best-estimate from the methods discussed in the next section.

6.4.2.2 Lidar ratio

To obtain the extinction coefficient from the nitrogen channel signal (Eq.(6.9)) for a wide range of features requires some amount of smoothing/averaging. Instead of retrieving a smoothed extinction coefficient, FEX instead retrieves a smoothed lidar ratio profile. A quasi-high resolution extinction coefficient can then be obtained by multiplying the smoothed lidar ratio by the unsmoothed particulate backscatter coefficient. A smoothed high and low channel lidar ratio profile is calculated by smoothing both the extinction ($\alpha_{p,N}$, $\alpha^L_{p,N}$) and backscatter coefficients ($\beta_{p,EN}$, $\beta^L_{p,EN}$) using a 2-dimensional Gaussian (e.g. Jain et al., 1995)

$$\bar{X}_{\delta z,\delta t}(z,t) = \frac{M(z,t)}{\sum_{z'}\sum_{t'} k(z',t',\delta z,\delta t)} \frac{[X(z,t)M(z,t)] * k(z',t',\delta z,\delta t)}{M(z,t) * s(z',t',\delta z,\delta t)} \tag{6.15}$$

where X represents either the unsmoothed backscatter or extinction coefficient, M is a binary mask equal to 1 anywhere a feature is present and 0 otherwise, the $*$ symbol indicates the that the convolution is calculated, δz and δt define width of the height and time window, respectively, of the kernel k used for smoothing

$$k(z',t',\delta z,\delta t) = \exp\left\{-\frac{9}{2}\left[\left(\frac{z'}{\delta z}\right)^2 + \left(\frac{t'}{\delta t}\right)^2\right]\right\} \tag{6.16}$$

where z' and t' are

$$z' = \left\{-\frac{(\delta z - 1)}{2} + n \mid n = 0, 1, ...\delta z - 1\right\} \tag{6.17}$$

and

$$t' = \left\{-\frac{(\delta t - 1)}{2} + n \mid n = 0, 1, ...\delta t - 1\right\}, \tag{6.18}$$

respectively. The kernel s is the same size at kernel k with $s(z',t',\delta z,\delta t) = 1$. In words, Eqs. (6.15)–(6.18) create a smoothed quantity using a 2-dimensional Gaussian distribution and employs the knowledge of feature location by only considering pixels with the same feature present. In addition, potential large biases in the overlap function, which can be greatly exaggerated since it appears in the slope term in Eq. (6.9), are avoided by setting $M(z,t) = 0$ where $z < z_O$. For the high channel $z_O = 1.5$ km and for the low channel $z_O = 0.6$ km. Above these altitudes the standard deviation of overlap functions derived by FEX are less than 10%. Using a Gaussian kernel over a moving average better preserves the spatial structure since bins closer to the pixel being smoothed are likely to possess more similar properties. In lieu of more advance nonlinear filters, using a linear convolution to apply the smoothing kernel allows for straightforward propagation of uncertainty. Smoothing is performed separately for each feature type to avoid mixing signals from dissimilar features. In addition to separate smoothed quantities for each feature type, multiple window sizes are used for smoothing as defined in Table 6.1. Finally, the ratio of these smoothed high and low channel extinction and backscatter coefficients are used to obtain smoothed values of the lidar ratio profiles for each feature type and at multiple levels of smoothing. Standard uncertainty propagation (Bevington and Robinson, 2002) is used to obtain the random error in the smoothed lidar ratios profiles. These multiple lidar ratio profiles are combined into single low ($S^L_{p,EN}$) and high ($S_{p,EN}$) channel estimates by taking the lidar ratios obtained using the least amount of smoothing needed for a pixel to achieve a random error less than 30%. A single estimate of the directly-retrieved lidar ratio profiles $S^{'}_{p,EN}$ are then derived by combining $S^L_{p,EN}$ and $S_{p,EN}$. Pixels with values of the lidar ratio from both the high and low channels are merged by: (1) using $S^L_{p,EN}$ below 5 km when either the high elastic or nitrogen channels uses a default overlap function (Thorsen et al., 2014, Chapter 5), (2) the channel with the least amount of smoothing is used, (3) when the same amount of the smoothing is performed, the value with the smaller random error is used. Small gaps in $S^{'}_{p,EN}$ of less than 1 km and 20 min are interpolated for using bilinear interpolation. Like with smoothing, each feature type is processed separately when interpolating.

Table 6.1: Window sizes used for the 2-dimension Gaussian filter (see section 6.4.2.2) for the various smoothing levels. Window sizes are given as the number of height bins followed by the number of time bins. There is no smoothing in level 1.

	Window size	
Level 1	1×1	(0.03 km×2 min)
Level 2	10×5	(0.3 km×10 min)
Level 3	20×15	(0.6 km×30 min)
Level 4	40×30	(1.2 km×60 min)
Level 5	80×60	(2.4 km×120 min)
Level 6	160×120	(4.8 km×240 min)

Layer-averaged values of the lidar ratio are determined using the transmission-loss method. The optical depth of layers consisting of a single feature type and bounded by clear-sky both above and below are determined using Eq. (6.13). Instead of a single value, the median value of both the above-layer ($z = z_t$) and below-layer ($z = z_b$) terms in Eq. (6.13) over a 500 m portion of clear-sky are used. The layer optical depth τ_ℓ and the directly-retrieved lidar ratio profiles using the Raman method $S^{'}_{p,EN}$ are used as constraints on the Fernald solution to the elastic lidar equation (Eq. (6.5)). When using the Fernald solution, the boundary condition at $z = z_0$ for the layer is set in the clear-sky above (i.e. the far-field) which ensures numerical stability (Klett, 1981). For layers with a τ_ℓ estimate, an initial guess at the layer-average lidar ratio $\bar{S}_{p,E}$ is made and the particulate backscatter is solved for using Eq. (6.5). Iterations are performed by adjusting the layer-average lidar ratio $\bar{S}_{p,E}$ and resolving for the particulate backscatter until Eq. (6.14) is satisfied. When making adjustments to $\bar{S}_{p,E}$ during these iterations, bins with a directly-retrieved $S^{'}_{p,EN}$ lidar ratios are not modified. For the lidar ratio best-estimate, only $\bar{S}_{p,E}$ with relative errors less than 30% are used. Uncertainty in $\bar{S}_{p,E}$ is calculated by noting the standard deviation over the 500 m of the above-layer and below-layer terms and then performing standard error propagation.

The directly-retrieved lidar ratios with less than 30% relative uncertainty, i.e. the combined estimates of the lidar ratios from the Raman method $S^{'}_{p,EN}$ and the layer-averaged values $\bar{S}_{p,E}$ from the transmission-loss method, are used to infer the values for pixels where no estimate exists. Feature types are considered separately and three types of averages are determined

1. profile-averaged: using all directly-retrieved lidar ratios in each profile;

2. object-averaged: using all directly-retrieved lidar ratios in each 2-dimensional feature object (objects are composed of single feature type connected in 2-dimensions, see section 6.4.1 for more details);

3. daily-averaged: using all directly-retrieved lidar ratios in the same day being processed.

For all three types of averages, at least 25% of the pixels must have directly-retrieved values. For example, for a profile-averaged lidar ratio to be used, at least 25% of all bins in the profile for a single feature type must have a directly-retrieved value. Inferred lidar ratios using these three averages are assigned with preference given to using profile-averaged, then object-averaged and finally daily-averaged values. When none of these averaged values can be used, a climatological value of the lidar ratio is used based on the feature classification as given in Table 6.2. Table 6.2

gives the median and standard deviation of all directly-retrieved lidar ratios from August 2008 through July 2013 at SGP and December 2010 through May 2014 at TWP. The probability density functions (PDF) for these same periods are given in Fig. 6.6. The statistics in Table 6.2 and Fig. 6.6 represent some of the most comprehensive measurements of directly-retrieved lidar ratios to date, particularly for clouds. Further analysis of these lidar ratios will be the subject of a future publication.

Table 6.2: Median and standard deviation of the directly-retrieved lidar ratios for each feature type from December 2010 through May 2014 at the TWP site and from August 2008 through July 2013 at the SGP site.

	TWP		SGP	
Aerosol	41.69	±22.33	53.62	±26.70
Rain	5.23	±4.15	4.96	±3.81
Liquid	18.22	±7.95	19.69	±10.69
Ice	26.70	±6.60	22.04	±8.93
HOI	N/A		4.13	±2.94

Fig. 6.7 gives the lidar ratio retrieved by applying the Raman method to the high and low channel signals along with the resulting best-estimate lidar ratio on December 25 2012 at the Darwin TWP site. Also given in Fig. 6.7, to help provide context, is the scattering ratio derived using only the elastic channel (Thorsen et al., 2014, Chapter 5) and the classification of feature type. Throughout this day a large amount of cirrus exists, along with boundary-layer aerosol with a few liquid clouds embedded in it, and a small amount of mid-level liquid cloud towards the end of the day. The lidar ratio of the aerosol layer in the best-estimate (Fig. 6.7e) is obtained at various levels of smoothing using the Raman method applied to the high channel signals above 1.5 km (shades of red in Fig. 6.7f). Below 1.5 km, the Raman method applied to the low channel signals is used (shades of blue) with small gaps being filled in by interpolated values (purple). Below 600 m, where the Raman method is not attempted, a profile-averaged value is typically used (brown). In general, larger amounts of smoothing is required to obtain the lidar ratios for the cirrus layer. However, there exists portions of the cirrus layer at higher altitudes and those that are more tenuous for which the Raman method cannot be used to

obtain a lidar ratio with a random error less than 30%. In some instances the transmission method can be used to fill in the remainder of the layer (green). For the rest of the cirrus layer inferred values of the lidar ratio are used: either per-profile (brown) and per-object (pink) or per-day (orange) averages. In this example, no features require the use of a climatological lidar ratio.

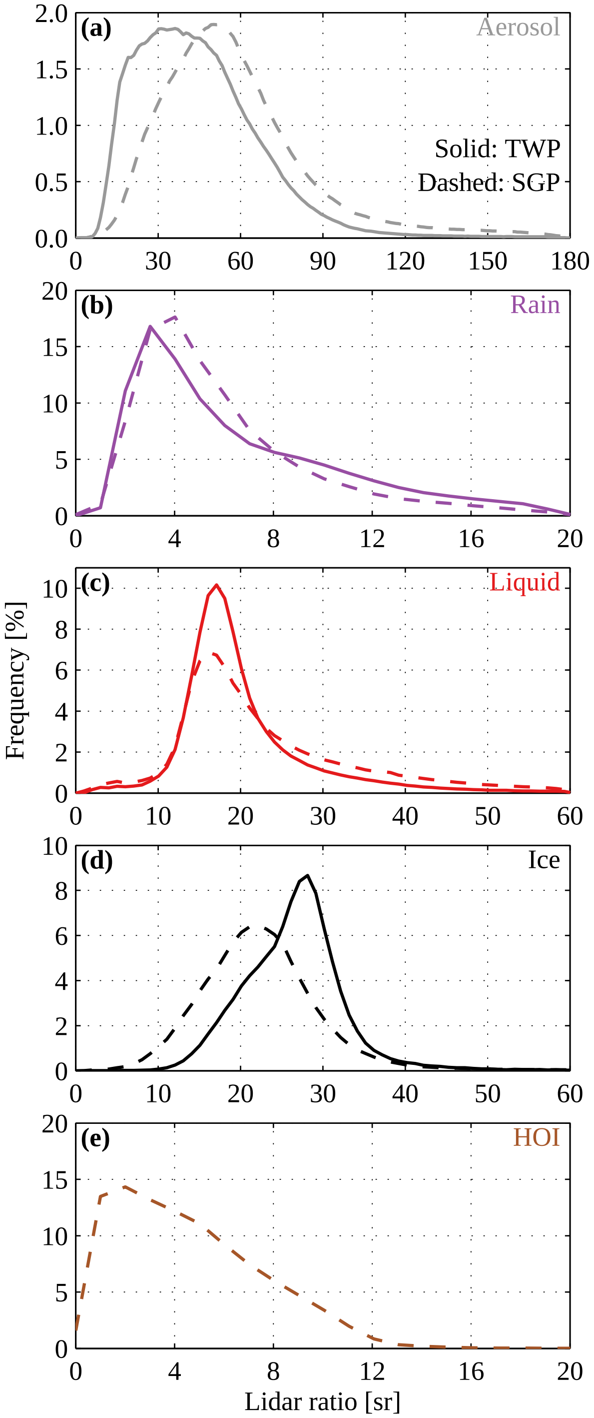

Figure 6.6: The probability density functions (PDFs) of directly retrieved lidar ratios by FEX from August 2008 through July 2013 at the SGP site (dashed lines) and December 2010 through May 2014 at the TWP site (solid lines). Separate PDFs are given for each feature type: (a) aerosol, (b) rain, (c) liquid cloud, (d) ice cloud, and (e) horizontally oriented ice (HOI). A bin size of 1 sr is used in all panels. The PDF of HOI for TWP is not shown due its small sample size.

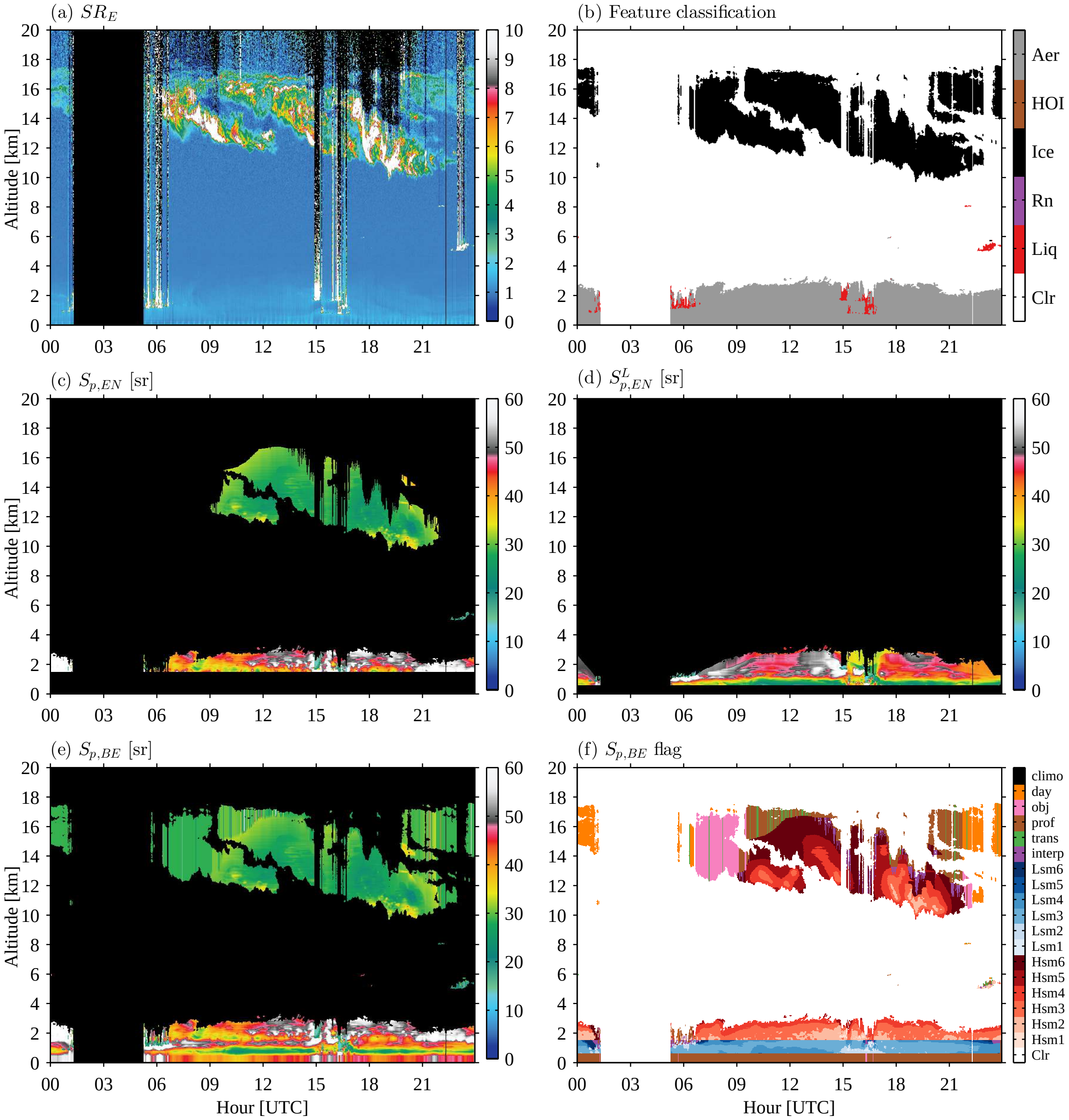

Figure 6.7: FEX's retrievals on December 25, 2012 at the Darwin TWP site. (a) The scattering ratio derived using only the elastic channel, (b) the classification of features as either liquid cloud (red), rain (purple), ice (black), horizontally oriented ice (HOI; brown) or aerosol (gray), (c) the lidar ratio derived using the Raman method applied to the high channel signals, (d) the lidar ratio derived using the Raman method applied to the low channel signals, (e) the best-estimate lidar ratio, and (f) flag indicating the type of retrievals used in the best-estimate lidar ratio. Shades of red/blue in panel (f) denote the level of smoothing (Table 6.1) used for the Raman method for the high/low channel signals. Other colors in panel (f) denote those pixels where the lidar is determined by: interpolation (purple), transmission-loss method (green), profile-averaged (brown), object-averaged (pink), daily-averaged (orange), and climatological values (black).

6.4.2.3 Multiple scattering

The above retrievals of the particular backscatter and lidar ratio require knowledge of the single scattering signals, i.e. $S^1_{\lambda_0}(z)$, $S^1_{\lambda_{N_2}}(z)$, $S^{1,L}_{\lambda_0}(z)$, $S^{1,L}_{\lambda_{N_2}}(z)$. However, only the total signal (i.e. single plus multiple scattering) is measured and therefore we introduce the multiple scattering function $F(z)$ to account for multiple scattering effects (e.g. Eqs. (6.4) and (6.10)). Although it is traditional for multiple scattering to be accounted for by a factor which modifies the particulate extinction (e.g. Kunkel and Weinman, 1976; Pal and Carswell, 1976; Platt, 1973; Young and Vaughan, 2009), it is not necessary to do so. Conceptually, the increased signal strength as photons remain in the receiver's FOV manifests itself as a combination of an apparent decrease in the extinction coefficient and apparent increase in the backscatter coefficient. Furthermore, introducing a function which modifies the entire lidar equation, as is done in this work, is more numerically convenient. Multiple scattering models require single scattering values as inputs, therefore any explicit treatment of multiple scattering requires iterations. If multiple scattering is accounted for by modifying the particulate extinction coefficient, the noisy signal slope must be dealt with (e.g. Wandinger, 1998).

The model from Hogan (2006, hereafter H06) is used to calculate the multiple scattering functions. This model has been shown to be as accurate as the widely used model by Eloranta (1998) but is several orders of magnitude faster, making it practical for use in an operational retrieval. The H06 model requires inputs of the laser wavelength, beam divergence and FOV (Table 5.1) and therefore separate functions are calculated for the high and low channels. Separate multiple scattering functions are also needed for the elastic and nitrogen channel signals as the phase function near 180° differs in each channel. For purely molecular backscattering, as occurs in the nitrogen channel, the phase function is near-isotropic around 180°. The elastic channel contains backscatter from particulates as well; therefore, the feature classification made by FEX is used to set the proper near-backscatter phase function in the H06 model whose parameterizations of ice and liquid cloud phase functions are given in Hogan (2008). The H06 model doesn't provide any parameterization of the phase function for rain and aerosol therefore the near-backscatter phase function for these bins are treated as liquid-like and isotropic, respectively. The H06 model also requires the particle size, specifically the equivalent-area radius, to determine the distribution of the forward scattered photons. The particle sizes used for each feature type and their respective references are given in Table 6.3. The ice particle size is parameterized as a function of extinction for which the best-estimate value is used. Other feature types use a single size for all multiple scattering calculations. Table 6.3 contains a combination of particle sizes expressed as effective, median volume and mean radii all of which are assumed to be approximately equal to the equivalent-area radius. Finally, the multiple scattering model requires molecular backscatter and extinction coefficients, which are calculated from radiosonde observations, and the single scattering particulate backscatter and extinction coefficients. The later requirement makes iterations necessary. An initial guess at the multiple scattering functions is made using the best-estimate values derived using the total signals. On the next iteration, these functions are used to obtain the single scattering signals needed for extinction retrieval with iterations continuing until the all bins in all four multiple scattering functions change by less than 1%.

Potential biases introduced by the multiple scattering functions in the best-estimate extinction were investigated. Two runs of FEX were performed with multiple years of TWP and SGP data using the high/low value or plus/minus one standard deviation of particle size as given in Table 6.3 for each feature type (no such test is performed for ice clouds since a single size is not specified). A third run of FEX was also performed to test the sensitivity to the near-backscatter phase function by using a liquid-like phase function for aerosols and an isotropic one for all other features. For aerosols, it is found that the assumed particle size and near-backscatter phase function introduces a median uncertainty of less than ±0.06% in the best-estimate extinction. The median extinction uncertainty in all other features is less than ±2%. The exception is for the near-backscatter phase function for rain: assuming it isotropic instead of liquid-like introduces a median uncertainty of about 5%.

6.5 Results

All results presented in this section are from data averaged to 2 min and 30 m from August 2008 through July 2013 at the SGP site and December 2010 through May 2014 at the TWP site. During these periods the RL experienced an uptime of 97% and 52% at the SGP and TWP site, respectively.

6.5.1 Vertical occurrence of features

Figure 6.8 gives the occurrence of liquid cloud, ice cloud (including both ROI and HOI), HOI, rain and aerosols at both the TWP and SGP sites. Several expected differences exists between the two sites such as a higher frequency of rain and ice cloud, especially at high altitudes, at the TWP site. The clouds at TWP show the characteristic tropical trimodal distribution (Johnson et al., 1999) with a lower altitude peak in liquid cloud amount, a mid-level peak in both liquid and ice cloud near the melting level, and an upper level peak in ice cloud below the tropopause. More aerosol exists below about 2 km at TWP while above 2 km more aerosol exists at SGP. A non-trivial amount of HOI occurs at SGP with its amount is comparable to liquid cloud amount at mid-levels. However, at TWP almost no HOI exists. This is consistent with the modeling study of Zhou et al. (2012) who showed that for a pointing angle of 3° both the depolarization and backscatter of HOI are similar to that of ROI. Given that the TWP RL is approximately 4–5° off-zenith (compared to 1–2° for SGP) we expect very little HOI to be identified.

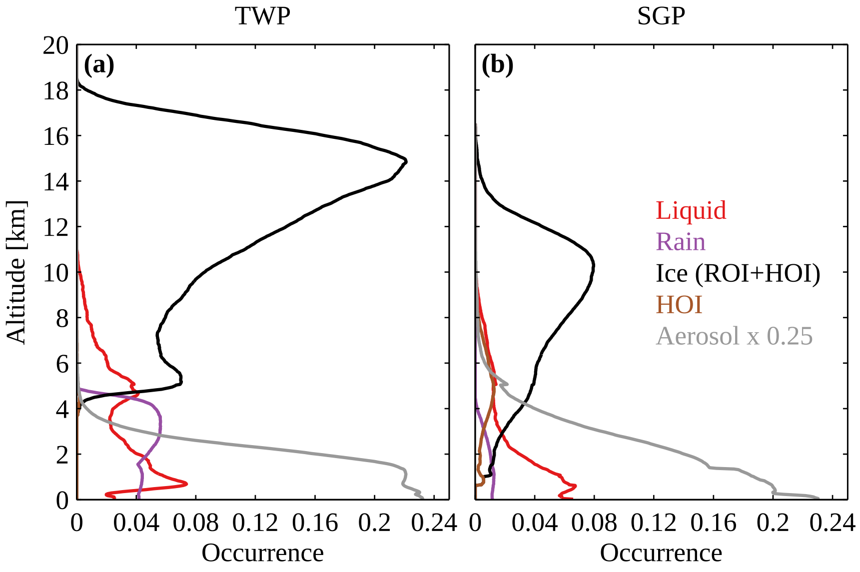

Figure 6.8: The vertical occurrence of feature types at the (a) TWP site and (b) SGP site. The feature types given are liquid cloud (red), rain (purple), ice (black), horizontally oriented ice (HOI; brown) or aerosol (gray). The ice occurrence profile includes both random oriented ice (ROI) and HOI. The aerosol occurrence profiles has been scaled by a factor of 0.25.

Table 6.3: Particle radii used in the multiple scattering model. Standard deviations are given in parentheses. For aerosols the bracketed values give the minimum and maximum sizes in the aerosol categories from Omar et al. (2005).

Feature type	Site	Size [μm]	Source	Reference
Ice & HOI	TWP SGP	$43.29\alpha^{0.2514}$	Power law derived from effective radius in-situ data where α is extinction in units of km^{-1}	Table 2 in Fu (1996)
Liquid	TWP	5.70 (±1.11)	Effective radius from multiple retrieval algorithms at TWP and SGP	Fig. 4 in Zhao et al. (2012)
	SGP	6.54 (±1.91)		
Rain	TWP	670 (±135)	C-band polarimetric radar retrievals near the TWP site of median volume drop radius	Table 1 in Thurai et al. (2010)
	SGP	770 (±165)	W-band Doppler radar spectra retrievals at SGP of median volume drop radius	Fig. 6 in Giangrande et al. (2012)
Aerosol	TWP SGP	3.02 [2.53 3.24]	Mean radius from Aerosol Robotic Network (AERONET) global climatology	Table 2 in Omar et al. (2005)

6.5.2 Frequency of extinction processing selections

Figures 6.9 and 6.10 show the frequency of the processing choices used by FEX for the particulate backscatter and lidar ratio best-estimates, respectively, for the TWP RL. We just present results from the TWP site as it is more challenging to perform extinction retrievals due to larger solar background noise and a higher tropopause, near which very optically thin cirrus frequently occur (e.g. Winker and Trepte, 1998; Wang et al., 1998; Fu et al., 2007; Dessler and Yang, 2003; Massie et al., 2010). Results for the SGP site are typically similar and any differences will be noted where appropriate. Figures 6.9 and 6.10 do not show the frequency profiles for HOI and rain as these features almost always have directly-retrieved values since the lidar ratio is used to identifying them. Therefore determining if a feature is rain or HOI is contingent on being able to use the Raman method to obtain the lidar ratio. For situations when these feature types occur we expect the Raman method to be typically usable since both feature types have relatively strong signals. For rain a strong signal is expected due to its proximity to the ground and for HOI because of the strong backscatter it induces.

About 90% of aerosols are able to use both directly-retrieved lidar ratios and backscatter coefficients (with the exception of below 600 m for the lidar ratio, see section 6.4.2.2). A directly-retrieved particulate backscatter coefficient is used for about 80% of liquid clouds. For the liquid cloud lidar ratio, the solar background exerts some influence since about 80–90% of lidar ratios are directly-retrieved at night compared to 50% during the daytime where there is more of a reliance on profile and daily-averaged values. With ice clouds, there is a clear influence of the solar background in both the particulate backscatter and lidar ratio processing choices. For both the particulate backscatter and lidar ratio about 75% of nighttime ice clouds use a directly-retrieved value below about 15 km. At SGP the amount is larger: about 85% of nighttime ice clouds use a directly-retrieved values, regardless of altitude. At TWP during the daytime the majority of ice clouds above 5 km need to use the Fernald solution to obtain the particulate backscatter coefficient. Similar daytime frequency profiles exist at SGP, although the change to the majority of ice cloud using the Fernald solution occurs above 8 km instead. For the ice cloud lidar ratio retrieval during the day (Fig. 6.10c) the Raman method is used for the majority of profiles only at lower altitudes and its use steadily decreases to zero at about

14 km. At these higher altitudes there is a heavier reliance on transmission-loss estimates, object and daily averages. The use of climatological values are needed for less than 5% of ice cloud below 12 km. However, above 12 km the presence of thin cirrus makes climatological lidar ratios necessary for about 20% of ice clouds. At SGP, where cirrus are typically thicker, there is no such increase in the amount of climatological lidar ratios with altitude during the day: about 5% of ice clouds need to use a climatological value regardless of altitude.

Figure 6.11 gives the amount of smoothing required to obtain the lidar ratio with Raman method applied to the high channel signals at TWP. Here day and night are not shown separately since applying a fixed maximum uncertainty makes for a similar pattern of smoothing levels. This fixed error requirement produces a lidar ratio dataset with consistent error characteristics across the diurnal cycle at the expense of having less lidar ratio retrievals during the daytime. For liquid cloud (Fig. 6.11b) the majority of the lidar ratios can be obtained with either no smoothing or at the second level of smoothing (0.3 km×10 min). For aerosol and ice cloud, almost no lidar ratios can be obtained without some amount of smoothing. Both aerosol and ice cloud smoothing amounts increase with altitude. The overall pattern of smoothing amounts for the low channel Raman method or at SGP are similar to those presented in Fig. 6.11.

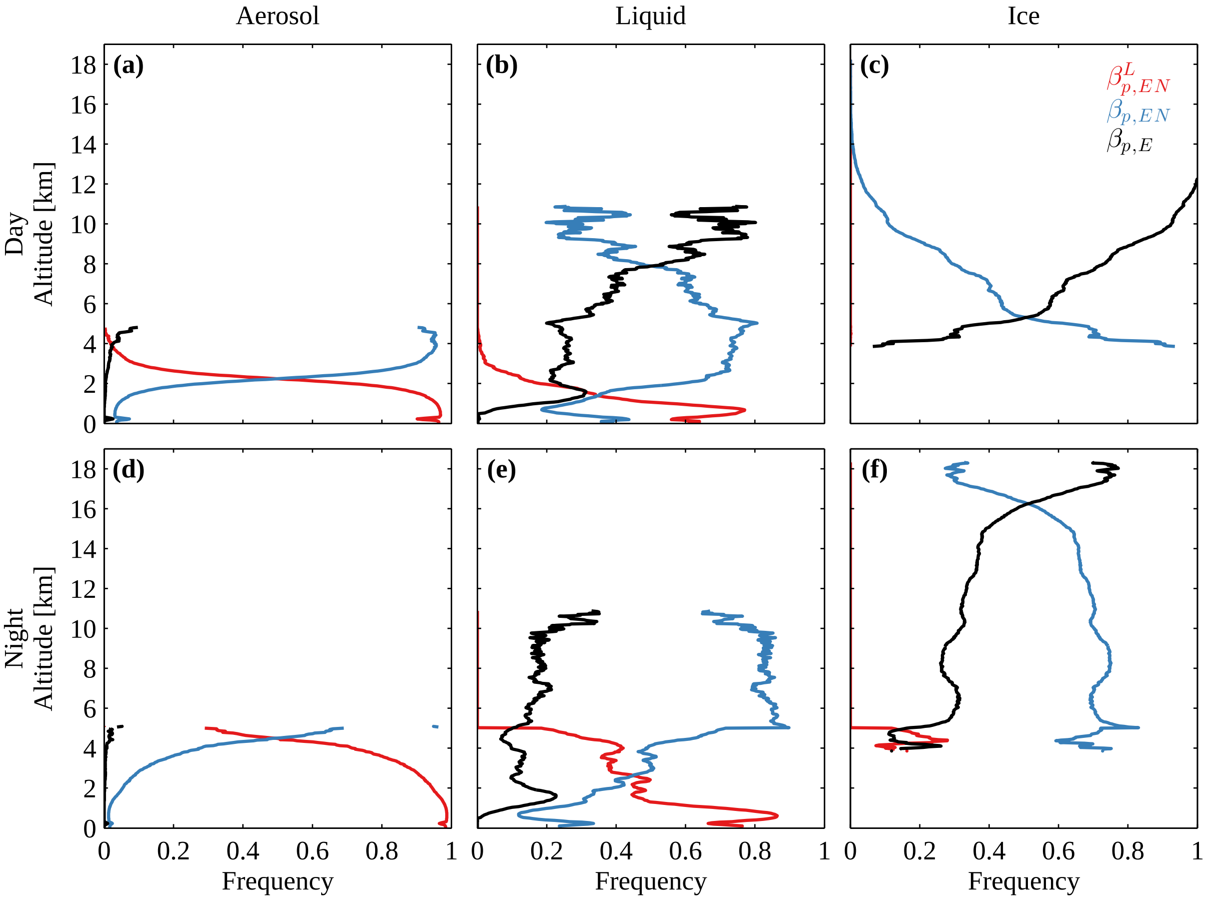

Figure 6.9: The frequency of values used in the particulate backscatter best-estimate at the TWP site with values obtained from: the scattering ratio derived using both the low elastic and nitrogen channels (red), the scattering ratio derived using both the high elastic and nitrogen channels (blue), and the Fernald solution to the elastic lidar equation (black). Frequency is normalized by the number of bins at each altitude with a feature either (a,d) aerosol, (b,e) liquid cloud or (c,f) ice cloud. Frequency profiles are shown separately for (a,b,c) daytime and (d,e,f) nighttime profiles.

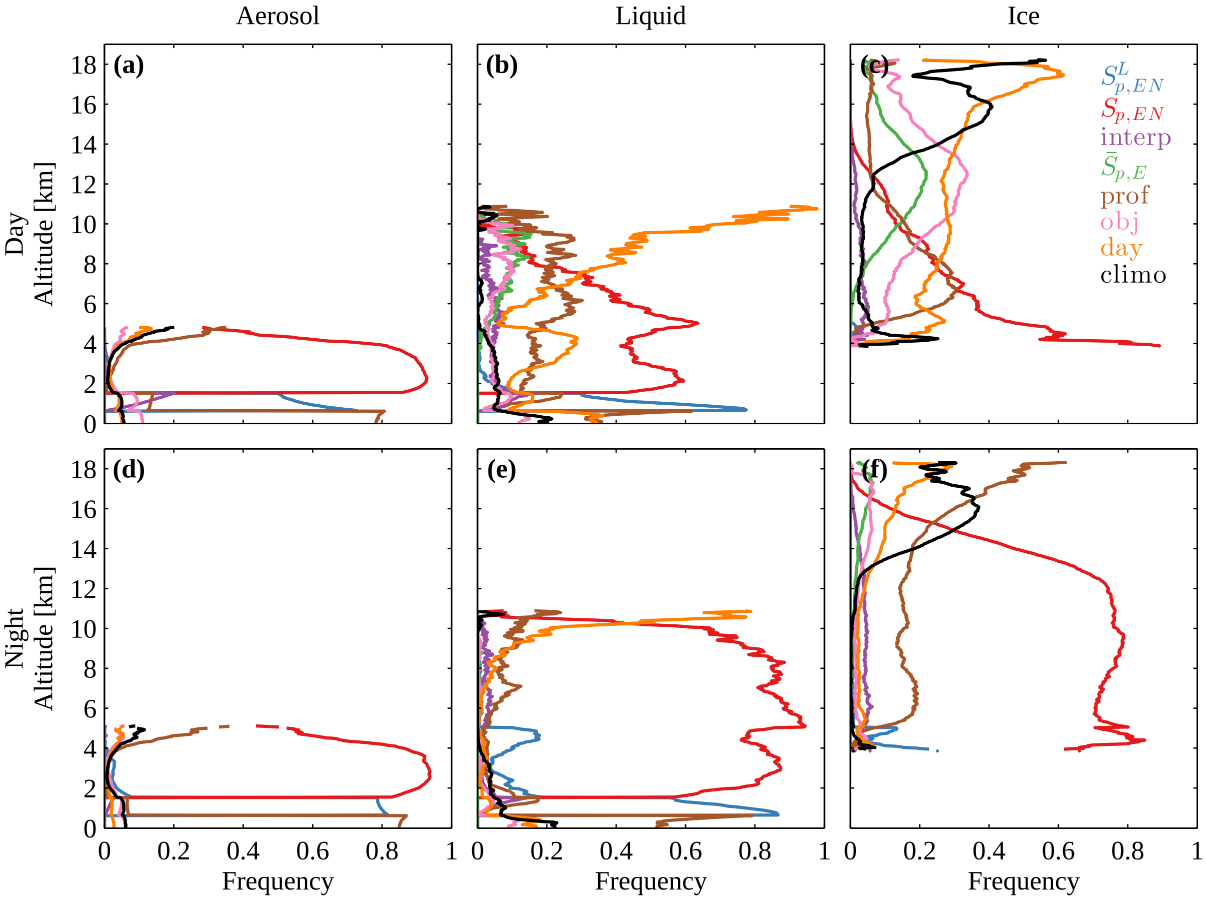

Figure 6.10: The frequency of values used in the lidar ratio best-estimate at the TWP site with values obtained from: the Raman method using the low channel signals (blue), the Raman method using the high channel signals (red), interpolation (purple), the transmission-loss method (green), profile-averages (brown), object-averaged (pink), daily-averages (orange), and climatological values (black). Frequency is normalized by the number of bins at each altitude with a feature either (a,d) aerosol, (b,e) liquid cloud or (c,f) ice cloud. Frequency profiles are shown separately for (a,b,c) daytime and (d,e,f) nighttime profiles.

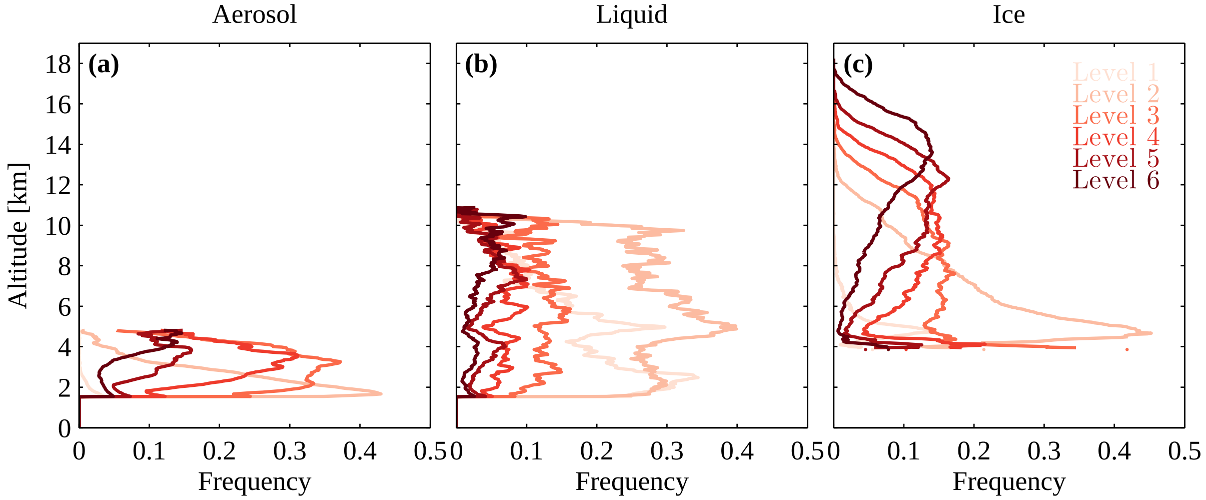

Figure 6.11: The frequency of smoothing levels (Table 6.1) used in the lidar ratio derived from the Raman method using the high channel signals at the TWP site. Increasingly darker shades of red represent larger amounts of smoothing. Frequency is normalized by the number of bins at each altitude with a feature either (a) aerosol, (b) liquid cloud or (c) ice cloud.

6.5.3 Multiple scattering errors

Errors due to ignoring multiple scattering vary with retrieval method and the quantity being analyzed. For example, for the particulate backscatter coefficient obtained from the scattering ratio using both the elastic and nitrogen channels there is a partial cancellation of multiple scattering effects (Wandinger, 1998). But quantities that use only a single signal such as the Fernald solution or Raman method for extinction will have larger contributions from multiple scattering. Here, for brevity, we only focus on the effect of multiple scattering on the best-estimate extinction. A box plot of the relative errors are given in Fig. 6.12. Similar error distributions exist at TWP and SGP. Multiple scattering effects for aerosols are small, with upper/lower quartiles of about ±2%. For hydrometeors, multiple scattering typically causes extinction to be biased low, although appropriate corrections varies in both range and sign. The large size of rain translates to the largest errors with median errors around -35%. Typical errors in liquid and ice cloud extinction range from up to about -30% to near zero. At SGP, HOI has a wide range of errors with a median close to -2%. The errors in extinction presented in Fig. 6.12 illustrates the importance of explicitly treating multiple scattering when using systems similar to the ARM RL for cloud retrievals.

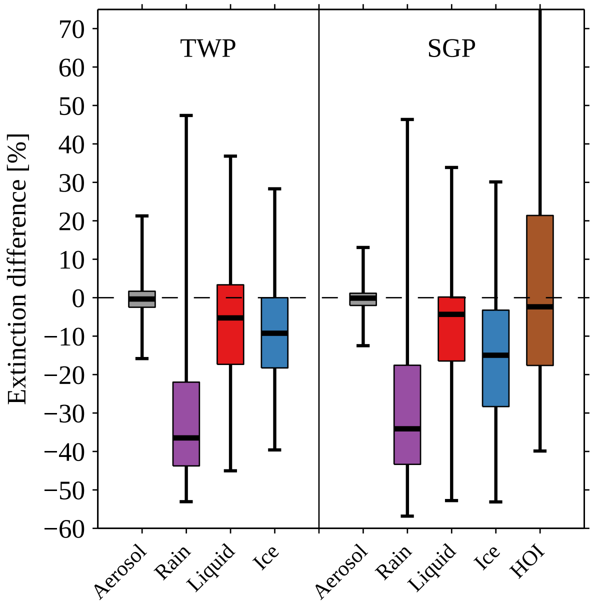

Figure 6.12: Box plot of the relative error in the particulate extinction retrievals by neglecting multiple scattering at the TWP (left) and SGP (right) site. The colored boxes give the interquartile ranges with the thick black line denoting the median. The whiskers give the 5^{th} and 95^{th} percentiles. The error in HOI for TWP is not shown due its small sample size.

6.5.4 Sun photometer comparison

Validating FEX's cloud extinction retrieval is difficult since no instrument at the ARM sites makes comparable measurements. However, for aerosol extinction, the ARM sites are equipped with CIMEL sun photometers (Holben et al., 1998) allowing for the comparison of daytime aerosol optical depth as shown in Fig. 6.13. The coincident sun photometer optical depth is calculated at 355 nm by applying the mean 380 nm/340 nm Angstrom exponent to the 340 nm channel optical depth. Cloud-screened sun photometer data is used (Smirnov et al., 2000) and profiles where the RL detected clouds are also excluded. Good agreement in Fig. 6.13 validates several portions of FEX including: the extinction retrieval itself, identifying the feature as aerosol, and the detection of features since extinction retrievals are only performed where a feature is detected.

As shown in section 6.5.2 a directly-retrieved aerosol extinction coefficient isn't always possible. Therefore to evaluate what is expected to be the most accurate profiles from FEX, Fig.

6.13a,c compares only the subset of FEX profiles where all aerosol bins above 1.5 km (i.e. the lowest height used in the high channel Raman method lidar ratio retrieval) have directly-retrieved extinction. In this comparison, bias errors are 4.2% and -8.2% (relative to the RL) at TWP and SGP, respectively. We consider this agreement to be reasonably good considering that the sun photometer is measuring optical depth along a different path through the atmosphere and the lack of direct lidar ratio estimates from the RL at lower altitudes. Fig. 6.13b,d shows the same comparison but includes all profiles regardless of the type of extinction retrieval performed. The agreement here is very similar to the directly-retrieved extinction comparison an indication that the best-estimate methodology is capable of producing accurate estimates of aerosol extinction.

The overall biases of about 4–8% are considerably better than those found by Schmid et al. (2006) who concluded, through a comprehensive comparison of multiple instruments, that a 15–20% bias is typical among different measurements of visible optical depth and errors are likely larger in the ultra-violet. Turner et al. (2002), using the original RL extinction algorithm, performed a similar comparison at SGP finding a bias of about 30%.

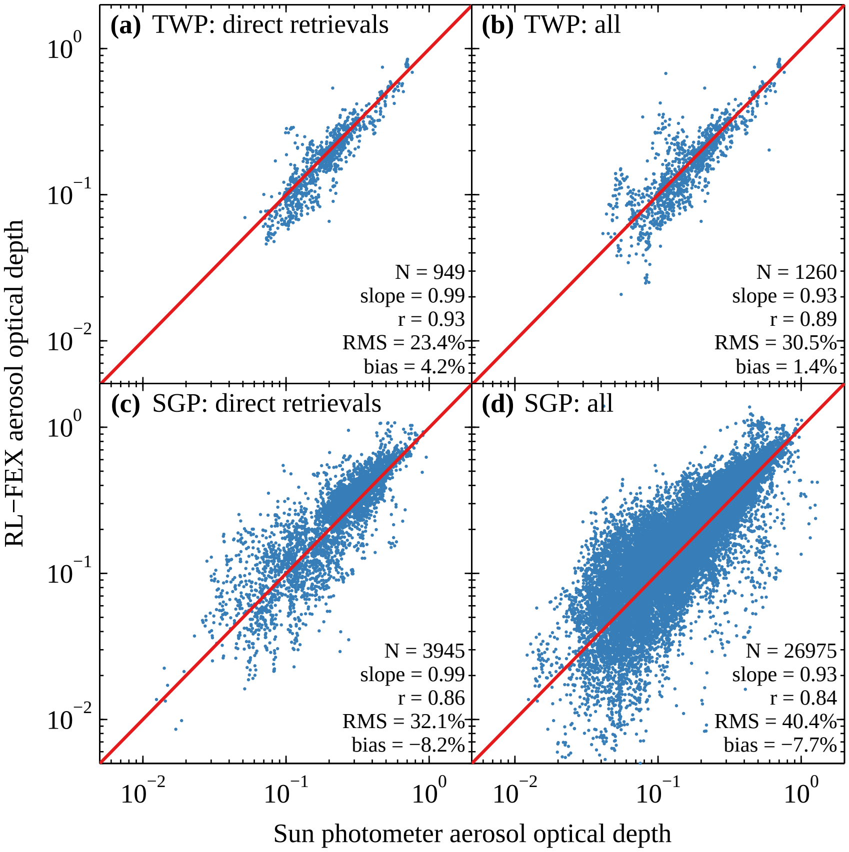

Figure 6.13: Comparison of aerosol optical depth derived from RL-FEX and a collocated sun photometer at the (a,b) TWP and (c,d) SGP site. Panels (a,c) are for the subset of profiles where the directly-retrieved extinction coefficients are available for all aerosol bins above 1.5 km and (b,d) for all profiles regardless of the type of retrieval used. The one-to-one line is shown in red. Summary statistics are given in the lower right of each panel: the sample size (N), the slope of the linear regression line, the correlation coefficient (r), the root-mean-squared error (RMS, relative to the mean RL optical depth), the bias error (mean difference relative to the mean RL optical depth).

6.6 Summary

Presented in this work is an automated retrieval of extinction from the ARM RL which is part 2 of the Feature detection and EXtinction retrieval (FEX) algorithm. Part 1 of this work is given in (Thorsen et al., 2014, Chapter 5) which focused on feature detection. The intent is to run FEX operationally within the ARM Data Management Facility (DMF) with the output being made available to the general user community via the ARM website (http://www.arm.gov/).

The objective of this work is to obtain the best-estimate of particulate backscatter and lidar ratios for all detected features. Depending on the SNR, the particulate backscatter is directly-determined from the scattering ratio derived from both the high/low elastic and high/low nitrogen channels, or from the Fernald solution to the elastic lidar equation using the best-estimate lidar ratio profile. The best-estimate lidar ratio profiles are directly-retrieved using a combination of the elastic and nitrogen channel signals with adaptive amounts of smoothing applied or the layer-averaged lidar ratio using the transmission-loss method. The uncertainty is required to be less than 30% for both types of retrievals. When this is not possible, directly-retrieved lidar ratios are used to inferred lidar ratios for the day being process. When neither directly-retrieved nor an inferred value can be determined, a climatological lidar ratio is used. Multiple-years of data at both the SGP and TWP show that climatological values of the lidar ratio are only necessary for less than about 5% of features, except for thin cirrus at the TWP where above 12 km around 20% of clouds use a climatological lidar ratio.

The process of retrieving extinction in FEX is supported by a classification of feature type into aerosol, water cloud, ice cloud, rain, or HOI. For the latter two feature types directly-retrieved lidar ratios are used to assist in their identification. The contribution of multiple scattering is explicitly considered in each range bins. We show that errors in extinction when ignoring multiple scattering are significant for hydrometeors: for clouds most corrections fall in the range from 0–30% while median errors in rain are about 35%. Errors in aerosol extinction due to multiple scattering are relatively small (±2%). The accuracy at both the TWP and SGP sites in aerosol optical depth is established through a comparison with collocated multiple-year sun photometer observations.

Chapter 7

CONCLUSION

This thesis started by investigating the accuracy of tropical cirrus cloud observations from elastic backscatter lidar datasets: the ground-based ARM MPLs and the CALIPSO satellite (Chapter 2). The radiative effect of tropical clouds from space-borne and ground-based remote sensors was then quantified by combining the aforementioned lidar observations with cloud radar observations (Chapter 3). The more advanced ARM RL was compared to both the MPL and CALIPSO to quantify its relative sensitivity and to identify diurnal biases in MPL and CALIPSO macrophysical properties (Chapter 4). Finally, recognizing the need for a retrieval algorithm to match the potential of the ARM RL, a new automated algorithm for feature detection and extinction retrieval was developed (Chapters 5 and 6). Here the major findings of each chapter are reviewed (section 7.1) and a discussion of possible future directions for work in this subject area are given (section 7.2).

7.1 Summary

Chapter 2 of this thesis examined statistics of CALIPSO and ground-based lidar observations over a 31 month period. Ground-based lidar observations were taken from the MPLs at the three ARM TWP sites: Manus, Nauru and Darwin. Analyzed for consistency in transparent profiles is the cloud occurrence, top height, base height, geometrical thickness, optical depth and the number of cloud layers per profile. For lower altitudes (< 7 km), the MPL cloud occurrence profiles are significantly larger and at higher altitudes (> 10 km), the CALIPSO occurrence profiles are significantly larger. About half the difference at higher altitudes is attributed to differences in spatial resolution. However, even after accounting for resolution differences, the CALIPSO cloud occurrence still remains significantly larger. During the daytime this discrepancy is even larger with the MPL detecting very few clouds at higher altitudes. It is also found that both CALIPSO and the MPL show that cirrus occur less frequently during the daytime. Other cloud properties beside cloud occurrence are compared for cirrus clouds only. Despite the lower frequency of occurrence of MPL cirrus, nighttime observations of cloud top and base heights typically show good agreement. But daytime MPL cloud tops and bases occur at significantly lower altitudes than those observed by CALIPSO. Cirrus geometrical thickness comparisons show similar agreement during both the nighttime and daytime with the same diurnal cycle present in both sets of observations: cirrus are thinner during the daytime than at night. Comparisons of cloud layer optical depths are made using four different retrieval techniques. Although the precise agreement in ice cloud optical depth varies between the four retrieval techniques, they mostly agree to within the 95% confidence level.

Chapter 3 assessed the accuracy of radiative heating and cloud radiative forcing profiles from July 2006 through December 2010 at the Darwin ARM site using ARM and A-train observations of clouds. The MPL and CALIPSO observations are supplemented by MMCR and CloudSat observation, respectively, to obtain cloud properties with combined radar/lidar retrievals used for ice clouds and radar only or lidar only retrievals for liquid clouds. Statistically significant differences up to 1.43 K/day exist between the mean ARM and A-train net cloud radiative forcing profiles. The largest differences occurs from about 12 to 17 km where the A-train cloud forcing is larger. These altitudes also correspond to large difference in lidar cloud occurrence profiles with CALIPSO detecting more clouds above 12 km than the MPL. To isolate the effects of various dataset differences on the radiative heating rate profiles a Monte-Carlo method is designed. Using this Monte-Carlo technique, new ARM and A-train datasets are created with the same mean cloud occurrence profile. In these modified datasets the maximum difference in net cloud forcing reduced from 1.43 K/day to 0.28 K/day at these altitudes— indicating that cloud occurrence differences alone account for most of the discrepancies between ARM and A-train cloud radiative forcing profiles. The Monte-Carlo method is further applied to isolate the effects of sampling and cloud-microphysical retrieval differences, both cause smaller, but not insignificant, differences relative to the cloud occurrence differences.

Chapter 4 takes a first-look at ARM RL to assess its potential for tropical cirrus observations. The sensitivity of the RL is shown to be a large improvement over the MPL with the RL and CALIPSO cirrus occurrence in transparent profiles exhibiting excellent agreement at all altitudes when day and night observations are considered together. The RL observations are shown to have the smallest increase in noise due to the solar background with approximately a factor of 2 increase— about 4 times less than CALIPSO and 12 times less than the MPL. Therefore, the RL observations are used to determine the validity of MPL and CALIPSO diurnal cycles. Specifically, the diurnal cycle of cirrus geometrical thickness is examined. In terms of median layer thickness the RL, MPL and CALIPSO agree best at night while during the day both the MPL and CALIPSO cirrus layers are significantly thinner than the RL observations. The hourly variation of MPL cirrus layer thickness is shown to be well correlated with the sun— cirrus become thinner as the sun rises and thicker as the sun sets. The twice-daily CALIPSO observations show a day/night difference with a similar magnitude to that of the MPL. However, cirrus observations from the RL show a relatively constant thickness throughout the day with no significant difference between day and night observations. Therefore, the CALIPSO and MPL observations of cirrus clouds are biased towards smaller geometrical thicknesses during the daytime due to solar background noise. Physically, the solar background noise hampers the detection of the more tenuous cloud top and/or base, causing the cloud to appear geometrically thinner.

Chapters 5 and 6 present an automated algorithm for Feature detection and EXtinction retrieval (FEX) for the ARM RL. During the analysis performed in Chapter 4 the current ARM data products were found to miss many cirrus clouds and therefore a cirrus mask was created from the depolarization ratio. Such poor cloud detection is to be expected since the ARM RL was originally designed to measure water vapor and aerosols, not clouds. Therefore the goal of FEX in Chapters 5 and 6 is to provide a new automated algorithm capable of providing accurate cloud and aerosol properties. While these chapters focused on one particular lidar system, the FEX framework is flexible enough to be extended to other Raman or HSRL systems that can intrinsically separate signal returns from molecules and particulates.

The feature detection approach described in Chapter 5 is to analyze multiple quantities— scattering ratios derived using elastic and nitrogen channel signals from two FOVs, the scattering ratio derived using only the elastic channel, and the total volume depolarization ratio— for the presence of features. Range-dependent detection thresholds are determined for each profile separately by calculating the expected noise in a clear-sky signal. Using multiple quantities is shown to provide a more comprehensive feature mask as each has specific advantages and disadvantages. The multiple quantities also allow for consistency checks to reduce the rate of false detections. The depolarization ratio is shown to be particularly effective at detecting thin cirrus due to the the strong contrast between molecular and typical in-cloud values. Performance of the feature detection by FEX is established by comparing to collocated MPL and CALIPSO observations. Good agreement is found with both instruments when a fair comparison is made, i.e. only using high SNR situations for the MPL comparison and using the same amount of averaging for the CALIPSO comparison.

The method used to obtain cloud and aerosol (particulate) extinction by FEX was presented in Chapter 6. The algorithm works towards retrieving the best-estimate of particulate backscatter and lidar ratios for all detected features. Depending on the SNR, the particulate backscatter is taken from the values directly-determined using the scattering ratio derived from both the high/low elastic and high/low nitrogen channels, or from the Fernald solution to the elastic lidar equation using the best-estimate lidar ratio profile. The best-estimate lidar ratio is constructed from direct-retrievals performed using either: profiles from the Raman method with adaptive amounts of smoothing applied, or layer-averaged values from the transmission-loss method. These directly-retrieved lidar ratios are used to infer values for the day being processed. Finally, when neither directly-retrieved nor an inferred value can be determined, a climatological lidar ratio is used. These climatological values are necessary for only about 5% of features, except for thin cirrus at the TWP site where above 12 km around 20% of clouds use a climatological lidar ratio. The contribution of multiple scattering is explicitly considered in each range bin as neglecting to do so results in significant errors for hydrometeors. Extinction errors in clouds range from 0–30% while median errors in rain are about 35% due to multiple scattering effects. The TWP and SGP aerosol optical depth from FEX is shown to agree to within 4–8% to collocated multiple-year sun photometer observations.

7.2 Future directions

The continuously operated, automated ARM RLs paired with FEX provides an enormous wealth of water vapor, temperature, aerosol and cloud data which is unmatched by other remote sensors. The intent is to run FEX operationally within the ARM Data Management Facility (DMF) with the output being made available to the general user community via the ARM website (http://www.arm.gov/). While the SGP RL's abilities to obtain water vapor and aerosol properties have been used in previous studies (e.g. Ferrare et al., 2001; Turner et al., 2001; Ferrare et al., 2006), little work using cloud properties has been performed outside of what is presented in this thesis. Much of the most novel work lies in this direction: analyzing RL cloud properties and pairing them with the aerosol, water vapor and temperature measurements also made by the RL. In addition, little work has been done with measurements made by the TWP RL. This TWP system will eventually be moved to Graciosa Island in the Azores. A new ARM RL is being installed for operation at Oliktok Point, Alaska eventually making it possible to investigate processes in four different climate regimes. The detailed and accurate nature of these RL measurements provide unique science opportunities. In this section several potential areas to explore are discussed.

7.2.1 Lidar ratio climatology

The lidar ratio is an indicator of the target's microphysical properties (e.g. Burton et al., 2014) and is essential for determining extinction profiles from elastic backscatter lidars, e.g. the MPL and CALIPSO. Since CALIPSO makes global observations, global observations of the lidar ratio need to be specified. For aerosol retrievals, CALIPSO's algorithms make a classification of aerosol type and assign a single lidar ratio based on a global climatology (Omar et al., 2009). However, this lidar ratio climatology is not derived from lidars. Instead AERONET sun photometer measurements are used to infer the lidar ratio (Cattrall et al., 2005), as there does not exist a comparable network of HSRL/Raman lidars. For ice clouds, a single lidar ratio of 25 sr is used (Young et al., 2008) based on a climatology from the transmission-loss method applied to an elastic backscatter lidar in the midlatitudes (Sassen and Comstock, 2001). The lidar ratio for liquid clouds is less variable than either ice and aerosols (see Chapter 6) and so an expected theoretical value is used by CALIPSO (Young et al., 2008).

Although other methods exist, such as modeling (e.g. Ackermann, 1998) or multi-angle lidar measurements (e.g. Reagan et al., 1988), the most direct and accurate way to get the lidar ratio is to use HSRL or Raman lidars. However, the complexity of operating a HSRL or RL limits many studies of aerosol extinction and lidar ratios to short time periods (Ferrare et al., 1998;

Franke et al., 2001; Rogers et al., 2009; McPherson et al., 2010). The ARM SGP RL was the first automated Raman lidar designed to operate continuously, allowing for more comprehensive observations of aerosol extinction over the SGP site (Ferrare et al., 2001; Turner et al., 2001; Ferrare et al., 2006). In 2000, the European Aerosol Research Lidar Network (EARLINET; Matthais et al., 2004) was established with multiple sites across Europe the majority of which are equipment with Raman lidars. While not continuously operated like the ARM RL systems, participants in EARLINET perform observations on a fixed schedule to create an unbiased dataset of aerosol properties. Data from EARLINET has been used by a number of researchers allowing for an extensive depiction of aerosol properties on a continental scale (Mattis et al., 2004; Matthias et al., 2004; Balis, 2004; Amiridis et al., 2005; Sicard et al., 2011; McAuliffe and Ruth, 2013; Preiler et al., 2013).

All studies of vertically-resolved cloud extinction using HSRLs or RLs occur over very limited time periods: on the time scale of a few months or less (Grund and Eloranta, 1990; Ansmann et al., 1992; Reichardt, 1999; Eloranta et al., 2001; Reichardt et al., 2002; Sakai et al., 2003; Whiteman et al., 2004; Immler et al., 2007; Mona et al., 2007). The development of FEX given in Chapters 5 and 6 allows for the possibility to examine a much more comprehensive multi-year set of direct observations of cloud extinction and lidar ratios. Therefore a useful future study would be to analyze the climatology of ice cloud extinction and lidar ratios. Of interest is examining the vertical, seasonal, diurnal and regional dependence as none of these characteristics are well known. Delineating the RL ice cloud data by synoptic state (e.g. Evans et al., 2012) could prove insightful since ice cloud optical properties should vary depending on the mechanism which generated the cloud. For further context, the relationship of ice optical properties with microphysical parameters as measured by the RL (temperature, relative humidity and depolarization) could be examined. It would imperative to compare these lidar ratio results with previous literature estimates.

The TWP site is of particular interest as existing analysis of HSRL or RL-derived tropical cloud extinction is limited to 5 months of observations total across two studies (Whiteman et al., 2004; Immler et al., 2007). Even though HSRL/RL aerosol observations have been studied more thoroughly, the characterization of tropical aerosols has been limited to a only a couple of studies (Franke et al., 2001; Rogers et al., 2009).

7.2.2 Validation of spaceborne extinction retrievals

Accurate knowledge of the radiation budget of the Earth system (Stephens et al., 2012) is crucial to understanding responses of the climate system to greenhouse gas changes. In recent years, clouds and aerosols observations from the CALIPSO and CloudSat satellite have giving us better insight into global estimates of the surface radiation budget (Kato et al., 2011). Such calculations of the direct radiative effect of aerosols and clouds are dependent on accurate extinction retrievals. Typically, validation exercises use ground-based instruments as "truth" to assess the capabilities of satellite remote sensors. Although, as shown in this thesis, a MPL is not the best tool for such an evaluation of CALIPSO. And, as mentioned previously, many HSRL and RL campaigns are short-lived making comparisons to CALIPSO focused more on case studies than statistics (e.g. McPherson et al., 2010; Pappalardo et al., 2010; Wandinger et al., 2010; Rogers et al., 2011; Tesche et al., 2013; Burton et al., 2013; Kanitz et al., 2014; Kacenelenbogen et al., 2014). The large size of the ARM RL-FEX dataset allows for evaluation of CALIPSO aerosol and cloud extinction retrieval in two (and soon to be four) climate regimes over a wide range of conditions. Useful future work would be to compare RL-FEX cloud and aerosol extinction profiles to those from CALIPSO using multiple years of data. The proposed characterization of the lidar ratio climatology would help determine if potential discrepancies could be traced to unresolved lidar ratio variability by CALIPSO. For aerosol extinction, a focus would be on determining if extinction differences could be traced to a poor classification of aerosol type by CALIPSO since this can result in large differences in the retrieved extinction. Beside large statistical comparisons, individual case studies have the utility to pin down specific situations where CALIPSO retrievals may have issues. Since exactly coincident CALIPSO and RL cases are rare, this proposed work would develop a methodology to transform the 2-dimensional CALIPSO and ARM RL scenes onto the same grid using use forward and backward trajectories.

Some focus in this proposed work would also be on assessing CALIPSO's ability to separate clouds from aerosols (Liu et al., 2009). This is a more challenging task for CALIPSO due to the large distance between the target and the sensor. A much clearer separation of clouds from aerosols can be had from the ARM RL due to far superior SNR near the surface and the higher resolution of the data. Cloud contamination in aerosol retrievals is an even larger issue for passive sensors like MODIS or MISR which do not have the luxury of finely-resolved height information. For example Kaufman et al. (2005) found that cloud contamination in MODIS aerosol retrievals cause an optical depth increase of 0.025. The study of Kaufman et al. (2005) and many others (e.g. Chu, 2002; Zhang, 2005; Yu et al., 2006; Kahn et al., 2007; Mishchenko et al., 2010) rely on AERONET observations to assess passive satellite aerosol retrievals. However AERONET itself can be affected by cloud contamination (see section 7.2.4). Therefore in addition to a CALIPSO comparison, it would be informative to compare aerosol optical depth from MODIS and MISR to the ARM RL.

7.2.3 Radiative impact of lidar retrieval assumptions

The different methods of extinction retrieval performed by FEX (see Chapter 6) provides the first opportunity to comprehensively quantify potential errors in the direct radiative effect of clouds and aerosols when extinction is inferred from an elastic backscatter lidar. In such a study, heating rate profiles calculated using the FEX best-estimate extinction would be used as a reference. These would be compared to heating rate profiles calculated from extinction retrieved exclusively using the elastic channel signal of the RL. First, the efficacy of using a layer-averaged value of the lidar ratio from transmission-loss method would be investigated along with an analysis of how many layers the transmission-loss method can be successfully applied to. This comparison would establish how essential it is to know the vertical variation of the lidar ratio. Second, various values of assumed lidar ratio profiles would be used in the Fernald solution to the elastic lidar equation. This would evaluate how finely the lidar ratio must be specified for an elastic backscatter lidar. Specifically radiative heating rate calculations would be performed using a single climatological mean, a seasonal mean, and a monthly mean value of the lidar ratio for each feature type. These mean values will be determined from those lidar ratios directly-retrieved by FEX. An additional climatological value will also be tested, but taken from observations made at the other ARM site: i.e. the mean SGP value will be used for TWP calculations and vice versa to test the importance of regional variability. Instantaneous maximum errors in individual heating rate profiles will be examined along with potential biases in the mean heating rate profiles and the impact on inferred surface and TOA fluxes.

7.2.4 Evaluation of AERONET cloud screening

Global-wide aerosol observations from AERONET (Holben et al., 1998) are commonly used as the reference for satellite validation exercises (e.g. Chu, 2002; Zhang, 2005; Kaufman et al., 2005; Yu et al., 2006; Kahn et al., 2007; Mishchenko et al., 2010) and are also used to derive lidar ratio estimates for CALIPSO retrievals (Omar et al., 2009). While the measurement of optical depth from a sun photometer is relatively straightforward, determining if that optical depth is solely due to the presence of aerosols is not. A cloud screening process is applied to AERONET data (Smirnov et al., 2000) by flagging periods with high optical depth variability as cloudy. However clouds, especially thin cirrus like those that commonly occur in the tropics, can go undetected by this screening process. Using collocated MPL data at a single location Huang et al. (2011) and Chew et al. (2011) estimated that cloud contamination causes approximately a 5% and 14% bias, respectively, in AERONET optical depth. In a more comprehensive analysis also using MPL data of multiple AERONET sites Huang et al. (2012) found that about 5% of AERONET data are contaminated with cirrus although the overall impact on the inferred aerosol optical depth was not quantified in that study. However, as shown in this thesis, the MPL is not very sensitive to tropical thin cirrus particularly during the daytime when AERONET makes its measurements. Therefore using MPL observations to quantify AERONET cloud contamination, as all the aforementioned studies do, may underestimate its effect. The more sensitive ARM RL would provide a better assessment of AERONET cloud contamination.

In this thesis sun photometers (both which are part of AERONET) were used to validate FEX's aerosol optical depth (Fig. 6.13). In this comparison, the cloud screened AERONET data was used and an additional screening for clouds was performed using RL-FEX's cloud mask. Just using the AERONET cloud screening alone increases biases in this comparison by 18% and 3% at the TWP and SGP site, respectively: and indication of the poor performance of AERONET cloud screening at a tropical site like the TWP. However, no attempt was made to account for the line-of-sight differences between the instruments, something that would need to be examined in a potential future study. Furthermore, such a comparison with the RL would provide a better estimate of the optical depth bias introduced by the presence of clouds since the cloud optical depth can be more accurately retrieved. Attempts have been made to improve AERONET's cloud screening (Kaufman et al., 2006; Michalsky et al., 2010) although such studies did not evaluate their work against a lidar. Kaufman et al. (2006) found that cloud screening can actually be too rigorous at times causing biases in climatologies derived from AERONET. In the proposed work, an effort would be made to design a new cloud screening algorithm for AERONET using the RL as validation. Furthermore, the algorithm will focus on attempting to refine a method using MPL measurements as there exist a subset of AERONET sites that are also MPLNET sites, allowing for the potential algorithm to be useful for global climatologies.

7.2.5 Improvements to the FEX algorithm

One possible improvement to the current FEX algorithm is to implement multi-resolution feature detection (e.g. Vaughan et al., 2009). This could be achieved by adding an additional loop to the feature detection process which would start by detecting features and retrieving extinction at the highest possible resolution (10 s and 7.5 m), then removing the signal due to those detected features before moving on to larger amounts of averaging. A multi-resolution retrieval provides the added benefit of detecting features without unnecessarily distorting them since the minimal amount of averaging is used. In addition, the feature classification could be improved by using the RL observations themselves to derive temperature and wet-bulb temperature instead of radiosondes to give a more refined view of cloud phase. Determining cloud phase could also be improved by adding the capability to calculate the expected depolarization induced by multiple scattering through liquid drops to the Hogan (2006) model. This would eliminate the need to use the empirical relationship between multiple scattering and depolarization that is currently used by FEX. The multiple scattering signal itself could be exploited for the retrieval of cloud effective radius. Malinka and Zege (2003) showed that an analytical expression that includes the effects of multiple scattering can be derived for the nitrogen channel signal. With this analytical solution and the 2 ARM RL FOVs a retrieval of effective radius could be designed (e.g. Schmidt et al., 2013).

7.2.6 Synergy with radars

By design, FEX only uses observations from the RL itself and readily-available radiosonde observations. However, the ARM sites have many other remote sensing instruments. Future studies would naturally combine RL-FEX with other remote sensors with the combination of radar and lidar being particularly useful. Using these active instruments in tandem allows for the retrieval of ice cloud effective radius (e.g. Wang and Sassen, 2002; Delanoë and Hogan, 2008) and therefore also ice water content (Fu, 1996) providing everything needed for an accurate radiative heating rate calculation. Higher-quality radar+lidar retrievals will be made possible by the more accurate extinction retrievals provided RL-FEX and the new Ka-band ARM zenith radar (KAZR Widener et al., 2012), which is more sensitive than it predecessor the MMCR. As with using the MPL to evaluate the sensitivity of the MMCR (Chapter 3), a similar comparison using the next-generation-combination of the RL and KAZR would be needed to quantify undetected cloud by the KAZR and its radiative importance.

The addition of KAZR reflectively and spectral measurements to RL depolarization, backscatter and lidar ratios could provide the basis for a detailed feature classification algorithm (e.g. Shupe, 2007; Ceccaldi et al., 2013). A classification like this could be used to study the details of mixed phase clouds which are poorly replicated by climate and cloud-resolving models alike (e.g. Klein et al., 2009; Morrison et al., 2009; Fan et al., 2011; English et al., 2014). Many researchers typically use just radars for mixed-phase observations (e.g. Rambukkange et al., 2011; Luke et al., 2010) due to the limitation of lidars to penetrate thicker liquid clouds. However, the more powerful laser beam of the RL may alleviate some of these limitations allowing for the addition of depolarization to separate liquid from ice. Data from the new NSA RL will be of particular interest as high-latitude mixed-phase clouds strongly influence the Arctic's radiation budget (e.g. Shupe et al., 2006).

BIBLIOGRAPHY

Ackerman, S. A., R. E. Holz, R. Frey, E. W. Eloranta, B. C. Maddux, and M. McGill, 2008: Cloud Detection with MODIS. Part II: Validation. *J. Atmos. Oceanic Technol.*, **25**, 1073–1086, doi: 10.1175/2007JTECHA1053.1.

Ackerman, T. P., K.-N. Liou, F. P. J. Valero, and L. Pfister, 1988: Heating Rates in Tropical Anvils. *J. Atmos. Sci.*, **45 (10)**, 1606–1623, doi: 10.1175/1520-0469(1988)045<1606:HRITA>2.0.CO;2.

Ackerman, T. P., and G. M. Stokes, 2003: The Atmospheric Radiation Measurement Program. *Physics Today*, **56 (1)**, 38–44, doi: 10.1063/1.1554135.

Ackermann, J., 1998: The Extinction-to-Backscatter Ratio of Tropospheric Aerosol: A Numerical Study. *J. Atmos. Oceanic Technol.*, **15 (4)**, 1043–1050, doi: 10.1175/1520-0426(1998)015<1043:tetbro>2.0.co;2.

Alvarez, J. M., M. A. Vaughan, C. A. Hostetler, W. H. Hunt, and D. M. Winker, 2006: Calibration Technique for Polarization-Sensitive Lidars. *J. Atmos. Oceanic Technol.*, **23 (5)**, 683–699, doi: 10.1175/JTECH1872.1.

Amiridis, V., D. S. Balis, S. Kazadzis, A. Bais, E. Giannakaki, A. Papayannis, and C. Zerefos, 2005: Four-year aerosol observations with a Raman lidar at Thessaloniki, Greece, in the framework of European Aerosol Research Lidar Network (EARLINET). *J. Geophys. Res.*, **110 (D21)**, doi: 10.1029/2005jd006190.

Anderson, T. L., 2003: Variability of aerosol optical properties derived from in situ aircraft measurements during ACE-Asia. *J. Geophys. Res.*, **108 (D23)**, ACE 151ACE 1519, doi: 10.1029/2002jd003247.

Anselmo, T., and Coauthors, 2006: Cloud Aerosol LIDAR Infrared Pathfinder Satellite Observations (CALIPSO). Tech. rep., Data Management System and Data Products Catalog, CALIPSO doc., rel. 2.3, Doc. PC-SCI-503.

Ansmann, A., M. Riebesell, and C. Weitkamp, 1990: Measurement of atmospheric aerosol extinction profiles with a Raman lidar. *Opt. Lett.*, **15 (13)**, 746–748, doi: 10.1364/OL.15.000746.

Ansmann, A., U. Wandinger, M. Riebesell, C. Weitkamp, and W. Michaelis, 1992: Independent measurement of extinction and backscatter profiles in cirrus clouds by using a combined raman elastic-backscatter lidar. *Appl. Opt.*, **31 (33)**, 7113, doi: 10.1364/ao.31.007113.

Austin, R. T., A. J. Heymsfield, and G. L. Stephens, 2009: Retrieval of ice cloud microphysical parameters using the CloudSat millimeter-wave radar and temperature. *J. Geophys. Res.*, **114**, D00A23, doi: 10.1029/2008JD010049.

Balis, D. S., 2004: Optical properties of Saharan dust layers as detected by a Raman lidar at Thessaloniki, Greece. *Geophys. Res. Lett.*, **31 (13)**, doi: 10.1029/2004gl019881.

Bankert, R. L., 1994: Cloud Classification of AVHRR Imagery in Maritime Regions Using a Probabilistic Neural Network. *J. Appl. Meteor.*, **33 (8)**, 909918, doi: 10.1175/1520-0450(1994)033<0909:ccoaii>2.0.co;2.

Barnes, W., T. Pagano, and V. Salomonson, 1998: Prelaunch characteristics of the Moderate Resolution Imaging Spectroradiometer (MODIS) on EOS-AM1. *IEEE Trans. Geosci. Remote Sens.*, **36 (4)**, 1088–1100, doi: 10.1109/36.700993.

Baum, B. A., V. Tovinkere, J. Titlow, and R. M. Welch, 1997: Automated Cloud Classification of Global AVHRR Data Using a Fuzzy Logic Approach. *J. Appl. Meteor.*, **36 (11)**, 15191540, doi: 10.1175/1520-0450(1997)036<1519:accoga>2.0.co;2.

Beard, K. V., 1976: Terminal Velocity and Shape of Cloud and Precipitation Drops Aloft. *J. Atmos. Sci.*, **33 (5)**, 851–864, doi: 10.1175/1520-0469(1976)033<0851:TVASOC>2.0.CO;2.

Behrendt, A., and T. Nakamura, 2002: Calculation of the calibration constant of polarization lidar and its dependency on atmospheric temperature. *Opt. Express*, **10 (16)**, 805–817, doi: 10.1364/OE.10.000805.

Bevington, P., and D. Robinson, 2002: *Data Reduction and Error Analysis for the Physical Sciences*. 3rd ed., McGraw-Hill.

Borg, L. A., R. E. Holz, and D. D. Turner, 2011: Investigating cloud radar sensitivity to optically thin cirrus using collocated Raman lidar observations. *Geophys. Res. Lett.*, **38 (5)**, doi: 10.1029/2010GL046365.

Bringi, V. N., and V. Chandrasekar, 2001: *Polarimetric Doppler Weather Radar: Principles and Applications*. Cambridge University Press, 636 pp.

Bringi, V. N., V. Chandrasekar, J. Hubbert, E. Gorgucci, W. L. Randeu, and M. Schoenhuber, 2003: Raindrop Size Distribution in Different Climatic Regimes from Disdrometer and Dual-Polarized Radar Analysis. *J. Atmos. Sci.*, **60 (2)**, 354–365, doi: 10.1175/1520-0469(2003)060<0354:RSDIDC>2.0.CO;2.

Bucholtz, A., 1995: Rayleigh-scattering calculations for the terrestrial atmosphere. *Appl. Opt.*, **34 (15)**, 2765–2773, doi: 10.1364/AO.34.002765.

Burton, S. P., R. A. Ferrare, M. A. Vaughan, A. H. Omar, R. R. Rogers, C. A. Hostetler, and J. W. Hair, 2013: Aerosol classification from airborne HSRL and comparisons with the CALIPSO vertical feature mask. *Atmos. Meas. Tech.*, **6 (5)**, 13971412, doi: 10.5194/amt-6-1397-2013.

Burton, S. P., M. A. Vaughan, R. A. Ferrare, and C. A. Hostetler, 2014: Separating mixtures of aerosol types in airborne High Spectral Resolution Lidar data. *Atmos. Meas. Tech.*, **7 (2)**, 419436, doi: 10.5194/amt-7-419-2014.

Campbell, J. R., D. L. Hlavka, E. J. Welton, C. J. Flynn, D. D. Turner, J. D. Spinhirne, V. S. Scott, and I. H. Hwang, 2002: Full-Time, Eye-Safe Cloud and Aerosol Lidar Observation at Atmospheric Radiation Measurement Program Sites: Instruments and Data Processing. *J. Atmos. Oceanic Technol.*, **19**, 431, doi: 10.1175/1520-0426(2002)019<0431:FTESCA>2.0.CO;2.

Carswell, A. I., and S. R. Pal, 1980: Polarization anisotropy in lidar multiple scattering from clouds. *Appl. Opt.*, **19 (24)**, 4123–4126, doi: 10.1364/AO.19.004123.

Cattrall, C., J. Reagan, K. Thome, and O. Dubovik, 2005: Variability of aerosol and spectral lidar and backscatter and extinction ratios of key aerosol types derived from selected Aerosol Robotic Network locations. *J. Geophys. Res.*, **110 (D10)**, doi: 10.1029/2004jd005124.

Ceccaldi, M., J. Delano, R. J. Hogan, N. L. Pounder, A. Protat, and J. Pelon, 2013: From CloudSat-CALIPSO to EarthCare: Evolution of the DARDAR cloud classification and its comparison to airborne radar-lidar observations. *J. Geophys. Res.*, **118 (14)**, 79627981, doi: 10.1002/jgrd.50579.

Chen, W.-N., C.-W. Chiang, and J.-B. Nee, 2002: Lidar Ratio and Depolarization Ratio for Cirrus Clouds. *Appl. Opt.*, **41 (30)**, 6470–6476, doi: 10.1364/AO.41.006470.

Chepfer, H., G. Cesana, D. Winker, B. Getzewich, M. Vaughan, and Z. Liu, 2012: Comparison of two different cloud climatologies derived from CALIOP attenuated backscattered measurements (Level 1): the CALIPSO-ST and the CALIPSO-GOCCP. *J. Atmos. Oceanic Technol.*, doi: 10.1175/JTECH-D-12-00057.1.

Chew, B. N., J. R. Campbell, J. S. Reid, D. M. Giles, E. J. Welton, S. V. Salinas, and S. C. Liew, 2011: Tropical cirrus cloud contamination in sun photometer data. *Atmos. Environ.*, **45 (37)**, 67246731, doi: 10.1016/j.atmosenv.2011.08.017.

Chu, D. A., 2002: Validation of MODIS aerosol optical depth retrieval over land. *Geophys. Res. Lett.*, **29 (12)**, doi: 10.1029/2001gl013205.

Clothiaux, E. E., T. P. Ackerman, G. G. Mace, K. P. Moran, R. T. Marchand, M. A. Miller, and B. E. Martner, 2000: Objective determination of cloud heights and radar reflectivities using a combination of active remote sensors at the ARM CART sites. *J. Appl. Meteor.*, **39 (5)**, 645–665, doi: 10.1175/1520-0450(2000)039<0645:ODOCHA>2.0.CO;2.

Clothiaux, E. E., G. G. Mace, T. P. Ackerman, T. J. Kane, J. D. Spinhirne, and V. S. Scott, 1998: An Automated Algorithm for Detection of Hydrometeor Returns in Micropulse Lidar Data. *J. Atmos. Oceanic Technol.*, **15 (4)**, 1035–1042, doi: 10.1175/1520-0426(1998)015<1035:AAAFDO>2.0.CO;2.

Clothiaux, E. E., and Coauthors, 1999: The Atmospheric Radiation Measurement Program Cloud Radars: Operational Modes. *J. Atmos. Oceanic Technol.*, **16 (7)**, 819–827, doi: 10.1175/1520-0426(1999)016<0819:TARMPC>2.0.CO;2.

Comstock, J., A. Protat, S. A. McFarlane, J. Delanoë, and M. Deng, 2013: Assessment of Uncertainty in Cloud Radiative Effects and Heating Rates through Retrieval Algorithm Differences: Analysis using 3-years of ARM data at Darwin, Australia. *J. Geophys. Res.*, **118**, 4549–4571, doi: 10.1002/jgrd.50404.

Comstock, J. M., T. P. Ackerman, and G. G. Mace, 2002: Ground-based lidar and radar remote sensing of tropical cirrus clouds at Nauru Island: Cloud statistics and radiative impacts. *J. Geophys. Res.*, **107**, doi: 10.1029/2002JD002203.

Comstock, J. M., and K. Sassen, 2001: Retrieval of Cirrus Cloud Radiative and Backscattering Properties Using Combined Lidar and Infrared Radiometer (LIRAD) Measurements. *J. Atmos. Oceanic Technol.*, **18**, 1658–1673, doi: 10.1175/1520-0426(2001)018<1658:ROCCRA>2.0.CO;2.

Cooney, J., J. Orr, and C. Tomasetti, 1969: Measurements Separating the Gaseous and Aerosol Components of Laser Atmospheric Backscatter. *Nature*, **224**, 1098–1099, doi: 10.1038/2241098a0.

Corti, T., B. P. Luo, T. Peter, H. Vomel, and Q. Fu, 2005: Mean radiative energy balance and vertical mass fluxes in the equatorial upper troposphere and lower stratosphere. *Geophys. Res. Lett.*, **32 (6)**, L06 802, doi: 10.1029/2004GL021889.

Coulter, R., 2012: Micropulse Lidar (MPL) Handbook. Tech. Rep. DOE/SC-ARM/TR-019, U.S. Department of Energy.

De Tomasi, F., A. Blanco, and M. R. Perrone, 2003: Raman Lidar Monitoring of Extinction and Backscattering of African Dust Layers and Dust Characterization. *Appl. Opt.*, **42 (9)**, 1699, doi: 10.1364/ao.42.001699.

Dee, D. P., and Coauthors, 2011: The ERA-Interim reanalysis: configuration and performance of the data assimilation system. *Quart. J. Roy. Meteor. Soc.*, **137 (656)**, 553–597, doi: 10.1002/qj.828.

Delanoë, J., and R. J. Hogan, 2008: A variational scheme for retrieving ice cloud properties from combined radar, lidar, and infrared radiometer. *J. Geophys. Res.*, **113 (D7)**, D07 204, doi: 10.1029/2007JD009000.

Delanoë, J., and R. J. Hogan, 2010: Combined CloudSat-CALIPSO-MODIS retrievals of the properties of ice clouds. *J. Geophys. Res.*, **115**, D00H29, doi: 10.1029/2009JD012346.

Dessler, A. E., and P. Yang, 2003: The Distribution of Tropical Thin Cirrus Clouds Inferred from Terra MODIS Data. *J. Climate*, **16**, 1241–1247, doi: 10.1175/1520-0442(2003)16<1241:TDOTTC>2.0.CO;2.

Dinh, T. P., D. R. Durran, and T. P. Ackerman, 2010: Maintenance of tropical tropopause layer cirrus. *J. Geophys. Res.*, **115**, D02 104, doi: 10.1029/2009JD012735.

Dubovik, O., and Coauthors, 2006: Application of spheroid models to account for aerosol particle nonsphericity in remote sensing of desert dust. *J. Geophys. Res.*, **111 (D11)**, doi: 10.1029/2005jd006619.

Dupont, J.-C., M. Haeffelin, Y. Morille, J. M. Comstock, C. Flynn, C. N. Long, C. Sivaraman, and R. K. Newson, 2011: Cloud properties derived from two lidars over the ARM SGP site. *Geophys. Res. Lett.*, **38 (8)**, doi: 10.1029/2010GL046274.

Dupont, J.-C., and Coauthors, 2010: Macrophysical and optical properties of midlatitude cirrus clouds from four ground-based lidars and collocated CALIOP observations. *J. Geophys. Res.*, **115**, D00H24, doi: 10.1029/2009JD011943.

Efron, B., 1982: *The jackknife, the bootstrap and other resampling plans*, Vol. 38. SIAM, Philadelphia, PA, USA, 1-9 pp.

Eloranta, E. W., 1998: Practical Model for the Calculation of Multiply Scattered Lidar Returns. *Appl. Opt.*, **37 (12)**, 2464–2472, doi: 10.1364/AO.37.002464.

Eloranta, E. W., R. E. Kuehn, and R. E. Holz, 2001: Measurements of backscatter phase function and depolarization in cirrus clouds made with the university of wisconsin high spectral resolution lidar. *Advances in Laser Remote Sensing: Selected Papers Presented at the 20th International Laser Radar Conference*, A. Dabas, C. Loth, and J. Pelon, Eds., 255–258.

English, J. M., J. E. Kay, A. Gettelman, X. Liu, Y. Wang, Y. Zhang, and H. Chepfer, 2014: Contributions of Clouds, Surface Albedos, and Mixed-Phase Ice Nucleation Schemes to Arctic Radiation Biases in CAM5. *J. Climate*, **27 (13)**, 51745197, doi: 10.1175/jcli-d-13-00608.1.

Evans, S. M., R. T. Marchand, T. P. Ackerman, and N. Beagley, 2012: Identification and analysis of atmospheric states and associated cloud properties for Darwin, Australia. *J. Geophys. Res.*, **117 (D6)**, doi: 10.1029/2011JD017010.

Fan, J., S. Ghan, M. Ovchinnikov, X. Liu, P. J. Rasch, and A. Korolev, 2011: Representation of Arctic mixed-phase clouds and the Wegener-Bergeron-Findeisen process in climate models: Perspectives from a cloud-resolving study. *J. Geophys. Res.*, **116**, doi: 10.1029/2010jd015375.

Feldman, D. R., T. S. L'Ecuyer, K. N. Liou, and Y. L. Yung, 2008: Remote sensing of tropical tropopause layer radiation balance using A-train measurements. *J. Geophys. Res.*, **113 (D21)**, D21 113, doi: 10.1029/2008JD010158.

Fernald, F. G., 1984: Analysis of atmospheric lidar observations: some comments. *Appl. Opt.*, **23 (5)**, 652–653, doi: 10.1364/AO.23.000652.

Ferrare, R., and Coauthors, 2006: Evaluation of daytime measurements of aerosols and water vapor made by an operational Raman lidar over the Southern Great Plains. *J. Geophys. Res.*, **111 (D5)**, doi: 10.1029/2005JD005836.

Ferrare, R. A., S. H. Melfi, D. N. Whiteman, K. D. Evans, M. Poellot, and Y. J. Kaufman, 1998: Raman lidar measurements of aerosol extinction and backscattering: 2. Derivation of aerosol real refractive index, single-scattering albedo, and humidification factor using Raman lidar and aircraft size distribution measurements. *J. Geophys. Res.*, **103 (D16)**, 19 673, doi: 10.1029/98jd01647.

Ferrare, R. A., D. D. Turner, L. H. Brasseur, W. F. Feltz, O. Dubovik, and T. P. Tooman, 2001: Raman lidar measurements of the aerosol extinction-to-backscatter ratio over the Southern Great Plains. *J. Geophys. Res.*, **106 (D17)**, 20 333, doi: 10.1029/2000jd000144.

Foot, J. S., 1988: Some Observations of the Optical-properties of Clouds. 2. Cirrus. *Quart. J. Roy. Meteor. Soc.*, **114 (479)**, 145–164, doi: 10.1002/qj.49711447907.

Franke, K., A. Ansmann, D. Mller, D. Althausen, F. Wagner, and R. Scheele, 2001: One-year observations of particle lidar ratio over the tropical Indian Ocean with Raman lidar. *Geophys. Res. Lett.*, **28 (24)**, 45594562, doi: 10.1029/2001gl013671.

Fu, Q., 1996: An Accurate Parameterization of the Solar Radiative Properties of Cirrus Clouds for Climate Models. *J. Climate*, **9**, 2058–2082, doi: 10.1175/1520-0442(1996)009<2058:AAPOTS>2.0.CO;2.

Fu, Q., M. Baker, and D. L. Hartmann, 2002: Tropical cirrus and water vapor: an effective Earth infrared iris feedback? *Atmos. Chem. Phys.*, **2 (1)**, 31–37, doi: 10.5194/acp-2-31-2002.

Fu, Q., B. Carlin, and G. Mace, 2000: Cirrus horizontal inhomogeneity and OLR bias. *Geophys. Res. Lett.*, **27 (20)**, 3341–3344, doi: 10.1029/2000GL011944.

Fu, Q., Y. Hu, and Q. Yang, 2007: Identifying the top of the tropical tropopause layer from vertical mass flux analysis and CALIPSO lidar cloud observations. *Geophys. Res. Lett.*, **34**, L14 813, doi: 10.1029/2007GL030099.

Fu, Q., and K. Liou, 1992: On the Correlated k-Distribution Method for Radiative Transfer in Nonhomogenecous Atmospheres. *J. Atmos. Sci.*, **49**, 2139–2156, doi: 10.1175/1520-0469(1992)049<2139:OTCDMF>2.0.CO;2.

Fu, Q., and K. Liou, 1993: Parameterization of the radiative properties of cirrus clouds. *J. Atmos. Sci.*, **50**, 2008–2025, doi: 10.1175/1520-0469(1993)050<2008:POTRPO>2.0.CO;2.

Fu, Q., P. Yang, and W. B. Sun, 1998: An Accurate Parameterization of the Infrared Radiative Properties of Cirrus Clouds for Climate Models. *J. Climate*, **11**, 2223–2237, doi: 10.1175/1520-0442(1998)011<2223:AAPOTI>2.0.CO;2.

Fueglistaler, S., and Q. Fu, 2006: Impact of clouds on radiative heating rates in the tropical lower stratosphere. *J. Geophys. Res.*, **111 (D23)**, D23 202, doi: 10.1029/2006JD007273.

Gettelman, A., P. M. D. Forster, M. Fujiwara, Q. Fu, H. Vomel, L. K. Gohar, C. Johanson, and M. Ammerman, 2004: Radiation balance of the tropical tropopause layer. *J. Geophys. Res.*, **109 (D7)**, D07 103, doi: 10.1029/2003JD004190.

Giangrande, S. E., E. P. Luke, and P. Kollias, 2012: Characterization of Vertical Velocity and Drop Size Distribution Parameters in Widespread Precipitation at ARM Facilities. *J. Appl. Meteor. Climatol.*, **51 (2)**, 380391, doi: 10.1175/jamc-d-10-05000.1.

Gobbi, G. P., 1998: Polarization Lidar Returns from Aerosols and Thin Clouds: a Framework for the Analysis. *Appl. Opt.*, **37 (24)**, 5505–5508, doi: 10.1364/AO.37.005505.

Goldsmith, J. E. M., F. H. Blair, S. E. Bisson, and D. D. Turner, 1998: Turn-Key Raman Lidar for Profiling Atmospheric Water Vapor, Clouds, and Aerosols. *Appl. Opt.*, **37 (21)**, 4979–4990, doi: 10.1364/AO.37.004979.

Grund, C. J., and E. W. Eloranta, 1990: The 2728 October 1986 FIRE IFO Cirrus Case Study: Cloud Optical Properties Determined by High Spectral Resolution Lidar. *Mon. Wea. Rev.*, **118 (11)**, 23442355, doi: 10.1175/1520-0493(1990)118<2344:toficc>2.0.co;2.

Grund, C. J., and E. W. Eloranta, 1991: University of Wisconsin High Spectral Resolution Lidar. *Opt. Eng.*, **30**, 6–12.

Hair, J. W., and Coauthors, 2008: Airborne High Spectral Resolution Lidar for profiling aerosol optical properties. *Appl. Opt.*, **47 (36)**, 6734–6752, doi: 10.1364/AO.47.006734.

Haladay, T., and G. Stephens, 2009: Characteristics of tropical thin cirrus clouds deduced from joint CloudSat and CALIPSO observations. *J. Geophys. Res.*, **114**, D00A25, doi: 10.1029/2008JD010675.

Hall, T. J., and T. H. Vonder Haar, 1999: The diurnal cycle of west Pacific deep convection and its relation to the spatial and temporal variation of tropical MCSs. *J. Atmos. Sci.*, **56 (19)**, 3401–3415, doi: 10.1175/1520-0469(1999)056<3401:TDCOWP>2.0.CO;2.

Hartmann, D., J. Holton, and Q. Fu, 2001: The heat balance of the tropical tropopause, cirrus, and stratospheric dehydration. *Geophys. Res. Lett.*, **28 (10)**, 1969–1972, doi: 10.1029/2000GL012833.

Henderson, D., T. L'Ecuyer, D. Vane, G. Stephens, and D. Reinke, 2011: Level 2B Fluxes and Heating Rates and 2B Fluxes and Heating Rates w/ Lidar Process Description and Interface Control Document. Tech. rep., CloudSat Algorithm Process Description Documents.

Heymsfield, A. J., D. Winker, and G. J. van Zadelhoff, 2005: Extinction-ice water content-effective radius algorithms for CALIPSO. *Geophys. Res. Lett.*, **32 (10)**, L10 807, doi: 10.1029/2005GL022742.

Hogan, R., and E. O'Connor, 2004: Facilitating cloud radar and lidar algorithms: The Cloudnet Instrument Synergy/Target Categorization product. Tech. rep., Online, Cloudnet documentation.

Hogan, R. J., 2006: Fast approximate calculation of multiply scattered lidar returns. *Appl. Opt.*, **45 (23)**, 5984–5992, doi: 10.1364/AO.45.005984.

Hogan, R. J., 2008: Fast Lidar and Radar Multiple-Scattering Models. Part I: Small-Angle Scattering Using the Photon Variance–Covariance Method. *J. Atmos. Sci.*, **65 (12)**, 36213635, doi: 10.1175/2008jas2642.1.

Hogan, R. J., and A. J. Illingworth, 2000: Deriving cloud overlap statistics from radar. *Quarterly Journal of the Royal Meteorological Society*, **126 (569)**, 2903–2909, doi: 10.1002/qj.49712656914.

Hogan, R. J., M. P. Mittermaier, and A. J. Illingworth, 2006a: The retrieval of ice water content from radar reflectivity factor and temperature and its use in evaluating a mesoscale model. *J. Appl. Meteor. Climatol.*, **45 (2)**, 301–317, doi: 10.1175/JAM2340.1.

Holben, B., and Coauthors, 1998: AERONET— A Federated Instrument Network and Data Archive for Aerosol Characterization. *Remote Sens. Environ.*, **66 (1)**, 1 – 16, doi: 10.1016/S0034-4257(98)00031-5.

Hollars, S., 2004: Radiative regulations on cloud behaviors in the Tropical Western Pacific. M.S. thesis, Department of Atmospheric Sciences, University of Washington, Seattle.

Hu, Y., and Coauthors, 2009: CALIPSO/CALIOP Cloud Phase Discrimination Algorithm. *J. Atmos. Oceanic Technol.*, **26 (11)**, 2293–2309, doi: 10.1175/2009JTECHA1280.1.

Huang, J., N. C. Hsu, S.-C. Tsay, M.-J. Jeong, B. N. Holben, T. A. Berkoff, and E. J. Welton, 2011: Susceptibility of aerosol optical thickness retrievals to thin cirrus contamination during the BASE-ASIA campaign. *J. Geophys. Res.*, **116 (D8)**, doi: 10.1029/2010jd014910.

Huang, J., and Coauthors, 2012: Evaluations of cirrus contamination and screening in ground aerosol observations using collocated lidar systems. *J. Geophys. Res.*, **117 (D15)**, doi: 10.1029/2012jd017757.

Hunt, W. H., D. M. Winker, M. A. Vaughan, K. A. Powell, P. L. Lucker, and C. Weimer, 2009: CALIPSO Lidar Description and Performance Assessment. *J. Atmos. Oceanic Technol.*, **26 (7)**, 1214–1228, doi: 10.1175/2009JTECHA1223.1.

Immler, F., K. Krger, S. Tegtmeier, M. Fujiwara, P. Fortuin, G. Verver, and O. Schrems, 2007: Cirrus clouds, humidity, and dehydration in the tropical tropopause layer observed at Paramaribo, Suriname (5.8N, 55.2W). *J. Geophys. Res.*, **112 (D3)**, doi: 10.1029/2006jd007440.

Jain, R., R. Kasturi, and B. G. Schunck, 1995: *Machine vision*. McGraw-Hill New York, 549 pp.

Johnson, R. H., T. M. Rickenbach, S. A. Rutledge, P. E. Ciesielski, and W. H. Schubert, 1999: Trimodal Characteristics of Tropical Convection. *J. Climate*, **12 (8)**, 2397–2418, doi: 10.1175/1520-0442(1999)012<2397:TCOTC>2.0.CO;2.

Kacenelenbogen, M., and Coauthors, 2014: An evaluation of CALIOP/CALIPSOs aerosol-above-cloud detection and retrieval capability over North America. *J. Geophys. Res.*, **119 (1)**, 230244, doi: 10.1002/2013jd020178.

Kahn, R. A., M. J. Garay, D. L. Nelson, K. K. Yau, M. A. Bull, B. J. Gaitley, J. V. Martonchik, and R. C. Levy, 2007: Satellite-derived aerosol optical depth over dark water from MISR and MODIS: Comparisons with AERONET and implications for climatological studies. *J. Geophys. Res.*, **112 (D18)**, doi: 10.1029/2006jd008175.

Kanitz, T., and Coauthors, 2014: Surface matters: limitations of CALIPSO V3 aerosol typing in coastal regions. *Atmos. Meas. Tech.*, **7 (7)**, 20612072, doi: 10.5194/amt-7-2061-2014.

Kato, S., N. G. Loeb, D. A. Rutan, F. G. Rose, S. Sun-Mack, W. F. Miller, and Y. Chen, 2012: Uncertainty Estimate of Surface Irradiances Computed with MODIS-, CALIPSO-, and CloudSat-Derived Cloud and Aerosol Properties. *Surveys In Geophysics*, **33 (3-4)**, 395–412, doi: 10.1007/s10712-012-9179-x.

Kato, S., S. Sun-Mack, W. F. Miller, F. G. Rose, Y. Chen, P. Minnis, and B. A. Wielicki, 2010: Relationships among cloud occurrence frequency, overlap, and effective thickness derived from CALIPSO and CloudSat merged cloud vertical profiles. *J. Geophys. Res.*, **115**, D00H28, doi: 10.1029/2009JD012277.

Kato, S., and Coauthors, 2011: Improvements of top-of-atmosphere and surface irradiance computations with CALIPSO-, CloudSat-, and MODIS-derived cloud and aerosol properties. *J. Geophys. Res.*, **116**, D19 209, doi: 10.1029/2011JD016050.

Kaufman, Y., and Coauthors, 2005: A critical examination of the residual cloud contamination and diurnal sampling effects on MODIS estimates of aerosol over ocean. *IEEE Transactions on Geoscience and Remote Sensing*, **43 (12)**, 28862897, doi: 10.1109/tgrs.2005.858430.

Kaufman, Y. J., G. P. Gobbi, and I. Koren, 2006: Aerosol climatology using a tunable spectral variability cloud screening of AERONET data. *Geophys. Res. Lett.*, **33 (7)**, doi: 10.1029/2005gl025478.

Kingston, R., 1978: *Detection of Optical and Infrared Radiation*. Springer-Verlag.

Klein, S. A., and Coauthors, 2009: Intercomparison of model simulations of mixed-phase clouds observed during the ARM Mixed-Phase Arctic Cloud Experiment. I: single-layer cloud. *Quart. J. Roy. Meteor. Soc.*, **135 (641)**, 9791002, doi: 10.1002/qj.416.

Klett, J. D., 1981: Stable analytical inversion solution for processing lidar returns. *Appl. Opt.*, **20 (2)**, 211–220, doi: 10.1364/AO.20.000211.

Kratz, D. P., and F. G. Rose, 1999: Accounting for molecular absorption within the spectral range of the CERES window channel. *J. Quant. Spectrosc. Radiat. Transfer*, **61 (1)**, 83–95, doi: 10.1016/S0022-4073(97)00203-3.

Kunkel, K. E., and J. A. Weinman, 1976: Monte Carlo Analysis of Multiply Scattered Lidar Returns. *J. Atmos. Sci.*, **33 (9)**, 17721781, doi: 10.1175/1520-0469(1976)033<1772:mcaoms>2.0.co;2.

Lanzante, J., 1996: Resistant, robust and non-parametric techniques for the analysis of climate data: Theory and examples, including applications to historical radiosonde station data. *Int. J. Climatol.*, **16 (11)**, 1197–1226, doi: 10.1002/(SICI)1097-0088(199611)16:11<1197::AID-JOC89>3.0.CO;2-L.

Lebsock, M. D., and T. S. L'Ecuyer, 2011: The retrieval of warm rain from CloudSat. *J. Geophys. Res.*, **116**, D20 209, doi: 10.1029/2011JD016076.

L'Ecuyer, T. S., and J. H. Jiang, 2010: Touring the atmosphere aboard the A-Train. *Physics Today*, **63 (7)**, 070 000, doi: 10.1063/1.3463626.

L'Ecuyer, T. S., N. B. Wood, T. Haladay, G. L. Stephens, and J. Stackhouse, Paul W., 2008: Impact of clouds on atmospheric heating based on the R04 CloudSat fluxes and heating rates data set. *J. Geophys. Res.*, **113**, D00A15, doi: 10.1029/2008JD009951.

Lhermitte, R., 1990: Attenuation and Scattering of Millimeter Wavelength Radiation By Clouds and Precipitation. *J. Atmos. Oceanic Technol.*, **7 (3)**, 464–479, doi: 10.1175/1520-0426(1990)007<0464:AASOMW>2.0.CO;2.

Liljegren, J. C., and B. M. Lesht, 1996: Measurements of integrated water vapor and cloud liquid water from microwave radiometers at the DOE ARM Cloud and Radiation Testbed in the U.S. Southern Great Plains. *Presented at the IEEE International Geosciences and Remote Sensing Symposium (IGARSS)*, Lincoln, NB, USA.

Lilly, D. K., 1988: Cirrus Outflow Dynamics. *J. Atmos. Sci.*, **45 (10)**, 1594–1605, doi: 10.1175/1520-0469(1988)045<1594:COD>2.0.CO;2.

Lin, L., Q. Fu, H. Zhang, J. Su, Q. Yang, and Z. Sun, 2013: Upward mass fluxes in tropical upper troposphere and lower stratosphere derived from radiative transfer calculations. *J. Quant. Spectrosc. Radiat. Transfer*, **117 (0)**, 114–122, doi: 10.1016/j.jqsrt.2012.11.016.

Liou, K.-N., 1986: Influence of Cirrus Clouds on Weather and Climate Processes: A Global Perspective. *Mon. Wea. Rev.*, **114 (6)**, 1167–1199, doi: 10.1175/1520-0493(1986)114<1167:IOCCOW>2.0.CO;2.

Liou, K. N., Q. Fu, and T. P. Ackerman, 1988: A Simple Formulation of the Delta-4-stream Approximation For Radiative-transfer Parameterizations. *J. Atmos. Sci.*, **45 (13)**, 1940–1947, doi: 10.1175/1520-0469(1988)045<1940:ASFOTD>2.0.CO;2.

Liu, C., and A. J. Illingworth, 2000: Towards more accurate retrievals of ice water content from radar measurement of clouds. *J. Appl. Meteor.*, **39**, 1130–1146, doi: 10.1175/1520-0450(2000)039<1130:TMAROI>2.0.CO;2.

Liu, Z., R. Marchand, and T. Ackerman, 2010a: A comparison of observations in the tropical western Pacific from ground-based and satellite millimeter-wavelength cloud radars. *J. Geophys. Res.*, **115 (D24)**, doi: 0.1029/2009JD013575.

Liu, Z., N. Sugimoto, and T. Murayama, 2002: Extinction-To-Backscatter Ratio of Asian Dust Observed With High-Spectral-Resolution Lidar and Raman Lidar. *Appl. Opt.*, **41 (15)**, 2760, doi: 10.1364/ao.41.002760.

Liu, Z., and Coauthors, 2009: The CALIPSO Lidar Cloud and Aerosol Discrimination: Version 2 Algorithm and Initial Assessment of Performance. *J. Atmos. Oceanic Technol.*, **26 (7)**, 1198–1213, doi: 10.1175/2009JTECHA1229.1.

Liu, Z., and Coauthors, 2010b: The CALIPSO Cloud And Aerosol Discrimination: Version 3 Algorithm And Test Results. *25th International Laser Radar Conference.*

Lo, C., J. Comstock, and C. Flynn, 2006: An Atmospheric Radiation Measurement Value-Added Product to Retrieve Optically Thin Cloud Visible Optical Depth using Micropulse Lidar. Tech. Rep. DOE/SC-ARM/TR-077, U.S. Department of Energy.

Luke, E. P., P. Kollias, and M. D. Shupe, 2010: Detection of supercooled liquid in mixed-phase clouds using radar Doppler spectra. *J. Geophys. Res.*, **115 (D19)**, doi: 10.1029/2009jd012884.

Luo, Y., K.-M. Xu, H. Morrison, G. M. McFarquhar, Z. Wang, and G. Zhang, 2008: Multi-layer arctic mixed-phase clouds simulated by a cloud-resolving model: Comparison with ARM observations and sensitivity experiments. *J. Geophys. Res.*, **113 (D12)**, doi: 10.1029/2007JD009563.

Magono, C., 1953: On the growth of snow flakes and graupel. *Sci. Rep. Yokohama Natl. Univ.*, **2**, 18–40.

Malinka, A. V., and E. P. Zege, 2003: Analytical Modeling of Raman Lidar Return, Including Multiple Scattering. *Appl. Opt.*, **42 (6)**, 1075, doi: 10.1364/ao.42.001075.

Manton, M. J., and W. R. Cotton, 1977: Formulation of approximate equations for modeling moist deep convection on the mesoscale. Tech. rep., Colorado State University.

Marchand, R., G. G. Mace, T. Ackerman, and G. Stephens, 2008: Hydrometeor Detection Using Cloudsat— An Earth-Orbiting 94-GHz Cloud Radar. *J. Atmos. Oceanic Technol.*, **25 (4)**, 519–533, doi: 10.1175/2007JTECHA1006.1.

Massie, S. T., J. Gille, C. Craig, R. Khosravi, J. Barnett, W. Read, and D. Winker, 2010: HIRDLS and CALIPSO observations of tropical cirrus. *J. Geophys. Res.*, **115**, D00H11, doi: 10.1029/2009JD012100.

Mather, J. H., and S. A. McFarlane, 2009: Cloud classes and radiative heating profiles at the Manus and Nauru Atmospheric Radiation Measurement (ARM) sites. *J. Geophys. Res.*, **114**, D19 204, doi: 10.1029/2009JD011703.

Mather, J. H., S. A. McFarlane, M. A. Miller, and K. L. Johnson, 2007: Cloud properties and associated radiative heating rates in the tropical western Pacific. *J. Geophys. Res.*, **112 (D5)**, D05 201, doi: 10.1029/2006JD007555.

Matthais, V., and Coauthors, 2004: Aerosol Lidar Intercomparison in the Framework of the EARLINET Project. 1. Instruments. *Appl. Opt.*, **43 (4)**, 961–976, doi: 10.1364/AO.43.000961.

Matthias, V., and Coauthors, 2004: Vertical aerosol distribution over Europe: Statistical analysis of Raman lidar data from 10 European Aerosol Research Lidar Network (EARLINET) stations. *J. Geophys. Res.*, **109 (D18)**, doi: 10.1029/2004jd004638.

Mattis, I., A. Ansmann, D. Müller, U. Wandinger, and D. Althausen, 2004: Multiyear aerosol observations with dual-wavelength Raman lidar in the framework of EARLINET. *J. Geophys. Res.*, **109 (D13)**, doi: 10.1029/2004jd004600.

McAuliffe, M. A., and A. A. Ruth, 2013: Typical tropospheric aerosol backscatter profiles for Southern Ireland: The Cork Raman lidar. *Atmos. Res.*, **120-121**, 334342, doi: 10.1016/j.atmosres.2012.09.020.

McClatchey, R., R. W. Fenn, J. E. A. Selby, F. E. Volz, and J. S. Garing, 1972: Optical properties of the atmosphere. Tech. rep., Environmental Research Paper 411, Air Force Cambridge Research Laboratory.

McFarlane, S. A., J. H. Mather, and T. P. Ackerman, 2007: Analysis of tropical radiative heating profiles: A comparison of models and observations. *J. Geophys. Res.*, **112 (D14)**, D14 218–, doi: 10.1029/2006JD008290.

McPherson, C. J., J. A. Reagan, J. Schafer, D. Giles, R. Ferrare, J. Hair, and C. Hostetler, 2010: AERONET, airborne HSRL, and CALIPSO aerosol retrievals compared and combined: A case study. *J. Geophys. Res.*, **115**, doi: 10.1029/2009jd012389.

Measures, R. M., 1984: *Laser Remote Sensing: Fundamentals and Applications.* Krieger.

Melfi, S. H., 1972: Remote Measurements of the Atmosphere Using Raman Scattering. *Appl. Opt.*, **11 (7)**, 1605–1610, doi: 10.1364/AO.11.001605.

Michalsky, J., F. Denn, C. Flynn, G. Hodges, P. Kiedron, A. Koontz, J. Schlemmer, and S. E. Schwartz, 2010: Climatology of aerosol optical depth in north-central Oklahoma: 19922008. *J. Geophys. Res.*, **115 (D7)**, doi: 10.1029/2009jd012197.

Miles, N. L., J. Verlinde, and E. E. Clothiaux, 2000: Cloud Droplet Size Distributions in Low-Level Stratiform Clouds. *J. Atmos. Sci.*, **57 (2)**, 295–311, doi: 10.1175/1520-0469(2000)057<0295:CDSDIL>2.0.CO;2.

Miller, M., K. Johnson, P. Michael, and G. Mace, 2005: MICROBASE, A continuous baseline microphysical retrieval: status and future plans. *Fifteenth ARM Science Team Meeting*, **March 14-18; Daytona Beach, FL**.

Miller, S. W., and W. J. Emery, 1997: An Automated Neural Network Cloud Classifier for Use over Land and Ocean Surfaces. *J. Appl. Meteor.*, **36 (10)**, 13461362, doi: 10.1175/1520-0450(1997)036<1346:aanncc>2.0.co;2.

Miloshevich, L. M., A. Paukkunen, H. Vomel, and S. J. Oltmans, 2004: Development and validation of a time-lag correction for Vaisala radiosonde humidity measurements. *J. Atmos. Oceanic Technol.*, **21 (9)**, 1305–1327, doi: 10.1175/1520-0426(2004)021<1305:DAVOAT>2.0.CO;2.

Miloshevich, L. M., H. Voemel, D. N. Whiteman, and T. Leblanc, 2009: Accuracy assessment and correction of Vaisala RS92 radiosonde water vapor measurements. *J. Geophys. Res.*, **114**, D11 305, doi: 10.1029/2008JD011565.

Mishchenko, M. I., L. Liu, I. V. Geogdzhayev, L. D. Travis, B. Cairns, and A. A. Lacis, 2010: Toward unified satellite climatology of aerosol properties. *J. Quant. Spectrosc. Radiat. Transfer*, **111 (4)**, 540552, doi: 10.1016/j.jqsrt.2009.11.003.

Mona, L., and Coauthors, 2007: Characterization of the variability of the humidity and cloud fields as observed from a cluster of ground-based lidar systems. *Quart. J. Roy. Meteor. Soc.*, **133 (S3)**, 257–271, doi: 10.1002/qj.160.

Morrison, H., and Coauthors, 2009: Intercomparison of model simulations of mixed-phase clouds observed during the ARM Mixed-Phase Arctic Cloud Experiment. II: Multilayer cloud. *Quart. J. Roy. Meteor. Soc.*, **135 (641)**, 10031019, doi: 10.1002/qj.415.

Müller, D., A. Ansmann, I. Mattis, M. Tesche, U. Wandinger, D. Althausen, and G. Pisani, 2007: Aerosol-type-dependent lidar ratios observed with Raman lidar. *J. Geophys. Res.*, **112 (D16)**, doi: 10.1029/2006jd008292.

Murayama, T., 2003: An intercomparison of lidar-derived aerosol optical properties with airborne measurements near Tokyo during ACE-Asia. *J. Geophys. Res.*, **108 (D23)**, doi: 10.1029/2002jd003259.

Murayama, T., and Coauthors, 2001: Ground-based network observation of Asian dust events of April 1998 in east Asia. *J. Geophys. Res.*, **106 (D16)**, 18 345–18 359, doi: 10.1029/2000JD900554.

Newsom, R., 2009: Raman Lidar (RL) Handbook. Tech. Rep. DOE/SC-ARM/TR-038, U.S. Department of Energy.

Newsom, R. K., D. D. Turner, and J. E. M. Goldsmith, 2013: Long-Term Evaluation of Temperature Profiles Measured by an Operational Raman Lidar. *J. Atmos. Oceanic Technol.*, 1616–1634, doi: 10.1175/JTECH-D-12-00138.1.

Newsom, R. K., D. D. Turner, B. Mielke, M. Clayton, R. Ferrare, and C. Sivaraman, 2009: Simultaneous analog and photon counting detection for Raman lidar. *Appl. Opt.*, **48 (20)**, 3903–3914, doi: 10.1364/AO.48.003903.

Noel, V., and H. Chepfer, 2010: A global view of horizontally oriented crystals in ice clouds from Cloud-Aerosol Lidar and Infrared Pathfinder Satellite Observation (CALIPSO). *J. Geophys. Res.*, **115**, doi: 10.1029/2009jd012365.

Oliver, B. M., 1965: Thermal and quantum noise. *Proc. IEEE*, **53 (5)**, doi: 10.1109/PROC.1965.3814.

Omar, A. H., J.-G. Won, D. M. Winker, S.-C. Yoon, O. Dubovik, and M. P. McCormick, 2005: Development of global aerosol models using cluster analysis of Aerosol Robotic Network (AERONET) measurements. *J. Geophys. Res.*, **110 (D10)**, doi: 10.1029/2004jd004874.

Omar, A. H., and Coauthors, 2009: The CALIPSO Automated Aerosol Classification and Lidar Ratio Selection Algorithm. *J. Atmos. Oceanic Technol.*, **26 (10)**, 19942014, doi: 10.1175/2009jtecha1231.1.

Ono, A., 1969: The Shape and Riming Properties of Ice Crystals in Natural Clouds. *J. Atmos. Sci.*, **26 (1)**, 138–147, doi: 10.1175/1520-0469(1969)026<0138:TSARPO>2.0.CO;2.

Pal, S. R., and A. I. Carswell, 1976: Multiple scattering in atmospheric clouds: lidar observations. *Appl. Opt.*, **15 (8)**, 1990, doi: 10.1364/ao.15.001990.

Pappalardo, G., and Coauthors, 2010: EARLINET correlative measurements for CALIPSO: First intercomparison results. *J. Geophys. Res.*, **115**, doi: 10.1029/2009jd012147.

Platnick, S., M. King, S. Ackerman, W. Menzel, B. Baum, J. Riedi, and R. Frey, 2003: The MODIS cloud products: algorithms and examples from Terra. *IEEE Trans. Geosci. Remote Sens.*, **41 (2)**, 459–473, doi: 10.1109/TGRS.2002.808301.

Platt, C. M. R., 1973: Lidar and Radioinetric Observations of Cirrus Clouds. *J. Atmos. Sci.*, **30 (6)**, 1191–1204, doi: 10.1175/1520-0469(1973)030<1191:LAROOC>2.0.CO;2.

Platt, C. M. R., 1978: Lidar Backscatter from Horizontal Ice Crystal Plates. *J. Appl. Meteor.*, **17 (4)**, 482488, doi: 10.1175/1520-0450(1978)017<0482:lbfhic>2.0.co;2.

Powell, K., M. Vaughan, R. Rogers, R. Kuehn, W. Hunt, K. Lee, and T. Murray, 2010: The CALIOP 532-nm Channel Daytime Calibration: Version 3 Algorithm. *25th International Laser Radar Conference.*

Preiler, J., F. Wagner, J. L. Guerrero-Rascado, and A. M. Silva, 2013: Two years of free-tropospheric aerosol layers observed over Portugal by lidar. *J. Geophys. Res.*, **118 (9)**, 36763686, doi: 10.1002/jgrd.50350.

Protat, A., J. Delanoe, D. Bouniol, A. J. Heymsfield, A. Bansemer, and P. Brown, 2007: Evaluation of ice water content retrievals from cloud radar reflectivity and temperature using a large airborne in situ microphysical database. *J. Appl. Meteor. Climatol.*, **46 (5)**, 557–572, doi: 10.1175/JAM2488.1.

Protat, A., J. Delanoë, E. J. O'Connor, and T. S. L'Ecuyer, 2010: The Evaluation of CloudSat and CALIPSO Ice Microphysical Products Using Ground-Based Cloud Radar and Lidar Observations. *J. Atmos. Oceanic Technol.*, **27 (5)**, 793–810, doi: 10.1175/2009JTECHA1397.1.

Rambukkange, M. P., J. Verlinde, E. W. Eloranta, C. J. Flynn, and E. E. Clothiaux, 2011: Using Doppler Spectra to Separate Hydrometeor Populations and Analyze Ice Precipitation in Multilayered Mixed-Phase Clouds. *IEEE Geoscience and Remote Sensing Letters*, **8 (1)**, 108112, doi: 10.1109/lgrs.2010.2052781.

Raymond, D. J., 2000: The Hadley circulation as a radiative-convective instability. *J. Atmos. Sci.*, **57 (9)**, 1286–1297, doi: 10.1175/1520-0469(2000)057<1286:THCAAR>2.0.CO;2.

Reagan, J. A., M. V. Apte, A. Ben-David, and B. M. Herman, 1988: Assessment of Aerosol Extinction to Backscatter Ratio Measurements Made at 694.3 nm in Tucson, Arizona. *Aerosol Science and Technology*, **8 (3)**, 215–226, doi: 10.1080/02786828808959184.

Reichardt, J., 1999: Optical and geometrical properties of northern midlatitude cirrus clouds observed with a UV Raman lidar. *Physics and Chemistry of the Earth, Part B: Hydrology, Oceans and Atmosphere*, **24 (3)**, 255260, doi: 10.1016/s1464-1909(98)00047-1.

Reichardt, J., S. Reichardt, A. Behrendt, and T. J. McGee, 2002: Correlations among the optical properties of cirrus-cloud particles: Implications for spaceborne remote sensing. *Geophys. Res. Lett.*, **29 (14)**, 13–1–13–4, doi: 10.1029/2002GL014836.

Riihimaki, L. D., S. A. McFarlane, and J. M. Comstock, 2012: Climatology and Formation of Tropical Midlevel Clouds at the Darwin ARM Site. *J. Climate*, **25 (19)**, 6835–6850, doi: 10.1175/JCLI-D-11-00599.1.

Robinson, S. S., 2007: Improvements to the cirrus radiative properties parameterization in the

Fu-Liou Radiation Model and an evaluation of its dependence on ice crystal shape. M.S. thesis, University of Washington.

Rogers, R. R., and Coauthors, 2009: NASA LaRC airborne high spectral resolution lidar aerosol measurements during MILAGRO: observations and validation. *Atmos. Chem. Phys.*, **9 (14)**, 48114826, doi: 10.5194/acp-9-4811-2009.

Rogers, R. R., and Coauthors, 2011: Assessment of the CALIPSO Lidar 532 nm attenuated backscatter calibration using the NASA LaRC airborne High Spectral Resolution Lidar. *Atmos. Chem. Phys.*, **11 (3)**, 12951311, doi: 10.5194/acp-11-1295-2011.

Rose, F., and T. Charlock, 2002: New Fu-Liou code tested with ARM Raman lidar and CERES in pre-CALIPSO exercise. *Extended Abstract for 11th Conference on Atmospheric Radiation (AMS)*, Ogden, UT, USA, 3-7.

Rossow, W. B., and R. A. Schiffer, 1999: Advances in Understanding Clouds from ISCCP. *Bull. Amer. Meteor. Soc.*, **80**, 2261–2287, doi: 10.1175/1520-0477(1999)080<2261:AIUCFI>2.0.CO;2.

Russell, I., James M., and Coauthors, 1993: The Halogen Occultation Experiment. *J. Geophys. Res.*, **98 (D6)**, 10 777–10 797, doi: 10.1029/93JD00799.

Sakai, T., T. Nagai, M. Nakazato, Y. Mano, and T. Matsumura, 2003: Ice Clouds and Asian Dust Studied with Lidar Measurements of Particle Extinction-to-Backscatter Ratio, Particle Depolarization, and Water-Vapor Mixing Ratio over Tsukuba. *Appl. Opt.*, **42 (36)**, 7103, doi: 10.1364/ao.42.007103.

Sakai, T., and Coauthors, 2002: Case study of Raman lidar measurements of Asian dust events in 2000 and 2001 at Nagoya and Tsukuba, Japan. *Atmos. Environ.*, **36 (35)**, 54795489, doi: 10.1016/s1352-2310(02)00664-7.

Sassen, K., 1991: The Polarization Lidar Technique for Cloud Research: A Review and Current Assessment. *Bull. Amer. Meteor. Soc.*, **72 (12)**, 1848–1866, doi: 10.1175/1520-0477(1991)072<1848:TPLTFC>2.0.CO;2.

Sassen, K., 2002: Indirect climate forcing over the western US from Asian dust storms. *Geophysical Research Letters*, **29 (10)**, 103–1–103–4, doi: 10.1029/2001GL014051.

Sassen, K., and J. Comstock, 2001: A Midlatitude Cirrus Cloud Climatology from the Facility for Atmospheric Remote Sensing. Part III: Radiative Properties. *J. Atmos. Sci.*, **58**, 2112–2127, doi: 10.1175/1520-0469(2001)058<2113:AMCCCF>2.0.CO;2.

Schmid, B., and Coauthors, 2006: How well do state-of-the-art techniques measuring the vertical profile of tropospheric aerosol extinction compare? *J. Geophys. Res.*, **111 (D5)**, doi: 10.1029/2005jd005837.

Schmidt, J., U. Wandinger, and A. Malinka, 2013: Dual-field-of-view Raman lidar measurements for the retrieval of cloud microphysical properties. *Appl. Opt.*, **52 (11)**, 2235, doi: 10.1364/ao.52.002235.

Segelstein, D. J., 1981: The complex refractive index of water. M.S. thesis, University of Missouri– Kansas City.

Shupe, M. D., 2007: A ground-based multisensor cloud phase classifier. *Geophys. Res. Lett.*, **34 (22)**, L22 809, doi: 10.1029/2007GL031008.

Shupe, M. D., S. Y. Matrosov, and T. Uttal, 2006: Arctic Mixed-Phase Cloud Properties Derived from Surface-Based Sensors at SHEBA. *J. Atmos. Sci.*, **63 (2)**, 697711, doi: 10.1175/jas3659.1.

Sicard, M., and Coauthors, 2011: Seasonal variability of aerosol optical properties observed by means of a Raman lidar at an EARLINET site over Northeastern Spain. *Atmos. Chem. Phys.*, **11 (1)**, 175190, doi: 10.5194/acp-11-175-2011.

Slingo, A., 1989: A GCM Parameterization For the Shortwave Radiative Properties of Water Clouds. *J. Atmos. Sci.*, **46 (10)**, 1419–1427, doi: 10.1175/1520-0469(1989)046<1419:AGPFTS>2.0.CO;2.

Slingo, A., and J. M. Slingo, 1988: The Response of A General Circulation Model To Cloud

Longwave Radiative Forcing. 1. Introduction and Initial Experiments. *Quart. J. Roy. Meteor. Soc.*, **114 (482)**, 1027–1062, doi: 10.1002/qj.49711448209.

Slingo, J. M., and A. Slingo, 1991: The Response of A General Circulation Model To Cloud Longwave Radiative Forcing .2. Further studies. *Quart. J. Roy. Meteor. Soc.*, **117 (498)**, 333–364, doi: 10.1002/qj.49711749805.

Smirnov, A., B. Holben, T. Eck, O. Dubovik, and I. Slutsker, 2000: Cloud-Screening and Quality Control Algorithms for the AERONET Database. *Remote Sens. Environ.*, **73 (3)**, 337349, doi: 10.1016/s0034-4257(00)00109-7.

Spinhirne, J. D., W. D. Hart, and D. L. Hlavka, 1996: Cirrus Infrared Parameters and Shortwave Reflectance Relations from Observations. *J. Atmos. Sci.*, **53 (10)**, 1438–1458, doi: 10.1175/1520-0469(1996)053<1438:CIPASR>2.0.CO;2.

Stephens, G. L., 2005: Cloud feedbacks in the climate system: A critical review. *J. Climate*, **18 (2)**, 237–273, doi: 10.1175/JCLI-3243.1.

Stephens, G. L., and Coauthors, 2002: The CloudSat mission and the A-train - A new dimension of space-based observations of clouds and precipitation. *Bull. Amer. Meteor. Soc.*, **83 (12)**, 1771–1790, doi: 10.1175/BAMS-83-12-1771.

Stephens, G. L., and Coauthors, 2012: An update on Earths energy balance in light of the latest global observations. *Nature Geoscience*, **5 (10)**, 691696, doi: 10.1038/ngeo1580.

Stull, R., 2011: Wet-Bulb Temperature from Relative Humidity and Air Temperature. *J. Appl. Meteor. Climatol.*, **50 (11)**, 22672269, doi: 10.1175/jamc-d-11-0143.1.

Sun, W., G. Videen, S. Kato, B. Lin, C. Lukashin, and Y. Hu, 2011: A study of subvisual clouds and their radiation effect with a synergy of CERES, MODIS, CALIPSO, and AIRS data. *J. Geophys. Res.*, **116 (D22)**, doi: 10.1029/2011JD016422.

Swinbank, R., and A. O'Neill, 1994: A Stratosphere-Troposphere Data Assimilation System. *Mon. Wea. Rev.*, **122**, 686, doi: 10.1175/1520-0493(1994)122<0686:ASTDAS>2.0.CO;2.

Tanelli, S., S. Durden, E. Im, K. Pak, D. Reinke, P. Partain, J. Haynes, and R. Marchand, 2008: CloudSat's Cloud Profiling Radar After Two Years in Orbit: Performance, Calibration, and Processing. *IEEE Trans. Geosci. Remote Sens.*, **46 (11)**, 3560 –3573, doi: 10.1109/TGRS.2008.2002030.

Tesche, M., U. Wandinger, A. Ansmann, D. Althausen, D. Mller, and A. H. Omar, 2013: Ground-based validation of CALIPSO observations of dust and smoke in the Cape Verde region. *J. Geophys. Res.*, **118 (7)**, 28892902, doi: 10.1002/jgrd.50248.

Thompson, A. M., J. C. Witte, H. G. J. Smit, S. J. Oltmans, B. J. Johnson, V. W. J. H. Kirchhoff, and F. J. Schmidlin, 2003: Southern Hemisphere Additional Ozonesondes (SHADOZ) 1998-2000 tropical ozone climatology. 1. Comparison with Total Ozone Mapping Spectrometer (TOMS) and ground-based measurements. *J. Geophys. Res.*, doi: 10.1029/2005JD007042.

Thorsen, T. J., and Q. Fu, 2014: Automated retrieval of cloud and aerosol properties from the ARM Raman lidar, part 2: extinction methodology. *J. Atmos. Oceanic Technol., in review.*

Thorsen, T. J., Q. Fu, and J. Comstock, 2011: Comparison of the CALIPSO satellite and ground-based observations of cirrus clouds at the ARM TWP sites. *J. Geophys. Res.*, **116 (D21)**, D21 203, doi: 10.1029/2011JD015970.

Thorsen, T. J., Q. Fu, and J. M. Comstock, 2013a: Cloud effects on radiative heating rate profiles over Darwin using ARM and A-train radar/lidar observations. *J. Geophys. Res.*, **118 (11)**, 5637–5654, doi: 10.1002/jgrd.50476.

Thorsen, T. J., Q. Fu, J. M. Comstock, C. Sivaraman, M. A. Vaughan, D. M. Winker, and D. D. Turner, 2013b: Macrophysical properties of tropical cirrus clouds from the CALIPSO satellite and from ground-based micropulse and Raman lidars. *J. Geophys. Res.*, **118 (16)**, 9209–9220, doi: 10.1002/jgrd.50691.

Thorsen, T. J., Q. Fu, R. K. Newsom, D. D. Turner, and J. M. Comstock, 2014: Automated retrieval of cloud and aerosol properties from the ARM Raman lidar, part 1: feature detection. *J. Atmos. Oceanic Technol., in review.*

Thurai, M., V. N. Bringi, and P. T. May, 2010: CPOL Radar-Derived Drop Size Distribution Statistics of Stratiform and Convective Rain for Two Regimes in Darwin, Australia. *J. Atmos. Oceanic Technol.*, **27 (5)**, 932942, doi: 10.1175/2010jtecha1349.1.

Tobin, D. C., and Coauthors, 1999: Downwelling spectral radiance observations at the SHEBA ice station: Water vapor continuum measurements from 17 to 26 μm. *J. Geophys. Res.*, **104 (D2)**, 2081–2092, doi: 10.1029/1998JD200057.

Turner, D. D., R. A. Ferrare, and L. A. Brasseur, 2001: Average aerosol extinction and water vapor profiles over the Southern Great Plains. *Geophys. Res. Lett.*, **28 (23)**, 4441–4444, doi: 10.1029/2001gl013691.

Turner, D. D., R. A. Ferrare, L. A. H. Brasseur, W. F. Feltz, and T. P. Tooman, 2002: Automated Retrievals of Water Vapor and Aerosol Profiles from an Operational Raman Lidar. *J. Atmos. Oceanic Technol.*, **19 (1)**, 37–50, doi: 10.1175/1520-0426(2002)019<0037:AROWVA>2.0.CO;2.

Turner, D. D., B. M. Lesht, S. A. Clough, J. C. Liljegren, H. E. Revercomb, and D. C. Tobin, 2003: Dry Bias and Variability in Vaisala RS80-H Radiosondes: The ARM Experience. *J. Atmos. Oceanic Technol.*, **20 (1)**, 117–132, doi: 10.1175/1520-0426(2003)020<0117:DBAVIV>2.0.CO;2.

Vaughan, M., and Coauthors, 2010: Strategies for improved CALIPSO aerosol optical depth estimates. *25th International Laser Radar Conference.*

Vaughan, M. A., and Coauthors, 2009: Fully Automated Detection of Cloud and Aerosol Layers in the CALIPSO Lidar Measurements. *J. Atmos. Oceanic Technol.*, **26 (10)**, 2034–2050, doi: 10.1175/2009JTECHA1228.1.

Wandinger, U., 1998: Multiple-Scattering Influence on Extinction-and Backscatter-Coefficient Measurements with Raman and High-Spectral-Resolution Lidars. *Appl. Opt.*, **37 (3)**, 417, doi: 10.1364/ao.37.000417.

Wandinger, U., M. Tesche, P. Seifert, A. Ansmann, D. Mller, and D. Althausen, 2010: Size matters: Influence of multiple scattering on CALIPSO light-extinction profiling in desert dust. *Geophys. Res. Lett.*, **37 (10)**, n/an/a, doi: 10.1029/2010gl042815.

Wang, P.-H., P. Minnis, M. P. McCormick, G. S. Kent, G. K. Yue, D. F. Young, and K. M. Skeens, 1998: A study of the vertical structure of tropical (20°S-20°N) optically thin clouds from SAGE II observations. *Atmos. Res.*, **47-48**, 599 – 614, doi: 10.1016/S0169-8095(97)00085-9.

Wang, Z., and K. Sassen, 2001: Cloud Type and Macrophysical Property Retrieval Using Multiple Remote Sensors. *J. Appl. Meteor.*, **40**, 1665–1682, doi: 10.1175/1520-0450(2001)040<1665:CTAMPR>2.0.CO;2.

Wang, Z., and K. Sassen, 2002: Cirrus cloud microphysical property retrieval using lidar and radar measurements. Part I: Algorithm description and comparison with in situ data. *J. Appl. Meteor.*, **41 (3)**, 218–229, doi: 10.1175/1520-0469(2002)059<2291:CCMPRU>2.0.CO;2.

Whiteman, D. N., 2003: Examination of the Traditional Raman Lidar Technique. I. Evaluating the Temperature-Dependent Lidar Equations. *Appl. Opt.*, **42 (15)**, 2571–2592, doi: 10.1364/AO.42.002571.

Whiteman, D. N., B. Demoz, and Z. Wang, 2004: Subtropical cirrus cloud extinction to backscatter ratios measured by Raman Lidar during CAMEX-3. *Geophys. Res. Lett.*, **31 (12)**, doi: 10.1029/2004GL020003.

Whiteman, D. N., S. H. Melfi, and R. A. Ferrare, 1992: Raman lidar system for the measurement of water vapor and aerosols in the Earth's atmosphere. *Appl. Opt.*, **31 (16)**, 3068–3082, doi: 10.1364/AO.31.003068.

Widener, K., N. Bharadwaj, and K. Johnson, 2012: Ka-Band ARM Zenith Radar (KAZR) Handbook. Tech. Rep. DOE/SC-ARM/TR-038, U.S. Department of Energy.

Wilks, D., 1997: Resampling Hypothesis Tests for Autocorrelated Fields. *J. Climate*, **10**, 65–82, doi: 10.1175/1520-0442(1997)010<0065:RHTFAF>2.0.CO;2.

Winker, D., and M. Vaughan, 1994: Vertical distribution of clouds over Hampton, Virginia observed by lidar under the ECLIPS and FIRE ETO programs. *Atmos. Res.*, **34 (14)**, 117–133, doi: 10.1016/0169-8095(94)90084-1.

Winker, D. M., and C. R. Trepte, 1998: Laminar cirrus observed near the tropical tropopause by LITE. *Geophys. Res. Lett.*, **25 (17)**, 3351–3354, doi: 10.1029/98GL01292.

Winker, D. M., M. A. Vaughan, A. Omar, Y. Hu, K. A. Powell, Z. Liu, W. H. Hunt, and S. A. Young, 2009: Overview of the CALIPSO mission and CALIOP data processing algorithms. *J. Atmos. Oceanic Technol.*, doi: 10.1175/2009JTECHA1281.1.

Winker, D. M., and Coauthors, 2010: The CALIPSO Mission: A Global 3d View Of Aerosols And Clouds. *Bull. Amer. Meteor. Soc.*, doi: 10.1175/2009JTECHA1281.1.

Wiscombe, W. J., 1980: Improved Mie scattering algorithms. *Appl. Opt.*, **19 (9)**, 1505, doi: 10.1364/ao.19.001505.

Wood, R., 2005: Drizzle in stratiform boundary layer clouds. Part II: Microphysical aspects. *J. Atmos. Sci.*, **62 (9)**, 3034–3050, doi: 10.1175/JAS3530.1.

Wulfmeyer, V., S. Pal, D. Turner, and E. Wagner, 2010: Can Water Vapour Raman Lidar Resolve Profiles of Turbulent Variables in the Convective Boundary Layer? *Bound.-Layer Meteor.*, **136 (2)**, 253–284, doi: 10.1007/s10546-010-9494-z.

Yang, Q., Q. Fu, and Y. Hu, 2010: Radiative impacts of clouds in the tropical tropopause layer. *J. Geophys. Res.*, doi: 10.1029/2009JD012393.

Yorks, J. E., D. L. Hlavka, M. A. Vaughan, M. J. McGill, W. D. Hart, S. Rodier, and R. Kuehn, 2011: Airborne validation of cirrus cloud properties derived from CALIPSO lidar measurements: Spatial properties. *J. Geophys. Res.*, **116 (D19)**, doi: 10.1029/2011JD015942.

Young, S. A., 1995: Analysis of lidar backscatter profiles in optically thin clouds. *Appl. Opt.*, **34 (30)**, 7019–7031, doi: 10.1364/AO.34.007019.

Young, S. A., and M. A. Vaughan, 2009: The Retrieval of Profiles of Particulate Extinction from Cloud-Aerosol Lidar Infrared Pathfinder Satellite Observations (CALIPSO)

Data: Algorithm Description. *J. Atmos. Oceanic Technol.*, **26 (6)**, 1105–1119, doi: 10.1175/2008JTECHA1221.1.

Young, S. A., D. M. Winker, M. A. Vaughan, Y. Hu, and R. E. Kuehn, 2008: CALIOP Algorithm Theoretical Basis Document, Part 4: Extinction Retrieval Algorithms. Tech. rep., NASA.

Yu, H., and Coauthors, 2006: A review of measurement-based assessments of the aerosol direct radiative effect and forcing. *Atmos. Chem. Phys.*, **6 (3)**, 613666, doi: 10.5194/acp-6-613-2006.

Zhang, D., Z. Wang, and D. Liu, 2010: A global view of midlevel liquid-layer topped stratiform cloud distribution and phase partition from CALIPSO and CloudSat measurements. *J. Geophys. Res.*, **115 (D4)**, doi: 10.1029/2009JD012143.

Zhang, J., 2005: An analysis of potential cloud artifacts in MODIS over ocean aerosol optical thickness products. *Geophys. Res. Lett.*, **32 (15)**, doi: 10.1029/2005gl023254.

Zhang, Y. C., W. B. Rossow, A. A. Lacis, V. Oinas, and M. I. Mishchenko, 2004: Calculation of radiative fluxes from the surface to top of atmosphere based on ISCCP and other global data sets: Refinements of the radiative transfer model and the input data. *J. Geophys. Res.*, **109 (D19)**, D19 105, doi: 10.1029/2003JD004457.

Zhao, C., and Coauthors, 2012: Toward understanding of differences in current cloud retrievals of ARM ground-based measurements. *J. Geophys. Res.*, **117**, D10 206, doi: 10.1029/2011JD016792.

Zhou, C., P. Yang, A. E. Dessler, Y. Hu, and B. A. Baum, 2012: Study of Horizontally Oriented Ice Crystals with CALIPSO Observations and Comparison with Monte Carlo Radiative Transfer Simulations. *J. Appl. Meteor. Climatol.*, **51 (7)**, 14261439, doi: 10.1175/jamc-d-11-0265.1.

VITA

Tyler J. Thorsen was born on September 9, 1986 in Tucson, Arizona, but spent his formative years in Southington, Connecticut. As a young-pup Tyler developed an interest in weather. Tyler pursued this interest, leaving the good people from the great state of Connecticut to attend the Pennsylvania State University in August 2004. There his interest in weather shifted to focus more on the physics of the atmosphere. Tyler's first foray into research was performing radiative transfer calculations in stratocumulus clouds under the guidance of Professor Eugene Clothiaux. In May 2008, Tyler graduated with distinction from the Pennsylvania State University with a Bachelor of Science in meteorology and minor in mathematics.

Tyler began his graduate studies in September 2008 at the University of Washington under the direction of Professor Qiang Fu. His work in graduate school centered around lidar remote sensing with a particular focus on tropical cirrus clouds and Raman lidar systems. Tyler completed his Ph.D. in fall of 2014. Tyler is the recipient of a NASA postdoctorate fellowship and will perform research as part of the NASA CERES science team in Langley, Virginia.